



UNIVERSITAT
POLITÈCNICA
DE VALÈNCIA



UNIVERSITAT POLITÈCNICA DE VALÈNCIA

DEPARTAMENTO DE MÁQUINAS Y MOTORES TÉRMICOS

PhD Thesis

**The Eulerian-Lagrangian Spray Atomization
(ELSA) Model of the Jet Atomization in CFD
Simulations: Evaluation and Validation**

Presented by:

KHUONG Anh Dung

Directed by:

Dr. Sergio Hoyas

**A dissertation submitted for the degree of
Doctor of Industrial Engineering**

Valencia, September 2012



UNIVERSITAT
POLITÈCNICA
DE VALÈNCIA



UNIVERSITAT POLITÈCNICA DE VALÈNCIA

DEPARTAMENTO DE MÁQUINAS Y MOTORES TÉRMICOS

Tesis Doctoral

**El método ELSA de atomización de chorros en
simulaciones de dinámica de fluidos
computacional: evaluación y validación**

Presentada por:

KHUONG Anh Dung

Dirigida por:

Dr. Sergio Hoyas

Para la obtención del título de:

Doctor Ingeniero Industrial

Valencia, Septiembre 2012

Yo, Dr. Sergio Hoyas Calvo, doctor en Matemática Aplicada por la Universidad Complutense de Madrid, Profesor Titular del Departamento de Máquinas y Motores Térmicos y miembro del Instituto de Investigación CMT-Motores Térmicos, ambos pertenecientes a la Universitat Politècnica de València, como Director de tesis,

CERTIFICA:

Que D. Khuong-Anh Dung, Ingeniero Industrial por la Universidad de Ho-Chi Minh City, Vietnam, ha realizado la presente Tesis doctoral, “El método ELSA de atomización de chorros en simulaciones de dinámica de fluidos computacional: evaluación y validación” y que a su juicio reúne plenamente todos los requisitos necesarios para optar al Grado de Doctor a cuyos efectos será presentado en la Universitat Politècnica de València. El trabajo ha sido realizado bajo su dirección, autorizando su presentación ante el Tribunal Calificador. Y para que así conste se extiende el presente certificado,

Supervisor by:

Dr. Sergio Hoyas

Committee members attending the Dissertation Defense:

President: Prof. Dr. Jesús Benajes Calvo

Secretary: Prof. Dr. Raúl Payri

Members: Prof. Dr. Juan José Hernandez

Assoc. Prof. Dr. Blanca Giménez

Dr. Frédéric Ravet

ABSTRACT

The Eulerian-Lagrangian Spray Atomization (ELSA) model of the jet atomization in the CFD Simulations: Evaluation and Validation

Fuel sprays play a major role in order to achieve the required combustion characteristics and pollutant emissions reduction on internal combustion engines, and thus, an accurate prediction of its behavior is required to perform reliable engine combustion and pollutant simulations. A great effort both on experimental and theoretical studies of spray atomization and dispersion has been performed in the latest years. As a result, Computational Fluid Dynamics (CFD) calculations have become a standard tool not only for spray physics understanding but also for design and optimization of engine spray systems.

However, spray modeling in its different uses in the Internal Combustion Engine (ICE) context is still nowadays a challenging task due to the complex interrelated phenomena taking place, some of them still not fully understood. Primary atomization and secondary breakup, droplet collision, coalescence and vaporization, turbulent interactions between phases have to be solved under high Reynolds (so they are turbulent) and Weber numbers conditions due to the high speed (~ 500 m/s) and small nozzle diameter (~ 100 μm) imposed by current engine injection systems technologies. Moreover, Taylor numbers cover a wide range, according to the composition of the injected liquid. Those conditions make experimental observations quite challenging and probably insufficient, especially in the very near nozzle region, where primary atomization takes place.

Most of the CFD spray models are currently based on the Discrete Droplet Method. The continuous liquid jet is discretized into 'blobs' or 'parcels', which consists in a number of droplets with the same characteristics. A Lagrangian method is applied to track the liquid phase parcels, which are subject to breakup according to atomization models mainly based on the linear instability theory proposed by Reitz and later extended by Huh and Gosman for liquid turbulence effects to be considered. This approach has been successfully

Abstract

applied because it is computationally efficient and at the same time is able to provide reasonable agreements with experimental measurements. However, it requires extensive calibration, being this requirement its main drawback, which is caused, on the one hand, by the semi-empirical nature of the liquid phase sub-models, and, on the other hand, for both physical and numerical limitations on the near nozzle dense sprays region description.

In order to enhance Computational Fluid Dynamics (CFD) spray simulations, the ELSA model has been developed in recent years. Renault SA has integrated it very recently into the Star-CD CFD code. ELSA model is based on an Eulerian approach for the description of the dense spray region, where standard Discrete Droplet Model (DDM) method is not able to describe the flow. Within the diluted spray region, the ELSA model could switch to the traditional Lagrangian description of the liquid phase, taking advantage from well-established and previously developed sub-models. The goal of the ELSA model is to realistically describe the dense zone of the spray and the spray atomization.

According to the previous statements, the first purpose of this PhD thesis has been to perform a validation of the ELSA spray model implemented in the Star-CD code and check it against CMT-Motores Térmicos Institute database. This validation has been made for several engine conditions (evaporative or non-evaporative, cavitating nozzles, cold starting chamber, etc). In all cases, the ELSA model gave accurate and reasonable results, once a proper mesh is made.

After this validation, an extensive evaluation of the model in 3D has been made. Probably, the most important result of the thesis is the coupling between a flow coming from a cavitating nozzle (obtained in CMT by other researchers) and the spray. It is worthy to note that this was impossible with the methods described before, due to the first cell in DDM method has to be bigger than the nozzle. The results obtained in this 3D cavitating flow evaluation have also been quite satisfactory, and it has been possible to study the system nozzle-spray as a whole, without any fictitious velocity to model the cavitation effects.

RESUMEN

El modelo ELSA de atomización de chorros en simulaciones CFD: Evaluación y validación

La dinámica de fluidos computacional es una herramienta cada vez más útil para el análisis de procesos termo-fluido dinámicos. En el caso que nos preocupa, la atomización del chorro Diesel, el combustible sale de un pequeño orificio de forma líquida y se atomiza para después evaporarse, momento en el que se produce la combustión. Este proceso es ya de por sí muy complicado, habiendo efectos que todavía no están totalmente aclarados. A esta complicación se le añade el problema de la modelización de la turbulencia, ya que una simulación directa se queda fuera de los recursos del grupo de investigación.

El modelo ELSA (Eulerian-Lagrangian Spray Atomization) ha sido desarrollado durante los últimos 15 años y es un intento de poder modelar de forma realista este proceso, esencial para poder modelar correctamente la combustión. Este modelo ha sido recientemente implementado en el código de simulación de fluido dinámica Star-CD. El propósito del presente estudio es la mejora de las simulaciones CFD de chorros Diesel en el marco del este modelo. Concretamente, el objetivo general de la tesis es evaluar y validar esta nueva herramienta computacional de chorro, con aplicación práctica en los cálculos CFD del motor. Dentro de este objetivo general, se incluye evaluar y validar los diferentes sub-modelos que representan los fenómenos involucrados en la formación del chorro Diesel y en el desarrollo del mismo, desde la sección de la tobera hasta la evaporación completa del combustible, incluyendo la posible cavitación del combustible en la tobera.

El objetivo es centrarse en el acoplamiento y la coherencia entre los diferentes sub-modelos en lugar de en los procesos del chorro de forma aislada. Se propone hacer hincapié en la transición del flujo de la tobera interna para los cálculos iniciales del desarrollo del chorro. El trabajo también se centrará en la integración adecuada de los sub-modelos utilizados para la

Resumen

descripción de la región densa y diluida, en términos de ruptura de la vena líquida, la coalescencia, vaporización y evolución de las gotas.

Para poder llevar a cabo con éxito la investigación se ha realizado primero un exhaustivo análisis 2D del chorro, incluyendo parámetros de la modelización de la turbulencia, construyéndose después una simulación 3D de 360° en una tobera no cavitante. Por último, se ha realizado el acople con una tobera cavitante, que ha sido muy estudiada en nuestro instituto. En todos los casos, el comportamiento del modelo ELSA ha sido satisfactorio y los resultados concuerdan razonablemente con los experimentos. Es importante hacer notar que con este método hemos conseguido hacer un modelo completo del sistema tobera-chorro, sin necesidad de modelar el efecto de la cavitación por una velocidad ficticia.

RESUM

El model ELSA d'atomització de dolls en simulacions CFD: Avaluació i validació

La dinàmica de fluids computacional és una ferramenta cada vegada més útil per a l'anàlisi de processos termo-fluid dinàmics. En el cas que ens preocupa, l'atomització del doll Dièsel, el combustible ix de forma líquida d'un orifici menut i s'atomitza per a després evaporar-se, moment en què es produïx la combustió. Aquest procés ja és per si a soles molt complicat, havent-hi efectes que encara no estan totalment aclarits. A esta complicació se li afegix el problema de la modelització de la turbulència, ja que una simulació directa es queda fora dels recursos del grup d'investigació.

El model ELSA (Eulerian-Lagrangian Spray Atomization) ha sigut desenvolupat durant els últims 15 anys en un intent per poder modelar de forma realista aquest procés, essencial per a la correcta simulació de la combustió. El model ha sigut recentment implementat en el codi de simulació fluid dinàmica Star-CD. El propòsit del present estudi és la millora de les simulacions CFD de dolls Dièsel en el marc d'aquest model. Concretament, l'objectiu general de la tesi és avaluar i validar esta nova ferramenta computacional de doll, amb aplicació pràctica en els càlculs CFD del motor. Dins d'aquest objectiu general, s'inclou avaluar i validar els diferents sub-models que representen els fenòmens involucrats en la formació i el desenrotllament del doll Dièsel, des de la secció de la tovera fins a l'evaporació completa del combustible, incloent l'efecte de la possible cavitació del combustible en la tovera.

L'objectiu és fixar-se en l'acoblament i la coherència entre els diferents sub-models en compte de en els processos del doll de forma aïllada. Es proposa remarcar en la transició del flux de la tovera interna per als càlculs inicia'ls del desenrotllament del doll. El treball també se centrarà en la integració adequada dels sub-models utilitzats per a la descripció de la regió densa i diluïda, en termes de ruptura de la vena líquida, la coalescència, vaporització i evolució de les gotes.

Resum

Per a poder dur a terme amb èxit la investigació s'ha realitzat primer una exhaustiva anàlisi 2D del doll, per a incloure després paràmetres de la modelització de la turbulència, a continuació s'ha construït una simulació 3D de 360° en una tovera no cavitant. Finalment, s'ha realitzat l'acoblament amb una tovera cavitant, que ha sigut molt estudiada en el nostre institut. En tots els casos, el comportament del model ELSA ha sigut satisfactori i els resultats concorden raonablement amb els experiments. És important fer notar que amb aquest mètode hem aconseguit fer un model complet del sistema tovera-doll, sense que siga necessari modelar l'efecte de la cavitació fent us d'una velocitat fictícia.

ACKNOWLEDGMENTS

This thesis would not have been completed without the help of many. For all the below named persons and other nameless people involved in my last few years, I express my whole-hearted thanks and appreciation. First of all, the author gratefully appreciates my thesis supervisor, Associate Professor Sergio Hoyas for his advice, views, insights and encouragement during the last three years in both my master and PhD studies at UPV. Especially, he has spent a lot of time to share ideas, revises all papers, reports and thesis as well as answering all my doubts and queries. His instruction helps me to better communicate the scientific ideas, excellence in technical writing, properly presenting in the reports, and sharing the results. I have built my extensive knowledge in turbulence, fluid mechanics and computer science throughout the duration of my research period. He is always ready to help with a smile.

I would like to extend my greatly thanks to Dr. José M. Pastor who plays as an “unofficial” co-supervisor of my PhD thesis, for helping me on many theoretical and numerical simulations, formalizing ideas, technical discussion, comments and especially solving problem arose. He has an ambient knowledge of CFD, Diesel spray and engine modeling that fascinate me.

I wish to thank Dr. Antonio Gil for sharing his understanding and experience in CFD modeling and computer software. He was also the one who collaborated on writing several articles. I am grateful to Ms. Mariany Chavez who has kindly spent time on guiding me through the use of CFD software in internal combustion engine simulations, provided the initial knowledge of spray modeling and generously sharing her knowledge.

In particular, I thank Dr. Frédéric Ravet of Renault SA, France who has been actively proposed many useful suggestions, comments, pursued new directions in my research and fruitful discussions during the ongoing project over face-to-face meeting, e-mail, and video conference.

Acknowledgments

I gratefully acknowledge Dr. Anna Desportes and her team in CD-adapco for the use of latest Star-CD version with ELSA model, for providing user guide on which these simulations is based, and for continuously support and immediate response to all my queries.

My work would be incomplete without the experimental and numerical results obtained by various groups in our institute. As the major aim of this work is to validate the ELSA method with the latest experimental data available, a great collaboration and frequent interaction with other experienced research teams are needed. It leads to the success of the current project. Therefore, I spare a paragraph to thank for all of them who have provided of many experimental data and especially permitted me to use them in my research work and publication as well as for this thesis. Firstly, I would like to express my special thanks to Professor Raul Payri, and Associate Professor Francisco Javier Salvador for providing valuable experimental data, and share their internal flow numerical analysis and cavitation broad knowledge. Secondly, I appreciate the help of Dr. Jaime Gimeno on accessing the experimental database of Diesel sprays under non-evaporating conditions. Thirdly, I am grateful for Mr. Michele Bardi's support on providing experimental results under evaporating conditions. Lastly, I appreciate Mr. Jorge Martínez's help with the numerical analysis of inner cavitating nozzle flow that enable me to couple the internal flow and spray simulations.

I had a chance to work in collaboration with many other VECOM partners including both industrial partners (BMW, FIAT, AVL, IFP, LMS International, Fraunhofer, Arsenal research, and so on) and academic institutes (University of Porto, Politecnico di Torino, Katholieke Universiteit Leuven, Università degli Studi di Firenze, Aristotle University Thessaloniki, Czech Technical University in Prague) and interact with their scientific leaders such as Prof. Jan Macek, Dr. Bert Pluymers, Dr. Kuehnelt Helmut, Dr. Marco Pierini, and Dr. Reinhard Tatsch and over twenty fellows, experience researchers who shared with me a bundle of research activities and knowledge in vehicle modeling. The regularly training, workshop, and meeting by VECOM have helped to update my knowledge, latest technology and refine my presentation skills.

Acknowledgments

In the summer of 2010, as a VECOM fellow, I visited LMS International, and worked with Mr. Marco Gubitosa, and Dr. Ir. Stijn Donders. It provided a great opportunity to work with the LMS Imagine Lab AMESim Suite and couple 1D car simulation with 3D CFD code. I have enjoyed working for the company, especially thanked to his extremely well organized leadership and enthusiasm.

I appreciate the support provided by Prof. Francisco Payri, Prof. Jose M. Desantes Fernandez, and Prof. Jesús Benajes. They played a major role in managing the master course, PhD study and controlling all of my paperwork during my tenure with the research institute.

I have benefited from many papers, lecture notes and many seminars, which were provided and organized by Prof. Antonio Torregrosa. It horns my knowledge in the fields and extend my network with other scientist around the world.

I express my special thanks to Dr. Xandra Margot, the VECOM project coordinator. Her relentless works to ensure that the project outputs is delivered on time and mange many events within the project timeline. I thank to Dr. José Miguel Salavert for providing financial management of the project.

Moreover, I would like to thank following friends and PhD students: Dr. Pablo Fajardo, Mr. Roberto Navarro, Dr. Christopher Kolodziej, Mr. Johannes F. Winklinger, Mr. Simon, Mr. Pau Raga, Dr. Bracho, and Dr. Patouna for their open mindedness and friendship during my stay at CMT-Motores Térmicos, Universitat Politècnica de València and personal life in Valencia.

I have worked with Mr. Juan Manuel Mompó-Laborda in the LES project and we wrote a couple of papers in the numerical field. We shared the same office in these years, thus we are not only sharing the technical knowledge but also many aspects of personal life in daily conversation. He has been my true friend in Valencia. I will never forget his good humor and kindness, encouragement, and friendship. Still, his native Spanish language helps me to solve a bundle of problems in Spain.

I also thank my thesis committee for serving on the board, taking time to read, comment my thesis, and provide valuable feedback.

Acknowledgments

I would like to acknowledge the contribution of administrative staffs: Ricardo Lerma, Amparo Cutillas, M^a Carmen Haba, Elena Lerma, Teresa Martínez, Elvira Roig, Carmina Valero, and María Cristina Salvador who ensure all staff have what they need is an asset to the department. Especially, Julia Benet who has been taking care of my documentation work from the very beginning is deserved special mention.

I also have the honor of acknowledge the financial support of the VECOM project (Vehicle Concept Modeling), the European Community's Seventh Framework Program - EU FP7 Marie Curie Initial Training Network (ITN) Grant Agreement 213543. This project was also funded by Renault SA in the frame of the "validation and application of ELSA model" project. I am also gratefully to CMT-Motores Térmicos, Universitat Politècnica de València (UPV) for their overall help of this research, providing adequate computer power for scientific activities, all other supports and facilities. I would also thanks to the Computer Center of the Universitat Politècnica de València for the use of their facilities.

Last but not least, I would like to express my deeply gratitude to my wife, VU Anh Thu for her love and respect. I am indebted to my wife for being patient, providing me time, fully support in my research stage, and indirect and direct help to complete this thesis. I owe my parents who continuously support my further studying, my academic endeavors and stand by me through my life, any kind of situations and important decisions. My brother and sister-in-law as well as my whole family have been providing a stimulating and fun environment in which to learn and grow.

TABLE OF CONTENTS

Chapter 1 - Introduction.....	1
1.1 Overview and motivation.....	1
1.2 Research objectives & methodology.....	6
1.3 Outline of the thesis	7
Chapter 2 - Spray Fundamentals and CFD spray modeling	9
2.1 Spray fundamentals.....	9
2.1.1 Spray characterization.....	11
2.1.2 Liquid length	13
2.1.3 Spray penetration	13
2.1.4 Spray cone angle.....	13
2.2 Modeling fuel spray.....	14
2.3 Turbulent approaches to simulate turbulent two-phase flows in Diesel sprays	15
2.3.1 Reynolds-averaged Navier-stokes.....	15
2.3.1.1 High Reynolds number $k-\epsilon$ model.....	16
2.3.1.2 RNG $k-\epsilon$	17
2.3.1.3 Chen $k-\epsilon$	17
2.3.2 Large-Eddy Simulation	18
2.3.3 Direct Numerical Simulation	20
2.4 Following droplets: Eulerian or Lagrangian?.....	22
2.4.1 Discrete Droplet Model	23

Table of Contents

2.4.2	Eulerian-Eulerian approach	24
2.4.3	Eulerian–Lagrangian approach.....	24
2.5	Interface Tracking Methods	27
2.5.1	Level set method	27
2.5.2	Ghost Fluid Method	28
2.5.3	Volume Of Fluid.....	29
2.5.4	Other methods.....	31
2.5.5	Numerical tools for liquid spray models	31
Chapter 3 - Eulerian-Lagrangian Spray Atomization (ELSA)		
	Methodology	41
3.1	Overview.....	41
3.2	Mathematical formulation.....	45
3.2.1	Eulerian liquid-spray mixture zone.....	47
3.2.2	Liquid/gas interface density	50
3.2.3	Transition zone and the initialization of the Lagrangian model	53
Chapter 4 - ELSA model validation..... 57		
4.1	Numerical configuration: a practical approach	57
4.1.1	Geometry and computational domain.....	57
4.1.2	Boundary conditions	61
4.2	ELSA assumptions and inputs	64
4.3	2D validation	66
4.3.1	Spray penetration	68
4.3.2	Time steps	70
4.3.3	Schmidt number	71
4.3.4	Generating new parcels.....	74
4.3.5	Turbulent coefficient and models.....	75
4.3.5.1	<i>High Reynolds $k-\varepsilon$ turbulence model</i>	75

Table of Contents

4.3.5.2	<i>RNG k-ε turbulence model</i>	76
4.3.5.3	<i>Chen k-ε turbulence model</i>	78
4.3.5.4	<i>The difference amongst three turbulence models</i>	79
4.3.6	Break-up models.....	80
4.3.7	Weber criteria for the collision.....	83
4.3.8	Non break-up and break-up.....	85
4.3.9	Coalescence.....	86
4.3.10	Injection pressure, chamber pressure and fuels.....	89
4.3.11	Lagrangian vs. ELSA models.....	92
4.3.12	The 2D/3D meshes dependence.....	93
4.4	Evaporating Diesel sprays simulation.....	95
4.4.1	Sandia experimental data.....	97
4.4.1.1	Number of parcels created.....	97
4.4.1.2	Injection pressure.....	99
4.4.1.3	Mixture fraction.....	100
4.4.2	Experimental data from CMT.....	101
4.4.3	Spray A experiments performed at CMT.....	104
4.4.3.1	Injection pressure.....	106
4.4.3.2	Injection temperature.....	109
4.4.3.3	Chamber pressure and density.....	110
4.4.3.4	Chamber temperature.....	111
Chapter 5 - Cavitating nozzles modeling with ELSA.....		117
5.1	Grid dependency.....	123
5.2	Effect of injection pressure.....	125
5.3	Effect of nozzle diameter and velocity input.....	129
5.4	Effects of fuel type.....	131
Chapter 6 - Conclusions and Recommendations.....		139
6.1	Conclusions.....	139
6.2	Recommendations of future work.....	141

Table of Contents

Chapter 7 - List of papers	143
Appendix A – A literature review on Atomization and break-up in Diesel sprays	a
Appendix B - Inlet diameter in CFD sprays modeling.....	ee
Appendix C - Bernoulli velocity in spray modeling	gg
Appendix D - Discharge coefficient.....	ii
Appendix E - Area coefficient and nozzle diameter for low temperature.....	kk
Appendix F - Unit Conversion	ll
Appendix G - Fuel chemical and physical properties	nn
Appendix H - DF2 properties.....	oo

LIST OF FIGURES

Figure 1-1: European Emission standards for Diesel passenger cars: HC (g/kWh) + NO _x (g/kWh) (the plot taken data from [1] and [2]).	1
Figure 1-2: European Emission standards for Diesel passenger cars: PM (g/kWh) (the plot taken data from [1] and [2]).	2
Figure 1-3: Historical and forecast EU-25 road fuel demand [4].	3
Figure 1-4: Complex phenomenon in the combustion chamber (Adapted from [5]).	5
Figure 2-1: Experimental image showing the spray and combustion processes in internal combustion engine [2].	10
Figure 2-2: Visualization of a spray taken at 825 μ s after the start of the injection ($P_{inj} = 80$ MPa, $D_0 = 0.14$ μ m, and $\rho_{cha} = 20$ kg/m ³) [5].	11
Figure 2-3: Diagram of Macroscopic and microscopic spray characteristics.	12
Figure 2-4: Macroscopic spray parameters.	12
Figure 2-5: Schematic of various stages starting from internal nozzle flow to soot formation in Diesel sprays [13].	14
Figure 2-6: RANS Eulerian-Lagrangian Spray Atomization (ELSA) simulation of droplets in Diesel spray.	16
Figure 2-7: Visualization of Numerical Simulation using (a) LES approach [26]; (b) DNS approach [27].	18
Figure 2-8: Various spray regions classified in LES model by Apte et al., 2012 [36].	19
Figure 2-9: DNS simulation of Diesel sprays. Computational domain is 0.3 mm x 0.3 mm x 2.2 mm, grid size is 128 x 128 x 896, $D_0 = 100$ μ m, $U = 100$ m/s, $\rho_{inj} = 696$ kgm ⁻³ , $\rho_{cha} = 50$ kgm ⁻³ , computing time 10,000 h on 14 processors (Lebas et al., 2009 [42]).	20
Figure 2-10: The development of DNS model applied in liquid/gas two-phase modeling ([2] and [42]).	21

List of Figures

Figure 2-11: A schematic showing treatment of particles using the Lagrangian approach (Adapted from Vujanovic et al., 2009 [43]). Each dotted circle represents for a parcel.....	23
Figure 2-12: A schematic showing treatment of particles using the Eulerian approach (Adapted from Vujanovic et al., 2009 [43]).	24
Figure 2-13: The comparison and setup conditions for Eulerian-Eulerian model and Eulerian-Lagrangian model (Habchi and Martinez, 2010 [56], Martinez et al., 2010 [57]).....	26
Figure 2-14: The detail description of the boundary conditions (Sanjose, 2009 [58]).	26
Figure 2-15: The coupled Level Set, Volume Of Fluid and Ghost Fluid Method in modeling liquid jet and primary break-up near the jet nozzle (Menard et al., 2007 [63]).....	28
Figure 2-16: The 3D simulation by (a) Tanguy and Berlemont, 2005 [66]: ethanol droplet, $We = 60$, $Oh = 0.02$, impact parameter 0.5. (b) Ashgriz and Poo, 1990 [65]: Water droplet, $We = 83$, impact parameter 0.43.	29
Figure 2-17: Liquid Atomization using principally Volume Of Fluid method (Zaleski et al. and d'Alembert's team [78]).	30
Figure 3-1: The flow diagram for the development of the ELSA model.....	46
Figure 3-2: Three spray zones in ELSA model.	47
Figure 4-1: Quasi-2D thin wedge representing an axisymmetric combustion chamber.	58
Figure 4-2: The 3-Dimensional cylindrical mesh.....	58
Figure 4-3: The first cell is made up of equal segments in the axial and radial direction: quasi-2D thin wedge (on the left) and 3D geometry (on the right).....	59
Figure 4-4: Different mesh structure at the inlet of the computational domain.	60
Figure 4-5: Mesh structure at the cross-sectional nozzle exit.	61
Figure 4-6: Inlet boundary condition is located at the area highlighted in red for (a): quasi-2D thin wedge mesh (left); and (b) 3D mesh (right).....	62

List of Figures

Figure 4-7: Boundary conditions in quasi-2D thin wedge.....	63
Figure 4-8: Boundary conditions in 3D mesh.....	64
Figure 4-9: Injection rate with different injection pressures ($P_{inj} = 40$ MPa, 80 MPa, and 180 MPa respectively).....	67
Figure 4-10: Velocity profile at different injection pressures ($P_{inj} = 40$ MPa, 80 MPa, and 180 MPa respectively).....	68
Figure 4-11: Similarity and difference of spray penetration thresholds under non-evaporative and evaporative conditions.....	69
Figure 4-12: Comparison of different definitions for computing the spray penetration (N_2 ; $P_{inj} = 80$ MPa; $P_{cha} = 2$ MPa).	69
Figure 4-13: Comparison of the effects of various time steps: Spray Penetration (N_2 ; $P_{inj} = 80$ MPa; $P_{cha} = 2$ MPa).	70
Figure 4-14: Comparison of the effect of time step: number of droplets.....	71
Figure 4-15: Comparison of the effect of time step: SMD (N_2 ; $P_{inj} = 80$ MPa; $P_{cha} = 2$ MPa).	71
Figure 4-16: Spray penetration with different Schmidt number of 0.5 vs. 0.9 vs. 1.0 respectively (N_2 ; $P_{inj} = 80$ MPa; $P_{cha} = 2$ MPa).....	72
Figure 4-17: Spray spreading angle with different Schmidt number of 0.5, 0.9, and 1 respectively (N_2 ; $P_{inj} = 80$ MPa; $P_{cha} = 2$ MPa).	73
Figure 4-18: Number of droplets with different Schmidt of 0.5, 0.9, and 1 respectively (N_2 ; $P_{inj} = 80$ MPa; $P_{cha} = 2$ MPa).	73
Figure 4-19: Spray penetration for different Nparcel number (N_2 ; $P_{inj} = 80$ MPa; $P_{cha} = 2$ MPa).	74
Figure 4-20: Number of droplets for different Nparcel number (N_2 ; $P_{inj} = 80$ MPa; $P_{cha} = 2$ MPa).	74
Figure 4-21: Spray penetration with different ($k-\epsilon$ /RNG- $C_{\epsilon 1}$) of 1.60, 1.52, and 1.42 respectively (N_2 ; $P_{inj} = 80$ MPa; $P_{cha} = 2$ MPa).	77
Figure 4-22: Spray spreading angle with different ($k-\epsilon$ /RNG- $C_{\epsilon 1}$) of 1.60, 1.52, and 1.42 respectively (N_2 ; $P_{inj} = 80$ MPa; $P_{cha} = 2$ MPa). ...	77
Figure 4-23: Number of droplets with different ($k-\epsilon$ /RNG- $C_{\epsilon 1}$) of 1.60, 1.52, and 1.42 respectively (N_2 ; $P_{inj} = 80$ MPa; $P_{cha} = 2$ MPa).	78
Figure 4-24: Spray penetration comparing amongst $k-\epsilon$ /high ReN, $k-\epsilon$ /RNG, and $k-\epsilon$ /Chen (N_2 ; $P_{inj} = 80$ MPa; $P_{cha} = 2$ MPa).	79

List of Figures

Figure 4-25: Spray spreading angle comparing amongst k- ϵ /high ReN, k- ϵ /RNG, and k- ϵ /Chen (N_2 ; $P_{inj} = 80$ MPa; $P_{cha} = 2$ MPa).....	80
Figure 4-26: Spray penetration with different break-up models	81
Figure 4-27: Spray spreading angle with different break-up models.....	81
Figure 4-28: Number of droplets and Axial velocity with different break-up models (N_2 ; $P_{inj} = 80$ MPa; $P_{cha} = 2$ MPa).....	82
Figure 4-29: Spray penetration with different Weber_crit number of 6, 8.4, 12, 60, and 120 respectively (N_2 ; $P_{inj} = 80$ MPa; $P_{cha}=2$ MPa). ...	83
Figure 4-30: Spray spreading angle with different Weber_crit number of 6, 8.4, 12, 60, and 120 respectively (N_2 ; $P_{inj} = 80$ MPa; $P_{cha} = 2$ MPa).....	84
Figure 4-31: Number of droplets with different Weber_crit number of 6, 8.4, 12, 60, and 120 respectively (N_2 ; $P_{inj} = 80$ MPa; $P_{cha} = 2$ MPa)...	84
Figure 4-32: Spray penetration with and without break-up	85
Figure 4-33: Spray spreading angle with and without break-up.....	86
Figure 4-34: Spray penetration with and without coalescence for different break-up models (N_2 ; $P_{inj} = 80$ MPa; $P_{cha} = 2$ MPa).....	87
Figure 4-35: Spray spreading angle with and without coalescence for different break-up models (N_2 ; $P_{inj} = 80$ MPa; $P_{cha} = 2$ MPa).....	87
Figure 4-36: Axial velocity with and without coalescence for different break-up models (N_2 ; $P_{inj} = 80$ MPa; $P_{cha} = 2$ MPa).....	88
Figure 4-37: Number of droplets with and without coalescence for different break-up models (N_2 ; $P_{inj} = 80$ MPa; $P_{cha} = 2$ MPa).....	88
Figure 4-38: Spray penetration with different chamber pressure of 0.28 MPa vs. 0.54 MPa, and density of 22 k/m ³ and 37 kg/m ³ respectively (SF6; $P_{inj} = 40$ MPa).	89
Figure 4-39: Spray penetration with different chamber pressure of 0.28 MPa vs. 0.54 MPa, and density of 22 k/m ³ and 37 kg/m ³ respectively (SF6; $P_{inj} = 80$ MPa).	90
Figure 4-40: Spray penetration with different chamber pressure of 0.28 MPa vs. 0.54 MPa, and density of 22 k/m ³ and 37 kg/m ³ respectively (SF6; $P_{inj} = 180$ MPa).	90

List of Figures

Figure 4-41: Spray penetration with different chamber pressure of 2 MPa vs. 5 MPa, and density of 22 k/m ³ and 37 kg/m ³ respectively	91
Figure 4-42: Spray penetration with different chamber pressure of 2 MPa vs. 5 MPa, and density of 22 k/m ³ and 37 kg/m ³ respectively	91
Figure 4-43: Spray penetration with different chamber pressure of 2 MPa vs. 5 MPa, and density of 22 k/m ³ and 37 kg/m ³ respectively	92
Figure 4-44: Comparison of SMD between the Lagrangian and ELSA models (N ₂ ; P _{inj} = 80 MPa; P _{cha} = 2 MPa).....	93
Figure 4-45: Spray penetration of 3D and 2D mesh	94
Figure 4-46: Spray cone angle of 3D and 2D mesh.....	94
Figure 4-47: Number of droplets of 3D and 2D mesh	95
Figure 4-48: Velocity profile of Spray A case (n-dodecane, P _{inj} = 150 MPa, P _{cha} = 6 MPa).	97
Figure 4-49: Liquid, vapor penetration with different Nparcel number of 1, 10, 20, and 200 respectively (P _{inj} = 150 MPa; P _{cha} = 6 MPa).	98
Figure 4-50: Spray spreading angle and number of droplets with different Nparcel number of 1, 10, 20, and 200 respectively (P _{inj} = 150 MPa; P _{cha} = 6 MPa).	98
Figure 4-51: Liquid and vapor penetration for different injection pressure levels (50, 100, and 150 MPa).	99
Figure 4-52: Number of droplets and axial velocity for different injection pressure levels (50, 100, and 150 MPa).....	99
Figure 4-53: Centerline Mixture Fraction (P _{inj} = 150 MPa; ρ _{inj} = 718 kg/m ³ ; P _{cha} = 6 MPa).	100
Figure 4-54: Mixture Fraction at the cross sections 25mm, and 45 mm along the spray axis (P _{inj} = 150 MPa; ρ _{inj} = 718 kg/m ³ ; P _{cha} = 6 MPa).....	101
Figure 4-55: Injection rate measure (left) and averaged injection rate of n-dodecane at different P _{inj} and P _{cha} = 7 MPa. The disturbances at the plateau of the averaged injection rate seem to be an effect of reflection waves at the nozzle.....	101

List of Figures

Figure 4-56: Ensemble averaged velocity profile of n-dodecane at different P_{inj} and $P_{cha} = 7$ MPa. This profile was obtained from the injection rate.....	102
Figure 4-57: Liquid and vapor penetration for different injection pressure levels (30, 70, and 110 MPa).	103
Figure 4-58: Spray spreading angle for different injection pressure levels. ...	103
Figure 4-59: Number of droplets for different injection pressure levels.....	104
Figure 4-60: Velocity profile of n-dodecane at different injection pressure and fixed chamber pressure equal to 6MPa.....	105
Figure 4-61: Velocity profile directly derived from experimental mass flow rate vs. the special adaptation for the ELSA modeling ($P_{inj} = 50$ MPa, $P_{cha} = 2$ MPa).	106
Figure 4-62: Liquid and vapor penetration at different injection pressure.	107
Figure 4-63: Spray spreading angle at different injection pressure.....	107
Figure 4-64: Liquid and vapor penetration at different injection pressures. ...	108
Figure 4-65: Spray cone angle at different injection pressures.....	108
Figure 4-66: Number of droplets and axial velocity at different injection pressures.	108
Figure 4-67: Liquid and vapor penetration at different injection temperature.	109
Figure 4-68: Spray spreading angle at different injection temperature.	109
Figure 4-69: Number of droplets and axial velocity at different injection temperature.....	110
Figure 4-70: Liquid and vapor penetration at different chamber density of 22.8, 7.6 kg/m ³ and pressure of 6, 2 MPa respectively (Ev17 vs. Ev18).	110
Figure 4-71: Spray cone angle at different chamber density of 22.8, 7.6 kg/m ³ and pressure of 6, 2 MPa respectively (Ev17 vs. Ev18)..	111
Figure 4-72: Number of active droplets and SMD at different chamber density of 22.8, 7.6 kg/m ³ and pressure of 6, 2 MPa respectively (Ev17 vs. Ev18).	111
Figure 4-73: Liquid and vapor penetration at different chamber temperature.....	112
Figure 4-74: Spray spreading angle at different chamber temperature.....	112

List of Figures

Figure 4-75: Number of active droplets and axial velocity at different chamber temperature.....	112
Figure 5-1: The attached-sectional transparent window at one hole of multi-hole injector (left) and its schematic of inner cavitating nozzle flow (cavitation occurs mainly on the upper part) on the right.	118
Figure 5-2: A schematic of internal cavitating flow and the main parameters at the nozzle exit [15].	121
Figure 5-3: Time-averaged vapor field in the internal nozzle and the velocity profile at the nozzle outlet ($P_{inj} = 30$ MPa and different chamber pressure of 5 and 7 MPa respectively; cases Ca01 vs. Ca02).....	121
Figure 5-4: Time-averaged vapor field in the internal nozzle and the velocity profile at the nozzle outlet ($P_{inj} = 80$ MPa; $P_{cha} = 5$ and 7 MPa; cases Ca05/Ca06 ^c /Ca07 ^f vs. Ca08 ^c /Ca09 ^f).....	122
Figure 5-5: Time-averaged vapor field in the internal nozzle and the velocity profile at the nozzle outlet ($P_{inj} = 160$ MPa; $P_{cha} = 5$ and 7 MPa; cases Ca10 vs. Ca11).....	123
Figure 5-6: Comparison of the spray penetration between fine mesh and coarse mesh (cases Ca06 ^c , Ca07 ^f , Ca08 ^c , and Ca09 ^f).	124
Figure 5-7: Comparison of the number of active droplets between fine mesh and coarse mesh (cases Ca06 ^c , Ca07 ^f , Ca08 ^c , and Ca09 ^f).....	124
Figure 5-8: Comparison of the centerline axial velocity between fine mesh and coarse mesh at 0.12ms (cases Ca06 ^c , Ca07 ^f , Ca08 ^c , and Ca09 ^f).....	125
Figure 5-9: Spray penetration and spray spreading angle at the constant chamber pressure of 5 MPa, injection pressures are 80 MPa and 160 MPa respectively (cases Ca05 vs. Ca10).....	125
Figure 5-10: Number of droplets and axial velocity at the constant chamber pressure of 5 MPa, injection pressures are 80 MPa and 160 MPa respectively (cases Ca05 vs. Ca10).....	126

List of Figures

Figure 5-11: Compared 2D velocity contour for different cross-sections (D is diameter) along the spray exit at the simulating time of 0.3 ms.	127
Figure 5-12: Full-view 3D velocity contour for different cross-sections (D is diameter) along the spray exit at the simulating time of 0.2 ms showing the comparison between $P_{inj} = 160$, and 80 MPa.	128
Figure 5-13: Spray penetration and spray spreading angle (Diesel, $P_{inj} = 80$ MPa, cases Ca12, Ca13 and Ca15).....	129
Figure 5-14: Averaged droplet diameter and axial velocity (Diesel, $P_{inj} = 80$ MPa, cases Ca12, Ca13 and Ca15).....	129
Figure 5-15: Spray penetration and spray spreading angle (BioDiesel, $P_{inj} = 80$ MPa, cases Ca18, Ca19, Ca17 and Ca20).	130
Figure 5-16: Averaged droplet diameter and axial velocity (BioDiesel, $P_{inj} = 80$ MPa, cases Ca18, Ca19, Ca17 and Ca20).	130
Figure 5-17: Spray penetration with different types of fuel and break-up setting ($P_{inj} = 80$ MPa, $P_{cha} = 5$ MPa; cases Ca05 vs. Ca07 ^f).....	131
Figure 5-18: Time-averaged vapor field in the internal nozzle and the velocity profile at the nozzle outlet compared between Diesel and BioDiesel ($P_{inj} = 80$ MPa and different chamber pressure of 17 and 18 MPa respectively, cases Ca12, Ca14, Ca16, and Ca18).	132
Figure 5-19: Spray penetration with different types of fuel and changing the chamber pressures (Diesel vs. BioDiesel, $P_{inj} = 80$ MPa, $P_{inj} = 17$ and 18 MPa, cases Ca12, Ca14, Ca16, and Ca18).	133
Figure 5-20: Centerline axial velocity with different types of fuel and changing the chamber pressures (Diesel vs. BioDiesel, $P_{inj} = 80$ MPa, $P_{inj} = 17$ and 18 MPa, cases Ca12, Ca14, Ca16, and Ca18).	133
Figure 5-21: Spray spreading angle with different types of fuel and changing the chamber pressures ($P_{inj} = 80$ MPa, Diesel vs. BioDiesel, $P_{inj} = 17$ and 18 MPa; cases Ca12, Ca14, Ca16, and Ca18).	134

List of Figures

- Figure 5-22:** Averaged droplet diameter with different types of fuel and changing the chamber pressures (Diesel vs. BioDiesel, $P_{inj} = 80$ MPa, $P_{inj} = 17$ and 18 MPa, cases Ca12, Ca14, Ca16, and Ca18). 134
- Figure 5-23:** Compared spray profile in term of velocity between Diesel and BioDiesel for different cross-sections at 0.5 ms. 135

LIST OF TABLES

Table 2-1:	Comparison between Eulerian and Lagrangian approaches.....	22
Table 2-2:	A couple of CFD codes for spray modeling and simulation.....	32
Table 3-1:	Comprehensive list of the main works which have developed the Eulerian-Lagrangian approach and the ELSA model sorted chronologically.....	42
Table 4-1:	Computational cases under non-evaporative conditions.....	67
Table 4-2:	Numerical studies of different Schmidt number.....	72
Table 4-3:	Coefficients of the high Reynolds $k-\epsilon$ turbulence model.....	75
Table 4-4:	Coefficients of the RNG $k-\epsilon$ turbulence model.	76
Table 4-5:	Computational cases of the RNG $k-\epsilon$ turbulence model.....	76
Table 4-6:	Coefficients of the Chen's $k-\epsilon$ turbulence model.	78
Table 4-7:	Computational cases of the Chen $k-\epsilon$ turbulence model.	79
Table 4-8:	Computational cases for several break-up models.	81
Table 4-9:	The results of break-up models.....	82
Table 4-10:	Numerical studies on the Weber criteria for collision.....	83
Table 4-11:	Numerical studies on the spray break-up model and coalescence.	86
Table 4-12:	Mesh information and CPU time between 2D and 3D mesh.....	93
Table 4-13:	Fuel chemical and physical properties.	96
Table 4-14:	Computational cases corresponding to Spray A from SANDIA... ..	97
Table 4-15:	Total generated droplets and remained droplets for different injection pressure levels (50, 100, and 150 MPa).....	100
Table 4-16:	Computational cases for different injection pressure levels.	102
Table 4-17:	Computational cases corresponding to Spray A from CMT.	105
Table 5-1:	Nozzle parameters.....	118
Table 5-2:	Mesh information between coarse vs. fine mesh.	118
Table 5-3:	Several computation cases and setting conditions in ELSA modeling coupling with the internal nozzle flow.....	119
Table 5-4:	Pressure and area coefficient.	120
Table 5-5:	Fuel properties of Diesel and BioDiesel [3].	120
Table 5-6:	The example of typical CPU time in coupling modeling.	136

NOMENCLATURE

A	Nozzle hole area / Cross-sectional area	[m ²]
A_{eff}	Effective cross-sectional area	[m ²]
A_0	Real-size geometrical cross-sectional area	[m ²]
a_{coll}	Strain rate	[s ⁻¹]
α_1	Model constant	[-]
b	Viscous damping coefficient	[-]
C_a	Orifice area-contraction coefficient	[-]
C_{bl}	Empirical coefficient for bag break-up	[-]
C_{s1}	Empirical coefficient for bag break-up	[-]
C_d	Nozzle discharge coefficient	[-]
C_μ	k- ϵ constants	[-]
$C_{\epsilon 1}$	k- ϵ constants	[-]
$C_{\epsilon 2}$	k- ϵ constants	[-]
D_d	Instantaneous droplet diameter	[m]
D_{eff}	Effective diameter for a cylindrical geometry	[m]
D_{eq}	Equivalent diameter	[m]
D_0	Geometrical diameter at nozzle outlet	[m]
D_s	Turbulent diffusion coefficient	[-]
D_{32}	Sauter Mean Diameter	[m]
F	External force analogous to aerodynamic forces	[N]
k	Stiffness	[N/m]
\tilde{k}	Turbulent kinetic energy for the Eulerian mixture	[m ² /s ²]
\tilde{k}_g	Turbulent kinetic energy for the gas phase	[m ² /s ²]
L_t	Turbulent length scale	[m]
\dot{M}	Momentum flux/ momentum flow rate	[kgm/s ²]

Nomenclature

\dot{m}	Mass flow rate/ injection rate	[kg/s]
n	Number of intervals	[-]
n_{drop}	Number of droplets per generated parcel	[-]
P	Pressure	[Pa]
\bar{P}	Mean pressure	[Pa]
P_{inj}	Injection pressure	[Pa]
P_{cha}	Chamber pressure	[Pa]
Re_d	Droplet Reynolds number	[-]
R_g	Gas constant	[-]
r	Radius of the nozzle hole	[m]
r_0	Radius of the mother drops	[m]
r_1	Radius of the drops obtained after break-up	[m]
r_{32}	Data model	[-]
Sc_t	Turbulent Schmidt number	[-]
$S_{EL}^{\tilde{Y}_l}$	Source term when droplet generation during the transition from Eulerian to Lagrangian formulation	[-]
$S_{EL}^{\tilde{\Omega}}$	Source term of the liquid/gas interface	[-]
T_{cha}	Chamber temperature	[K]
T_g	Mixture temperature	[K]
Δt	Change in time	[s]
u	Velocity	[m/s]
U_{ber}	Bernoulli's velocity	[m/s]
U_{eff}	Effective velocity	[m/s]
\tilde{U}_i	Eulerian velocity of the mixture / Favre averaged mean velocity	[m/s]
$\bar{U}_{i,l}$	Mean liquid velocity	[m/s]
u_{eff}	Inlet velocity	[m/s]
U_{rel}	Relative velocity between the gas and liquid drop	[m/s]
u_{th}	Theoretical velocity at the outlet section	[m/s]
V_s	Surface destruction coefficient	[m/s]

Nomenclature

V_{cell}	Volume of one transitional cell	[m ³]
x	Displacement of the droplet from its equilibrium position	[m]
Δx	Mesh size	[m]
Y_l	Liquid mass fraction	[-]
\tilde{Y}_l	Mean liquid mass fraction	[-]

SUBSCRIPTS AND SUPERSSCRIPTS

<i>ber</i>	<i>Bernoulli</i>
<i>cha</i>	<i>chamber</i>
<i>inj</i>	<i>injection</i>
<i>eq</i>	<i>equivalent</i>
<i>eq.</i>	<i>equation</i>
<i>eff</i>	<i>effective</i>
<i>f</i>	<i>fluid/ fluid fuel</i>
<i>l</i>	<i>liquid</i>
<i>g</i>	<i>gas</i>
<i>s</i>	<i>surface</i>
<i>v</i>	<i>vapor</i>

DIMENSIONLESS NUMBERS

<i>Oh</i>	Ohnesorge number
<i>Re</i>	Reynolds number
<i>Ta</i>	Taylor number
<i>We</i>	Weber number

Nomenclature

GREEK SYMBOLS

ε	Dissipation rate	m^2/s^3
μ	Absolute or Dynamic Viscosity	$\text{Pa}\cdot\text{s}$ or Ns/m^2 or kg/ms
ν	Kinematic viscosity	m^2/s
θ	Spray cone angle	$^\circ$
ρ	Density	kg/m^3
σ	Surface tension	N/m
σ_d	Surface tension coefficient	[-]
σ_k	k- ε constants	[-]
σ_ε	k- ε constants	[-]
ρ	Density	$[\text{kg}/\text{m}^3]$
$\bar{\rho}$	Mean density	$[\text{kg}/\text{m}^3]$
ρ_{cha}	Chamber gas density	$[\text{kg}/\text{m}^3]$
$\overline{\rho u_i'' u_j''}$	Reynolds stress tensor	[-]
$\overline{\rho u_j'' y''}$	Liquid turbulent diffusion flux of the liquid	[-]
$\tilde{\Omega}$	Liquid/gas interface per unity of mass	$[\text{m}^2/\text{kg}]$
$\tilde{\Omega}_{init}$	Initial value of liquid/gas surface density	[-]
$\dot{\tilde{\Omega}}_{mean}$	Mean value of liquid/gas surface density	[-]
$\dot{\tilde{\Omega}}_{turb}$	Turbulence value of liquid/gas surface density	[-]
$\dot{\tilde{\Omega}}_{coll}$	Collision value of liquid/gas surface density	[-]
$\dot{\tilde{\Omega}}_{coal}$	Coalescence value of liquid/gas surface density	[-]
$\bar{\Sigma}$	Liquid surface density	$[\text{m}^{-1}]$
$\bar{\Sigma}_{eq}$	Equilibrium surface density	[-]
τ_t/τ_{turb}	Turbulent time scale	[-]
τ_{coll}	Time scale of collision	[-]
$\tilde{\Phi}_l^{crit}$	Critical value of the Eulerian liquid volume fraction	[-]

ABBREVIATIONS

ASTM	American Society for Testing and Materials
CFD	Computational Fluid Dynamics
CFL	Courant-Friedrichs-Lewy
CMT	CMT-Motores Térmicos
DDM	Discrete Droplet Model
DI	Direct Injection
DNS	Direct Numerical Simulation
ECN	Engine Combustion Network
ELEG	Eulerian-liquid Eulerian-gas
ELSA	Eulerian-Lagrangian Spray Atomization
FVM	Finite Volume Method
FWI	First Wind-Induced
HMN	2,2,4,4,6,8,8-heptamethylnonane
ICE	Internal Combustion Engine
IMLS	Interfacial Marker-Level Set (Method)
ITM	Interface Tracking Methods
LDEF	Lagrangian-Droplet Eulerian-Fluid
LES	Large Eddy Simulation
LS	Level Set
PISO	Pressure Implicit with Splitting of Operators
RANS	Reynolds-averaged Navier-stokes
RLSG	Refined Level Set Grid
RNG	Re-Normalization-Group
SMD	Sauter Mean Diameter
SWI	Second Wind-Induced
VECOM	Vehicle Concept Modeling
VOF	Volume Of Fluid

Chapter 1 - Introduction

1.1 Overview and motivation

In the last decades, the entire world is facing two of the most important threats in its recent history. On the one hand, the global warming caused by the accumulation of particular gases, known as “greenhouse gases” and, on the other hand, the foreseen shortage of fossil fuels, which are right now the world's primary energy resource. These two threats are challenging the full society, and many changing concerning the energy availability and its use are forthcoming.

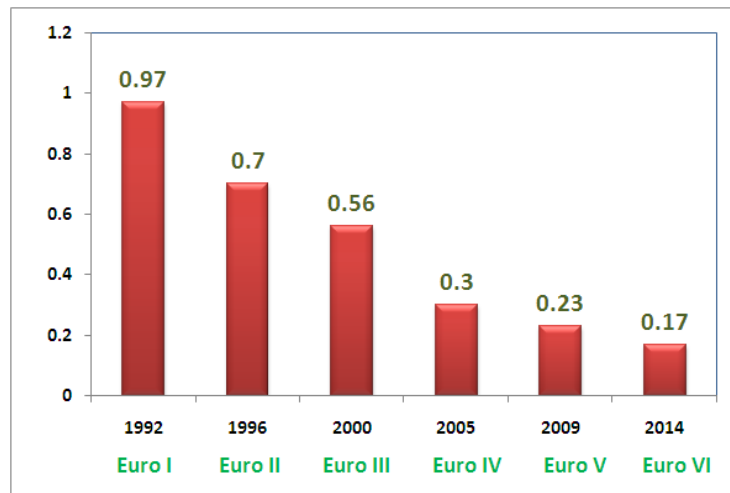


Figure 1-1: European Emission standards for Diesel passenger cars: HC (g/kWh) + NOx (g/kWh) (the plot taken data from [1] and [2]).

Undoubtedly, future internal combustion engines (ICE) in general, and those applied in transport applications in particular, will play a major role in both the short and long term management of these two environmental risks. The relevance of ICE can be easily understood considering that oil-based fossil

Chapter 1 - Introduction

fuels are nowadays the main input; whereas CO₂, which is one of the more aggressive “greenhouse gases”, is the main output of these thermal engines. Lowering internal combustion engine emission, while enhancing engine efficiency, and conserving or even reduce the fuel consumption is the key to the automotive industry.

Moreover, as Compression Ignition Engines, (CI, Diesel Engines) are overrepresented in European car pool, the EU focus in this sort of engines. European Regulation (EC) No 715/2007, which contains Euro5 and Euro6 Standards, set to a minimum the emissions of particulates Nitrogen Oxides (NO_x), Figure 1-1 and (PM, soot), Figure 1-2: the major pollutants of CI engines. In order to fulfill these highly restrictive standards, and similar ones approved by United States and Japan administrations, engine manufacturers and academia are performing a lot of research, but, as was stated, for instance, in Thermo-and Fluid Dynamic processes in Diesel Engines (THIESEL) conference 2010 [3], there are still many problems to be solved.

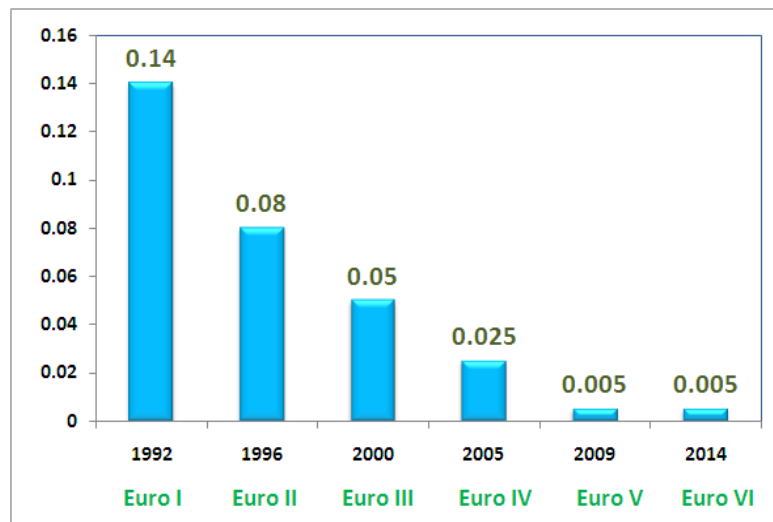


Figure 1-2: European Emission standards for Diesel passenger cars: PM (g/kWh) (the plot taken data from [1] and [2]).

Apart from this, there is a broad consensus about that cheap fossil fuel era is almost over. Although there is a big interest in building an alternative to fossil fuel vehicles, as can be electric cars or even nano-particles based

engines, it seems that there will not be a viable alternative in the next 20 years (see Figure 1-3). Talking about other fuels, hydrogen propelled cars are the future, but it seems that they always will be. Probably, the solution will be hybrid vehicles and, between them, the extended-range electric vehicles. These vehicles use pure electric propulsion. When the battery is depleted, an engine generator kicks in to sustain the battery power. This is a clear example of the “downsizing” of engine. Reducing the size of the engine but maintaining power, consumption and not increasing contaminants emissions is a big challenge.

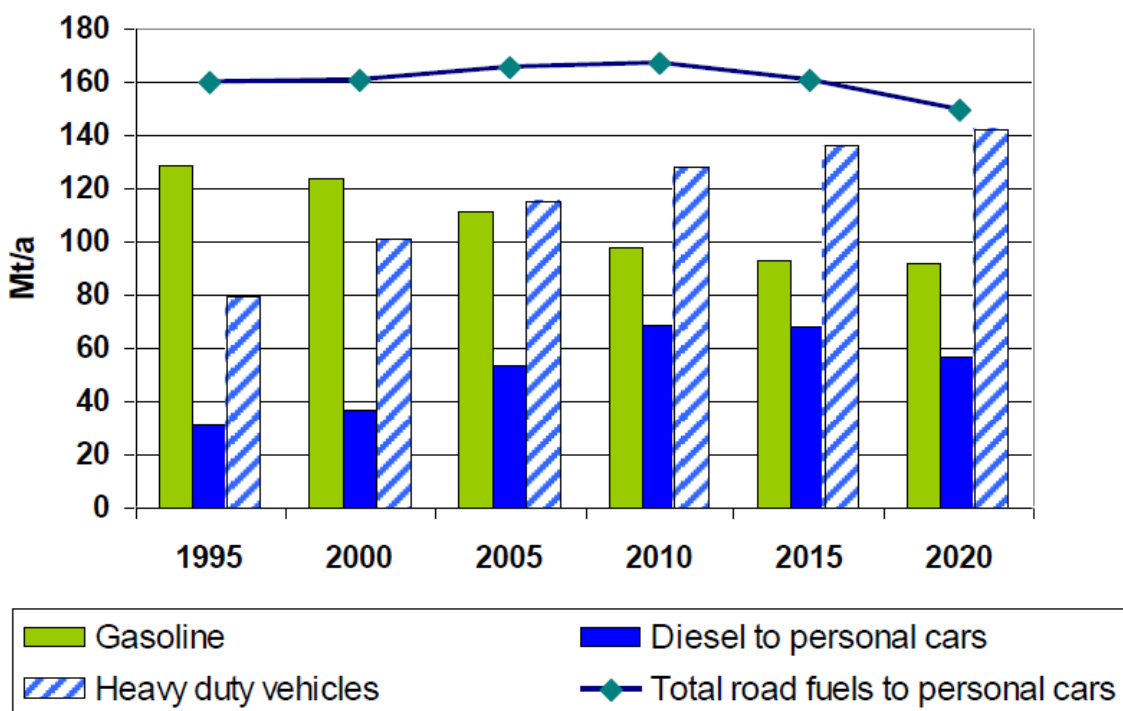


Figure 1-3: Historical and forecast EU-25 road fuel demand [4].

Even though we have made big advances over the last decade in the efficiency of the gasoline and Diesel engine, it is still much to improve about the humble combustion engine, and a lot of research to be done.

The compression-ignition or Diesel engine was developed in the late 19th century. Of course, very little remains from the original design. Nowadays, the injection is electronically controlled and common rail system is used in Diesel fuel spray. Fuel spray is injected from the injector through a micro-hole nozzle under a very high pressure. At this very moment, injection pressures up to 200

Chapter 1 - Introduction

MPa are common, and probably this pressure will be increased in the near future. Other promising technique, for example, is the new Piezo injector, which allows multi-shot injections due to its fast response.

As it is well known, the fuel injected at the chamber develops forming a spray. The knowledge of the behavior of this spray is of crucial importance for the ICE designing, but not only. In fact, sprays are important in many industrial applications such as manufacturing, aerospace, automotive, refinery, pharmaceutical, medical, agricultural, petrochemical and so forth. In our case, the automotive industry, the injection spray plays a crucial role in both gasoline and Diesel engines. More specifically, the understanding of spray evolution characteristics and its parameters influence strongly efficient fuel delivery. The objective is increasing the fuel efficiency, and thus the energy efficiency, but reducing the emission of pollutants in order to generate a highly efficient engine.

Therefore, it is necessary to understand the combustion physics and fuel spray. Fuel injection process and subsequent fuel-air mixing formation play a major role on combustion and pollutant formation on internal combustion engines. Thus, an accurate prediction of these processes is required in order to perform reliable engine combustion and pollutants formation simulations.

However, this is not an easy task in any way. Diesel fuel injection and spray formation modeling in direct injection engines are still a challenging task due to the complex interrelated phenomena taking places. Some of these processes, such as primary atomization or nozzle cavitation are still not fully understood. Part of this problem comes from the lack of experimental results in some regions of the nozzle-spray system. Particularly, there is little information about cavitating flows inside the fuel injectors and the spray behavior very close to the nozzle exit. It is important to emphasize here that the numerical simulations now place an important role in engine research and they are able to simulate and provide useful data in the absence of real experimental measurements. However, a numerical simulation made without a validation of the model can be thought as a very expensive way of wasting time and money.

CFD modeling of fuel spray in internal combustion engines is especially difficult due to the complexity of the combustion process and the turbulence

Chapter 1 - Introduction

process as shown in Figure 1-4. Hence, CFD models required to be developed and improved.

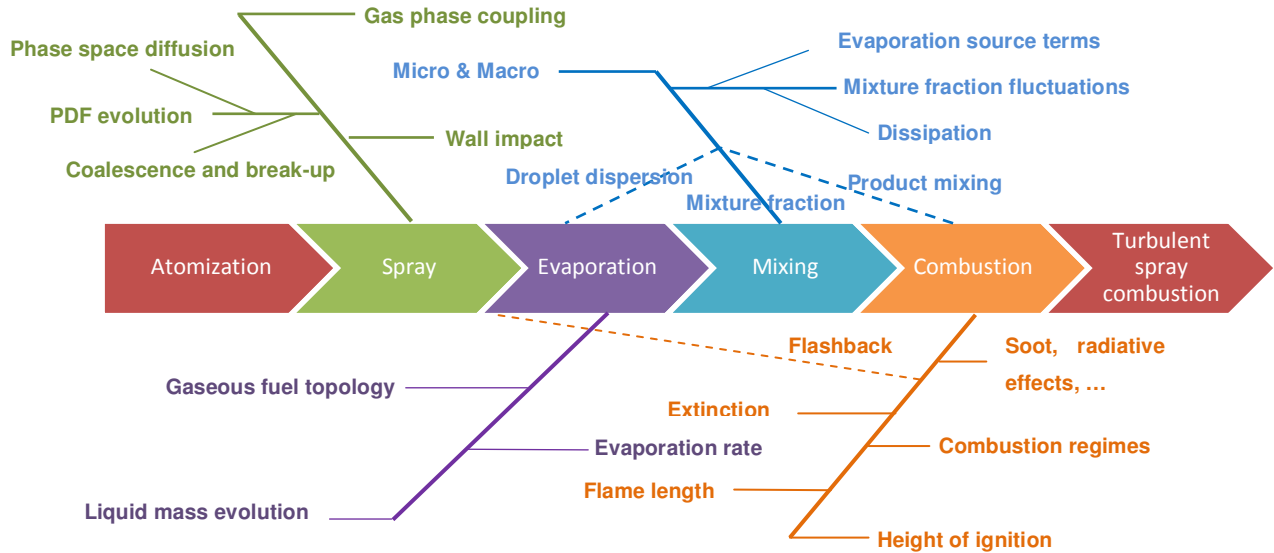


Figure 1-4: Complex phenomenon in the combustion chamber (Adapted from [5]).

Standard CFD spray simulations are based on Discrete Droplet Method (DDM), which uses a Lagrangian approach for following the droplets. This approach presents some drawbacks, and usually requires extensive calibration in order to be employed in engine simulations. Main issues come from both physical and numerical limitations on the near nozzle dense spray region description, including the fact that the first cell of the spray has to be bigger than the nozzle.

ELSA (Eulerian Lagrangian Spray Atomization) methodology resulted from the efforts of several groups and individual researchers, especially from France, over the course of the last decade. It will be described in detail in chapter 3. This model has been implemented in Adapco's CFD code Star-CD by RSA ([6], and [7]). ELSA method is based on an Eulerian approach for the description of the dense spray region, where standard DDM method cannot describe the spray. Within the diluted spray region, the ELSA model could switch to the traditional Lagrangian description of the liquid phase, taking advantage from well-established previously developed sub-models. The

objective of this approach is to improve the modeling of the primary break-up and secondary atomization processes simultaneously, simulating droplets in a more accurate way. It is worth mentioning that it is able to couple with the internal nozzle flow.

As we have said, it is necessary to validate the model with appropriate experimental data and examine the ELSA methodology in a wide range of conditions as well as various injector geometries. Therefore, a comparison with well-established experimental data from a number of leading experimental and computational research centers in internal combustion engine has been made. Obviously, most of the experimental results come from CMT institute. All the simulations carried out in this thesis have been made in a controlled non-realistic geometry, but using real engine values, as can be pressures, densities, nozzle diameter, etc. Once successfully validated, ELSA spray model will enable the uses of another tools, as can be, for instance, spray combustion tools, and help to reduce contaminants and fuel consumption.

1.2 Research objectives & methodology

According to the previous statements, the overall topic of the thesis is to validate the ELSA model implemented in Star-CD under real-engine conditions. Within this general objective, it is also included to evaluate and validate the model representing the phenomena involved in Diesel spray formation and the spray development from the nozzle outflow to the complete fuel vaporization. As it is one of the improvements of the ELSA method, an emphasis has been done on the transition from internal nozzle flows to initial spray development calculations. The work also focus on the proper integration of the sub-models employed for the description of the dense and diluted spray region, in terms of liquid break-up, vaporization and droplet dynamics. From the results obtained, the author assesses the potential and capabilities of the ELSA model for practical applications on CFD engine calculations.

1.3 Outline of the thesis

The purpose of this section is to provide a brief presentation of the entire document. The organization of the thesis is as followed:

Chapter 1: Introduction

Chapter 2: Spray Fundamentals and CFD spray modeling

Chapter 3: Eulerian-Lagrangian Spray Atomization Methodology

Chapter 4: ELSA model validation

Chapter 5: Cavitating nozzles modeling with ELSA

Chapter 6: Conclusions and Recommendations

Chapter 7: List of papers

Appendices

A basis understanding and significance of the project background, sources of motivation, aim and scope of the project have been firstly given in this chapter.

The state of the art about the spray modeling and the different theoretical approaches to the physics of sprays are briefly reported in chapter 2.

In Chapter 3, the detailed description of the ELSA Methodology, and its principle and computational procedure are presented together with the main governing equations of the model

Chapter 4 firstly presents the outcomes of the ELSA spray modeling under non-evaporating conditions. As a thought experiment, some results about increasing the temperature without using evaporation models are also presented.

Chapter 1 - Introduction

In Chapter 5, the studies of spray behavior by coupling of the internal cavitating flow in Diesel nozzle have been conducted. The results coming from this set of simulations will be also discussed there.

Chapter 6 presents the main conclusions of this job, together with the future work guessed for the ELSA model.

In Chapter 7, a list of publication of research articles, including submitted, accepted, in press, and published papers are sorted in chronological order and included for reference.

REFERENCES

- [1] European Commission Air Environment standards: Transport & Environment of Road Vehicles, Available at: <http://ec.europa.eu/environment/air/transport/>, last accessed by 25th June **2012**.
- [2] European Union Emission Standards, Cars and Light Trucks, Dieselnet, Available at <http://www.dieselnet.com/standards/eu/ld.php>, last accessed by 25th June **2012**.
- [3] CMT, Thermo-and fluid dynamic processes in Diesel Engines (THIESEL) conference 2010. Available at: <http://www.cmt.upv.es/Thiesel.aspx>, last accessed by 25th June **2012**.
- [4] European Commission, Well-to-wheels analysis of future automotive fuels and powertrains in the European context, Version 2c, March **2007**.
- [5] Reveillon, J.; Demoulin, F.X.; Pera, C.; Meftah, H.; Ducruix, S.; Durox, D. *Simulation approaches for spray combustion*. Autumn meeting of The Combustion Institute, British Section, Imperial College, **2007**.
- [6] Desportes, A.; Zellat, M.; Desoutter, G.; Abouri, D.; Liang, Y. *Validation and Application of the Eulerian-Lagrangian spray atomization. (ELSA) model for the Diesel injection simulation*. SAE Technical Paper, **2010**.
- [7] Desportes, A.; Zellat, M.; Desoutter, G.; Liang, Y.; Ravet, F. *Application of the Eulerian-Lagrangian spray atomization (ELSA) model for the Diesel injection simulation*. Conference on Thermo- and Fluid Dynamic Processes in Diesel Engines, **2010**.

Chapter 2 - Spray Fundamentals and CFD spray modeling

In this chapter we want to present the fundamentals of fuel spray physics, the basis of spray modeling, together with a comprehensive explanation of the most used CFD models in this field, and the numerical techniques suitable for Diesel sprays. This chapter is completed with the appendix A - “A literature review on Atomization and break-up in Diesel sprays”, where a review about the-state-of-the-art of atomization and break-up models is given.

2.1 Spray fundamentals

Sprays are of common use in many industrial processes. Different nozzles are designed to produce from very large spray sheet or ligaments (as can be an irrigation sprinkler) to very small droplets in DI engine sprays. In some applications, the fluids even can be premixed (fluid-gas premixing) or they may interact (fluid-fluid interactions) inside the nozzle. In modern Diesel engines, the fuel cavitates, i.e., there exist some zones of the nozzle where the fuel pressure is below the saturation pressure, so the fuel vaporizes itself. Solving those multiphase problems is already difficult, but they are really much harder in the ICE environment. On the one hand, the pressure and fluid velocity are high, which made the computations harder. On the other hand, at some distance of the nozzle, the fuel has a big level of atomization, and in order to produce the combustion, these droplets have to be vaporized.

Chapter 2 – Spray Fundamentals and CFD spray modeling

It is also important to note that the diameter nozzle size of the actual injector of ICE engines is tiny. Nozzle diameters are around 0.170mm, being the nowadays pressures up to 2000 bars. It is clear that experiments are hard, and even harder if we talk about cavitating flow, where very little has been investigated experimentally at actual scales. Due to its importance, and perhaps for its difficulty, an extensive experimental and theoretical study of fuel injection has been conducted for many years, and probably it will be for many years still.

Figure 2-1 shows an instant of the combustion process in a typical DI ICE (without swirl). It is possible to identify several regions including the inert part of the spray and the combustion flame (see in [1]).

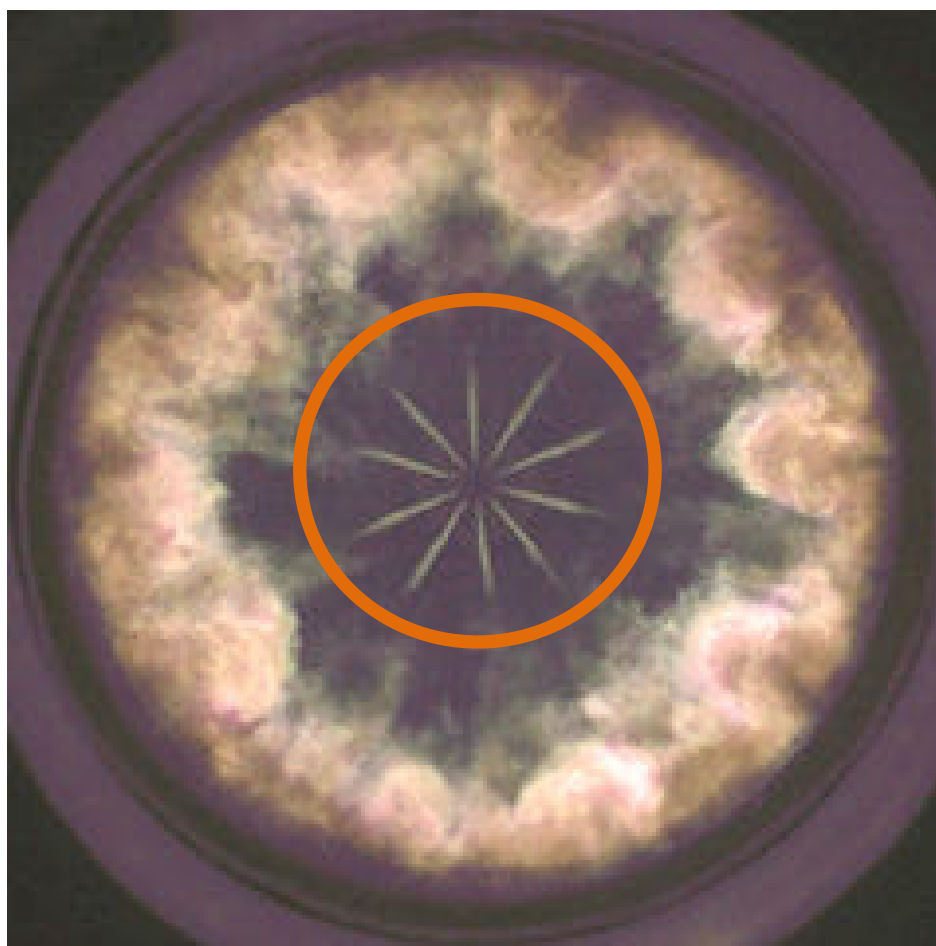


Figure 2-1: Experimental image showing the spray and combustion processes in internal combustion engine [2].

Generally, Diesel sprays are divided into two sub-regions ([3], [4] and [5]): firstly, the so-called steady region, which is a region located inside a conical-sharp of spray starting from the nozzle exit to approximately 60%-70% of the farthest distance of the whole spray. Secondly, the rest of the spray is defined as the unsteady or transient region as shown in Figure 2-2.

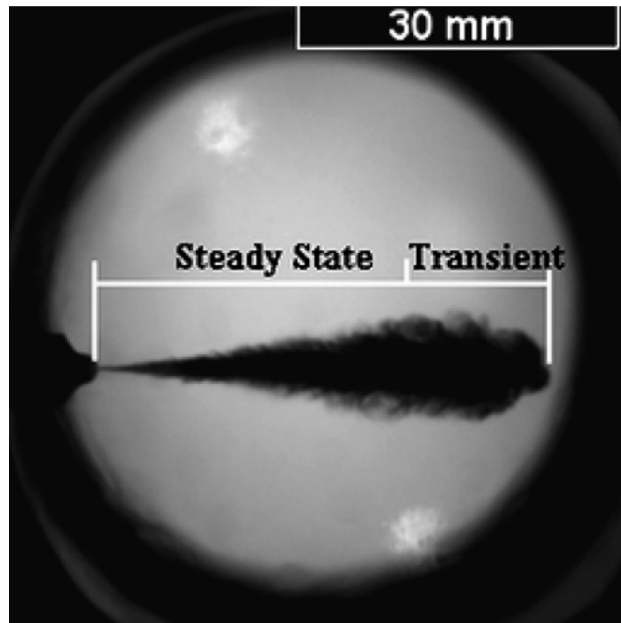


Figure 2-2: Visualization of a spray taken at $825\mu\text{s}$ after the start of the injection ($P_{inj} = 80\text{ MPa}$, $D_0 = 0.14\ \mu\text{m}$, and $\rho_{cha} = 20\text{ kg/m}^3$) [5].

2.1.1 Spray characterization

In order to understand the spray physics and optimize the performance of ICE, spray characterization studies have been extensively conducted during the last forty years, mostly using experimental techniques. The only numerical technique able to describe the physics of the spray is the Direct Numerical Simulation (DNS), described in 2.3.3, but the cost of this technique is huge, and unaffordable from the design point of view.

There exist many spray characteristics such as can be the spray cone angle, spray tip penetration, droplet size, velocity distributions, and many more that will be described in the following pages. Typically, spray characteristics are

classified into two sub-groups, macroscopic and microscopic, that are shown in Figure 2-3.

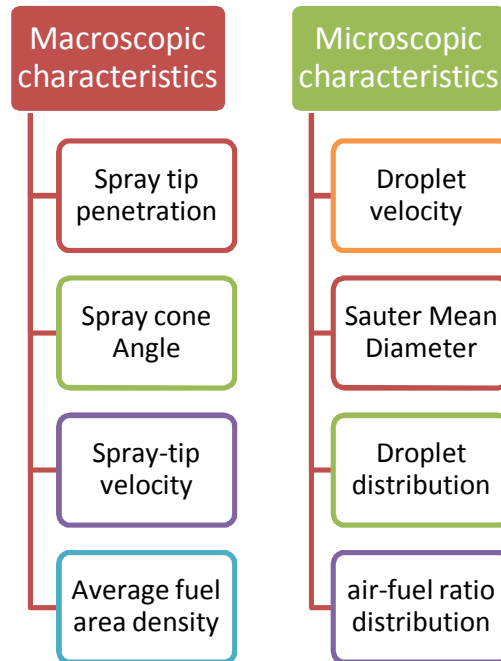


Figure 2-3: Diagram of Macroscopic and microscopic spray characteristics.

Figure 2-4 indicates the most important spray macro-scale characteristics, which consist of the spray tip penetration, the spray cone angle, and the spray width. The last two parameters are usually defined at 60% of the full spray penetration Lefebvre, 2011 [6] and 1989 [7].

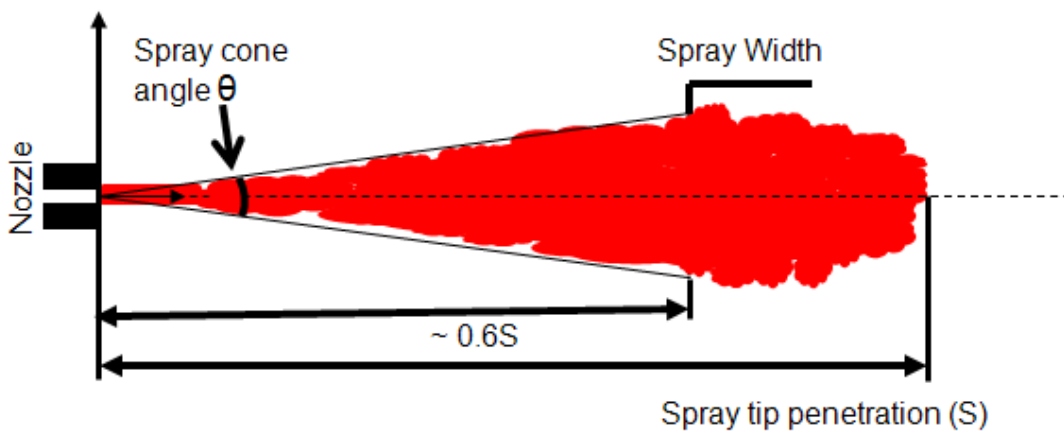


Figure 2-4: Macroscopic spray parameters.

2.1.2 Liquid length

An overview of the basic parameters of the spray is necessary before introducing the numerical methods used to model the spray behavior. The parameters linking the flow at the nozzle with the spray liquid length under evaporative condition were presented in [5], [8], [9], [10] and [11]. The liquid length (also called liquid penetration), LL, is defined as the distance from the nozzle exit to the farthest location where the fuel parcel on the spray axis has entrained enough higher-temperature gas to vaporize the fuel. In our case, it is computed numerically in this way, although there exist other models (see the previous references).

2.1.3 Spray penetration

Figure 2-4 presents the spray tip penetration (or simple called spray penetration). It is defined as the axial distance from the nozzle tip to the farthest location on the spray axis that the spray can reach (titled the tip spray, also the extreme point of the spray). Fortunately, the spray penetration is easily to be visualized and measured in the test rig, so there are many experimental results to compare with. This macroscopic parameter is very important in the fuel spray because it shows the size of the spray. As previously mentioned, the general amount of liquid-gas contained in the spray heavily affects on the following processes such can be mixing, combustion, and soot formation. Particularly, knowing this length is crucial when the spray impinges on the wall.

2.1.4 Spray cone angle

There are many different definitions of the spray cone angle in literature. Bae et al., 2002 [12] defined the spray angle as the angle between two lines

connecting the nozzle tip and two half-penetration points on the spray boundary, thus using the 50% of the spray penetration. In this thesis, we have used the definition of spray cone angle depicted in Figure 2-4 (60% of the spray penetration) [7].

2.2 Modeling fuel spray

The numerical analysis of fuel injection and combustion processes is divided into many sub models, due to its immense complexity. Some of them, for instance, are the modeling of the internal nozzle flow; spray break-up and evolution; flame structure and dynamics; turbulent combustion, and soot formation.

An idealized situation is shown in Figure 2-5. In general, sprays belong to a specific type of two-phase flows. The modeling of liquid-gas flows is quite complex as it involves turbulent phenomena, atomization, break-up, evaporation, heat and mass transfer and, mixing of fuel and gas. In spray modeling, the conservation equations for the liquid and the gas phase need to be solved simultaneously.

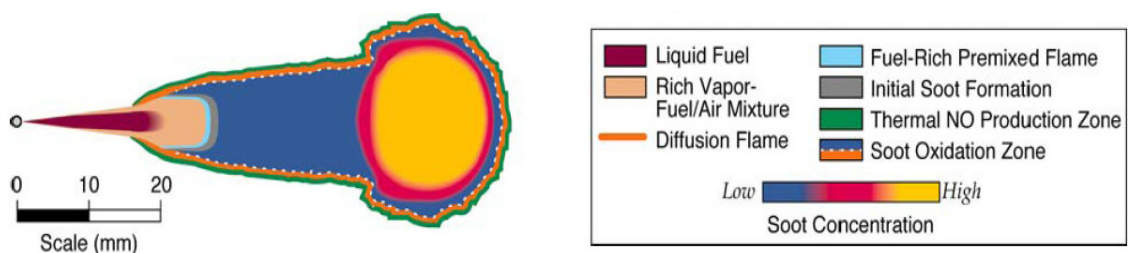


Figure 2-5: Schematic of various stages starting from internal nozzle flow to soot formation in Diesel sprays [13].

It is evident that the understanding of spray trajectories, evaporation is crucial because it directly affects the ignition and combustion processes and soot formation. On the other hand, the spray is characterized by the internal

nozzle flow characteristics. Thus, it is equally important to know or model the inlet condition as to use an accurate spray atomization model.

The general purpose of the CFD modeling is to solve a system or Partial Differential Equations, formed by the mass conservation equation, the Navier-Stokes equation and the Energy equation. As we will see, as the computation time are impracticable in most of the case, in many practical situations this set of equations are only solved for the mean fluid magnitudes whereas the turbulent fluctuations are modeled.

In this document, we are going to focus on the models, but not in the techniques used to solve the equations. Star-CD uses the well-known Finite Volume Method (FVM). We refer to the interest reader, for instance, to ([14], [15], [16] and [17]).

2.3 Turbulent approaches to simulate turbulent two-phase flows in Diesel sprays

2.3.1 Reynolds-averaged Navier-stokes

Reynolds-Averaged Navier-Stokes (RANS) methods have been used extensively in the industry due to their relative low cost and accuracy. It has been extensively used in the ICE context, but always after a careful validation. It is worthy to note that RANS only compute the mean of the fluid magnitudes, modeling, through the turbulent viscosity hypothesis, all the turbulent perturbations. Usually, all the different RANS methods have an equation for the transport of kinetic energy and other quantity, usually the dissipation, in order to obtain length and time scales. We have used this model throughout all the simulations made for this thesis. The example in Figure 2-6 shows a RANS simulation that uses the Eulerian-Lagrangian Spray Atomization approach.

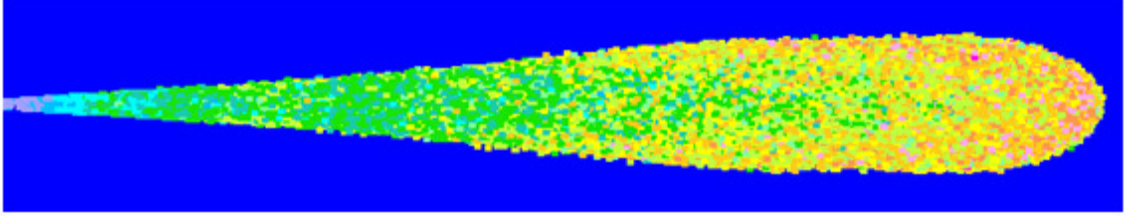


Figure 2-6: RANS Eulerian-Lagrangian Spray Atomization (ELSA) simulation of droplets in Diesel spray.

There are many RANS models, and there has been a continuous work in this field since the first RANS models were developed in the '60s. We will describe briefly the three turbulent models used in this work in section 2.3.1.1, 2.3.1.2, and 2.3.1.3. A detailed description of this and other models can be found in ([18], [19], [20] and [21]).

2.3.1.1 High Reynolds number k - ε model

Speziale, 1987 [22] proposed the High Reynolds number k - ε model employing similar equations as the standard k - ε model.

In this case, the equation for the transport of the kinetic energy and dissipation are:

$$\frac{\partial}{\partial t}(\rho k) + \frac{\partial}{\partial x_j} \left[\rho u_j k - \left(\mu + \frac{\mu_t}{\sigma_k} \right) \frac{\partial k}{\partial x_j} \right] = \mu_t (P + P_B) - \rho \varepsilon - \frac{2}{3} \left(\mu_t \frac{\partial u_i}{\partial x_i} + \rho k \right) \frac{\partial u_i}{\partial x_i} + \mu_t P_{NL} \quad (2.1)$$

$$\begin{aligned} \frac{\partial}{\partial t}(\rho \varepsilon) + \frac{\partial}{\partial x_j} \left[\rho u_j \varepsilon - \left(\mu + \frac{\mu_t}{\sigma_\varepsilon} \right) \frac{\partial \varepsilon}{\partial x_j} \right] = \\ C_{\varepsilon 1} \frac{\varepsilon}{k} \left[\mu_t P - \frac{2}{3} \left(\mu_t \frac{\partial u_i}{\partial x_i} + \rho k \right) \frac{\partial u_i}{\partial x_i} \right] + C_{\varepsilon 3} \frac{\varepsilon}{k} \mu_t P_B - C_{\varepsilon 2} \rho \frac{\varepsilon^2}{k} + C_{\varepsilon 4} \rho \varepsilon \frac{\partial u_i}{\partial x_i} + C_{\varepsilon 1} \frac{\varepsilon}{k} \mu_t P_{NL} \end{aligned} \quad (2.2)$$

The values of this constant are detailed in chapter 4, because the sprays do not use these model classical constants.

2.3.1.2 RNG k - ε

Yakhot and Orszag, 1986 [23] and Yakhot et al., 1992 [24] described the Re-Normalization-Group (RNG) k - ε model, which tries to obtain an equation for the dissipation equation directly from the Navier Stokes equation. In this case, these equations are:

$$\frac{\partial}{\partial t}(\rho k) + \frac{\partial}{\partial x_j} \left(\rho u_j k - \left(\mu + \frac{\mu_t}{\sigma_k} \right) \frac{\partial k}{\partial x_j} \right) = \mu_t (P + P_B) - \rho \varepsilon - \frac{2}{3} \left(\mu_t \frac{\partial u_i}{\partial x_i} + \rho k \right) \frac{\partial u_i}{\partial x_i} \quad (2.3)$$

$$\begin{aligned} \frac{\partial}{\partial t}(\rho \varepsilon) + \frac{\partial}{\partial x_j} \left(\rho u_j \varepsilon - \left(\mu + \frac{\mu_t}{\sigma_\varepsilon} \right) \frac{\partial \varepsilon}{\partial x_j} \right) = & C_{\varepsilon 1} \frac{\varepsilon}{k} \left[\mu_t P - \frac{2}{3} \left(\mu_t \frac{\partial u_i}{\partial x_i} + \rho k \right) \frac{\partial u_i}{\partial x_i} \right] + \\ & C_{\varepsilon 3} \frac{\varepsilon}{k} \mu_t P_B - C_{\varepsilon 2} \rho \frac{\varepsilon^2}{k} + C_{\varepsilon 4} \rho \varepsilon \frac{\partial u_i}{\partial x_i} - \frac{C_\mu \eta^3 (1 - \eta / \eta_0)}{1 + \beta \eta^3} \frac{\rho \varepsilon^2}{k} \end{aligned} \quad (2.4)$$

2.3.1.3 Chen k - ε

Chen, 1987 [25] proposed another model with some modifications in:

- The dissipation time scale, $\frac{k}{\varepsilon}$, is the only turbulent time scale used in closing the ε equation in the basic $k - \varepsilon$ model,
- The production time scale $\frac{k}{P}$ is used for the closure of the ε eq.,
- The claim for this extra time scale is that it allows the energy transfer mechanism of turbulence to respond more effectively to the mean strain rate [18].

Mathematical formulations:

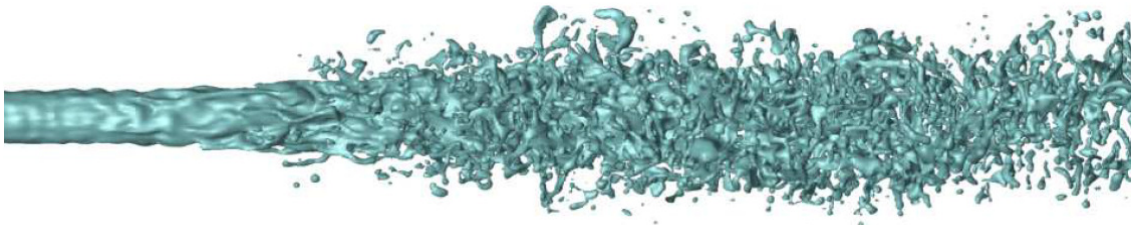
$$\frac{\partial}{\partial t}(\rho k) + \frac{\partial}{\partial x_j} \left(\rho u_j k - \left(\mu + \frac{\mu_t}{\sigma_k} \right) \frac{\partial k}{\partial x_j} \right) = \mu_t (P + P_B) - \rho \varepsilon - \frac{2}{3} \left(\mu_t \frac{\partial u_i}{\partial x_i} + \rho k \right) \frac{\partial u_i}{\partial x_i} \quad (2.5)$$

$$\begin{aligned} \frac{\partial}{\partial t}(\rho \varepsilon) + \frac{\partial}{\partial x_j} \left(\rho u_j \varepsilon - \left(\mu + \frac{\mu_t}{\sigma_\varepsilon} \right) \frac{\partial \varepsilon}{\partial x_j} \right) = \\ C_{\varepsilon 1} \frac{\varepsilon}{k} \left[\mu_t P - \frac{2}{3} \left(\mu_t \frac{\partial u_i}{\partial x_i} + \rho k \right) \frac{\partial u_i}{\partial x_i} \right] + C_{\varepsilon 3} \frac{\varepsilon}{k} \mu_t P_B - C_{\varepsilon 2} \rho \frac{\varepsilon^2}{k} + C_{\varepsilon 4} \rho \varepsilon \frac{\partial u_i}{\partial x_i} + C_{\varepsilon 5} \frac{\mu_t^2 P^2}{\rho k} \end{aligned} \quad (2.6)$$

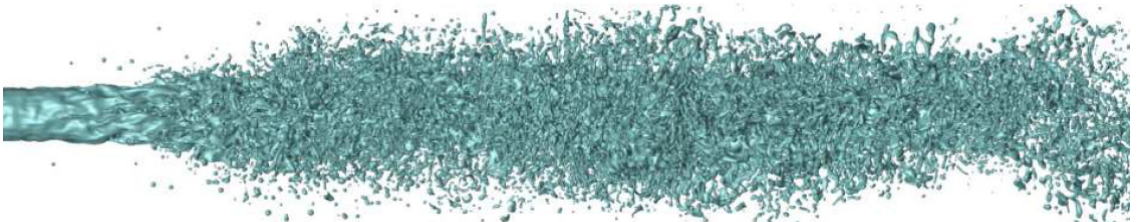
However, using the Chen model, there is no explicit account of compressibility or buoyancy effects.

2.3.2 Large-Eddy Simulation

Large-eddy simulation (LES) has significantly increased its roles in modeling internal combustion engine flows in the last 10 years.



a)



b)

Figure 2-7: Visualization of Numerical Simulation using (a) LES approach [26]; (b) DNS approach [27].

Chapter 2 – Spray Fundamentals and CFD spray modeling

As its name indicates LES methods simulate the largest eddies of the flows, where the energy resides. A proper LES method must simulate at least the 85% of the energy. The other 15% and all the dissipative scales are modeled using a filter. Thus, the resolution of the grid must be higher than in RANS. Another problem is that as large eddies remains, the problem is no steady anymore, increasing the cost.

Encouragingly, the instantaneous LES model provides a more detailed representation of the turbulent structures, captures the flow physics accurately in swirling and shows to be superior where significant turbulence is present rather than RANS model as presented in Figure 2-7.

However, apart from the fact that the cost of a LES is at least 2-3 orders of magnitude higher than RANS, LES presents some serious problems, as can be the turbulent conditions at the inlet and the impingement at the wall.

Apte Research Group of The Oregon State University has been conducted a detail study on Large Eddy Simulation of Sprays and Droplet-Laden Flows and a stochastic sub-grid model from 2003 – present ([28], [29], [30], [31], [32], [33], [34], [35], and [36]). Apte et al., 2012 [36] defined more regimes in LES method as presented in Figure 2-8.

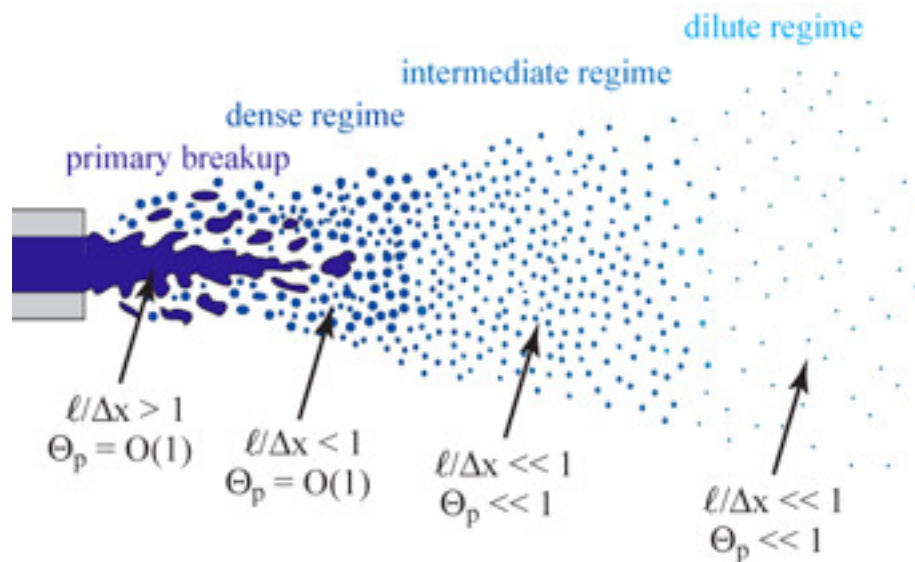


Figure 2-8: Various spray regions classified in LES model by Apte et al., 2012 [36].

Villers et al., 2004 [37] applied the Large Eddy Simulation for primary Diesel spray atomization. De Crevoisier, 2006 [38] modeled the high-pressure swirl injector spray atomization using the VOF-LES model. Liovic and Lakehal, 2007 [39] applied LES-VOF simulation of gas injection to compute the interface-turbulence interactions in large-scale bubbling processes. LES scheme for unstructured grid based on the principle of a mixture-theory-based Eulerian–Lagrangian approach is implemented to take into account volumetric displacements due to bubble motion and size variations by Mahesh, 2006 [40].

2.3.3 Direct Numerical Simulation

Direct Numerical Simulation (DNS) solves all the relevant turbulent scales. Its cost is prohibitively high. In recent years, DNS of primary breakup for Diesel spray has garnered attention of several research centers, e.g., Beau et al., 2006 [41], Lebas et al., 2009 [42] from CORIA (an example result presented in Figure 2-9). Chesnel, 2010 [26], utilized the Level Set procedure with sub-grid closures in DNS and LES frameworks. A review of DNS approach applied in multi-phase modeling and fuel spray is listed in the chronological order as presented in Figure 2-10.



Figure 2-9: DNS simulation of Diesel sprays. Computational domain is 0.3 mm x 0.3 mm x 2.2 mm, grid size is 128 x 128 x 896, $D_0 = 100 \mu\text{m}$, $U = 100 \text{ m/s}$, $\rho_{inj} = 696 \text{ kgm}^{-3}$, $\rho_{cha} = 50 \text{ kgm}^{-3}$, computing time 10,000 h on 14 processors (Lebas et al., 2009 [42]).

Chapter 2 – Spray Fundamentals and CFD spray modeling

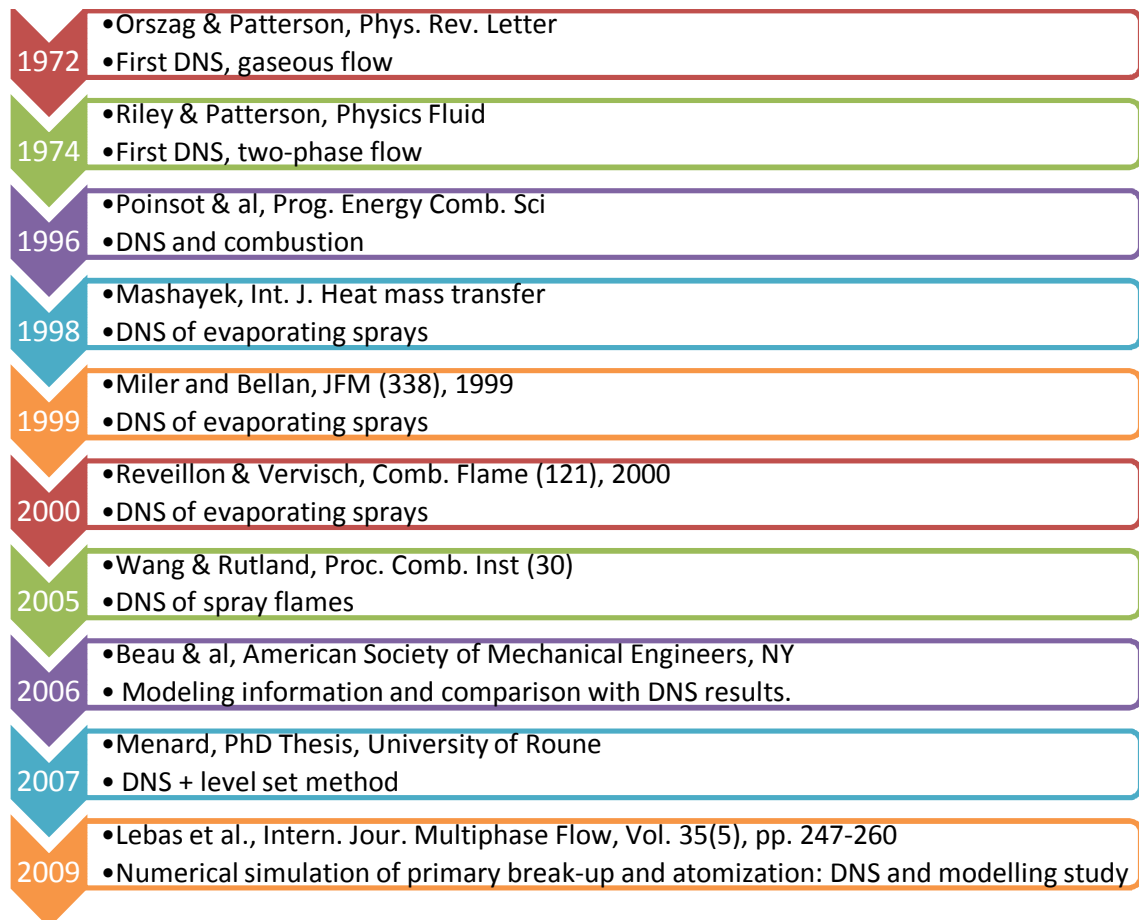


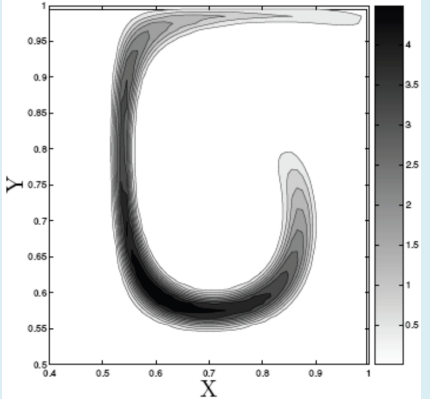
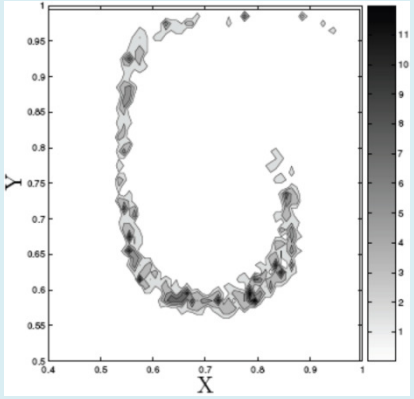
Figure 2-10: The development of DNS model applied in liquid/gas two-phase modeling ([2] and [42]).

The highly nonlinear phenomena controlling the fuel liquid breakup process and surface break-up, as well as the turbulent multi-phase flow can be captured in this approach. Nevertheless, the major drawback of the approach is that the computational times necessary for spray simulation are many orders of magnitude higher than LES or RANS. As a result, DNS simulations are still rare, needing a careful validation.

2.4 Following droplets: Eulerian or Lagrangian?

Table 2-1 summarized the key points of both Eulerian and Lagrangian approach. The advantages and disadvantages of both models can be also seen in this table.

Table 2-1: Comparison between Eulerian and Lagrangian approaches.

-	Eulerian approach	Lagrangian approach
Description	The fluid is described as a continuum.	Fuel is in form of drops.
Interface tracking [44]	The traditional Eulerian framework does not offer the interface tracking.	No interface tracking.
Advantages [45]	<ul style="list-style-type: none"> - Modeling liquid phase - Moderate computing cost - Couple easily with a gaseous phase. 	<ul style="list-style-type: none"> - Modeling particle motion - Widely used in both academic and industrial applications - Extensive history of validation.
Drawback	Crossing trajectory problems.	It is not a valid description for the liquid core and primary breakup in the dense spray.
Desired	Track the break-up phenomena and evaporating sprays evolution.	Reduce the computing time and memory.
Computing domain	 <p>Eulerian domain represented by a contour profile 100x100x10 (size).</p>	 <p>Lagrangian domain represented by parcels with much more drops 100x100x10⁵ (drop).</p>

Usually, the study of the Diesel sprays structure is splitting itself in two very different regions, depending on coherency of the fuel. In many applications, using the DDM method (explained below), the droplets are introduced directly and there no exists liquid core. The droplets are followed using a pure Lagrangian approach. Figure 2-11 shows how particles are

handled in Lagrangian framework. There exists however mixed approaches, which usually describe the liquid core using a Eulerian approach and then moving to Eulerian or Lagrangian methodology to follow the droplets.



Figure 2-11: A schematic showing treatment of particles using the Lagrangian approach (Adapted from Vujanovic et al., 2009 [43]). Each dotted circle represents for a parcel.

2.4.1 Discrete Droplet Model

Dukowicz, 1980 [46] proposed the Discrete Droplet Model (DDM) for spray modeling. Using Dukowicz's idea, the liquid flow is discretized into groups of droplets. Each one of these groups shares the same properties and is represented by a parcel. O' Rourke and Bracco, 1980 [47] developed another close parcels approach. Each parcels contained droplets with the same droplet parameters. These models obtain ordinary differential equations of motion for these parcels, which can be solved easily. Lagrangian framework is then utilized to track parcels. The main problem of this method is that it requires a first cell two or three times bigger than the nozzle diameter, so the profile of the velocity at the inlet is lost.

2.4.2 Eulerian-Eulerian approach

A Eulerian-Eulerian method or a two-fluid Eulerian-liquid Eulerian gas (ELEG) model provides a better prediction for the internal nozzle flow and the atomization region, and especially in the case of a two-phase flow with high concentration of droplets in some regions, e.g. at the dense zone of the Diesel sprays [43]. This methodology employs the volume or ensemble-averaged mass and momentum conservation equations to describe the time-dependent motion of fluid and gas phases [48]. Iyer and Abraham, 2005 [49] carried out ELEG computations and compared with measured results in a wide range of conditions. Fevrier et al., 2005 [50] proposed the Mesoscopic Eulerian Formalism (MEF), or the Euler-Euler model and constructed the mono-disperse formulation. Vujanovic et al., 2009 [43] improved the standard approach by introducing variable droplet size classes. Figure 2-12 depicts how particles are handled in Eulerian framework.

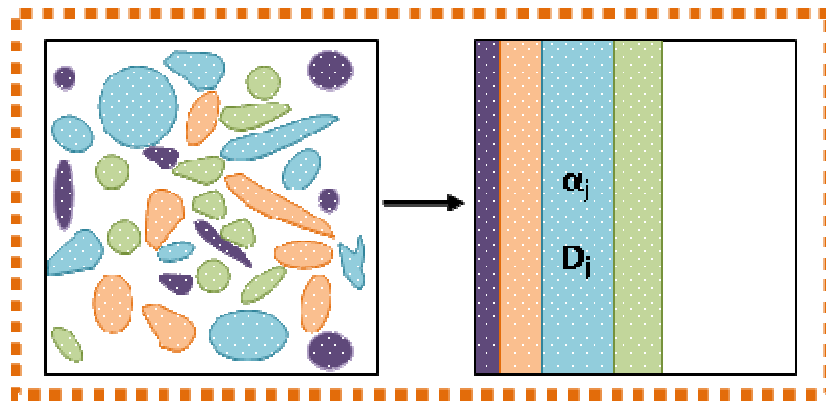


Figure 2-12: A schematic showing treatment of particles using the Eulerian approach (Adapted from Vujanovic et al., 2009 [43]).

2.4.3 Eulerian–Lagrangian approach

The disperse region of spray, is particularly well represented in the Lagrangian approach. The atomized fuel is represented by a set of droplets, which are followed through some transport equations. However, this

assumption is not adequate for the dense spray region. Hence, this approach takes advantage of each framework for solving its particular spray region, so an Eulerian–Lagrangian approach is a hybrid model able to describe both primary and secondary breakup in two-phase flow modeling. The involvement of Lagrangian model describes more accurately the dispersed spray region. However, the grid resolution close to the nozzle is very sensitive, and it still limits the capability of adequately representing this dense zone [43]. One of the drawbacks of this methodology is that a large number of droplets are created very close to the injector, causing a serious load imbalance (droplets are presented only in a few processors in a parallel computation) [36]. A so-called Lagrangian-Droplet Eulerian-Fluid (LDEF) method has been widely implemented in commercial software and is broadly employed in multidimensional spray models. The major disadvantage of this approach is that it is impossible to use adequate numerical resolution. As the resolution is only possible when the volume fraction of the droplets in a computational cell is less than 10% [51].

Andreani and Yadigaroglu, 1997 [52] applied 3-D Eulerian-Lagrangian model of dispersed flow film boiling including a mechanistic description of the droplet spectrum evolution. Giannadakis et al., 2004 [53] applied Eulerian–Lagrangian coupling model for cavitation modeling in single-hole Diesel injector. Chrigui, 2005 [54] used an Eulerian-Lagrangian approach to model Turbulent Reactive Multi-Phase Flows under Gas Turbine Combustor Conditions. Shams et al., 2011 [55] developed an Eulerian–Lagrangian approach for the simulation of turbulent bubbly flows in complex systems based on the volumetric coupling. In this complex flow, the Lagrangian frame was used to model the bubble dynamics of the dispersed phase. Figure 2-13 shows the difference between Eulerian-Eulerian model and Eulerian-Lagrangian model, and the boundary condition for the Eulerian-Eulerian model (also detailed in Figure 2-14). This methodology is not able to represent accurately the near nozzle region. A virtual inlet with effective diameter and velocity is situated 10 diameters away from the nozzle exit. This requires an estimation of these effective quantities, which usually is acquired through experimental techniques [9]. This simplification can lead to the loss of some information, and

especially this model is not able to represent accurately the nozzle flow particularities, such can be an internal cavitating flow. On the contrary, the Eulerian-Lagrangian methodology is able to describe the completely computational domain starting from the nozzle exit. Typically, the initial drop velocity is a function of the specified injection rate, cone angle, and so forth [56].

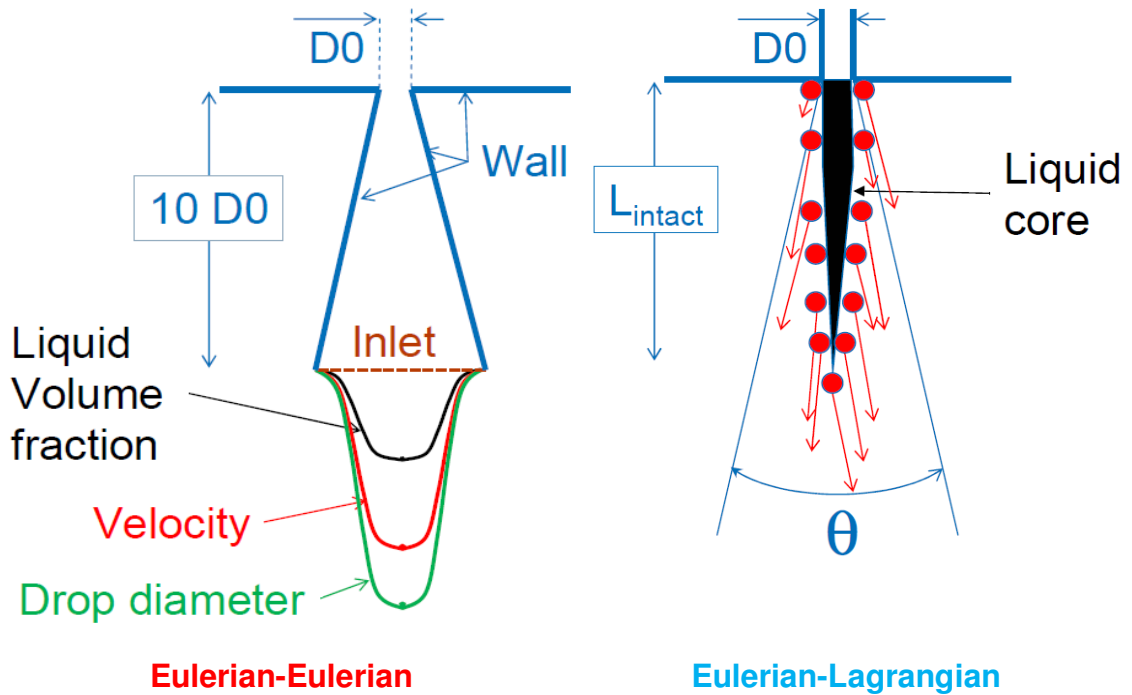


Figure 2-13: The comparison and setup conditions for Eulerian-Eulerian model and Eulerian-Lagrangian model (Habchi and Martinez, 2010 [56], Martinez et al., 2010 [57]).

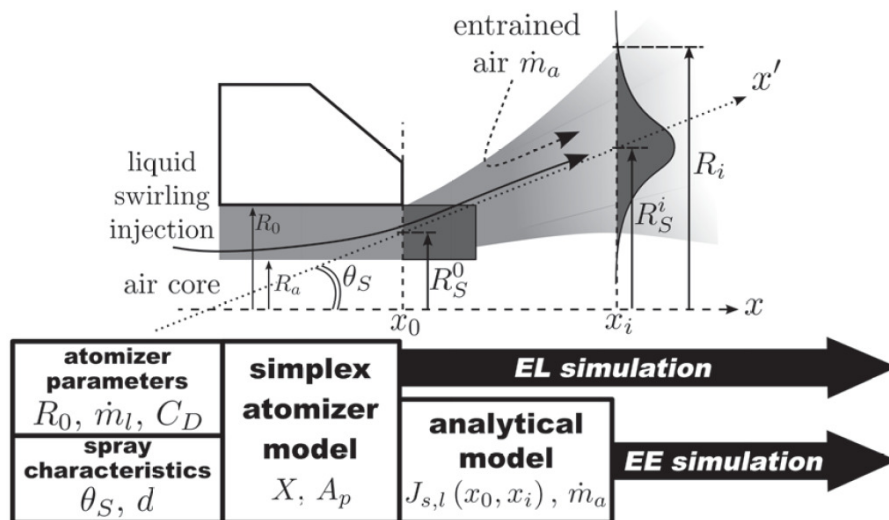


Figure 2-14: The detail description of the boundary conditions (Sanjose, 2009 [58]).

Another branch of Eulerian-Lagrangian approaches, especially designed for handling the atomization of Diesel sprays, is the Eulerian-Lagrangian Spray Atomization (ELSA) model, which has been utilized throughout this thesis. In the ELSA approach, the droplets velocity is obtained from the Eulerian liquid phase calculation. A comprehensive description of this method is detailed in the next chapter.

2.5 Interface Tracking Methods

The challenge in modeling the dense spray and atomization processes with aforementioned methods leads to the development of some advanced models. In this section, we present a review of five Interface Tracking Methods (ITMs). Generally, the key difference amongst the four methods is based on the equation used for the description of the topology of the liquid core and the biggest droplets. The ITMs have been applied in two-phase flow modeling in engine sprays recently, providing a reasonably resolution for modeling the interaction between fluid and gas phase, as well as correctly capture the surface and surface break-up.

2.5.1 Level set method

The original level set (LS) method was developed by Sethian (1999 [59], and 2001 [60]), and Osher & Fedkiw (2001 [61], and 2003 [62]) for interface tracking, solving a hyperbolic equation for the topology. This powerful technique quickly became popular in many applications; it has been widely applied in solving solid and fluid mechanics problems. For the fuel injection modeling, the LS method captures the liquid and gas interface, and follows it in time describing the liquid surface.

2.5.2 Ghost Fluid Method

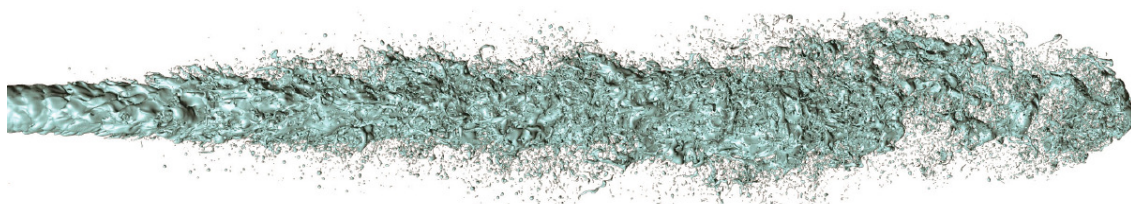


Figure 2-15: The coupled Level Set, Volume Of Fluid and Ghost Fluid Method in modeling liquid jet and primary break-up near the jet nozzle (Menard et al., 2007 [63]).

Fedkiw et al., 1999 [64] developed the Ghost Fluid Method (GFM). This method has been broadly used, including for making special effects for movies and videogames. Menard et al., 2007 [63] continued his work on 3D simulation of the primary break-up using the coupling Level Set – Volume Of Fluid and Ghost Fluid Method in which the level set method is utilized to capture the surface motion, an example result can be visualized in Figure 2-15.

Many authors undertook further adaptation of the model to suit the new physical problems. Ashgriz and Poo's works, 1990 [65] studied coalescence and separation in binary collisions of liquid drops. Tanguy and Berlemont, 2005 [66] applied the level set technique coupled with the ghost fluid method to solve the incompressible Navier-Stokes equations for various fuel droplet collision behaviors as shown in Figure 2-16. Sussman and Puckett, 2000 [67] indicated that the coupling of the level set and Volume Of Fluid methods ensure mass conservation. Balabel, 2011 [68] worked on a version of the level set method, called Interfacial Marker-Level Set (IMLS), and couple it with RANS formulation to model the dynamics of turbulent two-phase flow. Herrmann et al. 2004 [69], 2005 [70], and 2006 [71] implemented a method, namely a Refined Level Set Grid (RLSG) method, which can describe accurately the frontier.

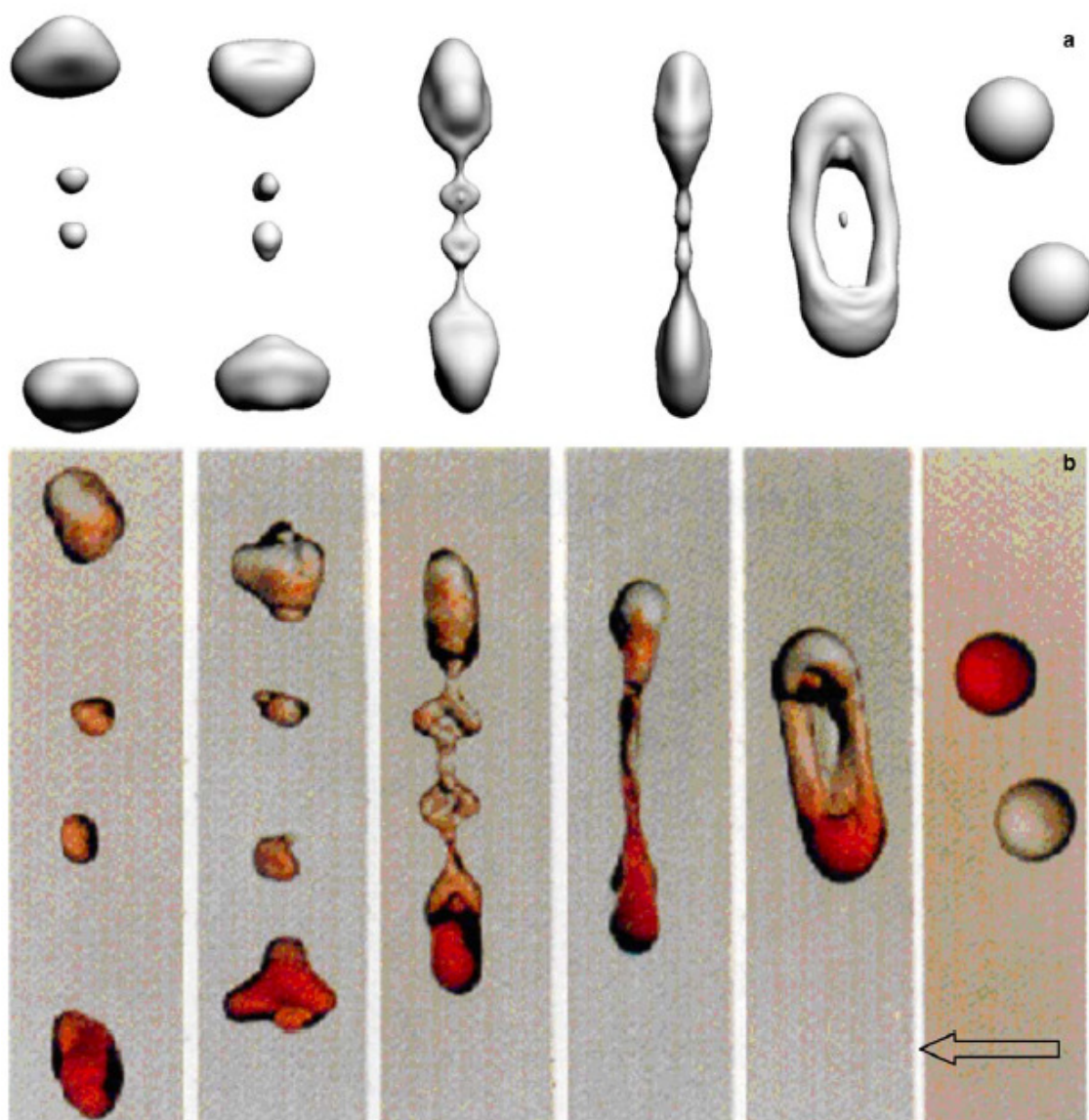


Figure 2-16: The 3D simulation by (a) Tanguy and Berlemont, 2005 [66]: ethanol droplet, $We = 60$, $Oh = 0.02$, impact parameter 0.5. (b) Ashgriz and Poo, 1990 [65]: Water droplet, $We = 83$, impact parameter 0.43.

2.5.3 Volume Of Fluid

Hirt and Nichols, 1981 [72] published a couple of papers on the Volume Of Fluid (VOF) method in sprays. The VOF models small-scale topology fragmentation, hence, it is very suitable for Diesel sprays. However, it remains expensive in computing time. Rider and Kothe, 1998 [73]; Rudman, 1998 [74]; Scardovelli and Zaleski, 1999 [75], 2000 [76]; and Gueyffier et al., 1999 [77]

applied VOF to track the cell shape and simulate topology changes, interface motion in multiphase flows.

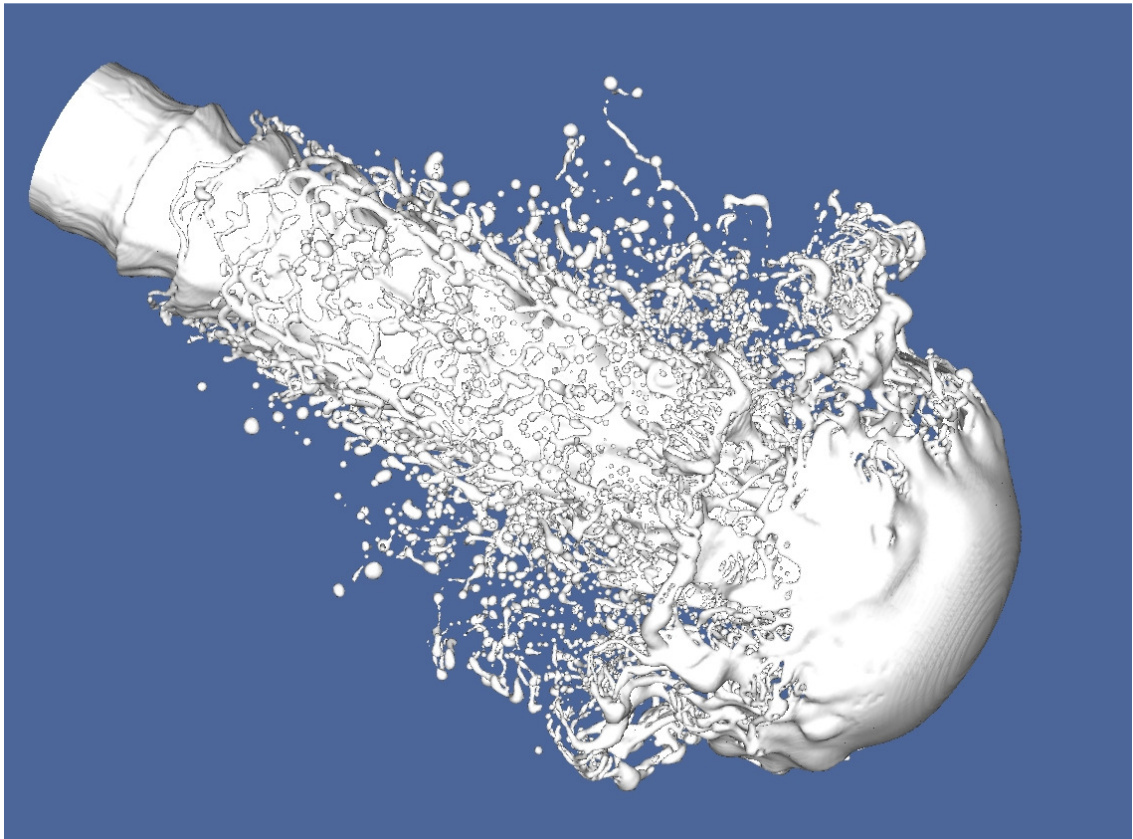


Figure 2-17: Liquid Atomization using principally Volume Of Fluid method (Zaleski et al. and d'Alembert's team [78]).

The Volume Of Fluid/Piecewise Linear Interface Construction (VOF/PLIC) has been developed by the team of DALEMBERT (Lafaurie et al., 1994 [79], Scardovelli and Zaleski, 1999 [75], and 2000 [76], Gueyffier et al., 1999 [77], Aulisa et al., 2003 [80], Scardovelli and Zaleski, 2003 [81], Aulisa et al., 2007 [82], Afkhami et al., 2009 [83], Cervone et al., 2009 [84], and Bornia et al., 2011 [85]). The results obtained well described the topology changes in the case of the detachment of a drop by gravity and showed a very good agreement with the capillary wave theory of small amplitudes, which confirms the correct calculation of the surface tension terms.

2.5.4 Other methods

Tryggvason et al., 2001 [86] developed a front tracking method for the computations of multiphase flow; Du et al., 2006 [87] provided a better understanding of the front tracking. The last Interface tracing method is the Lattice-Boltzmann Method. The state-of the-art of Lattice-Boltzmann Method was presented by Sankaranarayanan et al., 1999 [88], Takada et al., 2000 [89], and Inamuro et al., 2004 [90].

Concluding Remarks

Both Front-Tracking method and Lattice-Boltzmann method are not widely used in simulations of two-phase flow in internal combustion engine. On the contrary, the Level Set method and Volume Of Fluid method have been extensively used recently. Reveillon et al. 2007 [2] remarked that the Level Set Method does not conserve mass. The VOF method instead, is mass conservative, but a reconstruction of the interface is needed in each step. Thus, the best solution is association of both methods.

Recently, Chatzikyriakou et al., 2011 [91] showed various ITMs simulations performed with several CFD code and presented a comparison amongst them.

2.5.5 Numerical tools for liquid spray models

Many CFD packages are available for spray modeling and simulation as show in Table 2-2. The CFD code can solve single-phase flows or multi-phase flows, and 2D or 3D problems. In addition, different spray, and turbulent sub-models are implemented in each computational code. In our case, the code chosen was Star-CD.

Chapter 2 – Spray Fundamentals and CFD spray modeling

Table 2-2: A couple of CFD codes for spray modeling and simulation.

Software	Developer
Star-CD	CD-adapco
AVL Fire	AVL Advanced Simulation Technologies
ANSYSCFD/Fluent	ANSYS, INC
CONVERGE CFD	Convergent Science, Inc
KIVA	The Los Alamos National Labs The Engine Research Center at the University of Wisconsin - Madison
OpenFOAM	Silicon Graphics International Corp. (SGI)
CT-FUEL	Gamma Technologies
CFDS-FLOW3D	Computational Fluid Dynamics Services, Inc.
PHOENICS	CHAM ltd
CFD-ACE+	ESI-group
TransAT/ CMFD	ASCOMP GmbH
JETMIX/JETEVAP TESS™	Southwest Research Institute (SwRI)
SURFER Code	Université Pierre et Marie Curie
Gerris Code	Stephane Popinet at NIWA, NZ

REFERENCES

- [1] Igura, S.; Kadota, T.; Hiroyasu, H. *Translations of the Japanese Society of Mechanical Engineers*, 41, pp. 15-59, **1975**.
- [2] Reveillon, J.; Demoulin, F.X.; Pera, C.; Meftah, H.; Ducruix, S.; Durox, D. *Simulation approaches for spray combustion*. Autumn meeting of The Combustion Institute, British Section, Imperial College, **2007**.
- [3] Hiroyasu, H; Arai, M. *Structures of fuel sprays in Diesel engines*. SAE Paper 900475, **1990**.
- [4] Desantes, J.M.; Payri, R.; Salvador, F. J., Gil, A. *Deduction and validation of a theoretical model for a free Diesel spray*. *Fuel*, Vol. 7, pp.85-910, **2006**.
- [5] Desantes, J.M.; Payri, R.; Garcia J.M.; Salvador, F.J. *A contribution to the understanding of isothermal Diesel spray dynamics*. *Fuel* 86, pp. 1093-1101, **2007**.
- [6] Lefebvre, A. *Atomization, Thermopedia, Thermodynamics*. Heat & Mass Transfer, and Fluids Engineering, last edited online version by 3rd February 2011, last accessed by 25th June, 2012, **2011**.
- [7] Lefebvre, A. *Atomization and Sprays*, Hemisphere Publishing Corporation, New York, **1989**.

- [8] Payri, R.; Salvador, F.J.; Gimeno, J.; Zapata, L.D. *Diesel nozzle geometry influence on spray liquid-phase fuel penetration in evaporative conditions*. Fuel 87, pp. 1165-1176, **2008**.
- [9] Payri, R.; Salvador, F.J.; Gimeno, J.; de la Morena, J. *Study of cavitation phenomena based on a technique for visualizing bubbles in a liquid pressurized chamber*. International Journal of Heat and Fluid Flow 2009, Vol. 30, Issue 4, pp.768-777, ISSN 0142-727X. August, **2009**.
- [10] Payri, F.; Bermúdez, V.; Payri, R.; Salvador. *The influence of cavitation on the internal flow and the spray characteristics in Diesel injection nozzles*. F. Fuel 83, pp. 419 – 431, **2004**.
- [11] Desantes, J.M.; Payri, R.; Pastor, J.M.; Gimeno, J. *Experimental characterization of internal nozzle flow and Diesel spray behavior. Part I: Nonevaporative conditions*. Atomization And Sprays, Vol. 15(5), pp. 489–516, September, **2005**.
- [12] Bae, C.; Yu, J.; Kang, J.; Kong, J.; Cuenca, R.; Lee, K.O. *The Influence of Injectors Parameters on Diesel Spray*. THIESEL 2002, Valence, SPAIN, September, **2002**.
- [13] Dec, J.E. *A Conceptual Model of DI Diesel Combustion Based on Laser-Sheet Imaging*. SAE Paper No. 970873, **1997**.
- [14] Patankar, S.V. Numerical Heat and Mass Transfer. Hemisphere Publ. Corp., Washington, **1980**.
- [15] Hirsch, C. *Numerical Computation of Internal and External Flows*. John Willey & Sons, Vol. I & II, **1991**.
- [16] Versteeg, H.K.; Malalasekera, W. *Computational Fluid Dynamics*. Longman Scientific & Technical, **1995**.
- [17] Ferziger, J. H.; M. Peric. *Computational Methods for Fluid Dynamics*. Springer-Verlag, Berlin, **1996**.
- [18] *CD-Adapco*, Star-CD version 4.16.002, Methodology, **2011**.
- [19] Launder, B.E.; Spalding, D.B. *The numerical computation of turbulent flows*. Computer Methods in Applied Mechanics and Engineering, Vol. 3(2), pp. 269 – 289, **1974**.
- [20] Rodi, W. *Turbulence models for environmental problems. Prediction methods for turbulent flows*. Von Karman Institute for Fluids Dynamics. Lecture Series 1979-2, pp. 15–19, January **1979**.
- [21] El Tahry, S.H. *k- ϵ equation for compressible reciprocating engine flows*. AIAA, J. Energy, Vol. 7(4), pp. 345–353, **1983**.
- [22] Speziale, C.G. *On nonlinear k-l and k- ϵ models of turbulence*. J. Fluid Mech., 178, pp. 459-475, **1987**.

Chapter 2 – Spray Fundamentals and CFD spray modeling

- [23] Yakhot, V.; Orszag, S.A. *Renormalization group analysis of turbulence — I: Basic theory*. J. Scientific Computing, Vol. 1, pp. 1-51, **1986**.
- [24] Yakhot, V.; Orszag, S.A.; Thangam, S.; Gatski, T.B.; Speziale, C.G. *Development of turbulence models for shear flows by a double expansion technique*. Phys. Fluids, A4(7), pp. 1510-1520, **1992**.
- [25] Chen, Y.S.; Kim, S.W. *Computation of turbulent flows using an extended k - ϵ turbulence closure model*. NASA CR-179204, **1987**.
- [26] Chesnel, J. *Large Eddy Simulation for atomization: application to automotive engines injection*. PhD Thesis, University of Rouen, **2010**.
- [27] Menard, T. *Développement d'une méthode level-set pour le suivi d'interface. Application de la rupture de jet liquide*. PhD Thesis, University of Rouen, **2007**.
- [28] Apte, S.V.; Gorokhovski, M.; Moin, P. *LES of atomizing spray with stochastic modeling of spray break-up*. International Journal of Multiphase Flows, Vol. 29, pp. 1503-1522, **2003**.
- [29] Kim, W.W.; Apte, S.V.; Herrmann, M.; Ham, F. *Liquid film modeling in jet engine fuel injector*. Proceedings of the Summer Program, Center for Turbulence Research, Stanford University and NASA-AMES, pp. 305-314, **2004**.
- [30] Apte, S.V.; Ghosal, S. *A presumed PDF model for droplet evaporation / condensation in complex flows*. Annual Research Briefs, Center for Turbulence Research, Stanford University and NASA-AMES, pp. 209-221, **2004**.
- [31] Pozorski, J.; Apte, S.V. *Filtered particle tracking and subgrid-scale dispersion modeling in two-phase turbulent flows*. International Journal of Multiphase Flow, **2008**.
- [32] Shams, E.; Apte, S.V. *Modeling volumetric coupling in dispersed phase using Eulerian Lagrangian approach*. ILASS America's 21st Annual Conference on Liquid Atomization and Spray Systems, Orlando, FL, May **2008**.
- [33] Apte, S.V.; Mahesh, K.; Lundgren, T. *Accounting for finite-size effect in disperse two-phase flow*. International Journal of Multiphase Flow, Vol. 34 (4), pp. 260-271, **2008**.
- [34] Apte, S.V.; Mahesh, K.; Moin, P. *Large-eddy simulation of evaporating spray in a coaxial combustor*. Proceedings of the Combustion Institute, Vol. 32, Jan. **2009**.
- [35] Apte, S.V.; Mahesh, K.; Gorokhovski, M.; Moin, P. *Stochastic modeling of atomizing spray in a complex swirl injector using large eddy simulation*. Proceedings of the Combustion Institute, Vol. 32(2), pp. 2257 – 2266, **2009**.
- [36] Apte, S.V.; Mahesh, K.; Moin, P. *Large Eddy Simulation of Sprays and Droplet-Laden Flows*. Sprays and Spray Systems, Apte Research Group,

- <http://web.engr.oregonstate.edu/~sva/sprays.html>, last accessed by 25th June 2012.
- [37] De Villers, E.; Gosmanand, A.D.; Weller, H.G. *Large Eddy Simulation of primary Diesel spray atomization*. SAE Technical Paper, **2004**.
- [38] De Crevoisier, G. *VOF-LES modeling of a High Pressure-Swirl injector spray atomization*. Chalmers University of Technology, **2006**.
- [39] Liovic, P.; Lakehal, D. *Interface-turbulence interactions in large-scale bubbling processes*. Int. J. Heat and Fluid Flow, Vol. 28, pp. 127-144 , **2007**.
- [40] Mahesh, K.; Constantinescu, G.; Apte, S.; Iaccarino, G.; Ham, F.; Moin, P. *Large-eddy simulation of reacting turbulent flows in complex geometries*. Journal of Applied Mechanics, pp. 73-374, **2006**.
- [41] Beau, P.A.; Menard, T.; Lebas, R.; Berlemont, A.; Tanguy, S.; Demoulin, F.X. *Numerical jet atomization. Part II: modeling information and comparison with DNS results*. Miami, FL, United States, American Society of Mechanical Engineers, New York, NY 10016-5990, United States, **2006**.
- [42] Lebas, R.; Menard, T.; Beau, P.; Berlemont, A.; Demoulin, F. *Numerical simulation of primary break-up and atomization: DNS and modelling study*. International Journal of Multiphase Flow, Vol. 35(3), pp. 247 – 260, **2009**.
- [43] Vujanovic, M.; Edelbauer, W.; von Berg, E.; Tatschl, R.; Duic, N. *Numerical modeling of Diesel sprays with an Eulerian-Eulerian Approach*. AVL List GmbH, Austria, Uni. Of Zabreb, Croatia, 9th ERCOFTAC AHS Pilot Centre Meeting, **2009**.
- [44] Gouesbet, G.; Berlemont, A. *Eulerian and Lagrangian approaches for predicting the behaviour of discrete particles in turbulent flows*. Prog. Energy Combust. Sci. 25, 133, **1999**.
- [45] De Chaisemartin, S.; Laurent, F.; Massot, M.; Reveillon, J. *Evaluation of Eulerian multi-fluid versus Lagrangian methods for ejection of polydisperse evaporating sprays by vortices*. Submitted Journal of Computational Physics, **2007**.
- [46] Dukowicz, J.K. *A particle-Fluid Numerical Model for Liquid Sprays*. J. Comp. Physics, Vol. 35, pp. 229-253, **1980**.
- [47] O'Rourke, P.J.; Bracco, F.V. *Modeling of droplet interactions in thick sprays and a comparison with experiments*. Proc. Inst. Mech. Eng., Vol. 9 pp. 101–106, **1980**.
- [48] Van Sint Annaland, M.; Deen, N.G.; Kuipers, J.A.M. *Numerical simulation of gas bubbles behaviour using a three dimensional volume of fluid method*. Chemical Engineering Science, 60(11), pp. 2999–3011, **2005**.

- [49] Iyer, V.; Abraham, J. *Two-fluid modeling of spray penetration and dispersion under diesel engine conditions*. *Atomization and Sprays*, 15, 249-270, **2005**.
- [50] Fevrier, P.; Simonin, Olivier.; Squires, Kyle. *Partitioning of Particle Velocities in Gas-Solid Turbulent Flows into a Continuous Field and a Spatially Uncorrelated Random Distribution: Theoretical Formalism and Numerical Study*. *Journal of Fluid Mechanics*, 533, pp. 1-46, **2005**.
- [51] Iyer, V. *Modeling of diesel sprays using an Eulerian-liquid Eulerian-gas two-fluid model*. PhD thesis, Purdue University, **2011**.
- [52] Andreani, M.; Yadigaroglu, G. *A 3-D Eulerian-Lagrangian model of dispersed flow film boiling including a mechanistic description of the droplet spectrum evolution -I. The thermal-hydraulic model*. *International Journal of Heat and Mass Transfer*, Vol. 40(8), pp. 1753 – 1772, **1997**.
- [53] Giannadakis, E.; Gavaises, M.; Roth, H.; Arcoumanis, C. *Cavitation Modelling in Single-Hole Diesel Injector Based on Eulerian-Lagrangian Approach*. THIESEL 2004 Conference on Thermo- and Fluid Dynamic Processes in Diesel Engines, Valencia, September 10-13, **2004**.
- [54] Chrigui, M. *Eulerian-Lagrangian Approach for Modeling and Simulations of Turbulent Reactive Multi-Phase Flows under Gas Turbine Combustor Conditions*. Technische Universität Darmstadt, **2005**.
- [55] Shams, E.; Finn, J.; Apte, S. *A numerical scheme for Euler-Lagrange simulation of bubbly flows in complex systems*. *International Journal for Numerical Methods in Fluids*, Vol. 67(12), pp. 1865-1898, **2011**.
- [56] Habchi, C.; Martinez, L. *Eulerian-Eulerian and Eulerian-Lagrangian LES of Diesel sprays*. LES4ICE, IFP energies nouvelles, **2010**.
- [57] Martinez, L.; Benkenida, A.; Cuenot, B. *A model for the injection boundary conditions in the context of 3D simulation of Diesel Spray: Methodology and validation*. *Fuel*, Vol. 89(1), pp. 219 – 228, **2010**.
- [58] Sanjose, M. *Evaluation de la méthode Euler-Euler pour la simulation aux grandes échelles des chambres a carburant liquide*. University of Toulouse, **2009**.
- [59] Sethian, J.A. *Level set methods and fast marching methods*, second ed. Cambridge, U.K, Cambridge University Press, **1999**.
- [60] Sethian, J.A. *Evolution, implementation and application of level set and fast marching methods for advancing fronts*. *J. Comp. Phys.*, Vol. 169, pp. 503-555, **2001**.
- [61] Osher S.J.; Fedkiw, R.P. *Level set methods: An overview and some recent results*. *J. Comp. Phys.*, Vol. 169, pp. 463-502, **2001**.

Chapter 2 – Spray Fundamentals and CFD spray modeling

- [62] Osher, S; Fedkiw, R. *Level set methods and dynamic implicit interfaces*. New York: Springer, **2003**.
- [63] Menard, T.; Tanguy, S.; Berlemont, A. *Coupling level set/VOF/ghost fluid methods: validation and application to 3D simulation of the primary break-up of a liquid jet*. Int. J. Multiphase Flow 33, Vol. 5, pp. 510–524, **2007**.
- [64] Fedkiw, R.P.; Aslam, T.; Merriman, B.; Osher, S. *A non-oscillatory Eulerian approach to interfaces in multimaterial flows (the Ghost Fluid Method)*. J. Comput. Phys., 152 pp. 457-492, **1999**.
- [65] Ashgriz, N.; Poo, J.Y.; *Coalescence and separation in binary collisions of liquid drops*. J. Fluid Mech. 221, pp. 183–204, **1990**.
- [66] Tanguy, S.; Berlemont, A. *Application of a level set method for simulation of droplet collisions*. International Journal of Multiphase Flow, Vol. 31(9), pp. 1015 – 1035, **2005**.
- [67] Sussman, M.; Puckett, E.G. *A coupled level set and volume-of-fluid method for computing 3D and axisymmetric incompressible two-phase flows*. J. Comput. Phys. 162, pp. 301–337, **2000**.
- [68] Balabel, A. *Numerical prediction of turbulent thermocapillary convection in superposed fluid layers with a free interface*, International Journal of Heat and Fluid Flow, Vol. 32, Issue 6, pp. 1226-1239, December **2011**.
- [69] Herrmann, M. Annual Research Briefs 2004, pp. 15{30. Center for Turbulence Research, **2004**.
- [70] Herrmann, M. Annual Research Briefs 2005, pp. 3{18. Center for Turbulence Research, **2005**.
- [71] Herrmann, M. Annual Research Briefs 2006, pp. 167{184. Center for Turbulence Research, **2006**.
- [72] Hirt, C.W.; Nichols, B.D. *Volume Of fluid (VOF) method for the dynamics of free boundaries*. Journal of Computational Physics, Vol. 39 (1), pp. 201-225, **1981**.
- [73] Rider, W.J.; Kothe, D.B. *Reconstructing volume tracking*. J. Comp. Phys., Vol. 141, pp. 112-152, **1998**.
- [74] Rudman, M. *A volume-tracking method for incompressible multifluid flows with large density variations*. Int. J. Numer. Meth. Fluids, Vol. 28, pp. 357–378, **1998**.
- [75] Scardovelli, R.; Zaleski, S. *Direct numerical simulation of free-surface and interfacial flow*. Ann. Rev. Fluid Mech., Vol. 31, pp. 567—603, **1999**.
- [76] Scardovelli, R.; Zaleski, S. *Analytical relations connecting linear interfaces and volume fractions in rectangular grids*. J. Comput. Phys. 164, pp. 228-237, **2000**.

- [77] Gueyffier, D.; Li, J.; Nadim, A.; Scardovelli, S.; Zaleski, S. *Volume Of Fluid interface tracking with smoothed surface stress methods for three-dimensional flows*. J. Comput Phys., 152, pp. 423-456, **1999**.
- [78] Zaleski and Many researchers of d'Alembert. *Drops and bubbles: deformation, break-up, atomization*. At: <http://www.lmm.jussieu.fr/~zaleski/drops2.html>, last accessed by 25th June **2012**.
- [79] Lafaurie, B.; Nardone, C.; Scardovelli, R.; Zaleski, S.; Zanetti, G. *Modelling merging and fragmentation in multiphase flows with SURFER*. J. Comp. Phys. 113, pp. 134-147, **1994**.
- [80] Aulisa, E.; Manservigi, S.; Scardovelli, R.; Zaleski, S. *A geometrical area-preserving Volume-of-Fluid method*. J. Comput. Phys, 192, pp. 355-364, **2003**.
- [81] Scardovelli, R.; Zaleski, S. *Interface Reconstruction with Least-Square Fit and Split Eulerian-Lagrangian Advection*. Int. J. Numer. Meth. Fluids, Vol. 41, pp. 251-274, **2003**.
- [82] Aulisa, E.; Manservigi, S.; Scardovelli, R.; Zaleski, S. *Interface reconstruction with least-squares fit and split advection in three-dimensional Cartesian geometry*. J. Comput. Phys, 225, pp. 2301-2319, **2007**.
- [83] Afkhami, S.; Zaleski, S.; Bussmann, M. *A mesh-dependent model for applying dynamic contact angles to VOF simulations*. Journal of Computational Physics, 228, pp. 5370-5389, **2009**.
- [84] Cervone, A.; Manservigi, S.; Scardovelli, R.; Zaleski, S. *A geometrical predictor-corrector advection scheme and its application to the volume fraction function*. J. Comput. Phys, 228, pp. 406-419. **2009**.
- [85] Borgia, G.; Cervone, A.; Manservigi, S.; Scardovelli, R.; Zaleski S. *On the properties and limitations of the height function method in two-dimensional Cartesian geometry*. J. Comput. Phys., 230, pp. 851-862, **2011**.
- [86] Tryggvason, G.; Bunner, B.; Esmaeeli, A.; Juric, D.; Al-Rawahi, N.; Tauber, W.; Han, J.; Nas S.; Jan, Y.J. *A front tracking method for the computations of multiphase flow*. J. Comp. Phys., Vol. 169, pp. 708—759. No. **2001**.
- [87] Du, J.; Fix, B.; Glimm, J.; Jia, X.; Li, X.; Li Y.; Wu, L. *A simple package for front tracking*. J. Comp. Phys., Vol. 213, pp. 613-628, **2006**.
- [88] Sankaranarayanan, K.; Shan, X.; Kevrekidis I. G.; Sundaresan, S. *Bubble flow simulations with the Lattice Boltzmann method*. Chemical Engineering Science, Vol. 54, No. 21, pp. 4817-4823, **1999**.
- [89] Takada, N.; Misawa, M.; Tomiyama, A.; Fujiwara, S. *Numerical simulation of two- and three-dimensional two-phase fluid motion by Lattice Boltzmann method*. Computer Physics Communications, Vol. 129, No. 1-3, pp. 233-246, **2000**.

Chapter 2 – Spray Fundamentals and CFD spray modeling

- [90] Inamuro, T.; Ogata, T.; Tajima, S.; Konishi, N. *A Lattice Boltzmann method for incompressible two-phase flows with large density differences*. Journal of Computational Physics, Volume 198, No. 2, pp. 628-644, **2004**.
- [91] Chatzikyriakou, D.; Boungiorno, J.; Lakehal, D. *Benchmarks for interface-tracking codes in the consortium for advanced simulation of LWRs (CASL)*, The 14th International Topical Meeting on Nuclear Reactor Thermal Hydraulics, NURETH14-360, **2011**.

Chapter 3 - Eulerian-Lagrangian Spray Atomization (ELSA) Methodology

In the last decade, the Eulerian-Lagrangian Spray Atomization (ELSA) model has been developed for the simulations of Diesel spray in the academic research environment. In this chapter, the theoretical background of ELSA model for the description of Diesel sprays is described in detail and an overall view of governing equations are presented.

3.1 Overview

As is told in the previous chapters, the main idea of the ELSA method is to use the best description possible in the different regions of the spray. The Lagrangian approach is more appropriate for the description of the dispersed spray region. This approach has been successfully employed for a long time and poses a great advantage: its immense capabilities to include a bundle of sub-models including motions of particles/blobs/drops, droplets interaction (coalescence, collision, and wall impingement), secondary atomization, heat and mass transfer, and evaporation.

However, the pure Lagrangian methodology presents two problems: first, the initial conditions of the spray (including the cone angle or the number of droplets) are imposed and secondly the liquid volume fraction should be smaller than 0.6 [1]. Obviously, this is not true at the liquid core.

Chapter 3 – Eulerian-Lagrangian Spray Atomization (ELSA) Methodology

In order to overcome these problems, the ELSA method describes the liquid core and the region surrounding the nozzle using an Eulerian framework. Especially, the model is suitable for modeling turbulent sprays at high Weber number and high Reynolds number, as it happens in the DI engines sprays.

Table 3-1 shows a resume of the main studies about the Eulerian-Lagrangian approach in general and the Eulerian Lagrangian Spray Atomization (ELSA) model.

Table 3-1: Comprehensive list of the main works which have developed the Eulerian-Lagrangian approach and the ELSA model sorted chronologically.

Year	Author	Title	Journal/School
1998	Gouesbet & Berlemont	Eulerian and Lagrangian approaches for predicting the behavior of discrete particles in turbulent flows.	Progress in Energy and Combustion Science
2001	Patankar & Joseph	Modeling and numerical simulation of particulate flows by the Eulerian-Lagrangian approach.	Int. Journal of Multiphase Flow
2001	Vallet, Burluka & Borghi	Development of an Eulerian model for the “Atomization” of a liquid jet.	Atomization and Sprays
2002	Platzer & Sommerfeld	Modelling of turbulent atomization with a combined Euler/Lagrange Euler/Euler approach: starting with a two-fluid model in the dense spray region.	ILASS
2002	Blokkeel, Silvani, Demoulin & Borghi	An Eulerian model to improve the primary breakup modeling of atomizing jet.	ILASS
2003	Blokkeel, Barbeau & Borghi	A 3D Eulerian Model to Improve the Primary Breakup of Atomizing Jet.	SAE Technical Paper
2004	Ham, Young, Apte & Herrmann	A hybrid Eulerian-Lagrangian method of LES of atomizing spray.	Stanford University

Chapter 3 – Eulerian-Lagrangian Spray Atomization (ELSA) Methodology

2005	Lebas, Blokkeel, Beau & Demoulin	Coupling Vaporization Model With the Eulerian-Lagrangian Spray Atomization (ELSA) Model in Diesel Engine Conditions.	SAE Technical Paper
2005	Lebas, Blokkeel, Beau & Demoulin	ELSA Model: Slip Velocity and Vaporization Modeling in Diesel Engine Conditions.	ILASS
2006	PhD Thesis, Beau	Modélisation de l'atomisation d'un jet liquide. Application aux sprays Diesel.	Université de Rouen
2007	PhD Thesis, Ning	Development of a Next-generation Spray and Atomization Model Using an Eulerian-Lagrangian Methodology.	Uni. of Wisconsin, Madison
2007	PhD Thesis, Lebas	Modélisation Eulérienne de l'Atomisation Haute Pression. Influences sur la Vaporisation et la Combustion Induite.	Université de Rouen
2007	PhD Thesis, De Luca	Contribution à la modélisation de la pulvérisation d'un liquide phytosanitaire en vue de réduire les pollutions.	Université de la Méditerranée, Aix-Marseille II
2009	Ning & Reitz	An Eulerian-Lagrangian spray and atomization model with improved turbulence modeling.	Atomization and Sprays
2009	Lebas, Menard, Beau, Berlomont & Demoulin	Numerical simulation of primary break-up and atomization: DNS and modelling study.	Int. Journal of Multiphase Flow
2009	De Luca, Vallet, Borghi	Pesticide atomization modeling for hollow-cone nozzle.	Atomization and Sprays
2010	Desportes, Zellat, Desoutter, Liang & Ravet	Application of the Eulerian-Lagrangian Spray Atomization (ELSA) Model for the Diesel Injection Simulation.	Conference Thermo & Fluid Dynamic Processes in Diesel Engines

Chapter 3 – Eulerian-Lagrangian Spray Atomization (ELSA) Methodology

2010	Desportes, Zellat, Desoutter, Abouri & Liang	Validation and Application of the Eulerian-Lagrangian spray atomization (ELSA) model for the Diesel injection simulation.	Meeting at the SAE Congress
2010	Hermann	A parallel Eulerian interface tracking/Lagrangian point particle multi-scale coupling procedure.	Journal of Comput. Physics
2010	Master Thesis, Trask	Implementation of an Eulerian atomization model to characterize primary spray formation.	Uni. of Massachusetts Amherst
2010	Luret, Menard, Berlemont, Reveillon, Demoulin & Blokkeel	Modeling collision outcome in moderately dense sprays.	Atomization and Sprays
2011	Meslem, Honnet, Schwarz, Reveillon & Demoulin	Modelling of Cavitating Flows in Diesel Injector Nozzles to Consider its Impact on the Atomization.	ILASS
2011	Shams, Finn & Apte	A numerical scheme for Euler–Lagrange simulation of bubbly flows in complex systems.	International Journal for numerical methods in fluids
2011	Meslem, Honnet, Schwarz, Reveillon & Demoulin	Modelling of Cavitating Flows in Diesel Injector Nozzles to Consider its Impact on the Atomization.	ILASS
2011	Hoyas, Gil, Margot, Khuong-Anh & Ravet	Evaluation of the Eulerian–Lagrangian Spray Atomization (ELSA) model in spray simulations: 2D cases.	Mathematical and Computer Modelling
2011	Hoyas, Pastor, Khuong-Anh & Mompou-Laborda	Evaluation of the Eulerian-Lagrangian spray atomization (ELSA) in spray simulations.	Int. J. Vehicle Systems Modelling and Testing
2011	Hoyas, Pastor, Khuong-Anh &	Application and Evaluation of the Eulerian-Lagrangian Spray	SAE Technical Paper

Chapter 3 – Eulerian-Lagrangian Spray Atomization (ELSA) Methodology

	Mompo-Laborda	Atomization (ELSA) Model on CFD Diesel Spray Simulations.	
2011	Wang, Lee, Reitz & Diwakar	Numerical Simulation of Diesel Sprays Using an Eulerian-Lagrangian Spray and Atomization (ELSA) Model Coupled with Nozzle.	SAE Technical Paper
2012	Desantes, Hoyas, Gil, Khuong-Anh & Ravet	A Recent Eulerian-Lagrangian CFD Methodology For Modelling Direct Injection Diesel Sprays.	The Int. Conf. On Advances In Comp. Mechanics
2012	Hoyas, Gil, Fajardo, Khuong-Anh & Ravet	Evaluation and Validation of ELSA Model in Diesel Sprays: 3D Cavitating Nozzles Case.	Triennial Int. Conf. on Liquid Atomization and Spray Systems

3.2 Mathematical formulation

Vallet and Borghi, 1999 [2] presented some ideas about improving the atomization processes models of liquid jets. As aforementioned, Vallet et al., 2001 [3] presented the idea behind the ELSA model. In their work, there was a transport equation for liquid and gas phases. Based on this work, Blokkeel et al., 2002 [4] and 2003 [5] coupled this method with the Lagrangian framework for droplets. During the following years, Lebas et al., 2005 ([6], and [7]), Beau et al., 2006 [8] and the PhD thesis of Beau, 2006 [9], the PhD thesis of Lebas, 2007 [10] and Lebas et al., 2009 [11] presented the complete set of equations for the ELSA method, which was given this name then. The development and improvement process of ELSA model has been continuing since, with some minor additions. For instance, Ning et al., 2007 [12], and 2009 [13] improved the turbulent models. De Luca et al., 2009 [14] applied this model to liquid pesticides. Trask, 2010 [15] implemented this model in OpenFOAM open source code, and Desportes et al., 2010 ([16] and [1]) embedded the ELSA model into the Star-CD commercial code. The detailed development of ELSA model is shown in Figure 3-1.

Chapter 3 – Eulerian-Lagrangian Spray Atomization (ELSA) Methodology

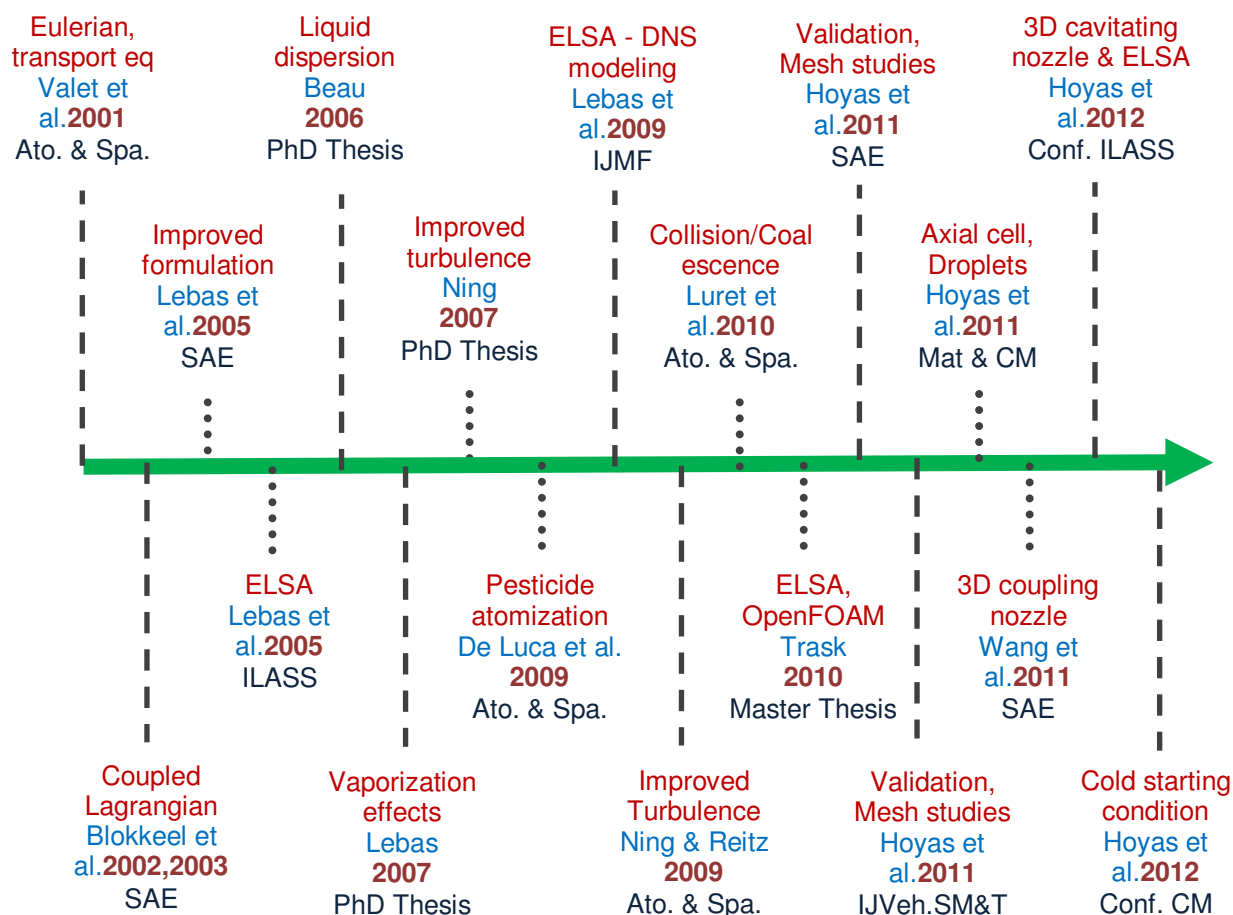


Figure 3-1: The flow diagram for the development of the ELSA model.

The mathematical formulation of ELSA method covered the three regions of the sprays, named Eulerian, Lagrangian and Transition zone. The main advantage of the code is that it knows exactly in which region is every cell of the grid. These three zones are depicted in Figure 2-1.

- **Eulerian mixture zone**: This is the closest zone to the nozzle. Liquid and gas phase are considered as a unique mixture flow, with a highly variable density.
- **Transition zone**: This region is a very thin boundary between the liquid and disperse regions. The switch from Eulerian to Lagrangian calculation is made here.

- **Lagrangian zone:** In this region, the spray is dispersed enough to use the classical Lagrangian tracking for droplets, but with the information coming from the Transition zone, without any other condition.

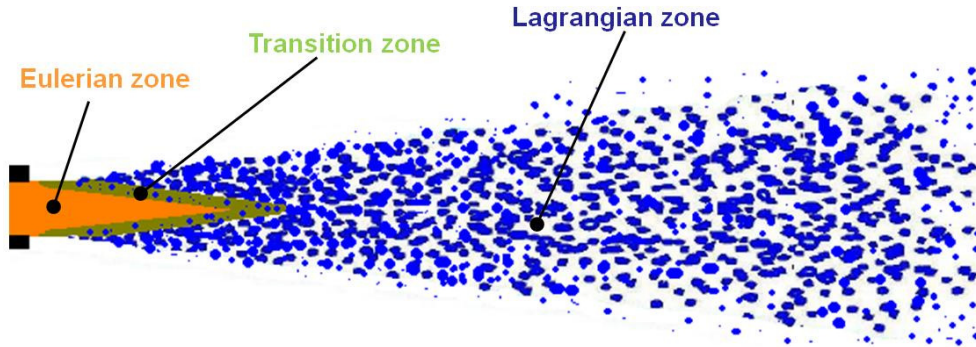


Figure 3-2: Three spray zones in ELSA model.

3.2.1 Eulerian liquid-spray mixture zone

From now on, the subscript l stands for liquid and g stands for gas, whereas i, j are the space direction. We define the mean liquid mass fraction, \tilde{Y}_l as:

$$\tilde{Y}_l = \frac{\overline{\rho_l Y_l}}{\bar{\rho}} \quad (3.1)$$

Where ρ is the density and Y_l is the liquid mass fraction. The variable with an overbar denotes the temporal average, and \bar{Y}_l is the mean liquid volume fraction. Intuitively, the mean density is defined as:

$$\bar{\rho} = \rho_l \bar{Y}_l + \rho_g (1 - \bar{Y}_l) \quad (3.2)$$

Chapter 3 – Eulerian-Lagrangian Spray Atomization (ELSA) Methodology

The following equations show the steps to obtain relation of mean density and mean liquid mass fraction. In case both liquid and gas densities be considered as constants as assumed by Vallet et al., 2001 [3], we can have the below expressions:

$$\frac{1}{\bar{\rho}} = \frac{\rho_g \rho_l + (\rho_g \bar{\rho}_l \bar{Y}_l - \rho_g \rho_l \bar{Y}_l) + (\rho_l \bar{\rho}_l \bar{Y}_l - \rho_l \rho_l \bar{Y}_l)}{\bar{\rho} \rho_g \rho_l} \quad (3.3)$$

$$\frac{1}{\bar{\rho}} = \frac{\rho_g \bar{\rho}_l \bar{Y}_l + \rho_l (\rho_l \bar{Y}_l + \rho_g (1 - \bar{Y}_l)) - \rho_l \rho_l \bar{Y}_l}{\bar{\rho} \rho_g \rho_l} = \frac{\rho_g \bar{\rho}_l \bar{Y}_l + \rho_l \bar{\rho} - \rho_l \rho_l \bar{Y}_l}{\bar{\rho} \rho_g \rho_l} \quad (3.4)$$

$$\frac{1}{\bar{\rho}} = \frac{\bar{\rho}_l \bar{Y}_l}{\bar{\rho} \rho_l} + \frac{\bar{\rho} - \rho_l \bar{Y}_l}{\bar{\rho} \rho_g} \quad (3.5)$$

Now it is expressed in terms of \tilde{Y}_l as:

$$\frac{1}{\bar{\rho}} = \frac{\tilde{Y}_l}{\rho_l} + \frac{1 - \tilde{Y}_l}{\rho_g} \quad (3.6)$$

The Favre averaged mean velocity is defined as:

$$\tilde{U}_i = \tilde{Y}_l U_{l,i} + (1 - \tilde{Y}_l) U_{g,i} \quad (3.7)$$

In addition, the mean pressure \bar{P} is given by the equation of state, taking into account the volume occupied by the liquid.

$$\begin{cases} \text{For } \tilde{Y}_l \neq 1 & \bar{P} = \frac{(1 - \tilde{Y}_l) \bar{\rho} R_g T_g}{1 - \bar{\rho} \tilde{Y}_l / \rho_l} \\ \text{For } \tilde{Y}_l = 1 & \bar{P} = \text{averaged pressures of neighboring cells} \end{cases} \quad (3.8)$$

Chapter 3 – Eulerian-Lagrangian Spray Atomization (ELSA) Methodology

In this equation, R_g is the gas constant and T_g is the mixture temperature. Then, the classical transport equations are solved for these mean variables.

$$\frac{\partial \bar{\rho}}{\partial t} + \frac{\partial \bar{\rho} \tilde{U}_j}{\partial x_j} = S_{EL}^{\tilde{Y}_i} \quad (3.9)$$

Vallet et al., 2001 [3] described the momentum equation as following:

$$\frac{\partial \bar{\rho} \tilde{U}_i}{\partial t} + \frac{\partial \bar{\rho} \tilde{U}_j \tilde{U}_i}{\partial x_j} = - \frac{\partial \bar{P}}{\partial x_i} - \frac{\partial \overline{\rho u_i'' u_j''}}{\partial x_j} + S_{EL}^{\tilde{U}_i} \quad (3.10)$$

Based on the classical Boussinesq equation, the Reynolds stress tensor $\overline{\rho u_i'' u_j''}$ is computed using the turbulent viscosity hypothesis.

$$\overline{\rho u_i'' u_j''} = -\bar{\rho} C_\mu \frac{\tilde{k}^2}{\tilde{\epsilon}} \left(\frac{\partial \tilde{u}_i}{\partial x_j} + \frac{\partial \tilde{u}_j}{\partial x_i} \right) + \frac{2}{3} \bar{\rho} \tilde{k} \delta_{ij} \quad (3.11)$$

In these equations, $S_{EL}^{\tilde{Y}_i}$ represents some source terms that are activated during the transition from Eulerian to Lagrangian. It should be noticed that the last equation does not contain any momentum exchange terms between liquid and gaseous phases.

Vallet et al., 2001 [3] formulated the transport equation for the liquid mass fraction:

$$\frac{\partial \bar{\rho} \tilde{Y}_l}{\partial t} + \frac{\partial \bar{\rho} \tilde{U}_j \tilde{Y}_l}{\partial x_j} = - \frac{\partial \overline{\rho u_j'' y_l''}}{\partial x_j} \quad (3.12)$$

The liquid turbulent diffusion flux of the liquid ($\overline{\rho u_j'' y_l''}$) is calculated using a gradient law approximation:

$$\overline{\rho u_j'' Y_l''} = - \frac{\mu_t}{Sc_t} \frac{\partial \tilde{Y}_l}{\partial x_j} \quad (3.13)$$

In this equation, μ_t is the dynamic turbulent viscosity and Sc_t is the turbulent Schmidt number.

Lebas et al., 2005 [6] proposed the following k- ϵ equations:

$$\frac{\partial \tilde{k}}{\partial t} + \tilde{u}_j \frac{\partial \tilde{k}}{\partial x_j} = C_\mu \frac{\tilde{k}^2}{\tilde{\epsilon}} \left(\frac{\partial \tilde{u}_i}{\partial x_j} + \frac{\partial \tilde{u}_j}{\partial x_i} \right) \frac{\partial \tilde{u}_i}{\partial x_j} + \frac{\partial}{\partial x_j} \left(\frac{C_\mu \tilde{k}^2}{\sigma_k \tilde{\epsilon}} \frac{\partial \tilde{k}}{\partial x_j} \right) - \tilde{\epsilon} \quad (3.14)$$

and

$$\frac{\partial \tilde{\epsilon}}{\partial t} + \tilde{u}_j \frac{\partial \tilde{\epsilon}}{\partial x_j} = C_{\epsilon 1} C_\mu \tilde{k} \left(\frac{\partial \tilde{u}_i}{\partial x_j} + \frac{\partial \tilde{u}_j}{\partial x_i} \right) \frac{\partial \tilde{u}_i}{\partial x_j} + \frac{\partial}{\partial x_j} \left(\frac{C_\mu \tilde{k}^2}{\sigma_\epsilon \tilde{\epsilon}} \frac{\partial \tilde{\epsilon}}{\partial x_j} \right) - C_{\epsilon 2} \frac{\tilde{\epsilon}^2}{\tilde{k}} \quad (3.15)$$

Where $C_\mu, C_{\epsilon 1}, C_{\epsilon 2}, \sigma_k, \sigma_\epsilon$ are model constants. Their detailed value will be presented in the next chapter.

3.2.2 Liquid/gas interface density

The liquid surface density $\bar{\Sigma}$ (m^{-1}) is defined as the quantity of liquid/gas interface per unit of volume. Vallet et al., 2001 [3] and Blokkeel et al., 2003 [5] modeled the transport equation for the liquid surface density. This equation has as a diffusion term, and neglects the effects of the spatial clustering of liquid elements. It is also assumed that $\bar{\Sigma}$ is universal, i.e., independent of the geometrical configuration of the flow and its boundary conditions. The equation is:

$$\frac{\partial \bar{\rho} \bar{\Sigma}}{\partial t} + \frac{\partial}{\partial x_j} (\bar{\rho} \tilde{u}_j \bar{\Sigma}) = \frac{\partial}{\partial x_j} \left(\bar{\rho} D_s \frac{\partial \bar{\Sigma}}{\partial x_j} \right) + \bar{\rho} (|A| + a_{coll}) \bar{\Sigma} - \bar{\rho} V_s \bar{\Sigma}^2 \quad (3.16)$$

This equation can be also expressed using the equilibrium surface density ($\bar{\Sigma}_{eq}$).

$$\frac{\partial \bar{\rho} \tilde{\Sigma}}{\partial t} + \frac{\partial}{\partial x_j} (\bar{\rho} \tilde{u}_j \tilde{\Sigma}) = \frac{\partial}{\partial x_j} \left(\bar{\rho} D_s \frac{\partial \tilde{\Sigma}}{\partial x_j} \right) + \alpha_1 \frac{\bar{\rho} \tilde{\Sigma}}{\tau_t} \left(1 - \frac{\tilde{\Sigma}}{\bar{\Sigma}_{eq}} \right) \quad (3.17)$$

Where the turbulent time scale is $\tau_t = k/\varepsilon$.

In these equations D_s stands for the turbulent diffusion coefficient; V_s stands for a surface destruction coefficient, with velocity dimension (m/s); A stands for the mean strain rate (s^{-1}) associated with the large-scale straining motion, a_{coll} stands for the strain rate (s^{-1}) related to the turbulence fluctuations, thus induced by the small scales and α_1 is a model constant. The detailed formulations for computing those variables are given by Ning et al., 2007 [12].

The liquid/gas interface $\tilde{\Omega} = \tilde{\Sigma}/\bar{\rho}$ is also transported. The mathematical formulation of this equation was described by Lebas et al., 2005 [6], [7]; and Beau et al., 2006 [8], Beau, 2006 [9]. This transport equation is analogous to the flame surface density equation.

$$\frac{\partial \bar{\rho} \tilde{\Omega}}{\partial t} + \frac{\partial \bar{\rho} \tilde{\Omega} \tilde{U}_j}{\partial x_j} = \frac{\partial}{\partial x_j} \left(\bar{\rho} \frac{v_t}{Sc_t} \frac{\partial \tilde{\Omega}}{\partial x_j} \right) + \bar{\rho} \cdot \left(\tilde{\Omega}_{init} + \tilde{\Omega}_{mean} + \tilde{\Omega}_{turb} + \tilde{\Omega}_{coll} + \tilde{\Omega}_{coal} \right) + S_{EL}^{\tilde{\Omega}} \quad (3.18)$$

Where $\tilde{\Omega}_{init}$, $\tilde{\Omega}_{mean}$, $\tilde{\Omega}_{turb}$, $\tilde{\Omega}_{coll}$ and $\tilde{\Omega}_{coal}$ are the initial, mean, turbulence, collision and coalescence value of liquid/gas surface density respectively and $S_{EL}^{\tilde{\Omega}}$ is the source term of the liquid/gas interface.

The production and destruction of liquid surface are accounted for the five liquid/gas surface densities. All the source terms in the right hand side relate to the liquid/gas surface density $\tilde{\Omega}$:

$$\dot{\tilde{\Omega}}_{init} = \begin{cases} 2 \frac{v_i}{Sc_t} \frac{6\bar{\rho}}{\rho_l \rho_g L_t} \frac{\partial \tilde{Y}_l}{\partial x_i} \frac{\partial \tilde{Y}_l}{\partial x_i}, & \text{if } \tilde{Y}_l(1-\tilde{Y}_l) \leq 0.001 \\ 2 \frac{v_i}{Sc_t} \frac{\tilde{\Omega}}{(1-\tilde{Y}_l)\tilde{Y}_l} \frac{\partial \tilde{Y}_l}{\partial x_i} \frac{\partial \tilde{Y}_l}{\partial x_i}, & \text{otherwise} \end{cases} \quad (3.19)$$

Where L_t is the turbulent length scale. At the liquid core close to the nozzle exit $\tilde{Y}_l \cong 1$, otherwise, the scale of the first liquid fragments is proportional to L_t . The three next terms correspond to the production of liquid surface density due to the mean and turbulent stresses, and collisions:

$$\dot{\tilde{\Omega}}_{mean} = \frac{\overline{\rho u_i'' u_j''}}{\bar{\rho} \tilde{k}} \frac{\partial \tilde{U}_i}{\partial x_j} \tilde{\Omega}; \quad \dot{\tilde{\Omega}}_{turb} = \frac{\tilde{\Omega}}{\tau_{turb}}; \quad \text{and} \quad \dot{\tilde{\Omega}}_{coll} = \frac{\tilde{\Omega}}{\tau_{coll}} \quad (3.20)$$

τ_{turb} and τ_{coll} are the characteristic time scale of turbulence and collisions respectively.

The last source term deals with destruction of surface density due to coalescence, $\dot{\tilde{\Omega}}_{coal}$:

$$\dot{\tilde{\Omega}}_{coal} = -\frac{1}{\tau_{coll}} \frac{\tilde{\Omega}^2}{\tilde{\Omega}_{crit}} \quad (3.21)$$

The Sauter Mean Diameter of droplet, D_{32} and the drop number density (drop number per unit of volume), n are then computed from the liquid surface density and liquid mass fraction:

$$n = \frac{\rho_l^2 \tilde{\Sigma}^3}{36\pi \rho Y_l^2} \quad (3.22)$$

$$D_{32} = \frac{\overline{6\rho\tilde{Y}_l}}{\rho_l\tilde{\Sigma}} \quad (3.23)$$

3.2.3 Transition zone and the initialization of the Lagrangian model

We rely on a critical value of the Eulerian liquid volume fraction to decide whether it should turn from Eulerian to Lagrangian. Beau, 2006 [8] and [9], gave the mathematical characterization of this parameter. The Lagrangian droplets are formed in the zones where the spray is assumed to be diluted enough. The equation is:

$$\tilde{\Phi}_l = \tilde{Y}_l \frac{\bar{\rho}}{\rho_l} \leq \tilde{\Phi}_l^{crit} \quad (3.24)$$

Where $\tilde{\Phi}_l^{crit}$ is the critical value of the Eulerian liquid volume fraction.

This criterion is based on the value of liquid volume fraction that is linked to the ratio of the mean free path between two droplets and the mean equivalent radius of the droplets in the cell. In our case, the transition is done mostly when the liquid volume fraction becomes lower than 0.01, as proposed by Desportes et al., 2010 ([16] and [1]). The transition zone is composed of the computational cells that form the border with the dense zone (i.e. the region where the liquid volume fraction is greater than 0.01). Only one parcel is generated per transition cell and per time step.

About the velocity of the droplets, Blokkeel et al., 2002 [4] computed it as:

$$\bar{U}_{l,i} = \tilde{U}_i + \frac{\overline{\rho u_i'' y''}}{\bar{\rho}\tilde{Y}_l} \quad (3.25)$$

Where $\bar{U}_{l,i}$ is the liquid velocity (droplets), and \tilde{U}_i is the Eulerian velocity of the mixture.

$$\tilde{k} = \tilde{Y}_l \tilde{k}_l + (1 - \tilde{Y}_l) \tilde{k}_g + \frac{1}{2} \overline{u_l Y_l} \overline{u_l Y_l} \left(\frac{1}{\tilde{Y}_l} + \frac{1}{1 - \tilde{Y}_l} \right) \quad (3.26)$$

Here \tilde{k} is the turbulent kinetic energy for the Eulerian mixture, \tilde{k}_l is the turbulent kinetic energy for the liquid phase and \tilde{k}_g is the turbulent kinetic energy for the gas phase.

It is important to stress again that this Eulerian calculation initializes the droplets, including all their characteristics. For instance, the diameter of the droplet is equal to the Sauter Mean Diameter, it is calculated by:

$$D_{32} = \frac{6\tilde{Y}_l}{\rho_l \tilde{\Omega}} \quad (3.27)$$

The number of droplets per generated parcel n_{drop} is obtained simply from mass conservation as below:

$$n_{drop} = \frac{\bar{\rho} \tilde{Y}_l V_{cell}}{\pi/6 \rho_l D_{32}^3} \quad (3.28)$$

where V_{cell} is the volume of one transitional cell.

REFERENCES

- [1] Desportes, A.; Zellat, M.; Desoutter, G.; Abouri, D.; Liang, Y. *Validation and Application of the Eulerian-Lagrangian spray atomization. (ELSA) model for the Diesel injection simulation*. SAE Technical Paper, **2010**.
- [2] Vallet, A.; Borghi, R. *Modélisation eulérienne de l'atomisation d'un jet liquide*, R. R. Acad. Sci. Paris, Ser. II b 327, pp. 1015-1020, **1999**.
- [3] Vallet, A.; Burluka, A.A.; Borghi, R. *Development of an Eulerian model for the atomization of a liquid jet*. Atomization and sprays, Vol. 11, pp. 619-642, **2001**.
- [4] Blokkeel, G.; Silvani, X.; Demoulin, F.X.; Borghi, R. *An Eulerian Model to Improve the Primary Breakup Modeling of Atomizing Jet*. ILASS-Europe 2002, Sept. 9-11, **2002**.

Chapter 3 – Eulerian-Lagrangian Spray Atomization (ELSA) Methodology

- [5] Blokkeel, G.; Barbeau B.; Borghi, R. *A 3D Eulerian Model to Improve the Primary Breakup of Atomizing Jet*. SAE Technical Paper 2003-01-0005, **2003**.
- [6] Lebas, R.; Blokkeel, G.; Beau, P.A.; Demoulin, F.X. *ELSA Model: Slip Velocity and Vaporization Modeling in Diesel Engine Conditions*. ILASS, 2005-01-0213. **2005**.
- [7] Lebas, R.; Blokkeel, G.; Beau, P.A.; Demoulin, F.X. *Coupling vaporization model with the Eulerian–Lagrangian Spray Atomization. (ELSA) model in Diesel engine conditions*. SAE Technical Papers, 2005-01-0213. **2005**.
- [8] Beau, P.A.; Menard, T.; Lebas, R.; Berlemont, A.; Tanguy, S.; Demoulin, F.X. *Numerical jet atomization. Part II: modeling information and comparison with DNS results*. Miami, FL, United States, American Society of Mechanical Engineers, New York, NY 10016-5990, United States. **2006**.
- [9] Beau, P.A. *Modélisation de l'atomisation d'un jet liquide – Application aux sprays Diesel*. Ph.D. Thesis, University of Rouen, **2006**.
- [10] Lebas R. *Modélisation Eulérienne de l'Atomisation haute pression – Influences sur la vaporisation et la combustion induite*. PhD thesis, University of Rouen, **2007**.
- [11] Lebas, R.; Menard, T.; Beau, P.; Berlemont, A.; Demoulin, F. *Numerical simulation of primary break-up and atomization: DNS and modelling study*. International Journal of Multiphase Flow, Vol. 35(3), pp. 247 – 260, **2009**.
- [12] Ning, W.; Reitz, R.D.; Lippert, A.M.; Diwakar, R. *Development of a next generation spray and atomization model using an Eulerian-Lagrangian methodology*. 17th Int. Multidimensional Engine Modeling User's Group Meeting, Detroit, MI, **2007**.
- [13] Ning, W.; Reitz, R.D.; Lippert, A.M. *An Eulerian-Lagrangian spray and atomization model with improved turbulence modeling*. Atomization and sprays, Vol. 19(8), pp. 727-739, **2009**.
- [14] De Luca, M.; Vallet, A.; Borghi, R. *Pesticide atomization modeling for hollow-cone nozzle*. Atomization and sprays, Vol. 19(8), pp. 741-753, **2009**.
- [15] Trask, N. *Implementation of an Eulerian atomization model to characterize primary spray formation*. University of Massachusetts Amherst, **2010**.
- [16] Desportes, A.; Zellat, M.; Desoutter, G.; Liang, Y.; Ravet, F. *Application of the Eulerian-Lagrangian spray atomization. (ELSA) model for the Diesel injection simulation*. Conference on Thermo- and Fluid Dynamic Processes in Diesel Engines, **2010**.
- [17] Luret, G.; Menard, T.; Berlemont, A.; Reveillon, J.; Demoulin, F.X.; Blokkeel, G. *Modeling collision outcome in moderately dense sprays*. Atomization and Sprays, Vol. 20(3), pp. 251-268, **2010**.

Chapter 4 - ELSA model validation

In this chapter we present the numerical cases used for validation, the meshes employed and the different parameters and relevant physical numbers against we have validated. The first section is devoted to the numerical setup and the second to practical ELSA assumptions and inputs. The last section of this chapter explains the 2D validation performed before simulating the more complicated 3D cases with cavitation, which are explained in chapter 5. Some of the research articles ([1] - [5]) that we have already published complete this chapter. These papers are attached in chapter 7 for reference.

4.1 Numerical configuration: a practical approach

The meshing process is probably the most important (and first) step in a CFD simulation. A good mesh can help to have a better convergence (or simply to have it at all), and thus faster and better results, but on the contrary a mesh with too much points can increase dramatically the cost of the simulation. In the case of a RANS simulation, where many parameters are fixed by experience and not from a detailed physical theory, we have seen, for instance, that one “constant” of the *k-epsilon* method depends critically on the mesh.

4.1.1 Geometry and computational domain

Most, if not all, of the problems of industrial interest that are modeled by CFD techniques are 3D. They usually are turbulent, which is a pure 3D effect. However, when using RANS, the best way of starting a problem is always using a 2D simplification. The main reason for this is the lower cost of the 2D

Chapter 4 – ELSA model validation

simulation against the 3D. Within the ELSA model, changing from 2D to 3D means to increase the memory by 50 and the time by 20. If we are studying the effect of the meshing in the first parameters of the dissipation equation, one hour of delay is not a problem. On the contrary, one month is a serious one.

In our case, using the ELSA methodology and droplets, more challenges arise. As the simulation runs, droplets are created continuously. Without an evaporation mechanism, these droplets remain in the simulation. At the final steps, there are millions of droplets in the simulation. This produces very big files, and is also a big problem for the post-processing, due to the large amount of memory needed to load $20e^6$ particles.

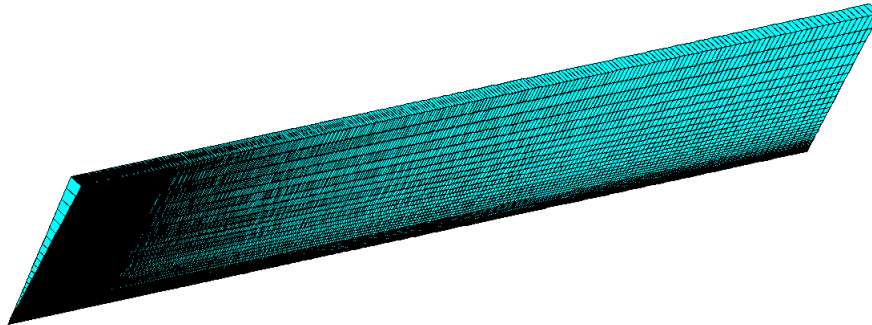


Figure 4-1: Quasi-2D thin wedge representing an axisymmetric combustion chamber.

Thus, in a first step, we have reduced the problem to a quasi-2D thin wedge (see Figure 4-1) to perform a preliminary validation of the method. On the contrary, it is necessary to use the full 3D cylindrical mesh when coupling with the internal nozzle flow, especially for cavitating flows.

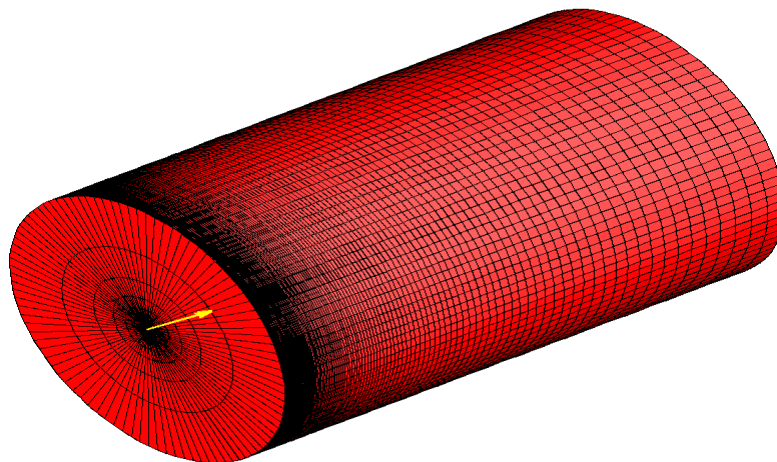


Figure 4-2: The 3-Dimensional cylindrical mesh.

Chapter 4 – ELSA model validation

All the simulations performed during this work have been done in the quasi-2D thin wedges or in the 3-Dimensional cylindrical meshes showed in Figure 4-2, taking different grid resolutions. The number of cells, vertex or the cell aspect ratio, is different in each case.

The wedge mesh is not really a 2D mesh because Star-CD cannot handle 2D meshes. In order to build this mesh, a simple 2D planar geometry is built in the 1st and 2nd dimension and then extrude in the 3rd dimension to build a volume with one cell thickness. This thickness is about 5 – 10 degrees, enough to provide good quality cells. A lower thickness can produce some problems due to the cell skewness, without any positive income.

All this cells can handle a reasonable amount of droplets. The average droplet size in ELSA is in the microns range or below, while the smallest cell has a size of around $(0.1D_0)^3$, where D_0 is the nozzle diameter. D_0 is around 100 microns in nowadays DI engines so even in the worst case there are room for thousand of droplets in the smallest cell.

The size of the cylinder showed in the Figure 4-2 is 100mm in the axial direction and 25mm in the radial. This is the only geometry simulated, but the size of the nozzle is not constant and depends on each particular problem. The maximum number of grid points has been (500, 50).

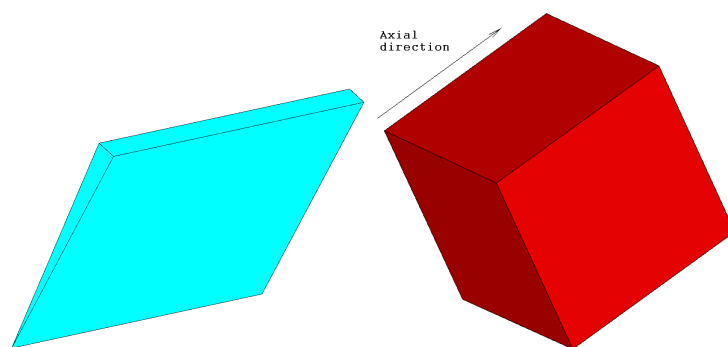


Figure 4-3: The first cell is made up of equal segments in the axial and radial direction: quasi-2D thin wedge (on the left) and 3D geometry (on the right).

Chapter 4 – ELSA model validation

In the case of the 2D mesh, in order to ensure the high quality mesh, the 1st cell is a square, presented in Figure 4-3, with $l = 0.1D_0$. This cell is extruded in axial and radial directions, increasing l by a factor. This produces very big cells at the end of the cylinder, where very little happens.

The 3D mesh for the full domain is more complex, as it has to account for the flow particularities. The details of the mesh are shown in Figure 4-4, the cross-sectional area at the nozzle exit is detailed. Please note that there not exists azimuthal symmetry. As a good mesh quality is critical, the actual mesh was divided into five sub-structures, each region was built with different mesh structure and ratio. The purpose is to minimize the sharp angles in the mesh, the presence of cells with tiny aspect ratios and prevent suddenly changes in cell sizes.

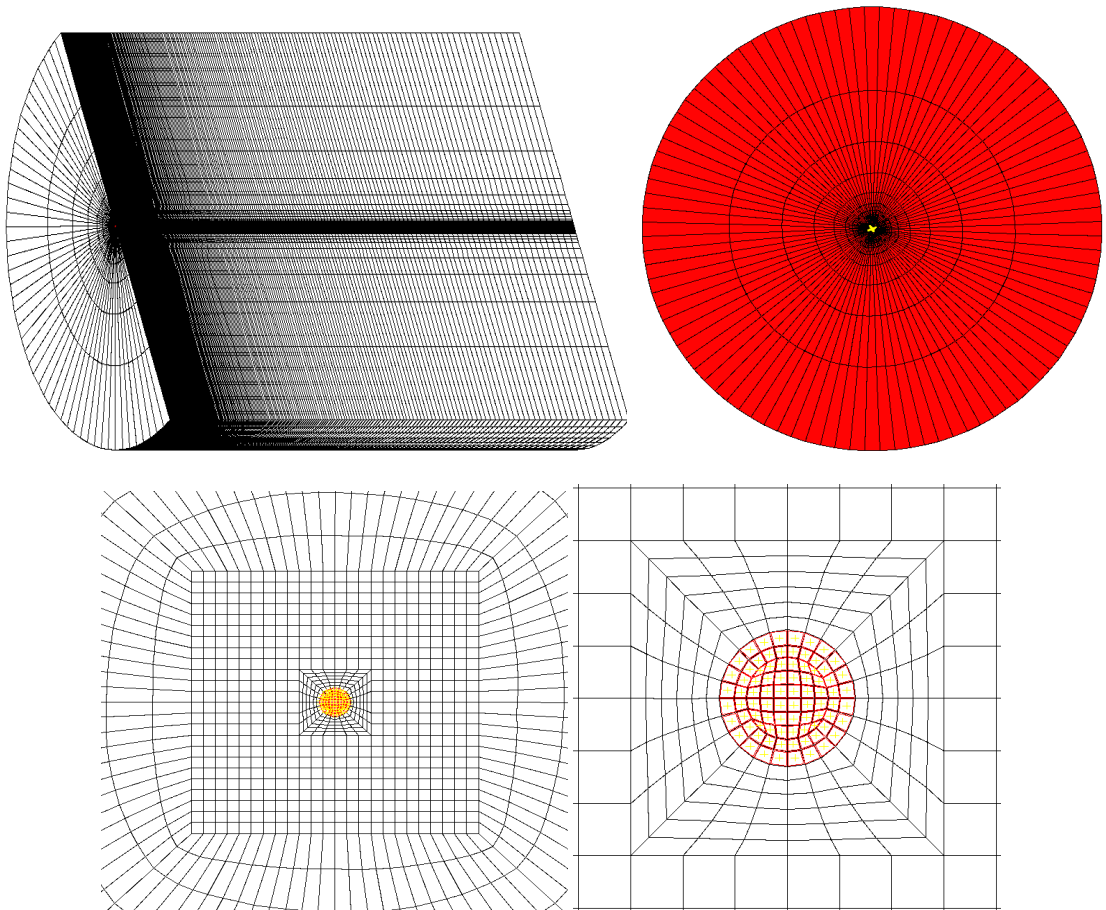


Figure 4-4: Different mesh structure at the inlet of the computational domain.

Chapter 4 – ELSA model validation

Hoyas et al. ([1], [2] and [3]) presented a detailed mesh study for the ELSA simulations in Star-CD. This research indicated ten segments along the nozzle hole diameter is enough. As a consequence, a 3D mesh was constructed in this manner creating 84 cells in total at the cross-sectional nozzle hole. For more comprehensive information about mesh structure refers to [1] and [2].

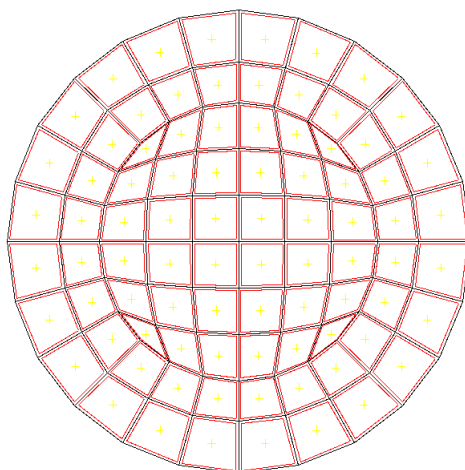


Figure 4-5: Mesh structure at the cross-sectional nozzle exit.

Although we have validated our computations using very different injectors (Multi-hole, single-hole, conical and cylindrical) in all the cases we have simulated just one spray in this academic geometry, as we are interested in the validation of ELSA and not, for the moment, in its direct application in real engine simulations.

4.1.2 Boundary conditions

Choosing the appropriate boundary conditions places an important role in the CFD model.

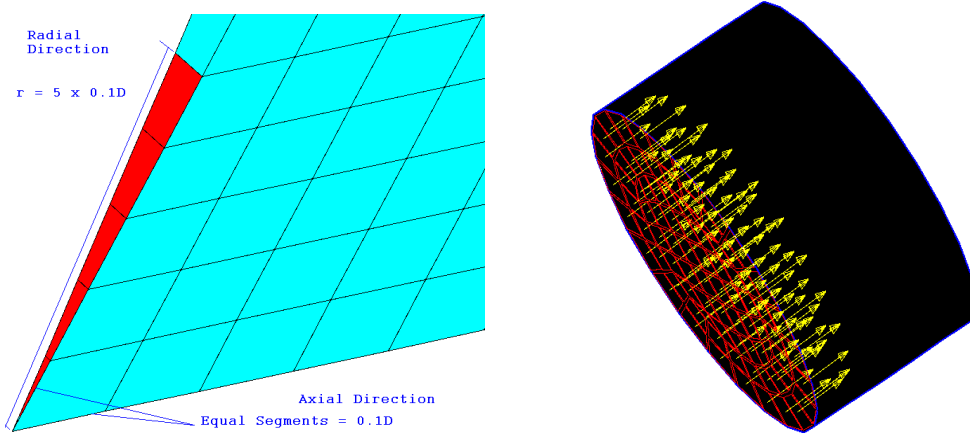


Figure 4-6: Inlet boundary condition is located at the area highlighted in red for (a): quasi-2D thin wedge mesh (left); and (b) 3D mesh (right).

A critical boundary condition is the velocity profile at the inlet, which obviously coincides with the nozzle exit. Figure 4-6 shows the cells used for the quasi-2D thin wedge domain (see in Figure 4-6a) and the points of the nozzle where the velocity is imposed at the 3D domain (refer to Figure 4-6b).

The key parameters for the inlet boundary condition are temperature, density, and the mass flow rate, the momentum flux or the velocity. Velocity profile is explicitly calculated from the momentum flux and the mass flow rate. Inlet velocity, u_{eff} is calculated as:

$$u_{eff} = \frac{\dot{m}}{\rho_f A_{eff}} = \frac{\dot{m}}{\rho_f C_a A_0} \quad (4.1)$$

With \dot{m} is the mass flow rate, ρ_f is the liquid fuel density, C_a is the orifice area-contraction coefficient, A_{eff} is the effective cross-sectional area and A_0 is real-size geometrical cross-sectional area at the nozzle exit respectively.

The effective area can be calculated as following:

$$A_{eff} = \frac{\dot{m}^2}{\rho_f \dot{M}} \quad (4.2)$$

Where \dot{M} stands for the momentum flux.

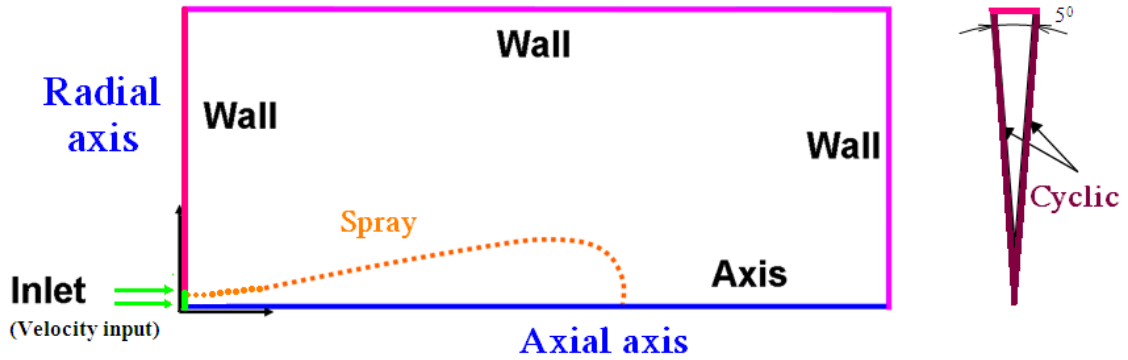


Figure 4-7: Boundary conditions in quasi-2D thin wedge.

In the cases where there is no information available about the injection rate in time, we have used Bernoulli's Equation, which can be simply applied for fluid flow between inlet and outlet to obtain the Bernoulli's velocity, U_{ber} . The appendix C - "Bernoulli velocity in spray modeling" shows how to obtain the equation (4.3).

$$U_{ber} = \sqrt{\frac{2(P_{inj} - P_{cha})}{\rho_f}} \quad (4.3)$$

Where ρ_f is the liquid fuel density, P_{inj} is the injection pressure, and P_{cha} is the chamber pressure. The effective velocity, U_{eff} linearly related to the Bernoulli's velocity through the nozzle discharge coefficient C_d and the orifice area-contraction coefficient C_a respectively. These two coefficients are obtained from experiments. The appendix D - "discharge coefficient" provides insight into the theory and formulation of C_d and its relations.

$$U_{eff} = \frac{C_d}{C_a} U_{ber} \quad (4.4)$$

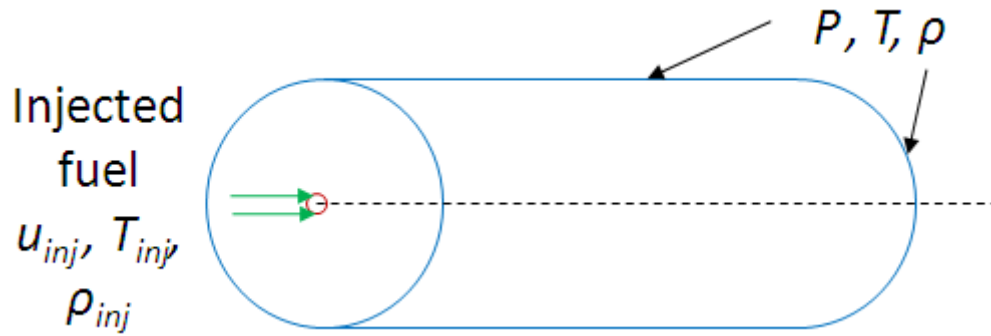


Figure 4-8: Boundary conditions in 3D mesh.

Figure 4-7 and Figure 4-8 show the boundaries in both quasi-2D thin wedge and 3D meshes. Those boundaries conditions have been used in all the computational cases shown.

In the 2D meshes, the azimuthal boundaries of the wedge use periodical boundary conditions, and a symmetric condition is imposed on the spray axis. We have not considered impingement at the walls, so the conditions at the furthest wall have little influence on the results.

4.2 ELSA assumptions and inputs

In order to use the ELSA method properly some constant or parameter values has been fixed. We have also made some approaches to the problem, in order to fulfill all the assumptions related to the ELSA model:

- Only spherical droplets represent for all particles.
- Droplets perfectly bounce back once contacted with the wall boundary.
- There is no gravity effect.
- Gradient based on velocity interpolation.
- Solution procedure is implicit pressure-based solution algorithm, namely Pressure Implicit with Splitting of Operators (PISO) algorithm. Issa, 1982 [6] and 1986 [7] proposed the PISO algorithm which is a pressure-velocity calculation procedure. The original work applied for the non-iterative computation of unsteady compressible flows. Not long after that,

it was widely spread for the iterative solution of steady state problems successfully [8].

- Starting atomization when volume fraction of liquid smaller than 0.01.
- Unless specified, when the Reitz-Diwakar break-up model is used the empirical coefficients of this model are $C_{b1} = 6$, $C_{b2} = \pi$, $C_{s1} = 0.5$ and $C_{s2} = 20$ ([9] and [10]).
- The “parcels” term in this thesis is the mathematical concept referred as fluid parcels. The fluid parcel represents a small amount of liquid moving with the liquid flow in space and time. It provides the average properties of fluid particles. The detailed explanation of the parcel in the Eulerian and Lagrangian description is mentioned in section 2.4. In general, number of parcels generated per cell equal to 1 in our calculations. Indeed, the use of small number of created parcels is also resulting in reduction of the storage requirements.
- The equations of compressible turbulent flows are used for the simulation of the flow.
- Surface tension coefficient of Eulerian liquid is constant.
- Liquid density in the Eulerian liquid is also constant.
- For the evaporation model, assumptions are quasi-stationary conditions at the droplet surface, homogeneous droplet temperature and internal circulation [11].

In the Lagrangian framework, it is crucial to specify the numerical parcels contained the droplets. As if a great number of droplets and parcels are created, this leads to an extremely high computational cost. On the contrary, if not enough numerical parcels are used, it results in a low level of resolution (Chaisemartin et al., 2007 [12]). Moreover, a large number of parcels in each cell of the computational domain is generally needed, thus yielding large memory requirement and computing cost. The model only generates parcels when the number of droplets per parcel (Nparcel) is greater than a specified number. For instance, the recommended value in ELSA for generating a new parcel is one. This mean one parcel contains one droplet. However, this may have a high cost, particularly in the 3D model. Increasing this value, the parcel

is only generated if it has enough number of droplets. If this number of droplets per parcel is high, the numerical prediction may be incorrect. Thus, it is a challenging task to specify the correct number for the simulation. It is recommended to set this value equals to one whenever possible, sacrificing memory instead of precision.

It is foremost important to note that the total number of droplets in time showing in this thesis is the remained droplets after each time step. This amount is completely different with the total number of generated droplets. Because many droplets have been disappeared due to the coalescence, absorption, evaporation, etc. Paper II in chapter 7 detailed droplet information and the study in this aspect.

4.3 2D validation

In this section, the determinant of the relevant experimental data and the validation of the ELSA model on the Diesel sprays in 2D and under non-evaporative conditions are presented. The effects of the grid size and computation domain were the first subject, chronologically speaking, of our research (Hoyas et al., 2011 [1], [2], and [3]). The grid constrains obtained, has been used in this study: 40-50 cells in the radial direction and 400-500 cells along the spray axis.

A first set of computational cases is tabulated in Table 4-1. In this table, the subscripts “*inj* or *i*” stand for the injection and “*cha* or *c*” stands for the chamber. This abbreviation will be used in the rest of the thesis, without further notification.

The experimental tests were carried out using the hydro-eroded seven-hole VCO injector, with conical holes. The averaged nozzle diameter is $D_0 = 0.140$ mm and $C_a = 0.86$. Chamber temperature remains constant at 25°C (298 K). Only one representative orifice is modeled. As is detailed in Table 4-1, three different injection pressures are investigated with two different chamber gases and at several different levels of chamber pressures and densities. The

Chapter 4 – ELSA model validation

experimental injection rate, with three different pressure levels is shown in Figure 4-9. The velocity profile for the inlet boundary conditions of the spray modeling, is directly derived from the mass flow rate as formulated in equation (4.1). For different injection pressures, it has been maintained the same amount of injected fuel equals to 45 mg ([13] and [14]) by adjusting the energizing time. The velocity profiles for these three pressures can be visualized in Figure 4-10.

Table 4-1: Computational cases under non-evaporative conditions.

Case	Fuel	P_{inj}	ρ_{inj}	Cha. Gas	P_{cha}	ρ_{cha}	
		[MPa]	[kg/m ³]		[MPa]	[kg/m ³]	
N-Ev01	Diesel	40	806 at 90 °C	N ₂	2	25	
N-Ev02					5	58	
N-Ev03					80	2	25
N-Ev04						5	58
N-Ev05						2	25
N-Ev06					180	5	58
N-Ev07		40		SF ₆	0.28	22	
N-Ev08					0.54	37	
N-Ev09					80	0.28	22
N-Ev10						0.54	37
N-Ev11						0.28	22
N-Ev12					180	0.54	37

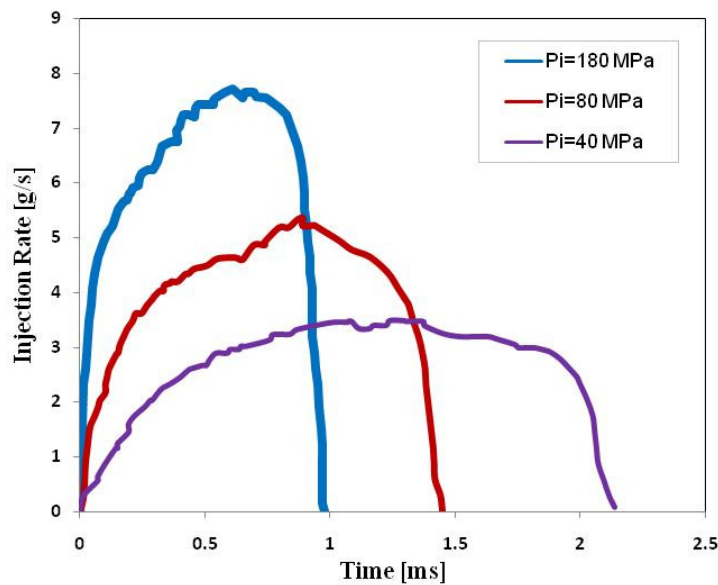


Figure 4-9: Injection rate with different injection pressures ($P_{inj} = 40$ MPa, 80 MPa, and 180 MPa respectively).

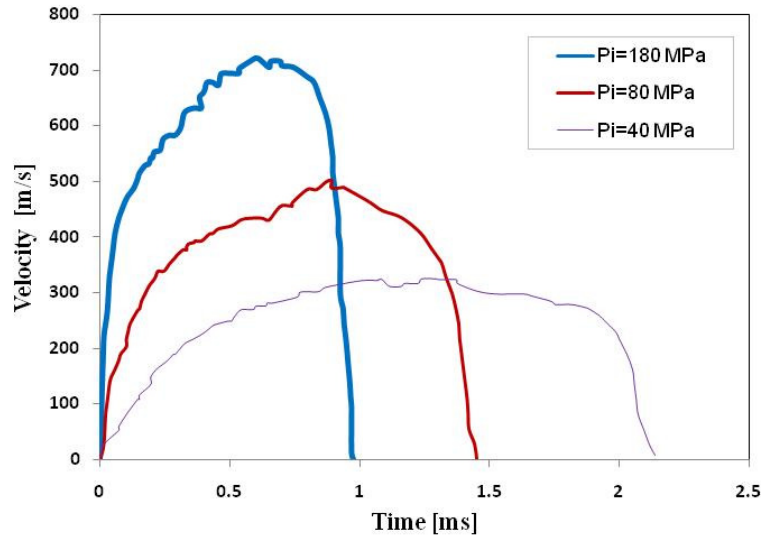


Figure 4-10: Velocity profile at different injection pressures ($P_{inj} = 40$ MPa, 80 MPa, and 180 MPa respectively).

Parametric studies were performed to evaluate the behavior of many parameters on the numerical results, and the difference amongst several thresholds, and the constraints of implemented model.

Most of these validation has been made for $P_{inj} = 80$ MPa, $P_{cha} = 2$ MPa. The vessel was filled by N_2 gas.

4.3.1 Spray penetration

Initially, it is important to decide the definitions and thresholds of the several spray characteristics used for validation. There not exists a unique definition of the spray tip penetration, the vapor penetration and the liquid length. Based on a long experience resulted from the comparison between models and experiments under different spray conditions and testing facilities, a couple of definitions and thresholds have been proposed in literature ([13] - [16]). A summary can be seen in Figure 4-11, with the most used thresholds for each definition.

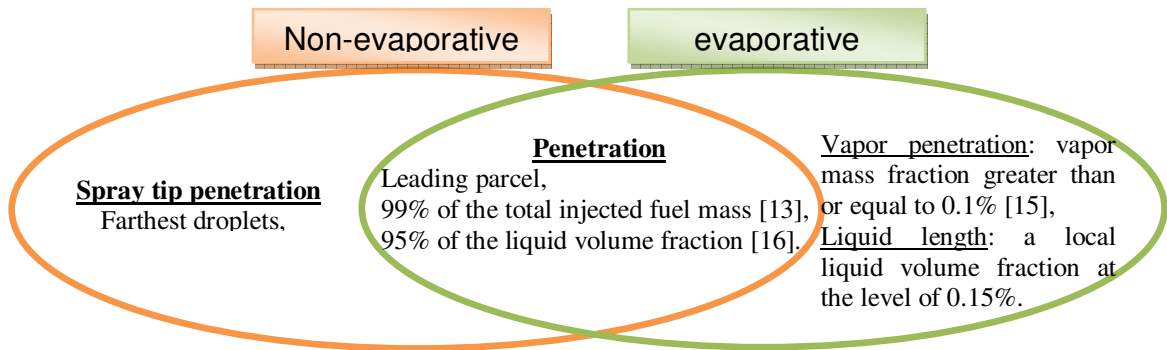


Figure 4-11: Similarity and difference of spray penetration thresholds under non-evaporative and evaporative conditions.

In the ELSA model, the liquid and vapor mass fraction are available outputs, liquid volume fraction can be derived. Hence, the macroscopic spray characteristics are feasible to be tracked using those outputs. Figure 4-12 shows the very slightly difference in the spray tip penetration when using three different criterions. Obviously, under non-evaporative conditions, the spray penetration is almost the same. As the liquid volume fraction is an averaged quantity, it is most useful than one point measures as can be the farthest droplet position, so we have selected the liquid volume based definition as our spray penetration.

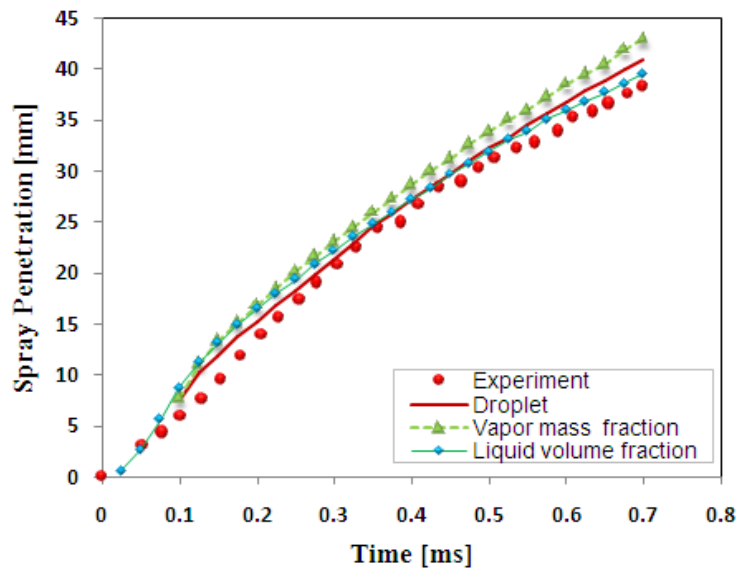


Figure 4-12: Comparison of different definitions for computing the spray penetration (N_2 ; $P_{inj} = 80 \text{ MPa}$; $P_{cha} = 2 \text{ MPa}$).

4.3.2 Time steps

The Courant-Friedrichs-Lewy (CFL) criterion is used in order to perform the maximum time step. This condition reads as $CFL = \frac{u\Delta t}{\Delta x}$, where u is the velocity, Δt and Δx is the change in time and mesh size respectively.

The CFL computed in this way need to be lower than 1, but 0.7 is usually preferred. As the droplets are followed using a Lagrangian framework, their cells are bigger than those of the liquid region, being the velocities lower, so this part is not a problem.

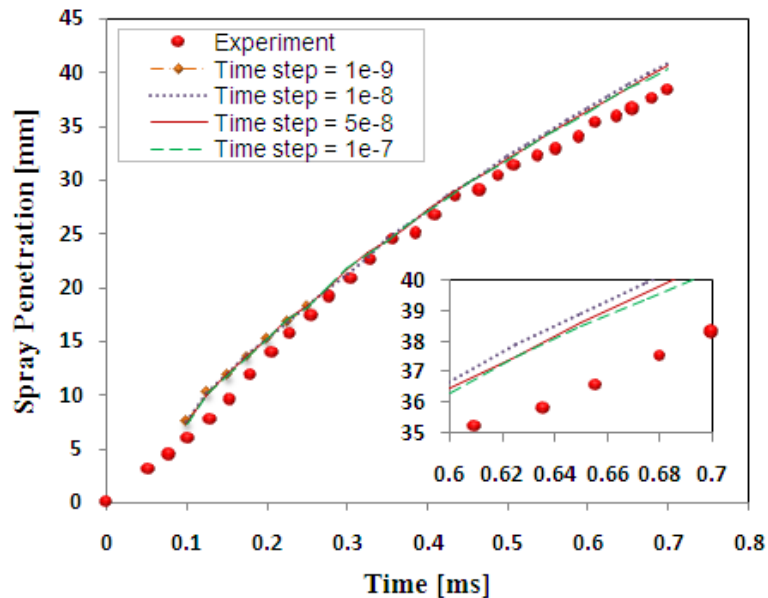


Figure 4-13: Comparison of the effects of various time steps: Spray Penetration (N_2 ; $P_{inj} = 80 \text{ MPa}$; $P_{cha} = 2 \text{ MPa}$).

Figure 4-13, Figure 4-14, and Figure 4-15 show the influence of different time step scale in term of spray penetration, number of droplets and Sauter Mean Diameter (SMD). That figures counsel to use $t = 1e^{-7}$, but in posterior 3D benchmarks, mostly in evaporating cases, we have seen that this values is too optimistic, and that has to be reduced to $t = 1e^{-8}$. As 2D cases are really fast, we have chosen this time step in all the calculations in order to facilitate comparisons between cases.

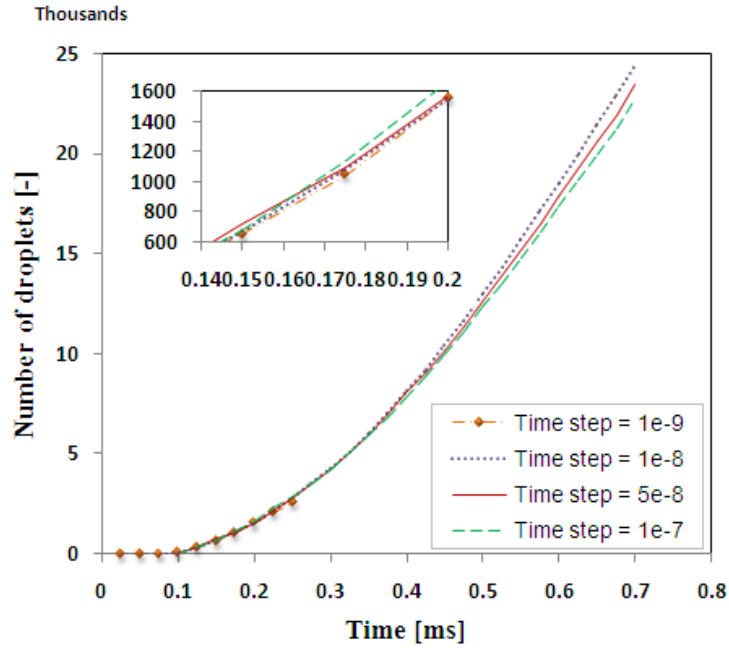


Figure 4-14: Comparison of the effect of time step: number of droplets (N_2 ; $P_{inj} = 80 \text{ MPa}$; $P_{cha} = 2 \text{ MPa}$).

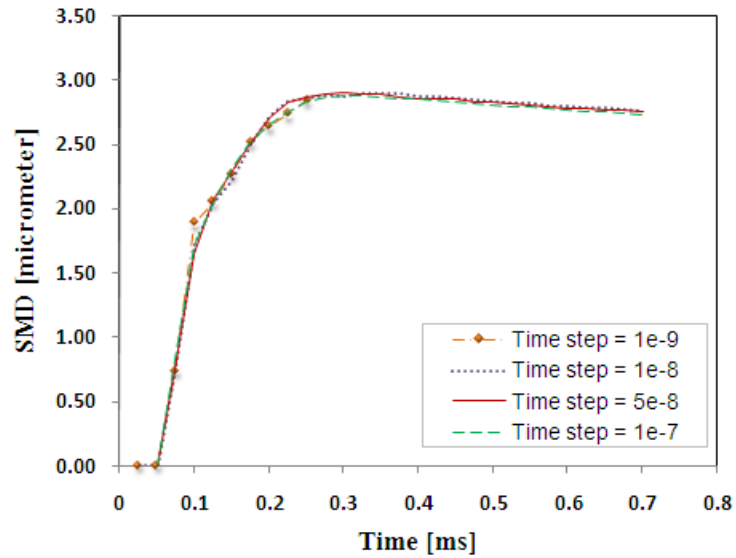


Figure 4-15: Comparison of the effect of time step: SMD (N_2 ; $P_{inj} = 80 \text{ MPa}$; $P_{cha} = 2 \text{ MPa}$).

4.3.3 Schmidt number

Schmidt number is defined as the ratio of momentum diffusivity (related by viscosity) and mass diffusivity. Fluid flows in which there are simultaneous

Chapter 4 – ELSA model validation

momentums and mass diffusion convection processes can be characterized by this dimensionless number. It is of great importance on sprays and it is generally equated to 1. Table 4-2 shows several tests on the Schmidt numbers. Three values of 0.5 (proposed by Salvador et al., 2011 [17]), 0.9, and 1.0 were investigated.

Table 4-2: Numerical studies of different Schmidt number.

Case	Schmidt	Fuel	P_{inj}	T_{inj}	ρ_{inj}	Cha. Gas	P_{cha}	T_{cha}
			[MPa]	[K]	[kg/m ³]		[MPa]	[K]
N-Ev13	0.5	n-dodecane	80	293	806	N ₂	2	298
N-Ev14	0.9	n-dodecane	80	293	806	N ₂	2	298
N-Ev15	1.0	n-dodecane	80	293	806	N ₂	2	298

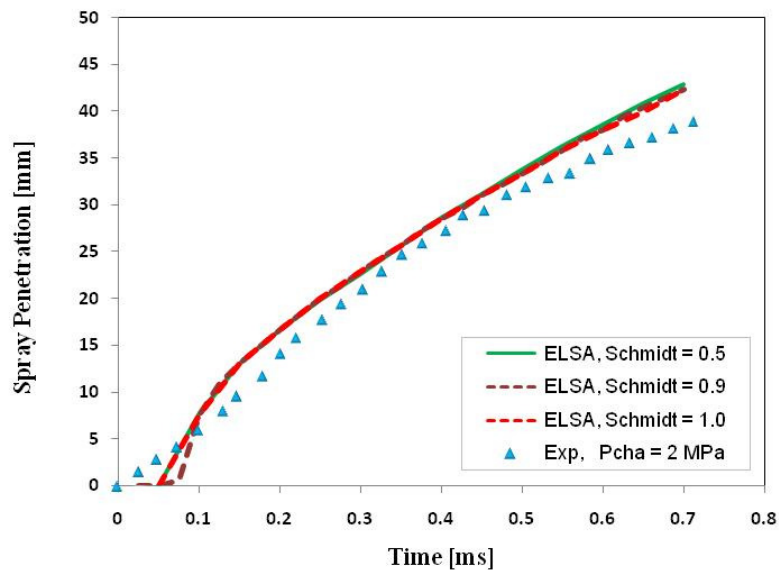


Figure 4-16: Spray penetration with different Schmidt number of 0.5 vs. 0.9 vs. 1.0 respectively (N₂; $P_{inj} = 80$ MPa; $P_{cha} = 2$ MPa).

There is no significantly change in term of spray penetration as shown in Figure 4-16, and Figure 4-17. On the contrary, as it is presented at Figure 4-18, Schmidt number is of great importance in the droplets generation mechanism. Because this dimensionless number relates directly with diffusivity viscosity/density and the diffusivity for mass transfer. As shown in eq. (3.13),

Chapter 4 – ELSA model validation

the liquid turbulent diffusion flux of the liquid decreases as turbulent Schmidt number increases. This last plot shows the evolution of the number of droplets against time, and is easy to see that for $t = 0.7$ ms, the droplets for $Sc = 0.5$ are nearly three times to those of $Sc = 1.0$. As it is recommended at Star-CD manual we have chosen $Sc = 0.9$.

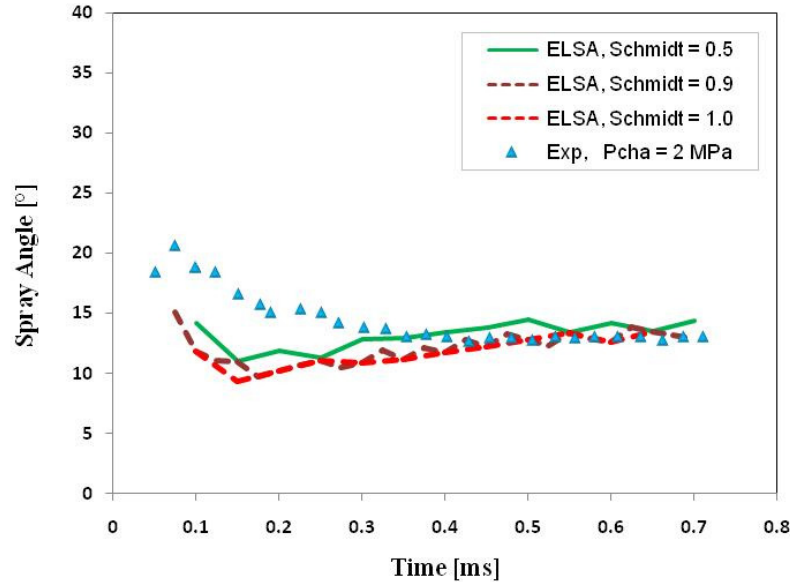


Figure 4-17: Spray spreading angle with different Schmidt number of 0.5, 0.9, and 1 respectively (N_2 ; $P_{inj} = 80$ MPa; $P_{cha} = 2$ MPa).

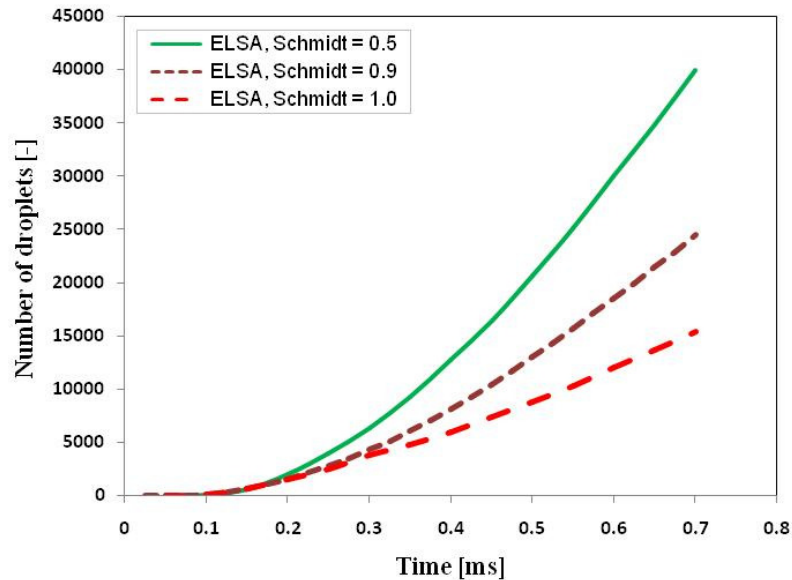


Figure 4-18: Number of droplets with different Schmidt of 0.5, 0.9, and 1 respectively (N_2 ; $P_{inj} = 80$ MPa; $P_{cha} = 2$ MPa).

4.3.4 Generating new parcels

As was stated previously new parcels are created when the number of droplets per parcel is greater than a specific number (N_{parcel}) defined by the modeler.

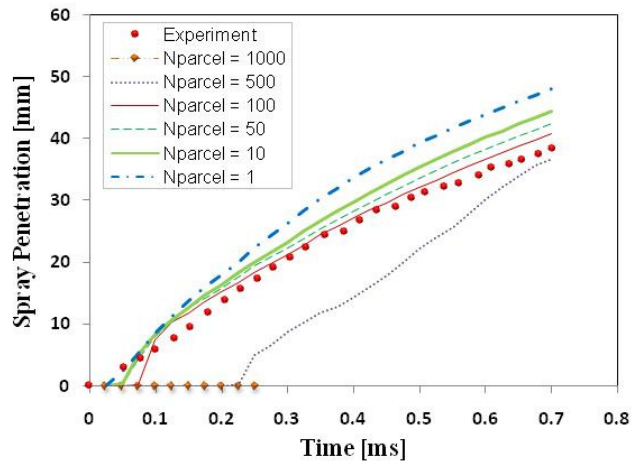


Figure 4-19: Spray penetration for different N_{parcel} number (N_2 ; $P_{inj} = 80$ MPa; $P_{cha} = 2$ MPa).

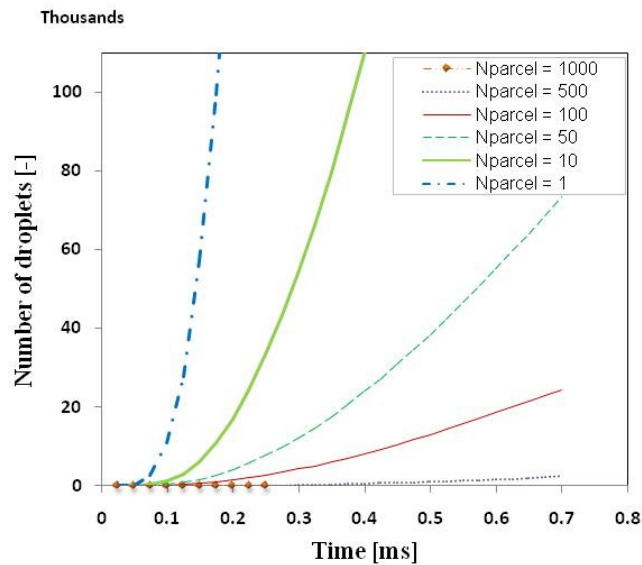


Figure 4-20: Number of droplets for different N_{parcel} number (N_2 ; $P_{inj} = 80$ MPa; $P_{cha} = 2$ MPa).

Obviously, the N_{parcel} number plays a major role in the results of ELSA model (see Figure 4-19 and Figure 4-20). In this particular case, for N_{parcel}

numbers close to one hundred (Figure 4-19) the ELSA model results are in best agreement with those obtained in measurements under non-evaporative condition. The spray penetration is generally good agreement for the Nparcel numbers changing from 10 – 100 when taking into account the scatter in experimental results. However, in the evaporative case, most of droplets are going to vaporize, thus this number has to be close to one in order to represent accurately the behavior of the spray.

4.3.5 Turbulent coefficient and models

There are many different RANS models in the literature. We have benchmarked the three most used in spray simulation. As a result, the modified *High Reynolds k-ε* has been chosen for the rest of this work, as it was able to represent better the spray at similar or lower computational cost. In all the cases some of the usual values for some constants of these models have to be recomputed. In the next tables, the standard value of $C_{\epsilon 1}$ are bold, while we have tested other two values of $C_{\epsilon 1}$ coefficients. The chosen one, coming from this benchmarking, has been underlined.

4.3.5.1 *High Reynolds k-ε turbulence model*

Table 4-3: Coefficients of the high Reynolds k-ε turbulence model.

C_{μ}	σ_k	σ_{ϵ}	σ_h	σ_m	$C_{\epsilon 1}$	$C_{\epsilon 2}$	$C_{\epsilon 3}$	$C_{\epsilon 4}$	K	E
0.09	1.0	1.22	0.9	0.9	1.44	1.92	1.44	-0.33	0.419	9.0
					1.52					
					<u>1.6</u>					

The investigation of this model and its $C_{\epsilon 1}$ has been detailed in three previous papers Hoyas et al. ([1], [2], and [3]) for one nozzle with a diameter of

112 μm using the following turbulent coefficients. The high Reynolds $k\text{-}\varepsilon$ turbulent coefficients are shown in Table 4-3. The underlined coefficient, 1.6, was chosen for the rest of this work.

4.3.5.2 RNG $k\text{-}\varepsilon$ turbulence model

The influence of RNG turbulent model and its parameters is shown in this section. In this following three cases, the RNG $k\text{-}\varepsilon$ turbulence model and the effects of $C_{\varepsilon 1}$ are tested. Table 4-4 and Table 4-5 show the computing parameters with $C_{\varepsilon 1}$ equals to 1.6, 1.52, and 1.42 respectively.

Table 4-4: Coefficients of the RNG $k\text{-}\varepsilon$ turbulence model.

C_{μ}	σ_k	σ_{ε}	σ_h	σ_m	$C_{\varepsilon 1}$	$C_{\varepsilon 2}$	$C_{\varepsilon 3}$	$C_{\varepsilon 4}$	κ	E	η_0	β
0.085	0.719	0.719	0.9	0.9	<u>1.42</u>	1.68	1.42	-0.387	0.4	9.0	4.38	0.012
					1.52							
					1.6							

Table 4-5: Computational cases of the RNG $k\text{-}\varepsilon$ turbulence model.

Case	$C_{\varepsilon 1}$	Fuel	P_{inj}	T_{inj}	ρ_{inj}	Cha. Gas	P_{cha}	T_{cha}
			[MPa]	[K]	[kg/m ³]		[MPa]	[K]
N-Ev16	1.6	n-dodecane	80	293	806	N ₂	2	298
N-Ev17	1.52	n-dodecane	80	293	806	N ₂	2	298
N-Ev16	1.42	n-dodecane	80	293	806	N ₂	2	298

The default value of 1.42 results in a good agreement with the experimental results of spray penetration, as is presented in Figure 4-21. When taking into account the spray spreading angle, it is a bit higher than

Chapter 4 – ELSA model validation

experimental data (see Figure 4-22). In all these figures, values above 1.52 do not show any significant difference.

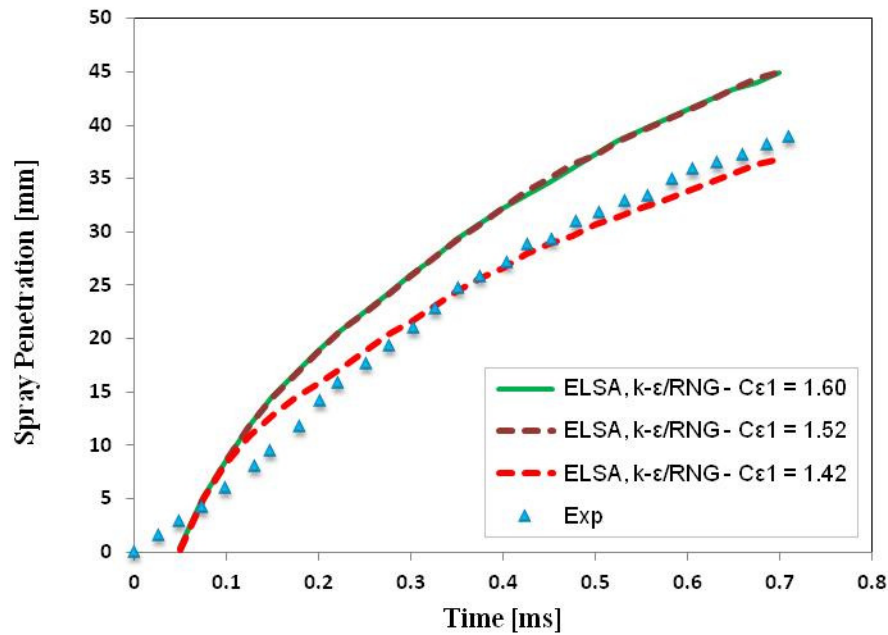


Figure 4-21: Spray penetration with different ($k\text{-}\epsilon/\text{RNG-}C_{\epsilon 1}$) of 1.60, 1.52, and 1.42 respectively (N_2 ; $P_{inj} = 80 \text{ MPa}$; $P_{cha} = 2 \text{ MPa}$).

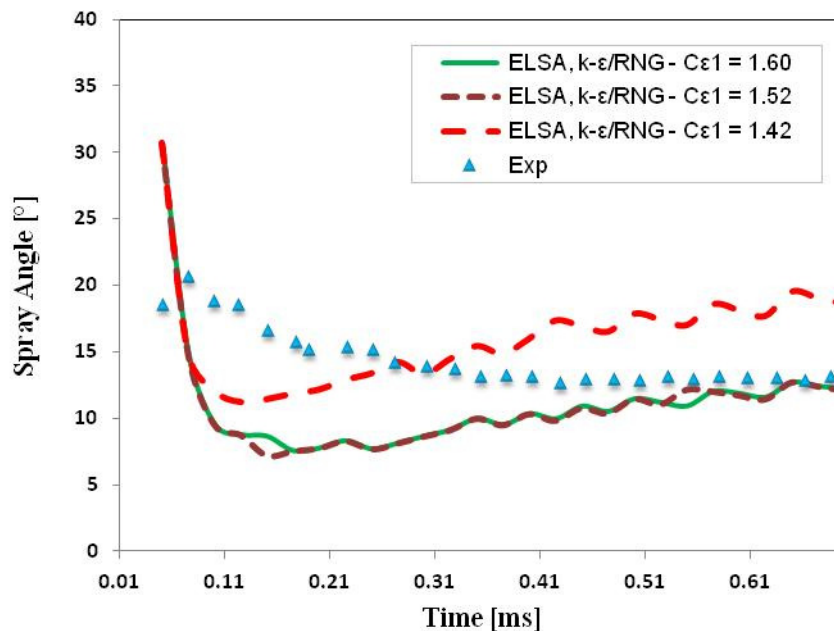


Figure 4-22: Spray spreading angle with different ($k\text{-}\epsilon/\text{RNG-}C_{\epsilon 1}$) of 1.60, 1.52, and 1.42 respectively (N_2 ; $P_{inj} = 80 \text{ MPa}$; $P_{cha} = 2 \text{ MPa}$).

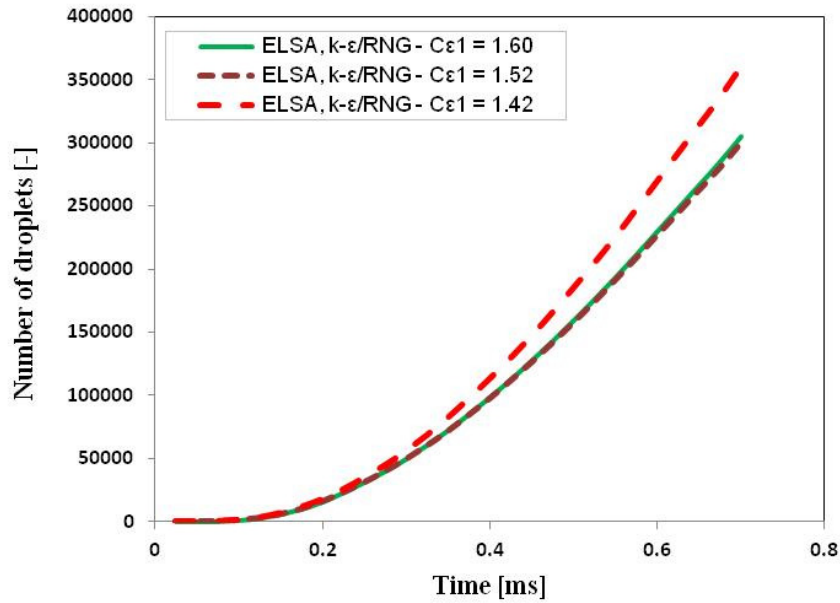


Figure 4-23: Number of droplets with different ($k\text{-}\epsilon/\text{RNG-}C_{\epsilon 1}$) of 1.60, 1.52, and 1.42 respectively (N_2 ; $P_{inj} = 80 \text{ MPa}$; $P_{cha} = 2 \text{ MPa}$).

4.3.5.3 Chen $k\text{-}\epsilon$ turbulence model

Table 4-6 and Table 4-7 present the turbulent coefficients and computational cases with Chen $k\text{-}\epsilon$ turbulence model respectively. Values of 1.15, 1.30, and 1.44 have been studied. The default value, 1.15, results in a best prediction. The numerical results of Chen $k\text{-}\epsilon$ turbulence model are plotted in the next section.

Table 4-6: Coefficients of the Chen's $k\text{-}\epsilon$ turbulence model.

C_μ	σ_k	σ_ϵ	σ_h	σ_m	$C_{\epsilon 1}$	$C_{\epsilon 2}$	$C_{\epsilon 3}$	$C_{\epsilon 4}$	$C_{\epsilon 5}$	\mathcal{K}	E
0.09	0.75	1.15	0.9	0.9	<u>1.15</u>	1.9	1.44	-0.33	0.25	0.4153	9.0
					1.30						
					1.44						

Table 4-7: Computational cases of the Chen $k-\epsilon$ turbulence model.

Case	$C_{\epsilon 1}$	Fuel	P_{inj} [MPa]	T_{inj} [K]	ρ_{inj} [kg/m ³]	Cha. Gas	P_{cha} [MPa]	T_{cha} [K]
N-Ev19	1.44	n-dodecane	80	293	806	N ₂	2	298
N-Ev20	1.30	n-dodecane	80	293	806	N ₂	2	298
N-Ev21	1.15	n-dodecane	80	293	806	N ₂	2	298

4.3.5.4 The difference amongst three turbulence models

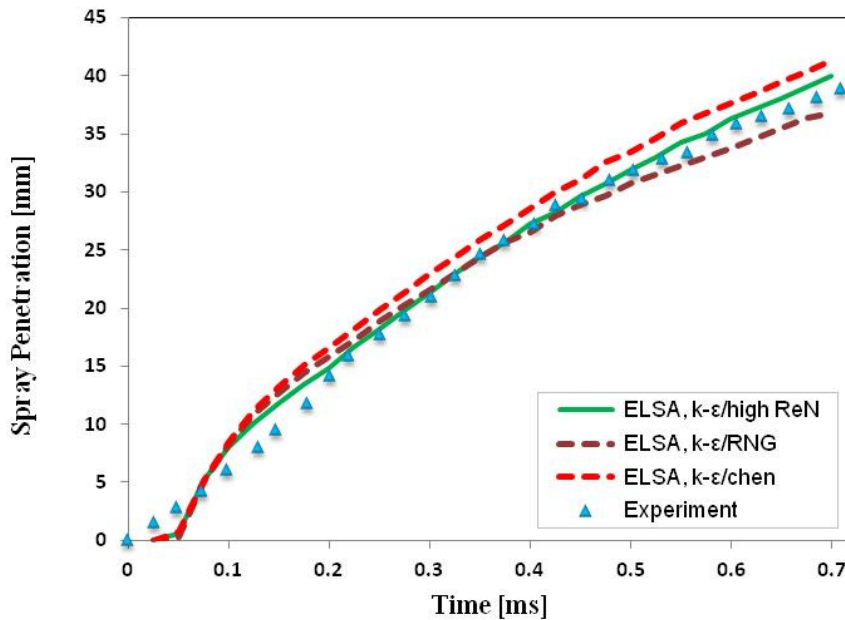


Figure 4-24: Spray penetration comparing amongst $k-\epsilon$ /high ReN, $k-\epsilon$ /RNG, and $k-\epsilon$ /Chen (N₂; $P_{inj} = 80$ MPa; $P_{cha} = 2$ MPa).

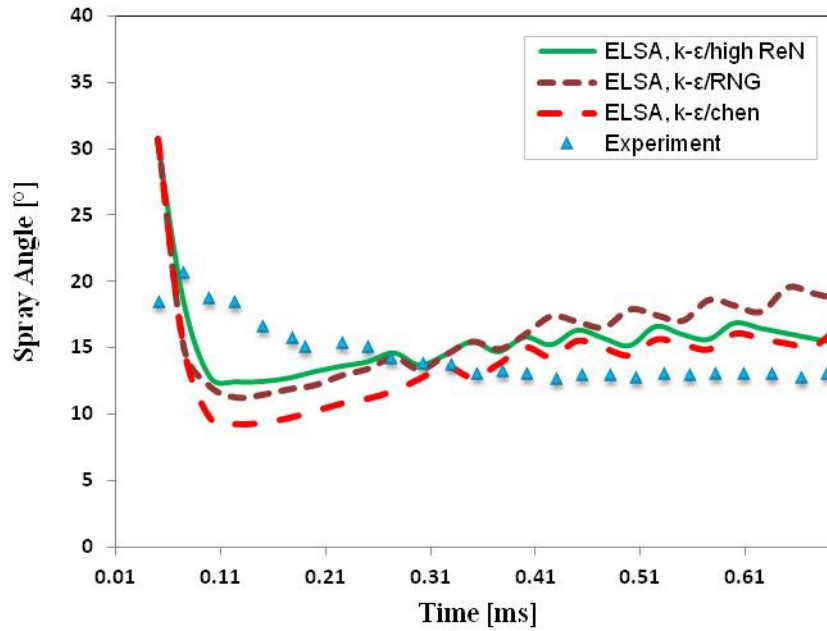


Figure 4-25: Spray spreading angle comparing amongst $k-\epsilon/\text{high ReN}$, $k-\epsilon/\text{RNG}$, and $k-\epsilon/\text{Chen}$ (N_2 ; $P_{inj} = 80 \text{ MPa}$; $P_{cha} = 2 \text{ MPa}$).

There is a slightly low value in the first instant of time in Figure 4-24, this is probably the effect of N_{parcel} number ($N_{parcel} = 100$) and low numbers of droplets at the beginning spray process, as can be seen in Figure 4-19, this was not happened in the lower number of N_{parcel} . Figure 4-24 and Figure 4-25 show the comparison amongst these three turbulent models. Globally, the high Reynolds number $k-\epsilon$, together with the adjusted $C_{\epsilon 1}$ constant, gives a better prediction. Consequently, this is used for the rest of this study.

4.3.6 Break-up models

Three Reitz-Diwakar (Reitz), Hsiang-Faeth (Hsiang), and Pilch- Erdman (Pilch) break-up models are validated in the following study described in Table 4-8. For more details on the theoretical approaches, see appendix A - “A literature review on Atomization and break-up in Diesel sprays”.

Chapter 4 – ELSA model validation

Table 4-8: Computational cases for several break-up models.

Case	Break-up	Fuel	P_{inj}	T_{inj}	ρ_{inj}	Cha. Gas	P_{cha}	T_{cha}
			[MPa]	[K]	[kg/m ³]		[MPa]	[K]
N-Ev22	<u>Reitz</u>	n-dodecane	80	293	806	N ₂	2	298
N-Ev23	<u>Hsiang</u>	n-dodecane	80	293	806	N ₂	2	298
N-Ev24	<u>Pilch</u>	n-dodecane	80	293	806	N ₂	2	298

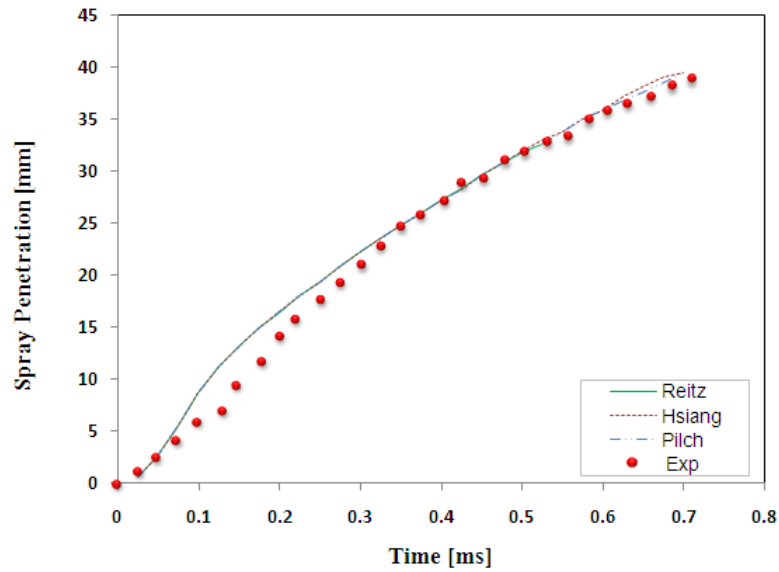


Figure 4-26: Spray penetration with different break-up models (N_2 ; $P_{inj} = 80$ MPa; $P_{cha} = 2$ MPa).

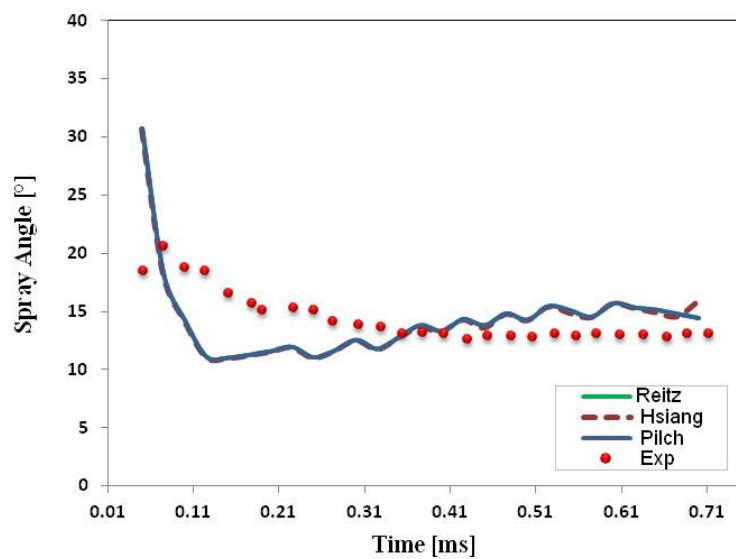


Figure 4-27: Spray spreading angle with different break-up models (N_2 ; $P_{inj} = 80$ MPa; $P_{cha} = 2$ MPa).

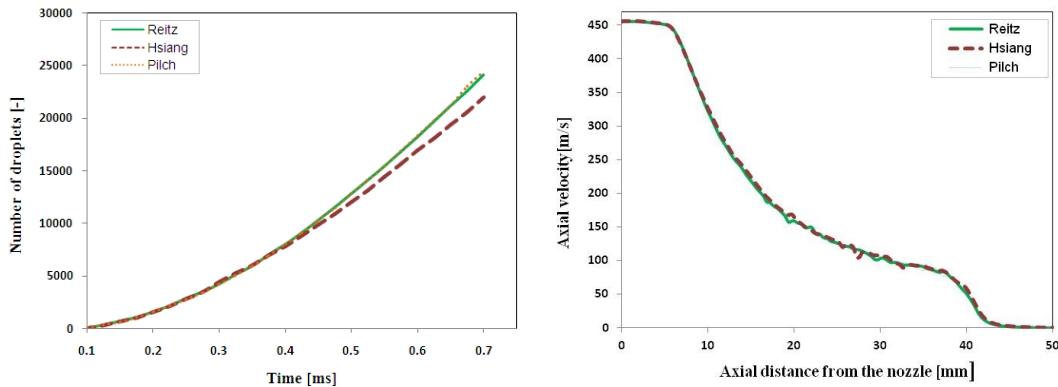


Figure 4-28: Number of droplets and Axial velocity with different break-up models (N_2 ; $P_{inj} = 80 \text{ MPa}$; $P_{cha} = 2 \text{ MPa}$).

Concerning on the effects of the various break-up models, the numerical analysis of these cases is summarized in Figure 4-26, Figure 4-27, and Figure 4-28. A mostly identical trend in spray penetration, spray cone angle, and axial velocity are observed. The main discrepancy amongst them is at the microscopic characteristics and computing time, as detailed in Table 4-9. Hsiang method produces less number of droplets than the other two, and as this model does not represent the similar properties that the Reitz and Pilch produced. Reitz break-up model produces the smallest droplet size and its CPU time is less than Pilch model. Moreover, the Reitz model is widely used in practice, thus Reitz model is the chosen one for the rest of the work.

Table 4-9: The results of break-up models.

Break-up models	Number of droplets	Min Drop Dia.	Max Drop Dia.	Avg. Drop Dia.	CPU time (h) for 0.7 ms/ 6 processors
Reitz	24120	2.985E-07	6.219E-06	2.7637E-06	6.7
Hsiang	21972	2.412E-07	6.472E-06	2.8844E-06	4
Pilch	24350	2.453E-07	6.275E-06	2.7718E-06	6.9

4.3.7 Weber criteria for the collision

The case studies in this section are shown in Table 4-10. As it is clear from Figure 4-29, Figure 4-30, and Figure 4-31, the only effect of this change is on the droplets generation, where the case equals to 6 generates slightly less particles. The case $Weber_crit = 12$ produced more droplets and the result in this case approach the stable results as in Figure 4-31 where there is almost no change once increasing from 8.4 to 120. Moreover, the recommended value is set to 12 in ELSA model Star-CD code based on the research of Qian and Law, 1997 [18] on the estimated $Weber_crit$ value that separates break-up and coalescence regime. As a result, we used this value in all other simulations.

Table 4-10: Numerical studies on the Weber criteria for collision.

Case	$Weber_crit$	Fuel	P_{inj}	T_{inj}	ρ_{inj}	Cha. Gas	P_{cha}	T_{cha}
			[MPa]	[K]	[kg/m ³]		[MPa]	[K]
N-Ev25	6	n-dodecane	80	293	806	N ₂	2	298
N-Ev26	8.4	n-dodecane	80	293	806	N ₂	2	298
N-Ev27	12	n-dodecane	80	293	806	N ₂	2	298
N-Ev28	60	n-dodecane	80	293	806	N ₂	2	298
N-Ev29	120	n-dodecane	80	293	806	N ₂	2	298

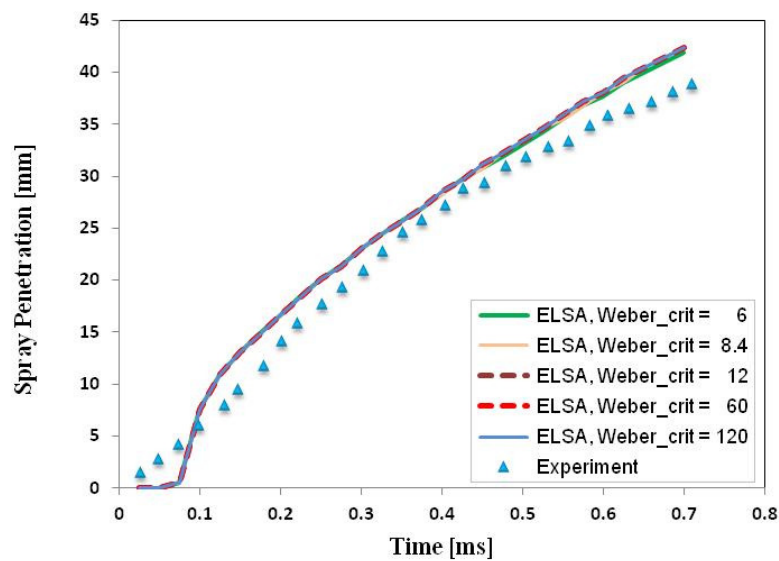


Figure 4-29: Spray penetration with different $Weber_crit$ number of 6, 8.4, 12, 60, and 120 respectively (N_2 ; $P_{inj} = 80$ MPa; $P_{cha} = 2$ MPa).

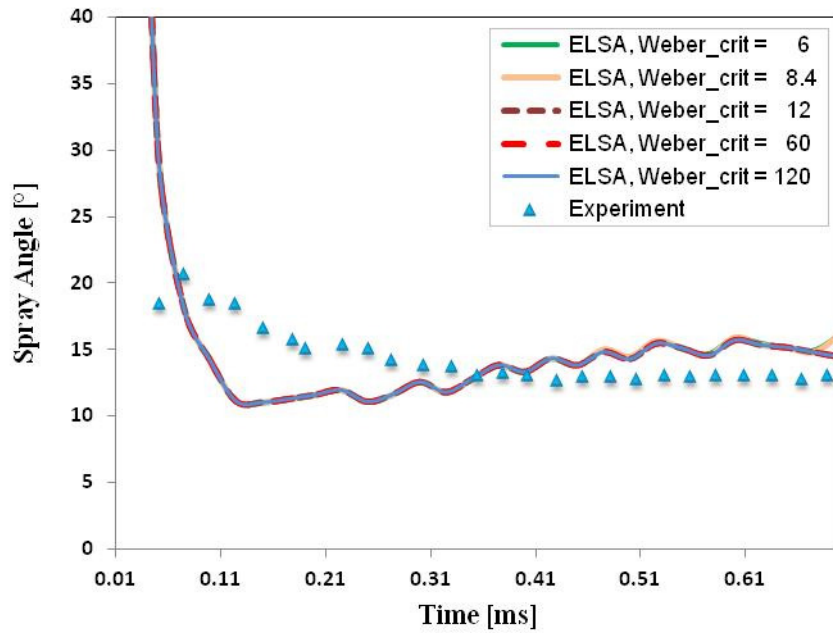


Figure 4-30: Spray spreading angle with different $Weber_crit$ number of 6, 8.4, 12, 60, and 120 respectively (N_2 ; $P_{inj} = 80$ MPa; $P_{cha} = 2$ MPa).

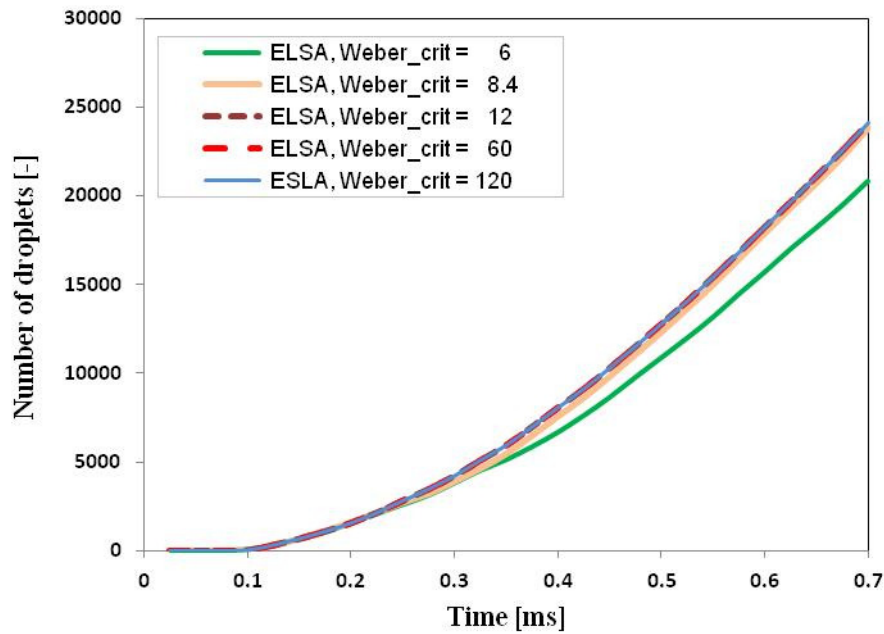


Figure 4-31: Number of droplets with different $Weber_crit$ number of 6, 8.4, 12, 60, and 120 respectively (N_2 ; $P_{inj} = 80$ MPa; $P_{cha} = 2$ MPa).

4.3.8 Non break-up and break-up

In these simulations, the influence of break-up models was tested, and it was compared with the same simulation but excluding the break-up models. From Figure 4-32 and Figure 4-33, it is seen that the predicted spray tip penetration and spray cone angle represents accurately the experimental penetration and reasonably the spray cone angle. The variation in terms of spray spreading angle and spray penetration between no breakup and Reitz breakup is negligible. To ensure a realistic result and more practice, the break-up model is used in the following cases.

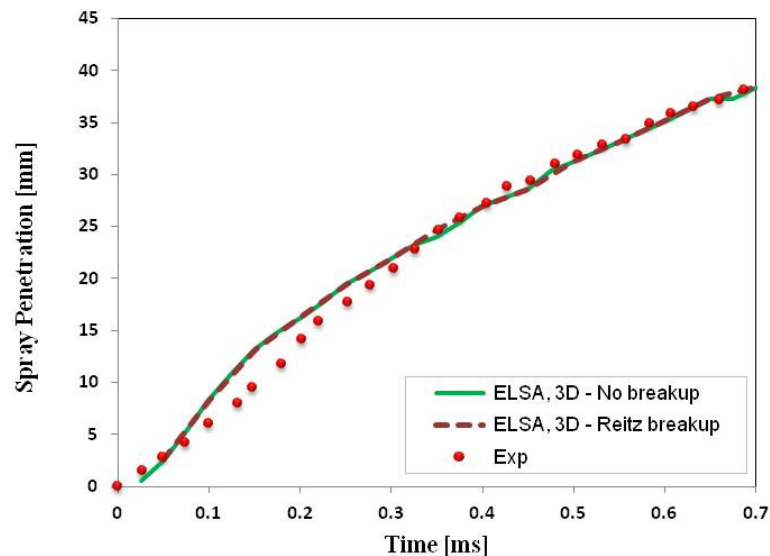


Figure 4-32: Spray penetration with and without break-up
(N_2 ; $P_{inj} = 80$ MPa; $P_{cha} = 2$ MPa).

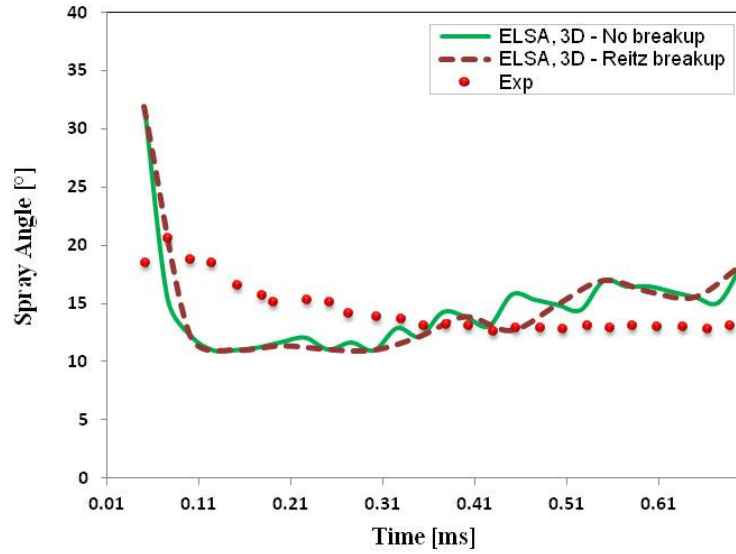


Figure 4-33: Spray spreading angle with and without break-up (N_2 ; $P_{inj} = 80 \text{ MPa}$; $P_{cha} = 2 \text{ MPa}$).

4.3.9 Coalescence

This study focuses on the coalescences and spray break-up sub-models. Set of cases are briefly summarized in Table 4-11.

Table 4-11: Numerical studies on the spray break-up model and coalescence.

Case	Break-up	Coalescence	Fuel	P_{inj}	T_{inj}	ρ_{inj}	Gas	P_{cha}	T_{cha}
				[MPa]	[K]	[kg/m ³]		[MPa]	[K]
N-Ev30	Reitz	Off	n-dodecane	80	293	806	N ₂	2	298
N-Ev31	Reitz	On	n-dodecane	80	293	806	N ₂	2	298
N-Ev32	Hsiang	Off	n-dodecane	80	293	806	N ₂	2	298
N-Ev33	Hsiang	On	n-dodecane	80	293	806	N ₂	2	298
N-Ev34	Pilch	Off	n-dodecane	80	293	806	N ₂	2	298
N-Ev35	Pilch	On	n-dodecane	80	293	806	N ₂	2	298

Chapter 4 – ELSA model validation

The results obtained indicate that coalescence have little effect, if any, on the spray penetration, spray spreading angle, and centerline velocity. This is shown in Figure 4-34, Figure 4-35, and Figure 4-36 respectively.

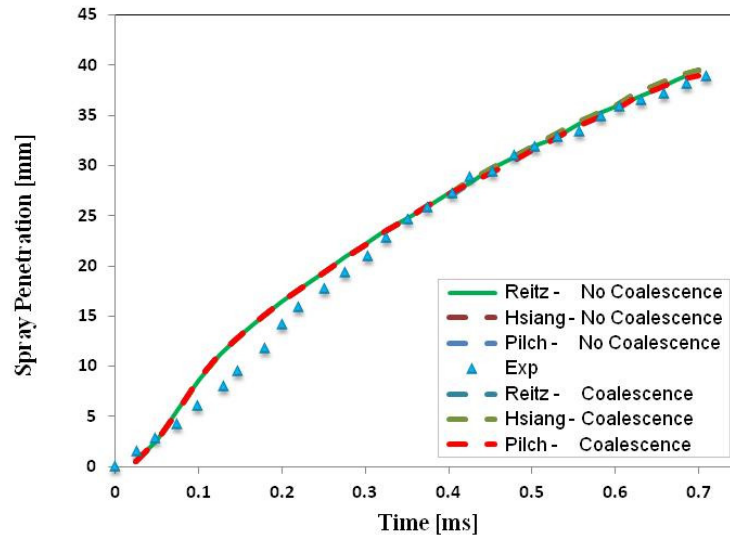


Figure 4-34: Spray penetration with and without coalescence for different break-up models (N_2 ; $P_{inj} = 80$ MPa; $P_{cha} = 2$ MPa).

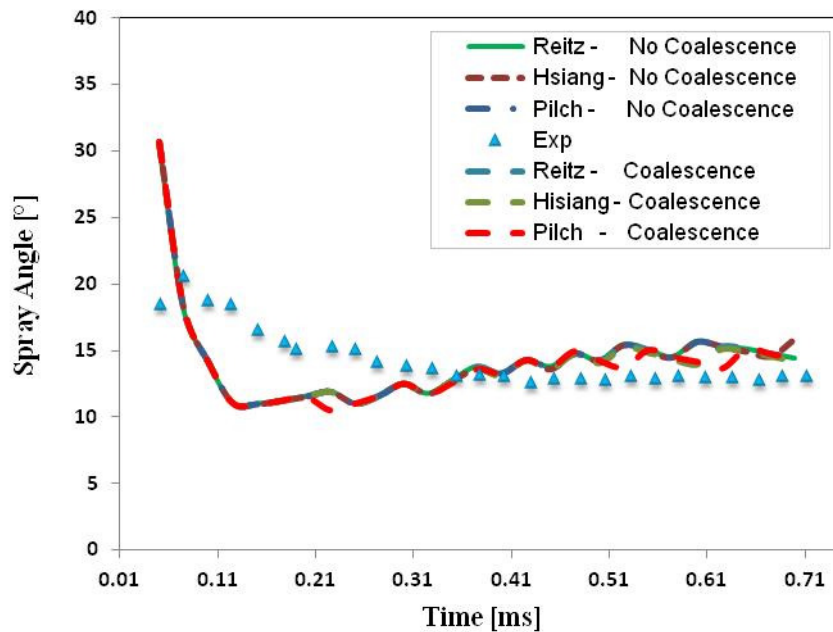


Figure 4-35: Spray spreading angle with and without coalescence for different break-up models (N_2 ; $P_{inj} = 80$ MPa; $P_{cha} = 2$ MPa).

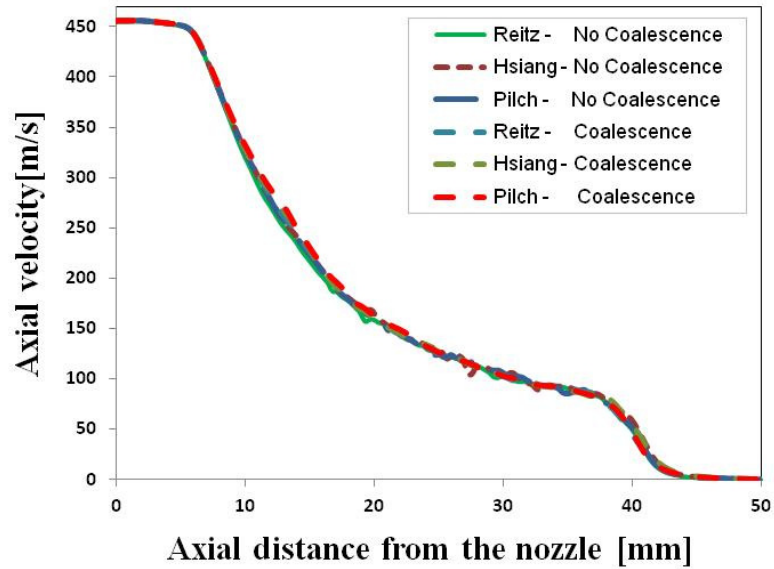


Figure 4-36: Axial velocity with and without coalescence for different break-up models (N_2 ; $P_{inj} = 80$ MPa; $P_{cha} = 2$ MPa).

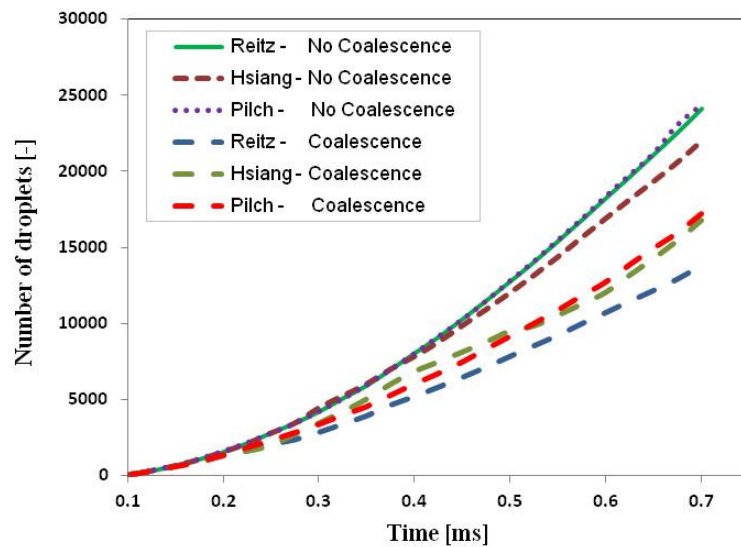


Figure 4-37: Number of droplets with and without coalescence for different break-up models (N_2 ; $P_{inj} = 80$ MPa; $P_{cha} = 2$ MPa).

However, as can be seen in Figure 4-37, the change in the number of droplets is significant, as it should be. Droplet coalescence process naturally reduces the number of droplets, as drops combine to create a single one. To reduce the complexity, no additional coalescence model is used in other calculations.

4.3.10 Injection pressure, chamber pressure and fuels

After these studies, the sub-models and parameters are fitted. The different possible values of injection and chamber pressures, as well as the gas present at the chamber are investigated in this section. The computational cases are described in Table 4-1, at the beginning of this section.

From Figure 4-38 to Figure 4-43, it can be seen that the ELSA model reproduces quite accurately the experimental results at $P_{inj} = 40$, and 80 MPa. In the case of $P_{inj} = 180$ MPa, the results are not good when the pressure at the chamber is below a certain threshold. For instance in Figure 5.42 and Figure 4-43, and using a constant injection pressure, if $P_{cha} = 5$ MPa, the results are accurate (better for N_2), whereas $P_{cha} = 2$ MPa are not. Pinzello, 2008 [13] also found a similar trend for the high injection pressure using a Lagrangian approach. Obviously, it is needed to improve the model here, especially when the Diesel engine spray can go up to 200 MPa.

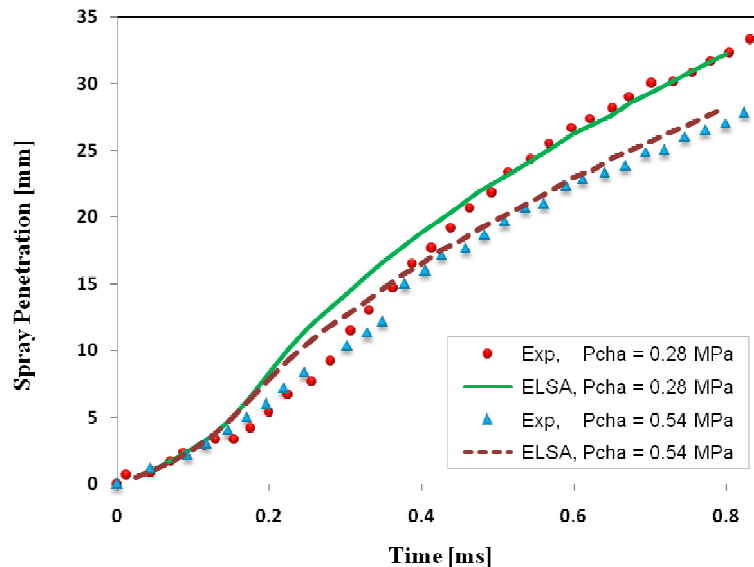


Figure 4-38: Spray penetration with different chamber pressure of 0.28 MPa vs. 0.54 MPa, and density of 22 kg/m^3 and 37 kg/m^3 respectively (SF_6 ; $P_{inj} = 40 \text{ MPa}$).

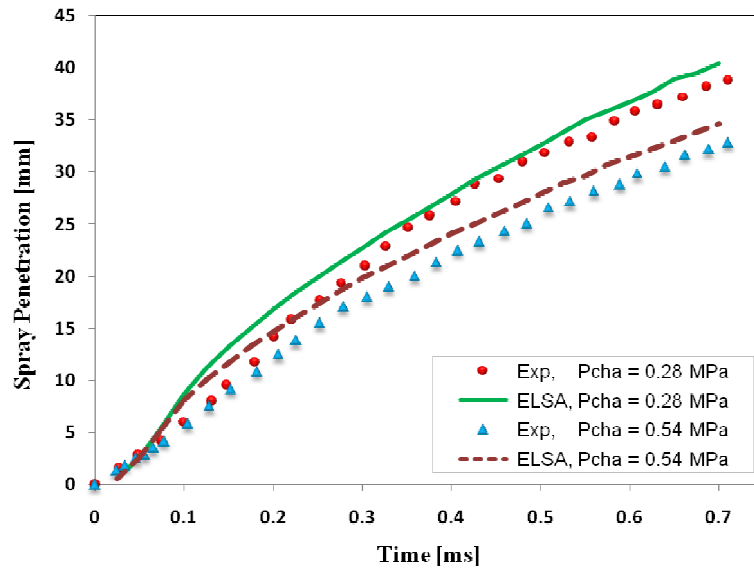


Figure 4-39: Spray penetration with different chamber pressure of 0.28 MPa vs. 0.54 MPa, and density of 22 k/m³ and 37 kg/m³ respectively (SF₆; $P_{inj} = 80$ MPa).

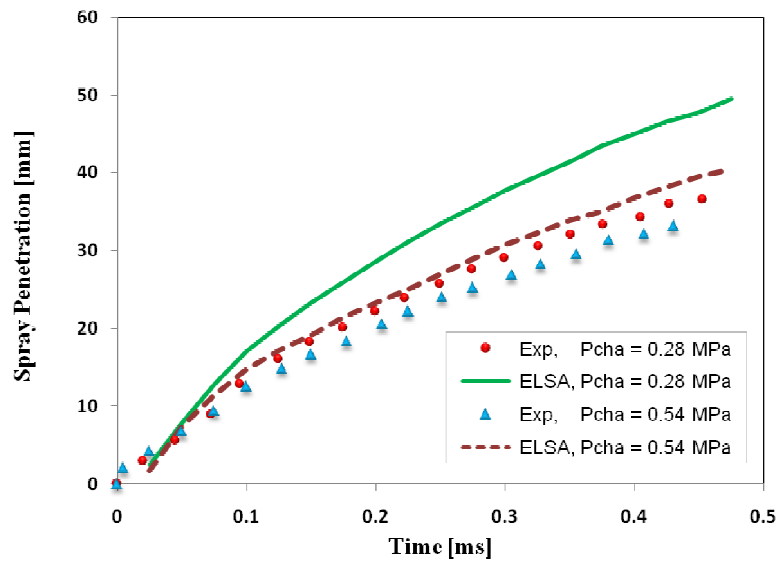


Figure 4-40: Spray penetration with different chamber pressure of 0.28 MPa vs. 0.54 MPa, and density of 22 k/m³ and 37 kg/m³ respectively (SF₆; $P_{inj} = 180$ MPa).

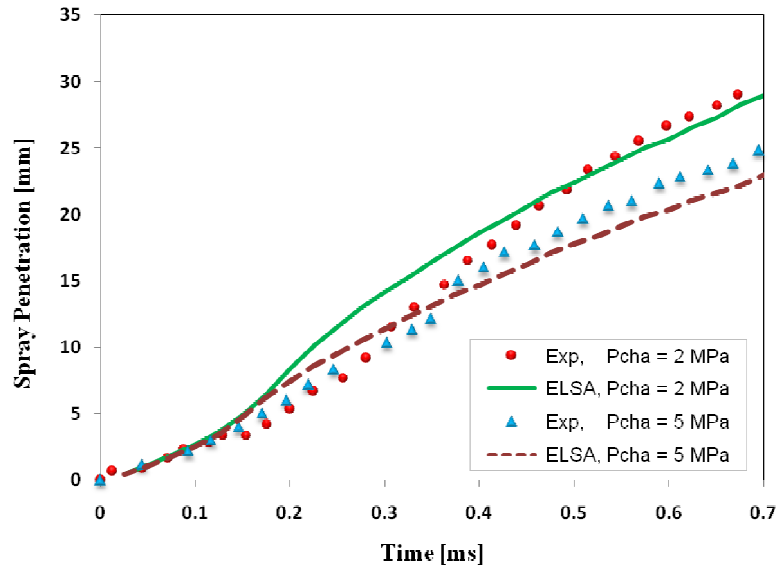


Figure 4-41: Spray penetration with different chamber pressure of 2 MPa vs. 5 MPa, and density of 22 kg/m³ and 37 kg/m³ respectively (N_2 ; $P_{inj} = 40$ MPa).

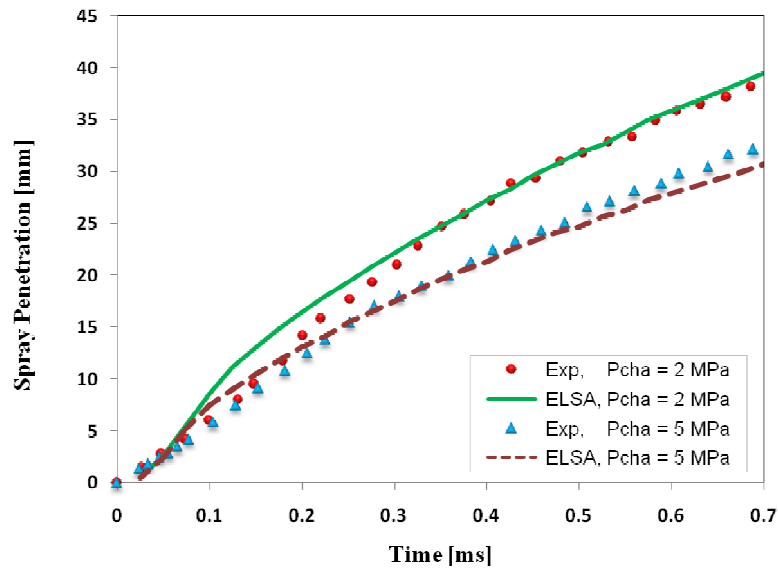


Figure 4-42: Spray penetration with different chamber pressure of 2 MPa vs. 5 MPa, and density of 22 kg/m³ and 37 kg/m³ respectively (N_2 ; $P_{inj} = 80$ MPa).

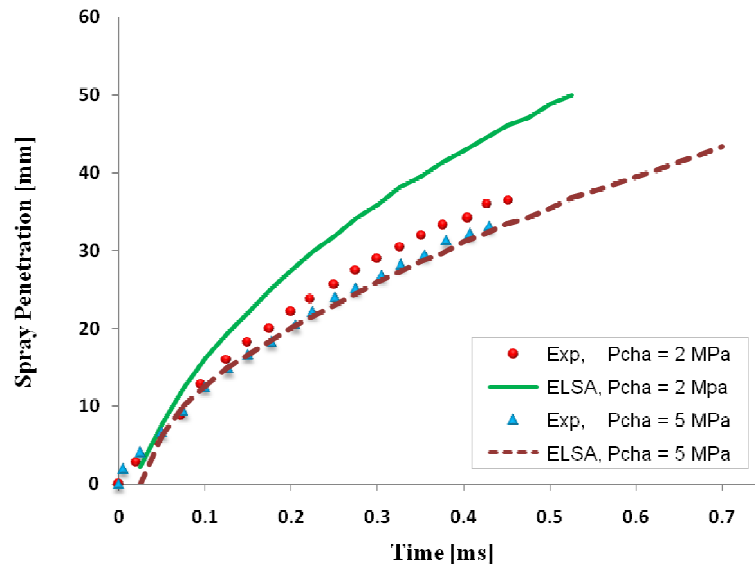


Figure 4-43: Spray penetration with different chamber pressure of 2 MPa vs. 5 MPa, and density of 22 kg/m^3 and 37 kg/m^3 respectively (N_2 ; $P_{inj} = 180 \text{ MPa}$).

4.3.11 Lagrangian vs. ELSA models

To highlight some of the important differences between Lagrangian and ELSA models, the averaged SMD diameter of both methods is shown in Figure 4-44. As the Lagrangian method assumed that the initial drop is equivalent to the nozzle size, which in this case is around $140 \mu\text{m}$, the SMD value before 0.4 ms is almost useless. Both methods converge after 0.6ms. Obviously, in ELSA model there is no droplet at the very beginning, when all the spray is close to the nozzle tip. Please note also that both methods converge to the same SMD, although they use a very different approach to the primary break-up.

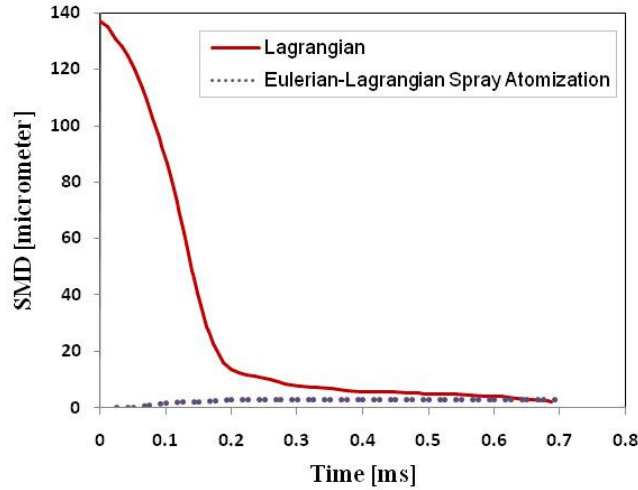


Figure 4-44: Comparison of SMD between the Lagrangian and ELSA models (N_2 ; $P_{inj} = 80 \text{ MPa}$; $P_{cha} = 2 \text{ MPa}$).

4.3.12 The 2D/3D meshes dependence.

As is said, the mesh dependency on the quasi-2D wedge domain has been thoughtful studied in some of our works (Hoyas et al., 2011 [1], [2], and [3]). In this section, we compare the 2D results with those obtained using a full 3D mesh. The number of cells on the radial direction remains the same, whereas it is a little bit decreased in the axial direction. Table 4-12 shows the mesh parameters using in these two cases and the CPU time needed for each simulation.

Table 4-12: Mesh information and CPU time between 2D and 3D mesh.

Mesh	Total cells	Total vertices	Transient time	Number of processors	CPU time (h)
2D	12000	24381	0.7 ms	12	5
3D	259200	268327	0.7 ms	12	114

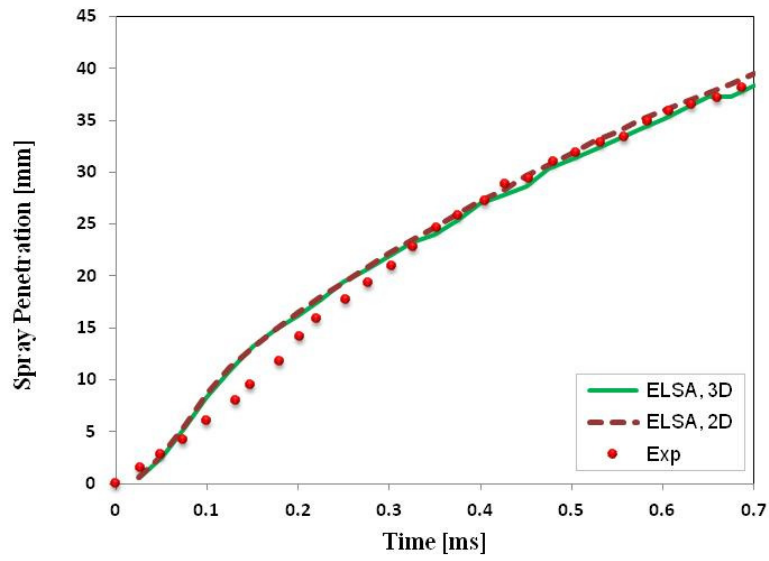


Figure 4-45: Spray penetration of 3D and 2D mesh (N_2 ; $P_{inj} = 80$ MPa; $P_{cha} = 2$ MPa).

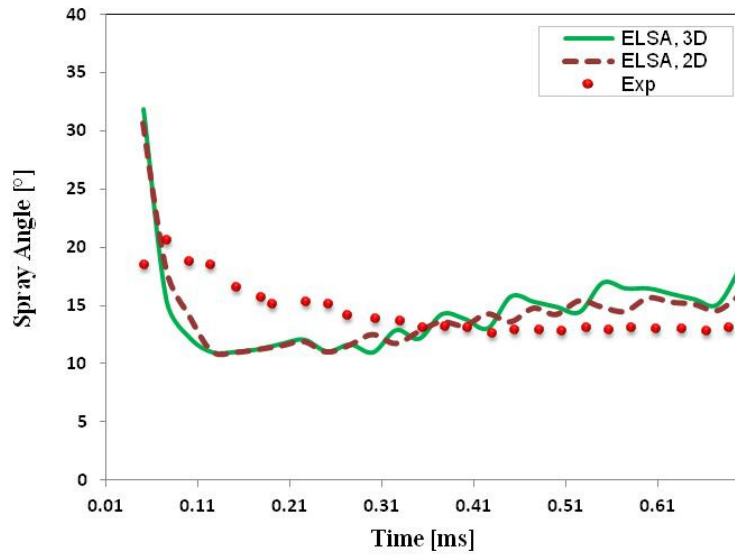


Figure 4-46: Spray cone angle of 3D and 2D mesh (N_2 ; $P_{inj} = 80$ MPa; $P_{cha} = 2$ MPa).

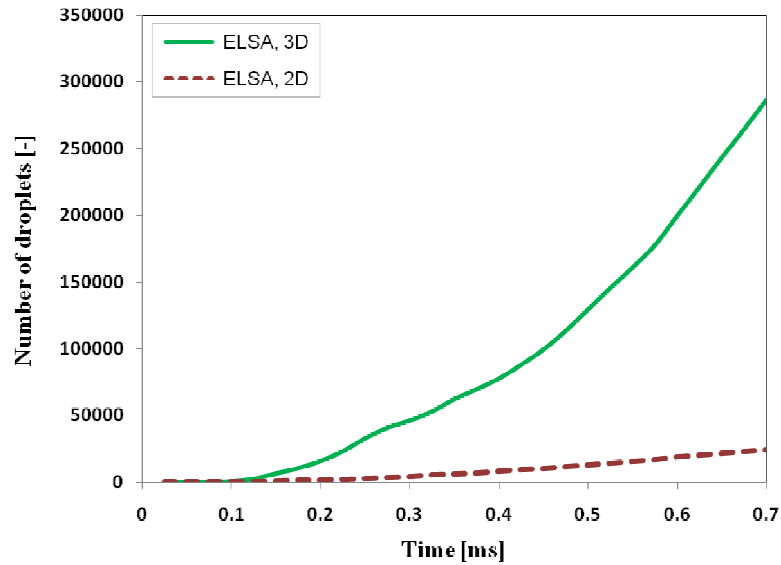


Figure 4-47: Number of droplets of 3D and 2D mesh (N_2 ; $P_{inj} = 80 \text{ MPa}$; $P_{cha} = 2 \text{ MPa}$).

The numerical results show a very good agreement between them and with the experimental results, as is shown in Figure 4-45 and Figure 4-46. From these plots, it is clear that there is no appreciable difference when changing from 2D to 3D for the spray penetration and the spray cone angle. This is not true, of course, for the droplets. Figure 4-32 presents the heavy effect of grid size on the number of droplets.

4.4 Evaporating Diesel sprays simulation

The evaporation of the spray droplets plays a crucial role in its combustion processes. Additional models of the heat-up and evaporation are taken into account in this section, in order to be able to work under evaporative conditions. The vapor region expands rapidly from the tip of the liquid fuel toward the chamber walls. The vapor created for the evaporating droplets is used as a source term for the vapor void fraction transport equation in the Eulerian formulation [11]. For the interested reader, the numerical theories of these models are detailed in [19], [20], [21], [22] and references therein.

Chapter 4 – ELSA model validation

In this thesis a couple of fuels were benchmarked under evaporative conditions, but only results about DF2 and n-dodecane are shown, as these are two of the most commonly used fuel for experiments. DF2 is based on a purely commercial fuel specification (ASTM D 975 Grade No. 2-D) [23]. The boiling temperature of DF2 is at 461 – 617 K. The main properties of both fuels are detailed in Table 4-13. A complete description of them can be found at the appendix G – “Fuel chemical and physical properties”, and appendix H – “DF2 properties”.

Table 4-13: Fuel chemical and physical properties.

Fuel	Formula	Density	Viscosity	Molar mass	Boiling point	Melting point
		[kg/m ³]	[kg/ms at 20°C]	[kg/kmol]	[K]	[K]
n-dodecane	C ₁₂ H ₂₆	746	1.35e ⁻³	170.34	489.35	263.55
DF2	C ₃ to C ₅	846	3e ⁻³	≈200	--	--

All the simulations made under evaporative conditions, in order to model the similar operating condition, the gas at the chamber is based on the recommended common mixing ratio proposed by Engine Combustion Network (ECN) group for the experimental “spray A” standard under non-reacting condition. The chamber gas components and mixing ratio is fixed to ensure the same inert chamber conditions applied. The percentages of volume of each component are as follows: 0% O₂, 89.71% N₂, 6.52% CO₂, and 3.77% H₂O. About the liquid length, it has been defined using the liquid volume fraction, as usual (Figure 4-11).

In the following pages, we will present the results about the validation of ELSA model in different injectors, characterized experimentally at different conditions at Sandia National Laboratory, CMT and ECN. In most of the case, the results were satisfactory, showing the possibilities of ELSA for modeling evaporative sprays.

4.4.1 Sandia experimental data

The first study that we want to present use the data coming from Spray A database obtained at Sandía. Details of these experiments can be found at Pickett et al., 2011 [24] and in the ECN website [25].

Table 4-14: Computational cases corresponding to Spray A from SANDIA.

Case	N_{parcel}	Fuel	P_{inj} [MPa]	T_{inj} [K]	ρ_{inj} [kg/m ³]	Cha. Gas	P_{cha} [MPa]	T_{cha} [K]
Ev01	1	n-dodecane	150	363	718	*0%O ₂	6	900
Ev02	10	n-dodecane	150	363	718	*0%O ₂	6	900
Ev03	20	n-dodecane	150	363	718	*0%O ₂	6	900
Ev04	200	n-dodecane	150	363	718	*0%O ₂	6	900
Ev05	1	n-dodecane	150	363	699	*0%O ₂	6	900
Ev06	1	n-dodecane	100	363	699	*0%O ₂	6	900
Ev07	1	n-dodecane	50	363	699	*0%O ₂	6	900

4.4.1.1 Number of parcels created

Let us present this case with the study of the effect of N_{parcel} on the spray behavior under evaporative conditions.

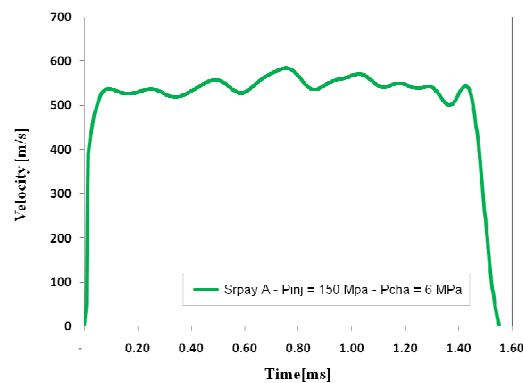


Figure 4-48: Velocity profile of Spray A case (n-dodecane, $P_{inj} = 150$ MPa, $P_{cha} = 6$ MPa).

Chapter 4 – ELSA model validation

The velocity profile at the inlet is given by Figure 4-48. Figure 4-49 shows the difference on liquid–vapor penetration for different *Nparcel* numbers. When these values are as low as 1, 10, 20, there is a small change in both vapor and liquid tip penetration. However, if *Nparcel* is increased until 200, the results are completely inaccurate, due to the fact many droplets are needed to form a single parcel, so the penetration grows very slowly. Similar results are obtained for the spray cone angle and droplets number.

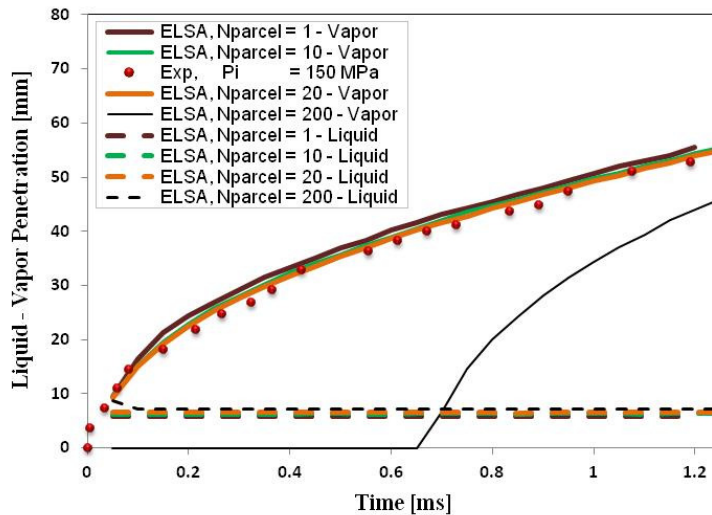


Figure 4-49: Liquid, vapor penetration with different *Nparcel* number of 1, 10, 20, and 200 respectively ($P_{inj} = 150 \text{ MPa}$; $P_{cha} = 6 \text{ MPa}$).

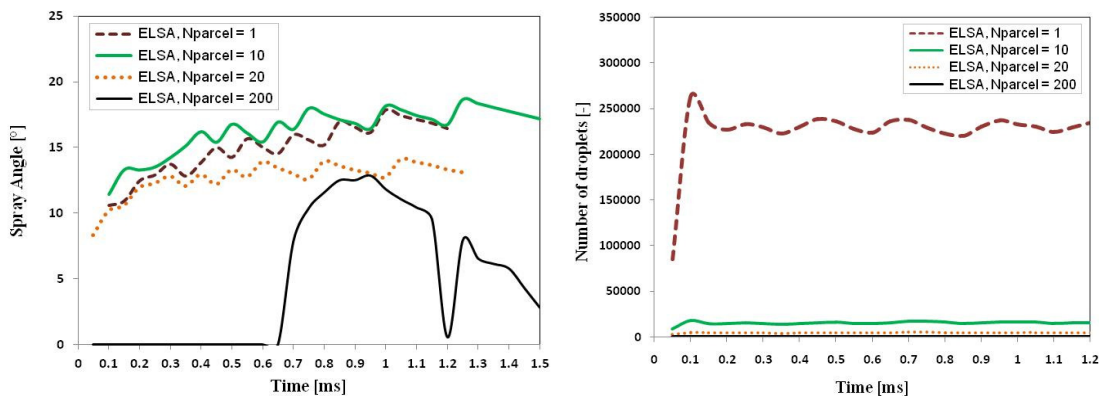


Figure 4-50: Spray spreading angle and number of droplets with different *Nparcel* number of 1, 10, 20, and 200 respectively ($P_{inj} = 150 \text{ MPa}$; $P_{cha} = 6 \text{ MPa}$).

4.4.1.2 Injection pressure

The agreement of vapor penetration, which is shown in Figure 4-51, is encouraging. Although there no exits experimental available data, in Figure 4-52, centerline axial velocity is reasonable.

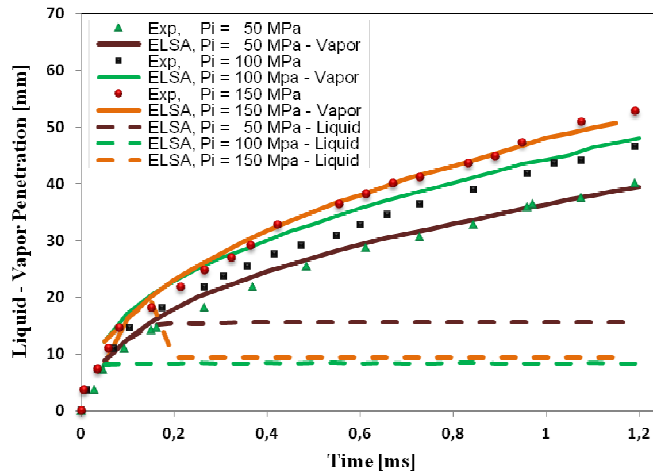


Figure 4-51: Liquid and vapor penetration for different injection pressure levels (50, 100, and 150 MPa).

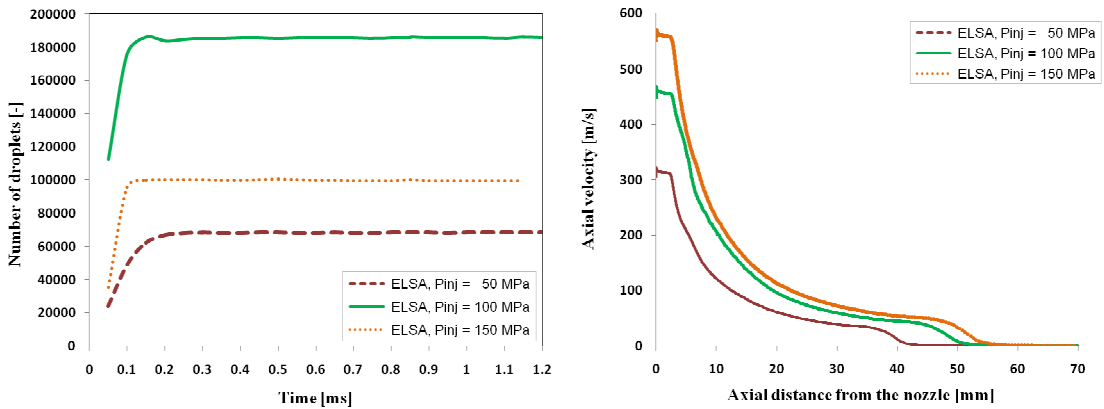


Figure 4-52: Number of droplets and axial velocity for different injection pressure levels (50, 100, and 150 MPa).

It is noted that the total number of generated droplets increases when the injection pressure increases as tabulated in Table 4-15. However, number of active droplets in case $P_{inj} = 150$ MPa is smaller than $P_{inj} = 100$ MPa

Chapter 4 – ELSA model validation

presented in Table 4-15 and Figure 4-52. Because at a certain level, the high injection pressure results high velocity, strong turbulence and smaller droplets size, those droplets are easily evaporated. Hence, the remained droplets are much smaller.

Table 4-15: Total generated droplets and remained droplets for different injection pressure levels (50, 100, and 150 MPa).

Case	P_{inj} (MPa)	Time (ms)	Total generated droplets	Active (remained) droplets
Ev05	150	1.1	13,963,044	99,686
Ev06	100	1.1	5,054,746	185,650
Ev07	50	1.1	1,177,383	68,399

4.4.1.3 Mixture fraction

Another valuable parameter is the mixture fraction, which is an important feature of the spray, as it provides information about the mixture formation process. Figure 4-53 and Figure 4-54 show the centerline mixture fraction and the mixture fraction value at different cross section. In both cases, the results can be only classified as reasonably good.

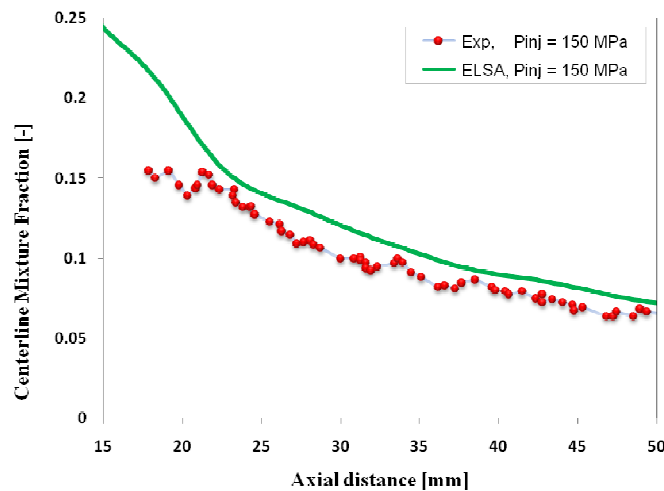


Figure 4-53: Centerline Mixture Fraction ($P_{inj} = 150$ MPa; $\rho_{inj} = 718$ kg/m³; $P_{cha} = 6$ MPa).

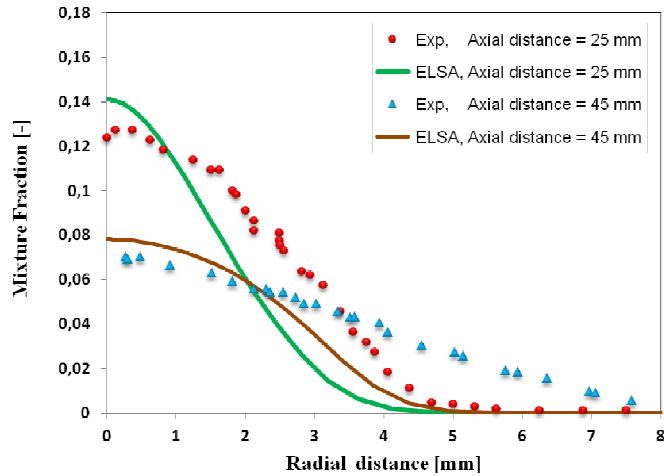


Figure 4-54: Mixture Fraction at the cross sections 25mm, and 45 mm along the spray axis ($P_{inj} = 150$ MPa; $\rho_{inj} = 718$ kg/m³; $P_{cha} = 6$ MPa).

4.4.2 Experimental data from CMT

Another set of experiments used for validation comes from our CMT institute. Some of these experiments were used for validation in the PhD thesis of Pinzello, 2008 [13] using a Lagrangian framework and with an injection pressure $P_{inj} = 70$ MPa.

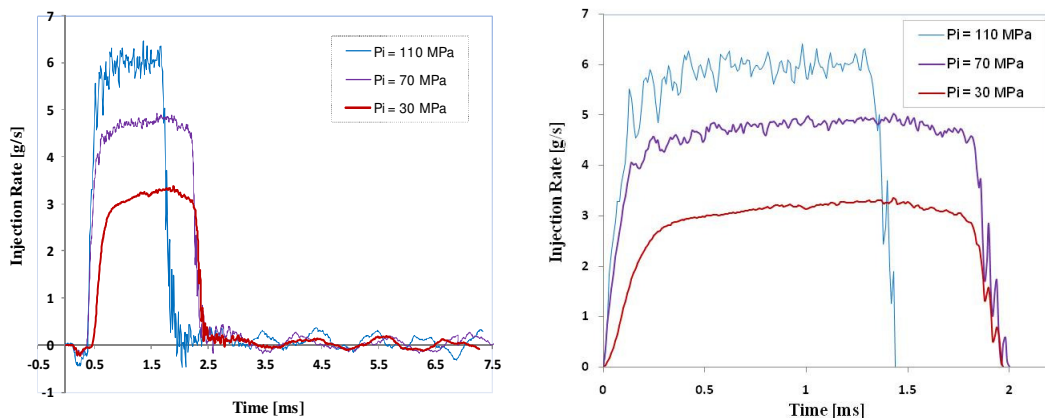


Figure 4-55: Injection rate measure (left) and averaged injection rate of n-dodecane at different P_{inj} and $P_{cha} = 7$ MPa. The disturbances at the plateau of the averaged injection rate seem to be an effect of reflection waves at the nozzle.

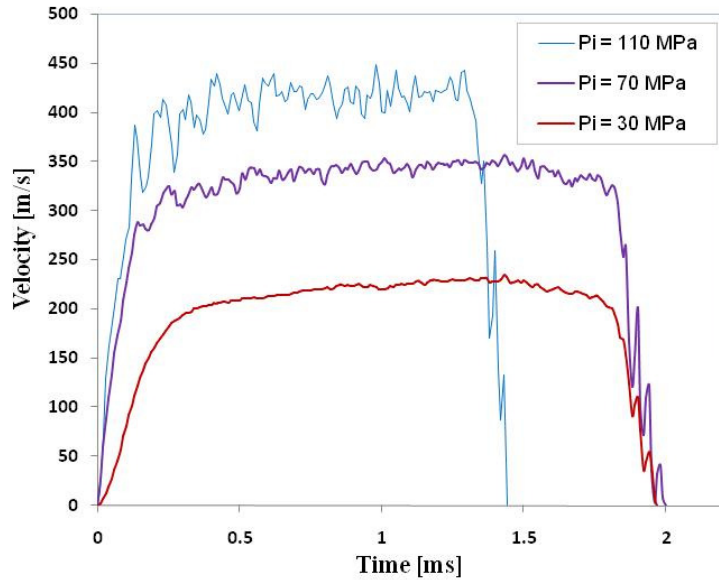


Figure 4-56: Ensemble averaged velocity profile of n-dodecane at different P_{inj} and $P_{cha} = 7 \text{ MPa}$. This profile was obtained from the injection rate.

Figure 4-55 and Figure 4-56 show the ensemble averaged injection rate and velocity profile, at different P_{inj} . The cases simulated are summarized in Table 4-16.

Table 4-16: Computational cases for different injection pressure levels.

Case	Fuel	P_{inj}	T_{inj}	ρ_{inj}	Gas	P_{cha}	T_{cha}	ρ_{cha}
		[MPa]	[K]	[kg/m ³]		[MPa]	[K]	[kg/m ³]
Ev08	n-dodecane	30	343	746	0%O ₂ *	6.93	885	26.40
Ev09		70						
Ev10		110						

*Non-reacting: 0% O₂, 89.71% N₂, 6.52% CO₂, and 3.77% H₂O

The effects of the injection pressure on the spray formation are examined by comparing them with the liquid spray penetration at the injection pressure of 70 MPa, which are the only experimental data available.

It is observed that the liquid penetrations predicted by the ELSA model are generally in extremely good agreement for this test case once it reaches the averaged peak. The offset in the liquid penetration occurred before 0.3ms dues to the effect of a variance of experimental injection rate measured by

Chapter 4 – ELSA model validation

sensor and the fitting at the velocity profile. Vapor and liquid penetration also show a very reasonable behavior, as it is shown in Figure 4-57.

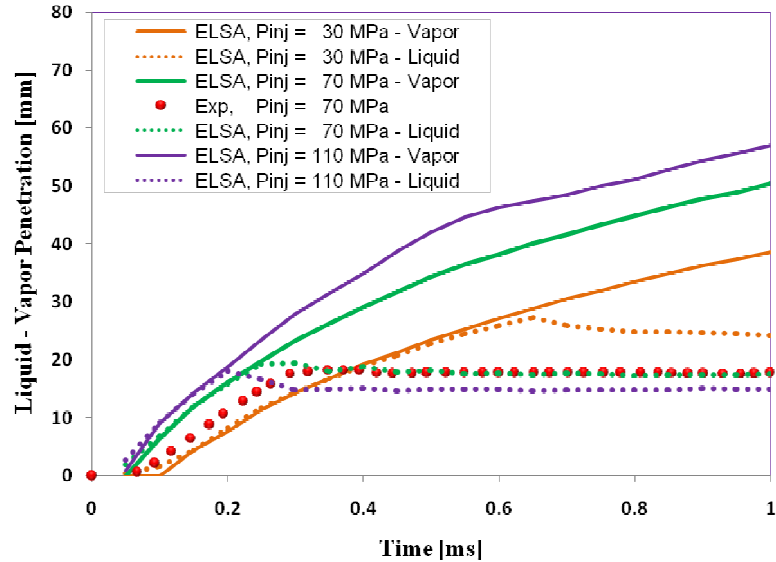


Figure 4-57: Liquid and vapor penetration for different injection pressure levels (30, 70, and 110 MPa).

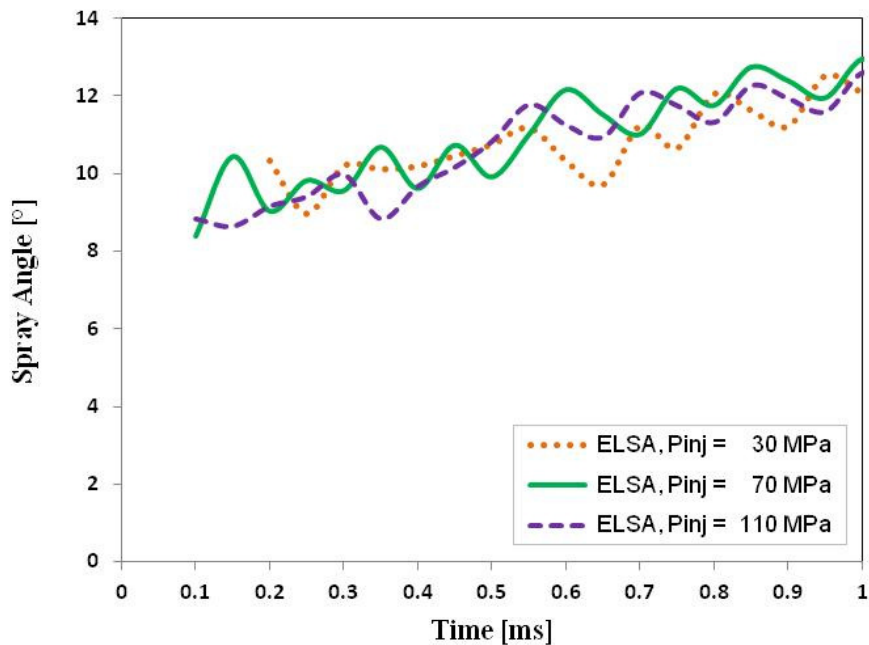


Figure 4-58: Spray spreading angle for different injection pressure levels.

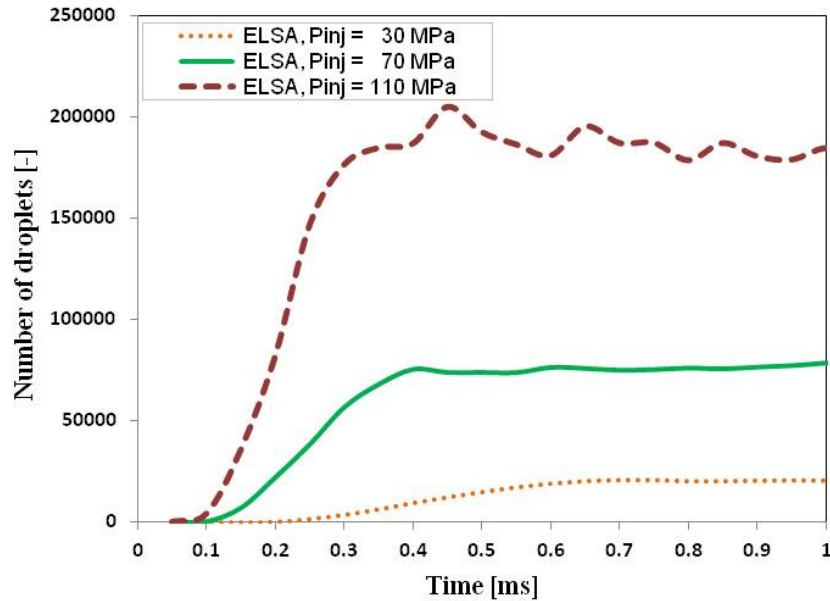


Figure 4-59: Number of droplets for different injection pressure levels.

Figure 4-58 shows the spray cone angle. The three pressures show a similar behavior. About the droplets, Figure 4-59, the effects of pressure is evidently captured, as more droplets are generated once the injection pressure is increased.

4.4.3 Spray A experiments performed at CMT

The “spray A” experiment series performed by CMT, Payri et al., 2012 [26] were also used for validation. The injector is Bosch type and the series number # 210675 see more details in [27]. In this study, we want to focus not only in pressures, but also in temperatures, both at the nozzle and the chamber. In all cases, the injection density is kept approximately $\rho_{inj} = 718$ kg/m³, for the first three cases where the injection temperature slightly change, there is a small different in the injection density. The set-up of these cases is listed in Table 4-17.

Table 4-17: Computational cases corresponding to Spray A from CMT.

Case	Fuel	P_{inj}	T_{inj}	Cha. Gas	P_{cha}	T_{cha}	ρ_{cha}
	n-dodecane	[MPa]	[K]		[MPa]	[K]	[kg/m ³]
Ev11	n-dodecane	180	343	0% O ₂ *	6	900	22.8
Ev12	n-dodecane	150	343	0% O ₂ *	6	900	22.8
Ev13	n-dodecane	100	343	0% O ₂ *	6	900	22.8
Ev14	n-dodecane	50	343	0% O ₂ *	6	900	22.8
Ev15	n-dodecane	100	288	0% O ₂ *	6	900	22.8
Ev16	n-dodecane	100	319	0% O ₂ *	6	900	22.8
Ev17	n-dodecane	50	343	0% O ₂ *	6	900	22.8
Ev18	n-dodecane	50	343	0% O ₂ *	2	900	7.6
Ev19	n-dodecane	50	343	0% O ₂ *	1.85	820	7.6

*Non-reacting: 0%O₂, 89.71% N₂, 6.52% CO₂, and 3.77% H₂O

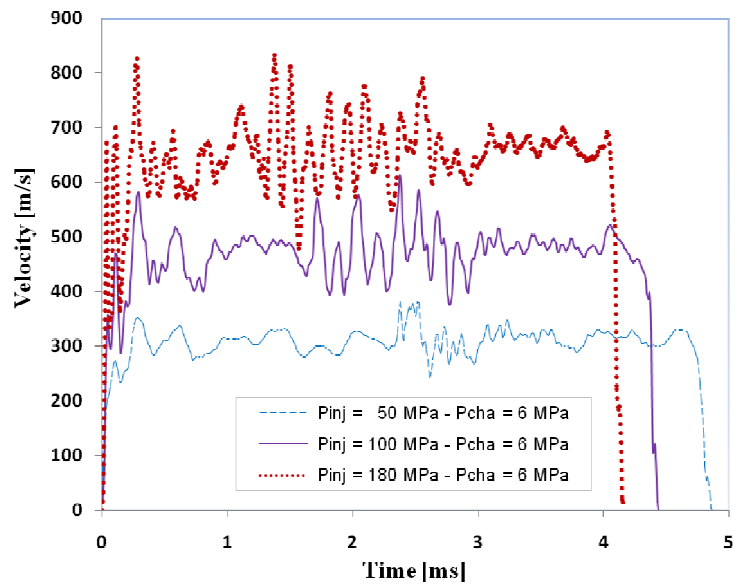


Figure 4-60: Velocity profile of n-dodecane at different injection pressure and fixed chamber pressure equal to 6MPa.

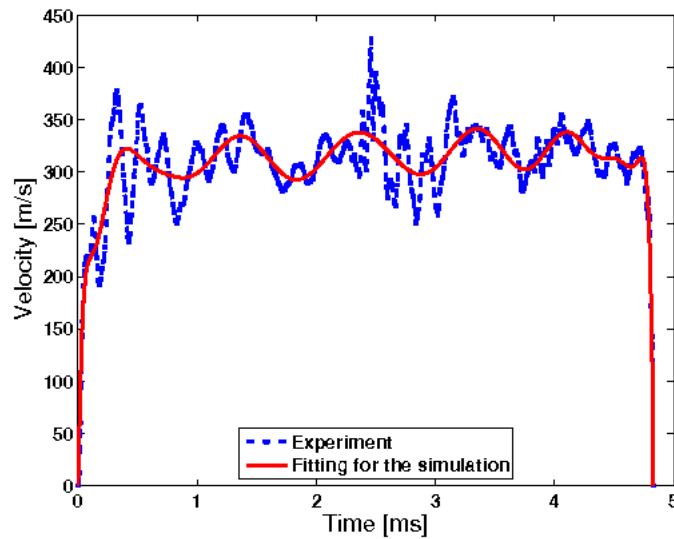


Figure 4-61: Velocity profile directly derived from experimental mass flow rate vs. the special adaptation for the ELSA modeling ($P_{inj} = 50$ MPa, $P_{cha} = 2$ MPa).

Figure 4-60 shows the velocity profile of three different injection pressures, which were derived directly from the mass flow rate and momentum flux. Unfortunately, the gradients of this velocity profile were high, and the simulation explodes. This is not only a problem of ELSA model, but a general one. Thus, a fitting curve as the one plotted in Figure 4-61 ($P_{inj} = 50$ MPa, $P_{cha} = 2$ MPa) has been used as inlet condition. The same procedure has been applied in the three curves of Figure 4-60.

4.4.3.1 Injection pressure

Firstly, we focus in the effects of moving P_{inj} . In Figure 4-62 and Figure 4-63, the vapor penetration and spray spreading angle were investigated with different injection pressure levels. Obviously, the agreement between the two numerical cases are reasonably and especially the experimental data is really good for $P_{inj} = 50$ MPa. Unfortunately, we do not have enough data to make an exact claim on the higher injection pressure $P_{inj} = 180$ MPa.

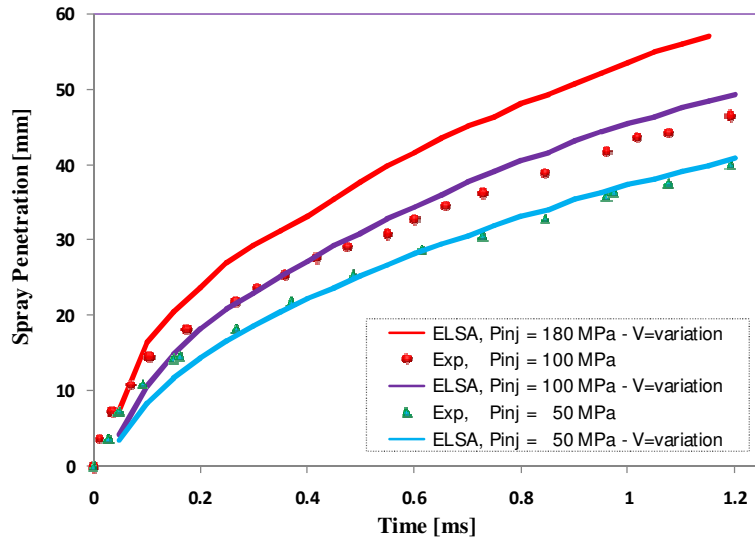


Figure 4-62: Liquid and vapor penetration at different injection pressure.

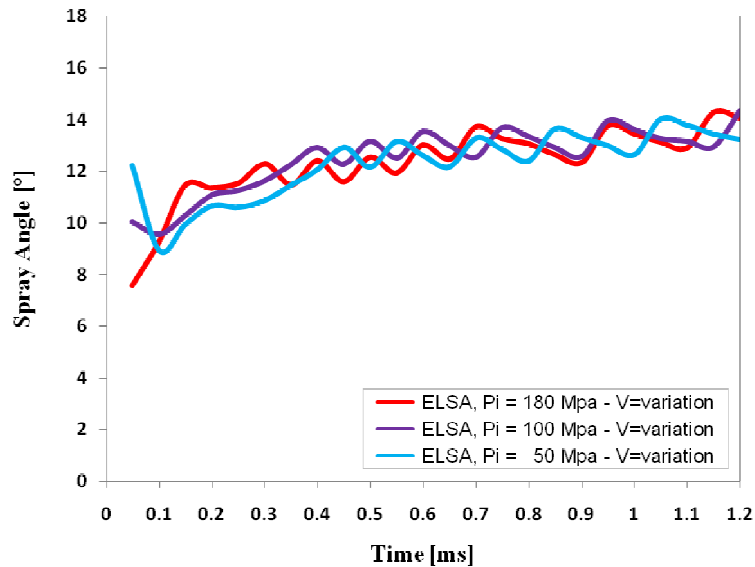


Figure 4-63: Spray spreading angle at different injection pressure.

The aforementioned cases were validated with the vapor penetration. Then, the following two cases taking $P_{inj} = 50$, and 100 MPa are compared with the liquid penetration and spray spreading angle. These results are shown in Figure 4-64 and Figure 4-65. In these cases, both the liquid penetration and spray cone angle are correctly simulated. Figure 4-66 again confirmed effects of the injection rate on the number of droplets.

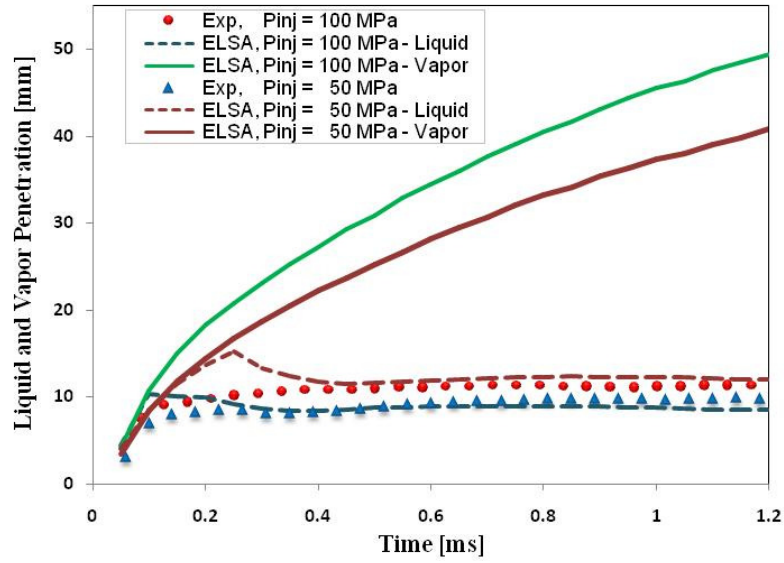


Figure 4-64: Liquid and vapor penetration at different injection pressures.

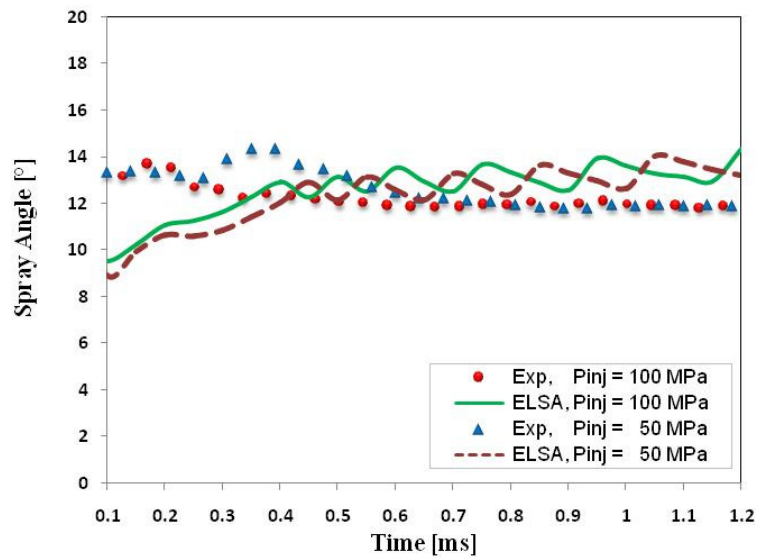


Figure 4-65: Spray cone angle at different injection pressures.

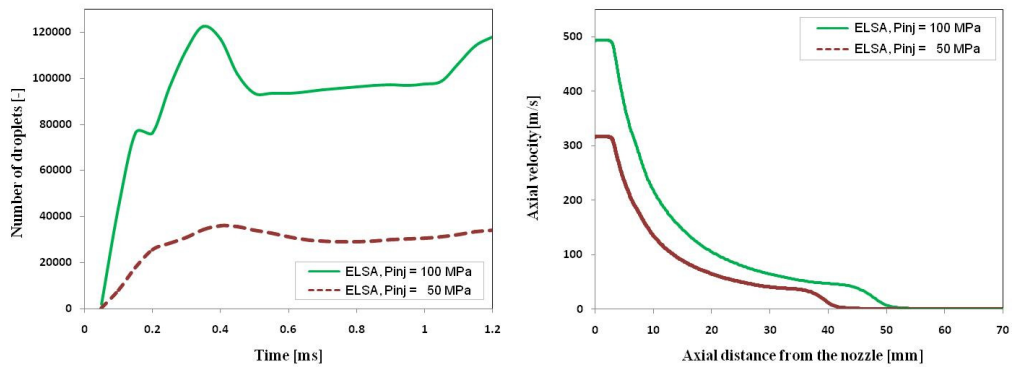


Figure 4-66: Number of droplets and axial velocity at different injection pressures.

4.4.3.2 Injection temperature

The effects of liquid temperature from the injection point are investigated in the following case. The liquid penetration obtained by ELSA model is compared with the experimental data available. The results are presented Figure 4-67. It agrees quite well, but the changes in the numerical model are smaller than in the experimental data. In these cases, it seems that a lower temperature at the nozzle produces more droplets.

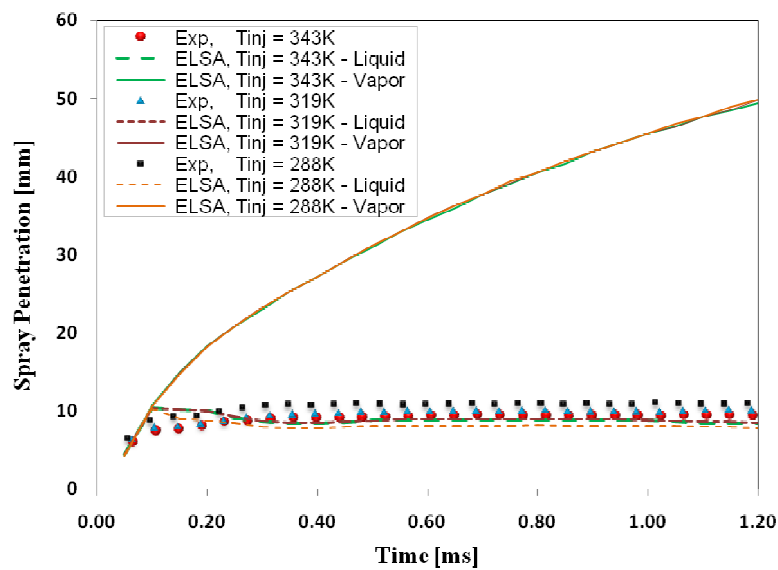


Figure 4-67: Liquid and vapor penetration at different injection temperature.

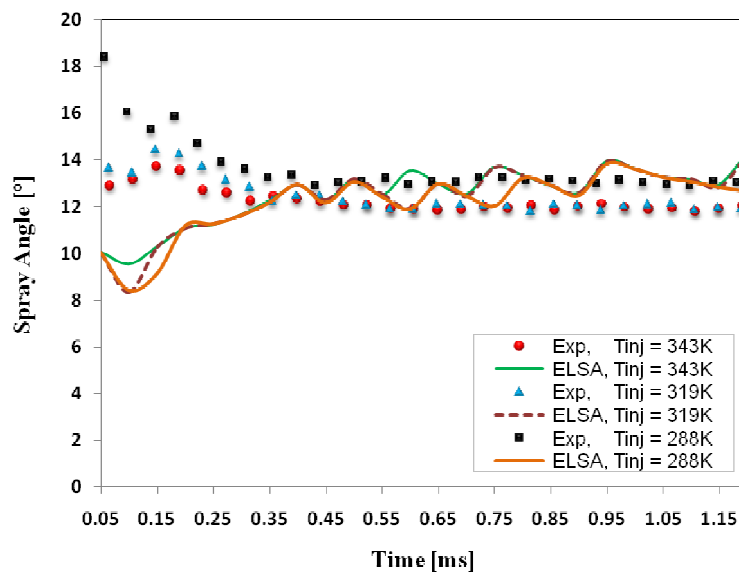


Figure 4-68: Spray spreading angle at different injection temperature.

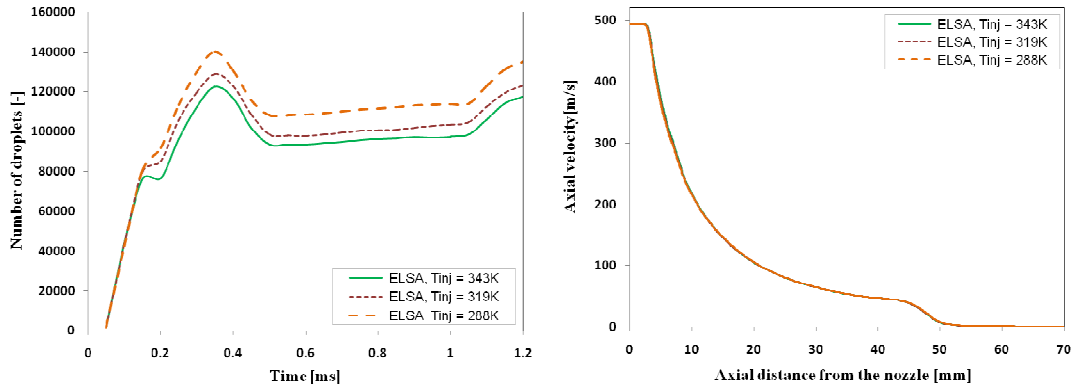


Figure 4-69: Number of droplets and axial velocity at different injection temperature.

4.4.3.3 Chamber pressure and density

The following parameter is the density at the chamber, caused by changes in pressure. Figure 4-70 and Figure 4-71 show the agreement with experimental data. The model recovers the spray penetration reasonably well, but the agreement is not so good in the case of the cone angle. About the droplets, Figure 4-72 shows that a lower chamber density retains more active droplets and with a higher velocity. Because the SMD of the case with chamber density equals to 22.8 kg/m^3 are smaller than the other case after 0.15ms, thus the droplets are vaporized at high rate.

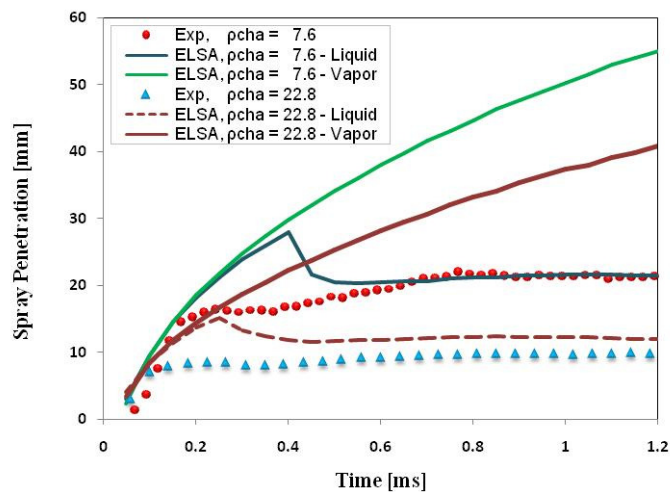


Figure 4-70: Liquid and vapor penetration at different chamber density of $22.8, 7.6 \text{ kg/m}^3$ and pressure of 6, 2 MPa respectively (Ev17 vs. Ev18).

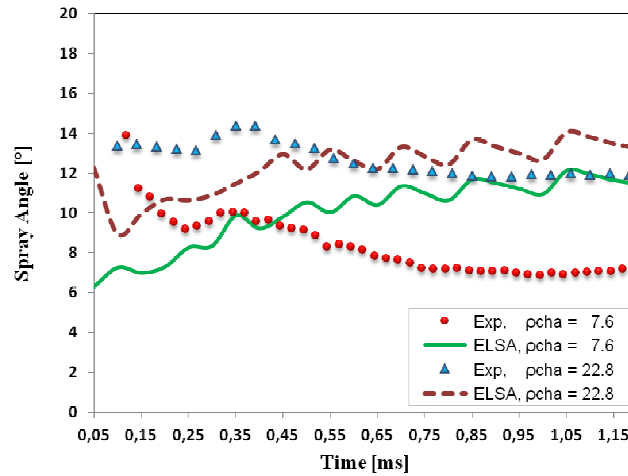


Figure 4-71: Spray cone angle at different chamber density of 22.8, 7.6 kg/m^3 and pressure of 6, 2 MPa respectively (Ev17 vs. Ev18).

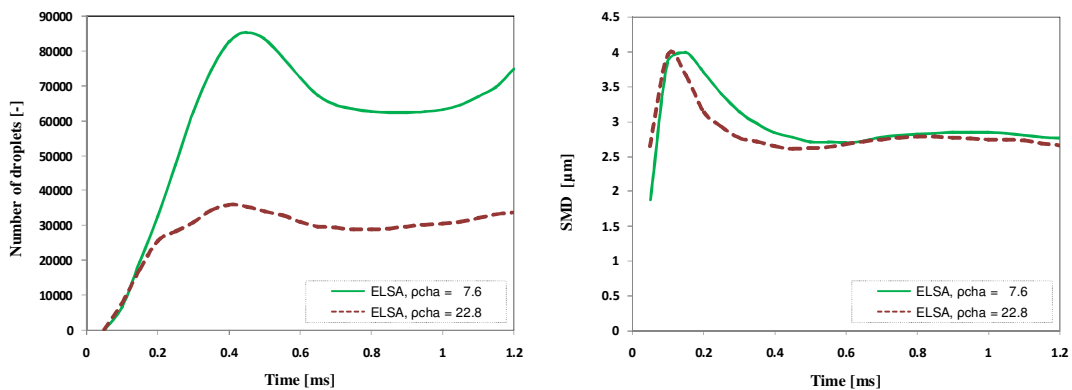


Figure 4-72: Number of active droplets and SMD at different chamber density of 22.8, 7.6 kg/m^3 and pressure of 6, 2 MPa respectively (Ev17 vs. Ev18).

4.4.3.4 Chamber temperature

The results moving the chamber temperature are quite similar as the previous one. The penetration is accurately represented (Figure 4-73), but the spray cone angle not (Figure 4-74). In Figure 4-75, a lower chamber temperature makes that droplets remain at the chamber, whereas the droplets are vaporized easily when the temperature is higher.

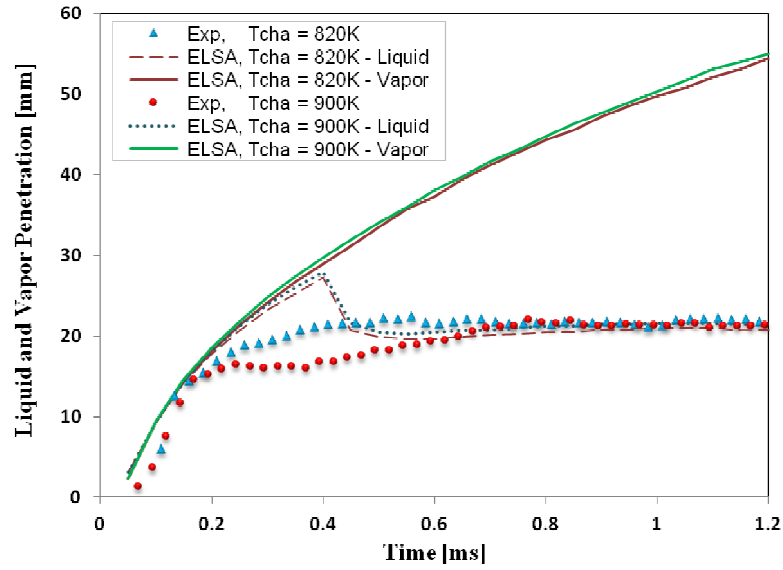


Figure 4-73: Liquid and vapor penetration at different chamber temperature.

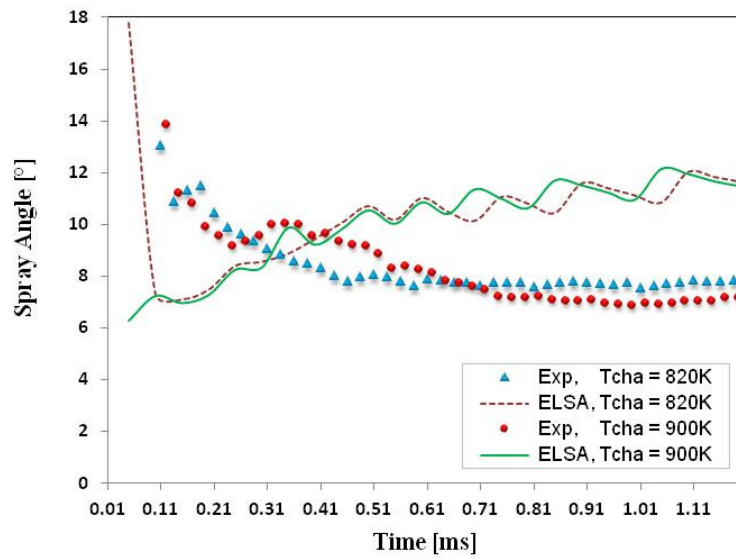


Figure 4-74: Spray spreading angle at different chamber temperature.

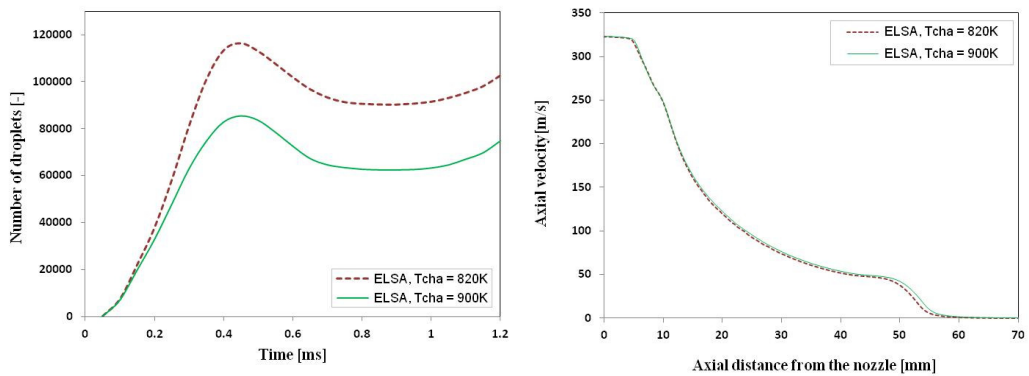


Figure 4-75: Number of active droplets and axial velocity at different chamber temperature.

REFERENCES

- [1] Hoyas, S.; Pastor, J.M.; Khuong-Anh, D.; Mompó-Laborda, J.M.; Ravet, F. *Evaluation of the Eulerian-Lagrangian Spray Atomization (ELSA) in spray simulations*. International Journal of Vehicle Systems Modelling and Testing, Vol. 6, Nos. 3/4, pp. 187-201, **2011**.
- [2] Hoyas, S.; Pastor, J.M.; Khuong-Anh, D.; Mompó-Laborda, J.M.; Ravet, F. *Application and Evaluation of the Eulerian-Lagrangian Spray Atomization (ELSA) Model on CFD Diesel Spray Simulations*. SAE Technical Paper, Vol. SAE-2011-37-0029(0), **2011**.
- [3] Hoyas, S.; Gil, A.; Margot, X.; Khuong-Anh, D.; Ravet, F. *Evaluation of the Eulerian-Lagrangian Spray Atomization (ELSA) in spray simulation: 2D cases*. Mathematical and Computer Modelling, In Press, **2011**.
- [4] Hoyas, S.; Gil, A.; Fajardo, P.; Khuong-Anh, D.; Ravet, F. (2012). *Evaluation and validation of ELSA model in Diesel sprays: 3D cavitating nozzles case*. International Conference on Liquid Atomization and Spray Systems, Germany, Sept **2012**.
- [5] Desantes, J.M.; Hoyas, S.; Gil, A.; Khuong-Anh, D.; Ravet, F. *A Recent Eulerian-Lagrangian CFD Methodology For Modelling Direct Injection Diesel Sprays*. The International Conference On Advances In Computational Mechanics (ACOME), August 14-16, 2012, Ho Chi Minh City, Vietnam, **2012**.
- [6] Issa, R.I. *Solution of the Implicit Discretized Fluid Flow Equations by Operator Splitting*, Mechanical Engineering Rep. FS-82-15, Imperial College, London, **1982**.
- [7] Issa, R.I. *Solution of the implicitly discretised fluid flow equations by operator-splitting*, J. Comp. Phys., Vol. 62, pp. 40-65, **1986**.
- [8] Sin, V.K.; Tong, T.Y. *Stagnation-Point Pressure Distribution and Wall Shear Stress: Numerical Simulation and Similarity Solution*, Proceedings of the World Congress on Engineering, Vol. II, ISBN: 978-988-18210-1-0, **2009**.
- [9] Reitz, R.D.; Diwakar, R. *Effect of drop breakup on fuel sprays*, SAE Technical Paper Series 860469, **1986**.
- [10] CD-Adapco, Star-CD version 4.16.002, *Methodology*, **2011**.
- [11] AVL Fire Product Description, *AVL FIRE Lagrangian multiphase*, Doc. No: 04-01-05010, AVL Advanced Simulation Technologies, **2009**.
- [12] De Chaisemartin S.; Laurent F.; Massot M.; Reveillon J. *Evaluation of Eulerian multi-fluid versus Lagrangian methods for ejection of polydisperse evaporating sprays by vortices*. Submitted Journal of Computational Physics, **2007**.

Chapter 4 – ELSA model validation

- [13] Pinzello, A. *Analysis of Fuel Sprays and Combustion Processes in Diesel Engines with a Combined Approach of CFD and Phenomenological Models*. PhD thesis, UPV, **2008**.
- [14] Margot, X.; Payri, R.; Gil, A.; Chavez, M.; Pinzello, A. *Combined CFD Phenomenological Approach to the Analysis of Diesel Sprays under Non-Evaporative Conditions*. SAE Technical Paper 2008-01-0962, **2008**.
- [15] Hawkes, E. *Model comparisons: n-heptane session (compared models and experiments of non-reacting n-heptane sprays performed in the Sandia constant volume chamber)*. Engine Combustion Network (ECN), ECN1 workshop, **2011**.
- [16] Kralj, C. *Numerical simulation of diesel spray processes*. PhD thesis, Imperial College, **1995**.
- [17] Salvador, F.J.; Ruiz, S.; Gimeno, J.; de la Morena, J. *Estimation of a suitable range for the Schmidt number in Diesel spray at high injection pressure through a theoretical derivation*. International Journal of Thermal Sciences, Vol. 50(9), pp. 1790-1798, **2011**.
- [18] Qian, J.; Law, C.K. Regimes of coalescence and separation in droplet collision. J. Fluid Mech., Vol. 331, pp. 59-80, **1997**.
- [19] Renksizbulut, M.; Yuen, M.C. *Numerical study of droplet evaporation in high temperature air stream*. J. Heat Transfer 105, pp. 384–388, **1983**.
- [20] Abou Al-Sood, M.M. *A numerical study of a droplet evaporating in a turbulent airflow*. Ph.D. Thesis, University of Manitoba, Canada, **2007**.
- [21] Abou Al-Sood, M.M.; Birouk, M. *A numerical study of the effect of turbulence on mass transfer from a single fuel droplet evaporating in a hot convective flow*. Int. J. Thermal Sci. 46, pp. 779–789, **2007**.
- [22] Abou Al-Sood, M.M.; Birouk, M. *Droplet heat and mass transfer in a turbulent airstream*. International Heat and Mass Transfer, Vol. 51, pp. 1313-1324, **2008**.
- [23] U.S. Department of Energy, Office of Energy Efficiency and Renewable Energy, Alternative Fuels Data Center. Available at: <http://www.afdc.energy.gov/afdc/fuels/properties.html>, last accessed by 25th June **2012**.
- [24] Pickett, L.M.; Manin, J.; Genzale, C.L.; Siebers, D.L.; Musculus, M.P.B.; Idicheria, C.A. *Relationship Between Diesel Fuel Spray Vapor Penetration / Dispersion and Local Fuel Mixture Fraction*. SAE Technical Paper. SAE Technical Paper, Vol. 4(1), pp. 764, **2011**.
- [25] ECN home, Engine Combustion Network (ECN). Available at: <http://www.sandia.gov/ecn>, last accessed by 25th June **2012**.

Chapter 4 – ELSA model validation

- [26] Payri, R.; Garcia-Oliver, J.M.; Bardi, M.; Manin, J. *Fuel temperature influence on Diesel sprays in inert and reacting conditions*. Applied Thermal Engineering, Vol. 35(0), pp. 185 – 195, **2012**.
- [27] ECN home. *Diesel spray combustion: “spray A” injector nozzle geometry*. Engine Combustion Network (ECN), Available at: <http://www.sandia.gov/ecn/cvdata/targetCondition/injectorNozGeom.php>, last accessed by 25th June **2012**.

Chapter 5 - Cavitating nozzles modeling with ELSA

Cavitation is a typical characteristic of nowadays Diesel injectors. As it is shown in this chapter, ELSA can accurately describe the sprays created by cavitating nozzles. In fact, to do so it is only necessary to introduce the velocity profile at the exit of a cavitating nozzle as the velocity inlet, without computing any effective quantity. This is the main advantage of ELSA against DDM methods. In this chapter, we have used the numerical database compiled by FJ. Salvador about cavitating nozzles and compared our results with experimental ones wherever possible. Special thanks are given to R .Payri, FJ. Salvador and Jorge Martínez-López for providing us a copy of their data, originally published at [1] - [5].

Cavitation appears at cylindrical nozzles, and does not need a high pressure to appear. Usually cavitation is also related to an increase of the turbulence level, which increases the mixture between the fuel and the gas at the chamber. In addition, as was studied by Tamaki et al., 2001 [6] cavitation can increase the breakup of the liquid phase, and thus improving the atomization.

From the experimental point of view, cavitation can be only studied indirectly in actual sizes, due to the high pressures of the injectors and the tiny size of the orifices. However, trusted numerical simulations made by Payri's group and Patouna et al., [7] - [11] can give an insight of the fluid magnitudes inside the nozzle.

There are two cavitation bubbles, being the upper one the most important. Figure 5-1 shows a typical multi-hole injector. One nozzle of this sort has been studied thoroughly from the experimental point of view at CMT.

Chapter 5 – Cavitating nozzles modeling with ELSA

These nozzle parameters are detailed in the Table 5-1. The nozzle conicity is indicated by the *k-factor*, $k\text{-factor} = (D_i - D_o)/10\mu\text{m}$ (see more details in [12]). The nozzle inlet and outlet diameter are the same, thus *k* equals to zero.

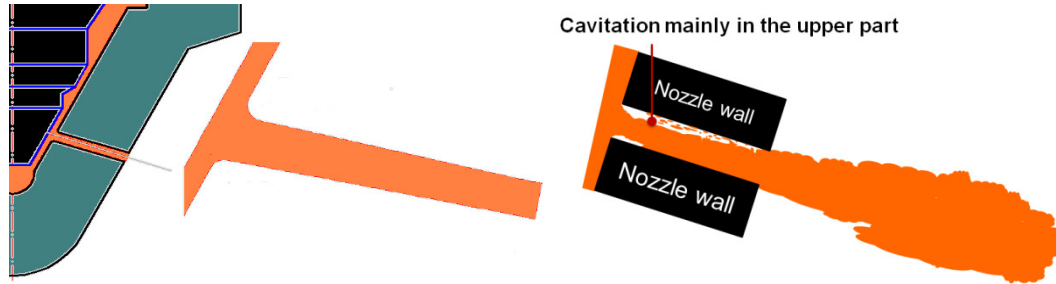


Figure 5-1: The attached-sectional transparent window at one hole of multi-hole injector (left) and its schematic of inner cavitating nozzle flow (cavitation occurs mainly on the upper part) on the right.

Table 5-1: Nozzle parameters.

Nozzle	D_i	D_o	<i>k-factor</i>	<i>r</i>	<i>L</i>	r/D_o	L/D_o
	[μm]	[μm]	[-]	[μm]	[μm]	[-]	[-]
6-hole	170	170	0	13	1000	0.076	5.882

The computations have been made in two different grids, having the coarser grid half of the vertex of the finer. Mesh information is given at Table 5-2. Lastly, the case studies are detailed in Table 5-3.

Table 5-2: Mesh information between coarse vs. fine mesh.

Mesh	Axial cells	Total cells	Total vertices
Coarse	150	259200	268327
Fine	300	518400	534877

Chapter 5 – Cavitating nozzles modeling with ELSA

Table 5-3: Several computation cases and setting conditions in ELSA modeling coupling with the internal nozzle flow.

Case	D_0	D_{eff}	Nozzle cavitation	V_{inj}	Fuel	P_{inj}	Gas	P_{cha}	T_{cha}
	[μm]	[μm]	Sim/Mod ²	[m/s]		[MPa]		[MPa]	[K]
Ca01*	170	-	Sim ²	Profile ¹	Diesel	30	N ₂	5	307.7
Ca02*	170	-	Sim ²	Profile ¹	Diesel	30	N ₂	7	307.7
Ca03*	170	165	Mod ²	V = 173	Diesel	30	N ₂	7	307.7
Ca04^a	170	-	Sim ²	V = 200	Diesel	30	N ₂	7	307.7
Ca05	170	-	Sim ²	Profile ¹	n-dodecane	80	Air	5	307.7
Ca06^c	170	-	Sim ²	Profile ¹	Diesel	80	N ₂	5	307.7
Ca07^f	170	-	Sim ²	Profile ¹	Diesel	80	N ₂	5	307.7
Ca08^c	170	-	Sim ²	Profile ¹	Diesel	80	N ₂	7	307.7
Ca09^f	170	-	Sim ²	Profile ¹	Diesel	80	N ₂	7	307.7
Ca10	170	-	Sim ²	Profile ¹	n-dodecane	160	Air	5	307.7
Ca11	170	-	Sim ²	Profile ¹	n-dodecane	160	Air	7	307.7
Ca12	170	-	Sim ²	Profile ¹	Diesel	80	N ₂	17	293
Ca13	170	165	Mod ²	V = 294	Diesel	80	N ₂	17	293
Ca14	170	-	Sim ²	Profile ¹	Diesel	80	N ₂	18	293
Ca15	170	165	Mod ²	V = 291	Diesel	80	N ₂	18	293
Ca16	170	-	Sim ²	Profile ¹	<u>BioDiesel</u>	80	N ₂	17	293
Ca17	170	165	Mod ²	V = 287	<u>BioDiesel</u>	80	N ₂	17	293
Ca18	170	-	Sim ²	Profile ¹	<u>BioDiesel</u>	80	N ₂	18	293
Ca19	170	165	Mod2	V = 285	<u>BioDiesel</u>	80	N ₂	18	293
Ca20	170	165	Mod ²	V = 285	<u>BioDiesel</u>	80	N ₂	17	293

* These cases presented in author's ICLASS paper.

^a Running case for a study with the same nozzle diameter.

¹ The velocity profile used comes from RANS performed in the nozzle.

² Sim stands for simulation, and Mod stands for modeling.

^c Coarse mesh as described in Table 5-2.

^f Fine mesh as described in Table 5-2.

Chapter 5 – Cavitating nozzles modeling with ELSA

Table 5-4 presents the different values of P_{inj} and P_{cha} studied. This table also gives us the value of the C_a coefficient, which has been computed experimentally [13]. Two fuels have been used: Repsol CEC RF-06-99 fuel [14], and a BioDiesel (made from soybean oil) [3]. Their basic properties are described in the Table 5-5.

Table 5-4: Pressure and area coefficient.

P_{inj}	P_{cha}	$\sqrt{P_{inj} - P_{cha}}$	C_a
[MPa]	[MPa]	$[\sqrt{MPa}]$	[-]
80	5	8.66	0.832
80	7	8.544	0.853
160	5	12.45	0.808
160	7	12.767	0.786
160	17	11.958	0.83
160	18	11.916	0.83

Table 5-5: Fuel properties of Diesel and BioDiesel [3].

Fuel	Density	Viscosity
	[kg/m ³]	[kg/ms at 20 °C]
Diesel	830	3.2831e ⁻³
BioDiesel	869.47	5.776e ⁻³

The evaporative studies and the comparisons with experimental database have been presented in an ILASS paper (Hoyas et al., 2012 [12]), attached in chapter 7. Evaporative models, however are prohibitive expensive in terms of computational time. As an example, most of the simulation took one month using eight cores just for simulating 1 ms. Moreover, at this very moment, the ELSA code in Star-CD cannot easily handle different fuel types under evaporative conditions, especially the additional fuels that are not available in the built-in library, e.g. sometimes the simulation explodes when using Diesel, and BioDiesel. Lack of understandings of fuel properties and the special handling in the solver are shown to be a limitation. In those cases, n-dodecane fuel properties were utilized (see more details in [12]). In order to reduce the complexity and increase the cases for investigation, all the simulations presented hereafter use non-evaporative conditions. However, there is a complete lack of experiments to compare with. Thus, we can only measure the coherency of the ELSA model, more than its accuracy.

Figure 5-2 presents several key parameters at the nozzle exit for cavitating nozzle. D_0 and A_0 are real-size nozzle geometric parameters, these are also the inlet for spray modeling. For this reason, the whole information at the nozzle exit such as density and velocity are directly transformed from internal flow to the spray simulation.

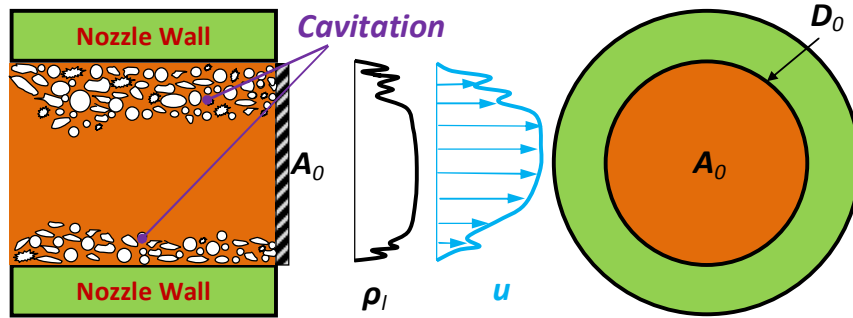


Figure 5-2: A schematic of internal cavitating flow and the main parameters at the nozzle exit [15].

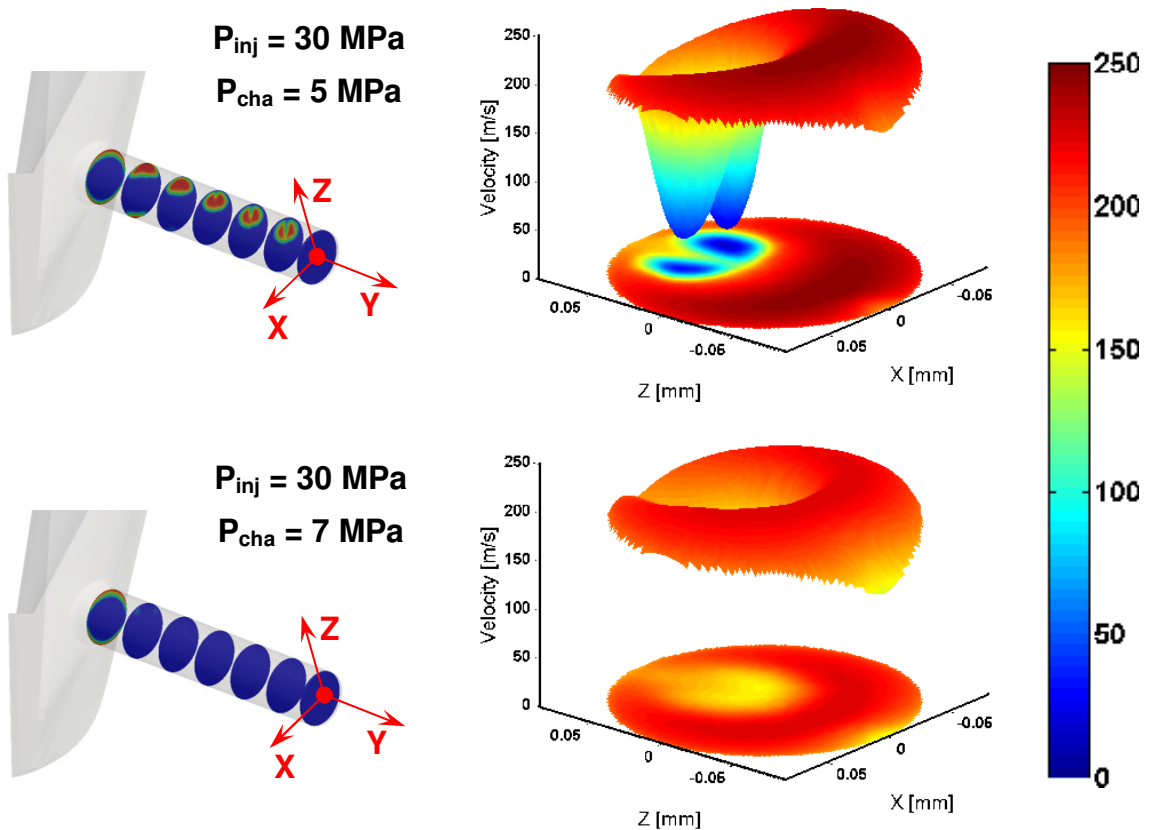


Figure 5-3: Time-averaged vapor field in the internal nozzle and the velocity profile at the nozzle outlet ($P_{inj} = 30$ MPa and different chamber pressure of 5 and 7 MPa respectively; cases Ca01 vs. Ca02).

Figure 5-3, Figure 5-4, Figure 5-5, and Figure 5-18 show the internal vapor field (photos on the left courtesy of the work of Martínez-López,

Chapter 5 – Cavitating nozzles modeling with ELSA

Salvador, and Payri [1] - [5]). All left figures show cavitation distribution expressed in term of the vapor field average in which the strong red color represents highest vapor level and the blue color for the pure liquid phase. Apart from Figure 5-3 where the full 3D view of cavitation distribution, all the other figures show at the middle planes. A little vapor field is observed close to the bottom whereas the major cavitation affects on the upper part. All right corresponding figures are the inlet velocity profiles employed for ELSA simulations that author derived and interpolated from the internal nozzle flow simulation on the left. As the strongly internal vapor produced in the nozzle close to the top, this cause the significantly reduction and variation in velocity on the upper areas at the nozzle exit, a slightly change also can be seen at the bottom.

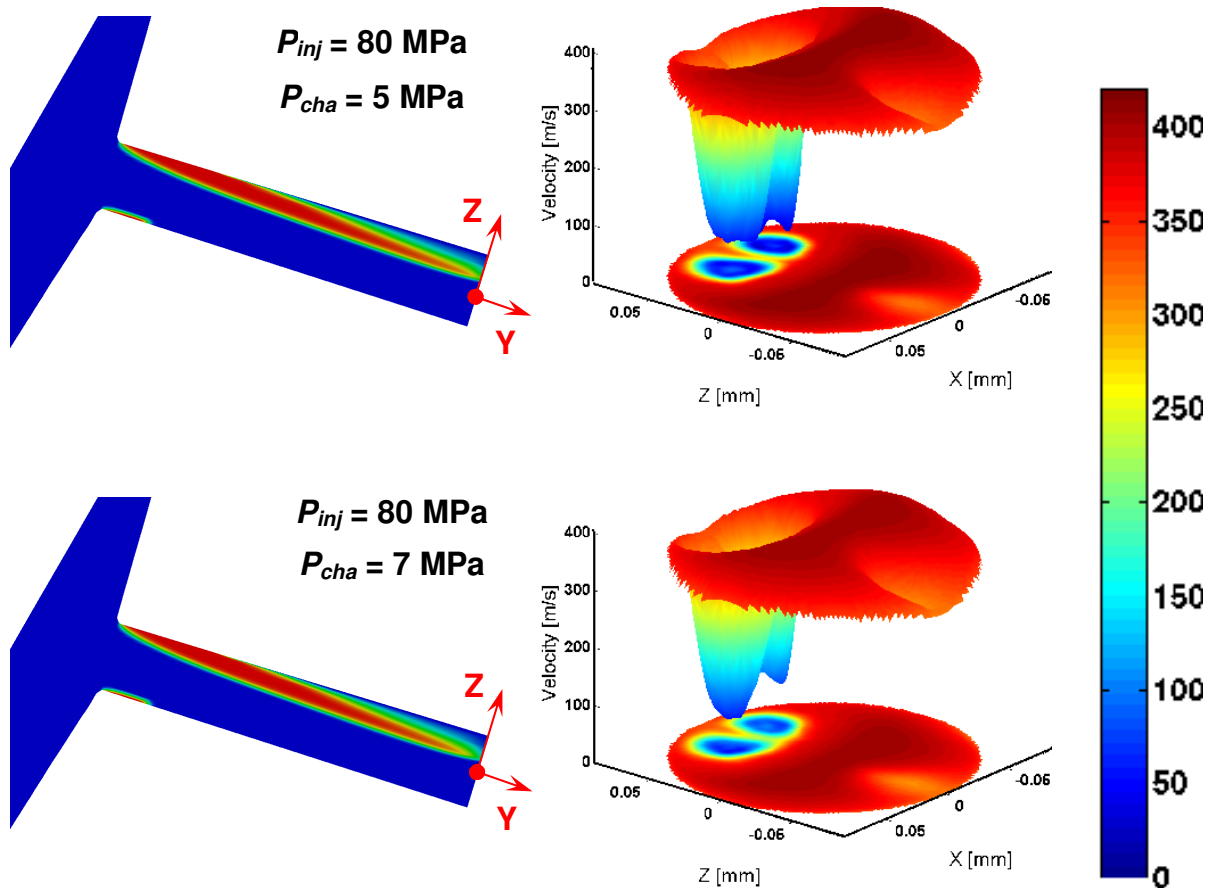


Figure 5-4: Time-averaged vapor field in the internal nozzle and the velocity profile at the nozzle outlet ($P_{inj} = 80 \text{ MPa}$; $P_{cha} = 5$ and 7 MPa ; cases $Ca05/Ca06^c/Ca07^f$ vs. $Ca08^c/Ca09^f$).

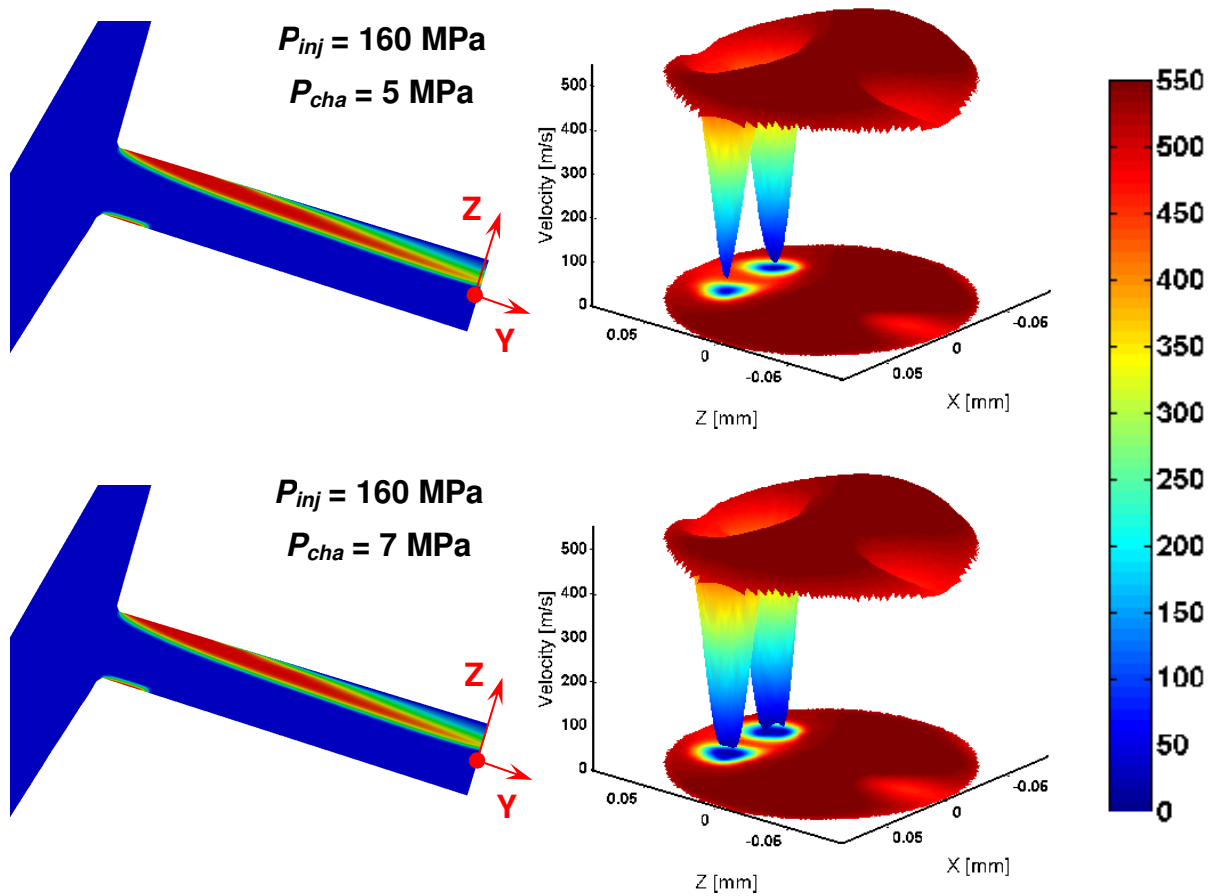


Figure 5-5: Time-averaged vapor field in the internal nozzle and the velocity profile at the nozzle outlet ($P_{inj} = 160$ MPa; $P_{cha} = 5$ and 7 MPa; cases Ca10 vs. Ca11).

5.1 Grid dependency

We study the effect of the 3D grid for two different chamber pressures hereafter. The spray penetration results in Figure 5-6 shows a great mesh dependency. The same happens when we performed the 2D simulations presented in [16]. So altogether, it can be concluded from these studies that the spray penetration decreases when the mesh size is increased.

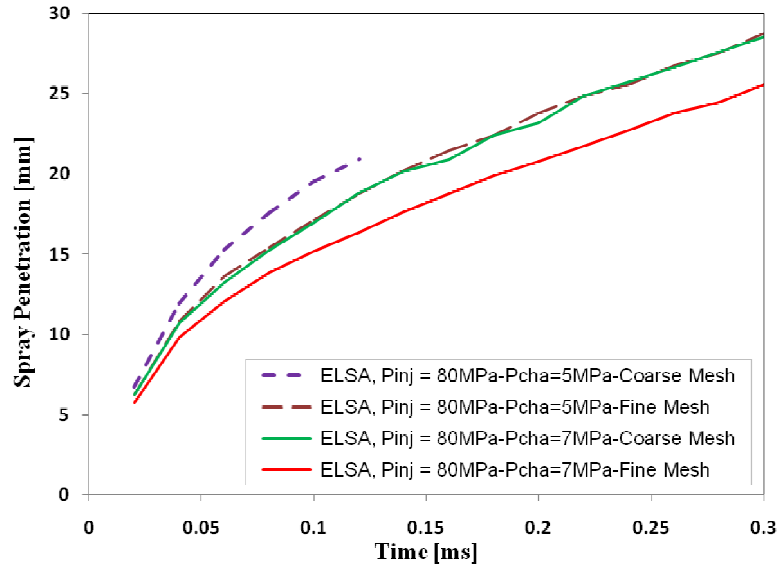


Figure 5-6: Comparison of the spray penetration between fine mesh and coarse mesh (cases Ca06^c, Ca07^f, Ca08^c, and Ca09^f).

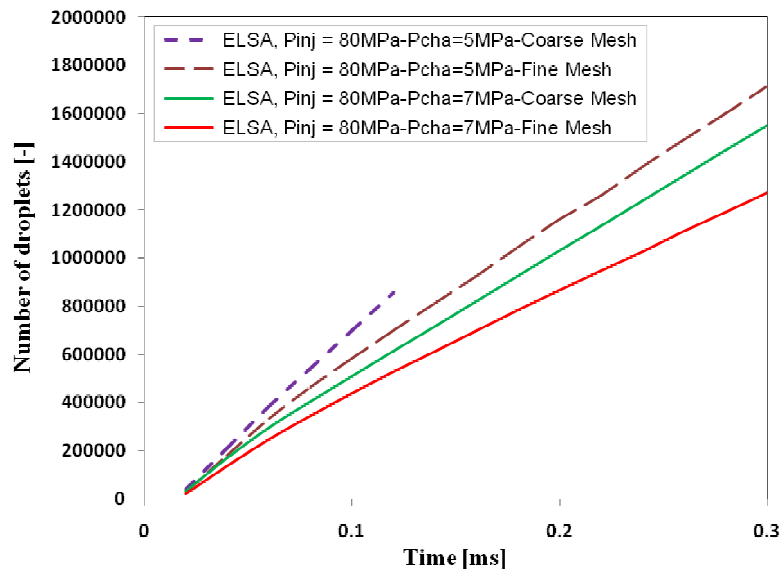


Figure 5-7: Comparison of the number of active droplets between fine mesh and coarse mesh (cases Ca06^c, Ca07^f, Ca08^c, and Ca09^f).

The number of active droplets is smaller for the fine mesh as seen in Figure 5-7, this is easily to explain by Figure 5-8 in which the centerline axial velocity slightly lower for the fine mesh. As the velocity increases, the break-up process and the motion of droplets are accelerated accordingly.

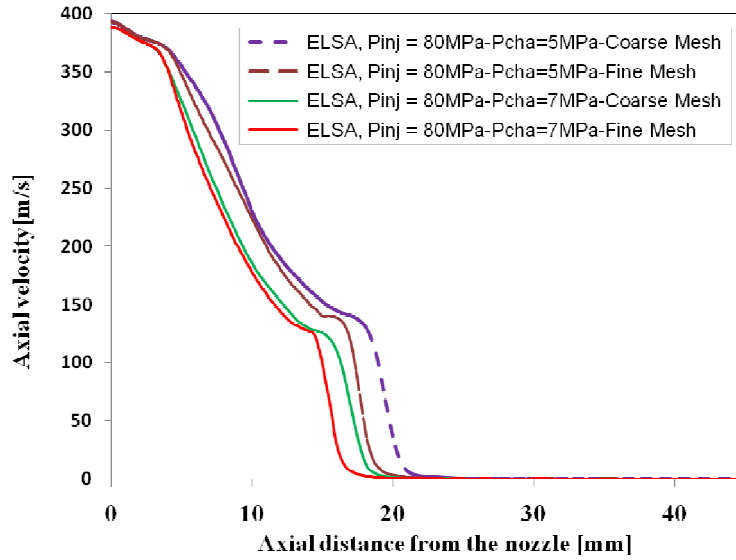


Figure 5-8: Comparison of the centerline axial velocity between fine mesh and coarse mesh at 0.12ms (cases Ca06^c, Ca07^f, Ca08^c, and Ca09^f).

5.2 Effect of injection pressure

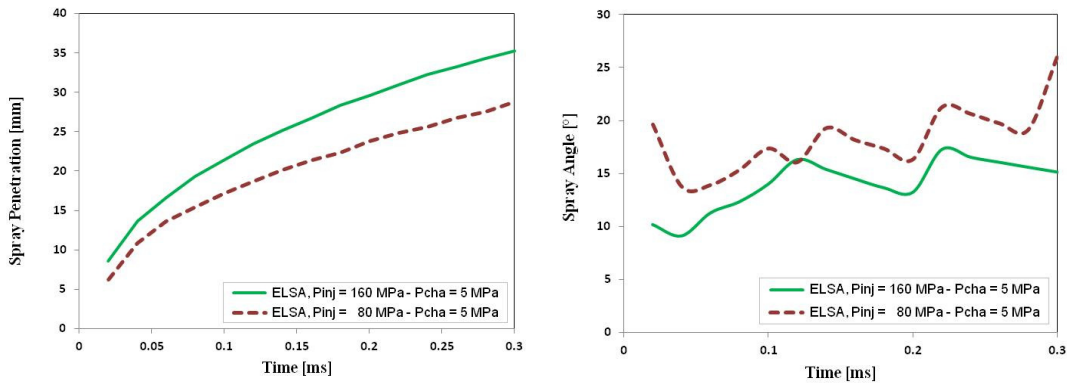


Figure 5-9: Spray penetration and spray spreading angle at the constant chamber pressure of 5 MPa, injection pressures are 80 MPa and 160 MPa respectively (cases Ca05 vs. Ca10).

In this section, the variation at the injection input is examined. Figure 5-9 and Figure 5-10, are coherent with spray theory. The spray penetration with the high injection pressure higher than the low pressure.

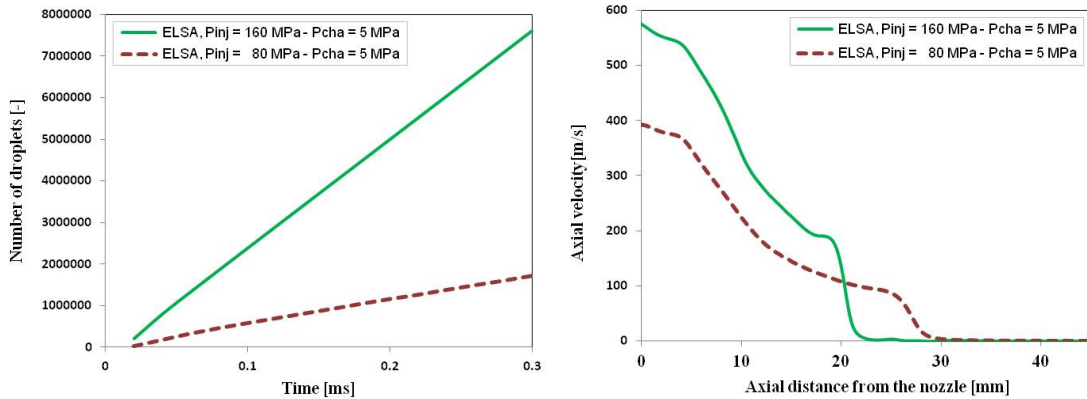


Figure 5-10: Number of droplets and axial velocity at the constant chamber pressure of 5 MPa, injection pressures are 80 MPa and 160 MPa respectively (cases Ca05 vs. Ca10).

Using the same scale and taking several circular sections with diameter of 0.24 mm perpendicular to the spray axis, Figure 5-11 plots simulated results at 0.3 ms spreading in sections at the distance of 1xD, 5xD, 10xD, 20xD, 5 mm, 10 mm respectively. Figure 5-11 and Figure 5-12 shows the influence of cavitation on the spray behavior where there is a non-uniform distribution across the cross sections. The velocity in case of injection pressure equals to 160 MPa can reach up to 600 m/s, while it only approximately 400 m/s with 80 MPa injection pressure. As can be seen from these figures, the influence of cavitating flow is very slightly at the distance above 20 mm.

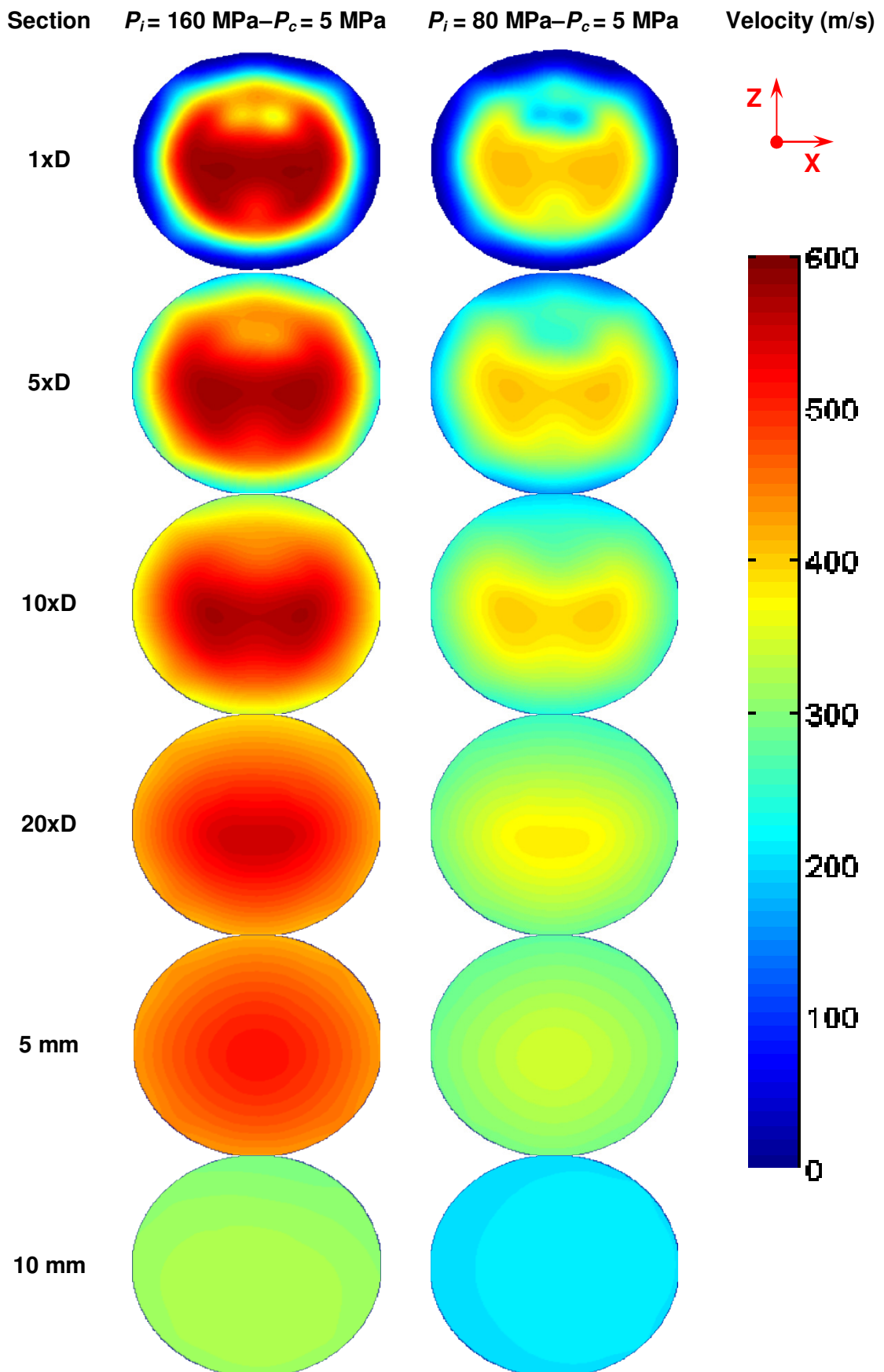


Figure 5-11: Compared 2D velocity contour for different cross-sections (D is diameter) along the spray exit at the simulating time of 0.3 ms.

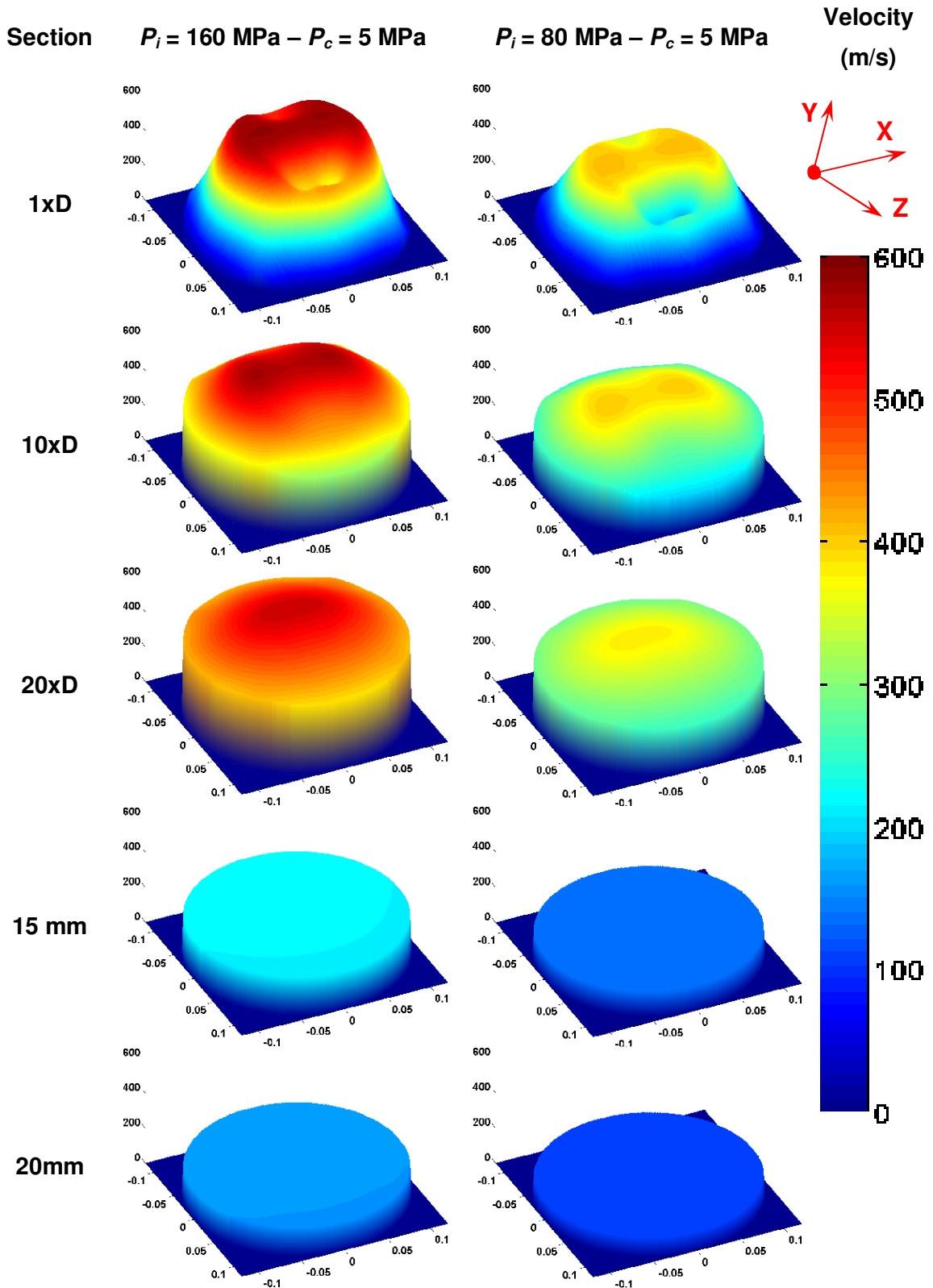


Figure 5-12: Full-view 3D velocity contour for different cross-sections (D is diameter) along the spray exit at the simulating time of 0.2 ms showing the comparison between $P_{inj} = 160$, and 80 MPa.

5.3 Effect of nozzle diameter and velocity input

Figure 5-13 and Figure 5-15 shows spray penetration and spray spreading angle for the constant injection pressure of 80 MPa, and the different chamber pressure of 17 MPa and 18 MPa respectively. Once applying the velocity profile coupling with nozzle flow simulations, these values are higher than using the effective diameter and effective velocity where the internal cavitation is ignored.

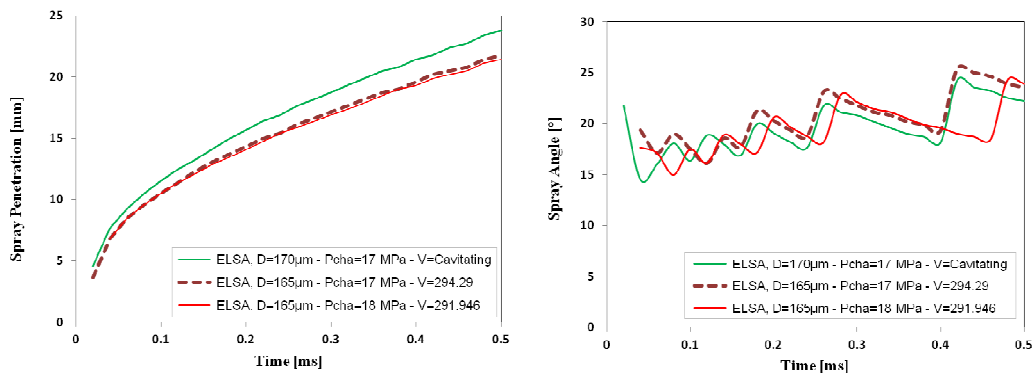


Figure 5-13: Spray penetration and spray spreading angle (Diesel, $P_{inj} = 80$ MPa, cases Ca12, Ca13 and Ca15).

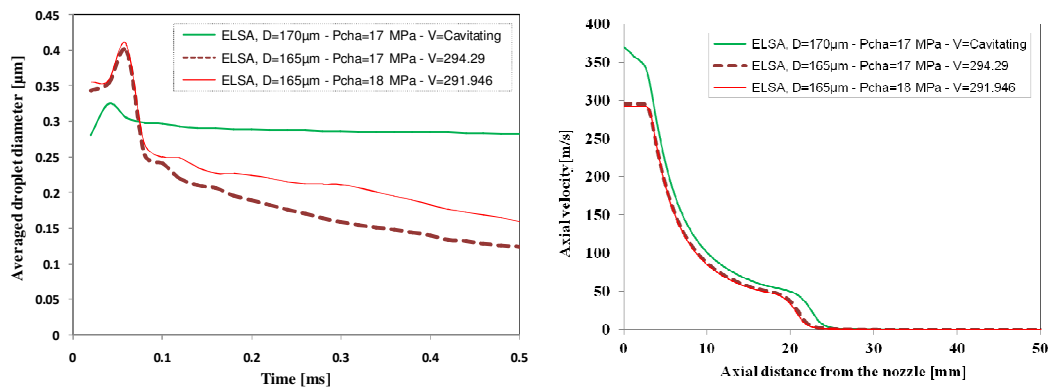


Figure 5-14: Averaged droplet diameter and axial velocity (Diesel, $P_{inj} = 80$ MPa, cases Ca12, Ca13 and Ca15).

The results given in Figure 5-14 and Figure 5-16 further show that the higher velocity on the centerline are obtained in both cavitating cases. As the

Chapter 5 – Cavitating nozzles modeling with ELSA

effective velocity is generally low in comparison with the averaged velocity across the whole nozzle section in case with cavitation. Obviously, the total amount of fuel is smaller when using the effective diameter. On the other hand, the droplets diameter for the cavitating coupling generates smaller droplets at beginning and slowly reduce in size, it is quite different with the constant velocity computations. Developed vortex cavitation in the internal nozzle flow results strong vortices and the mixture of vapor and liquid field in liquid flows after exiting the nozzle tip. As a result, the liquid flow starts to atomize right after it exits the nozzle top. It explains why the smaller size obtained before 0.08 ms. For the constant inlet velocity, the droplet diameter is smaller in case the higher velocity input.

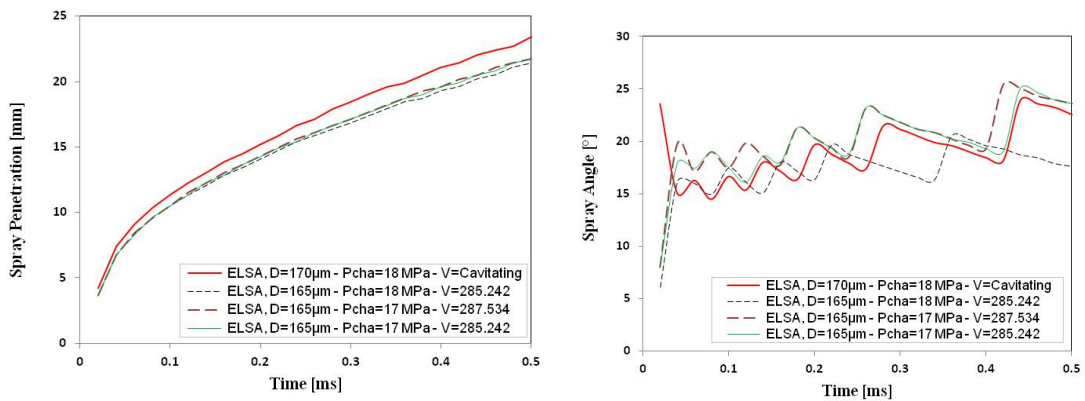


Figure 5-15: Spray penetration and spray spreading angle (BioDiesel, $P_{inj} = 80$ MPa, cases Ca18, Ca19, Ca17 and Ca20).

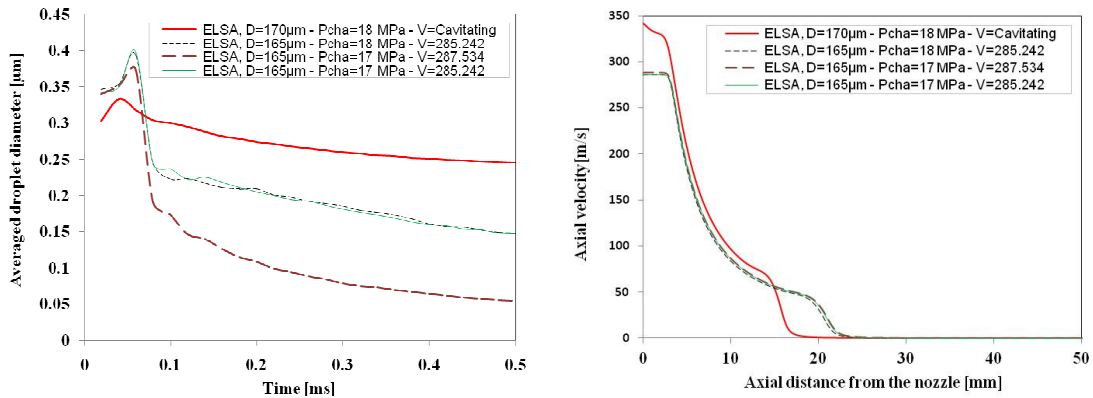


Figure 5-16: Averaged droplet diameter and axial velocity (BioDiesel, $P_{inj} = 80$ MPa, cases Ca18, Ca19, Ca17 and Ca20).

5.4 Effects of fuel type

The obtained results demonstrated the effects of changing in the fuel type under the same injection and chamber pressure. The spray penetration results showed in Figure 5-17 indicated the difference in the injection liquid between n-dodecane and DF2, the chamber gas consists of two different gases, however, it is almost the similar properties for air and nitrogen in the investigation. The spray penetration in case of DF2 is higher than n-dodecane, the density of DF2 is $830 \text{ (kg/m}^3\text{)}$ whereas the density of n-dodecane is only approximately $738 \text{ (kg/m}^3\text{)}$.

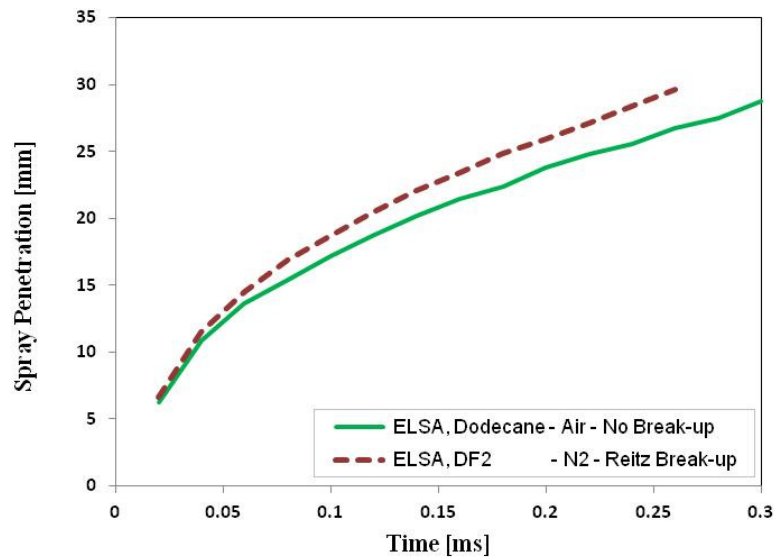


Figure 5-17: Spray penetration with different types of fuel and break-up setting ($P_{inj} = 80 \text{ MPa}$, $P_{cha} = 5 \text{ MPa}$; cases Ca05 vs. Ca07^f).

The second set of numerical investigation has been tested with Diesel and BioDiesel, in this study the different levels of chamber pressure are also studied. The velocity profile input at the inlet diameter in the ELSA modeling are shown in Figure 5-18, a slightly variation in fuel velocities is presented.

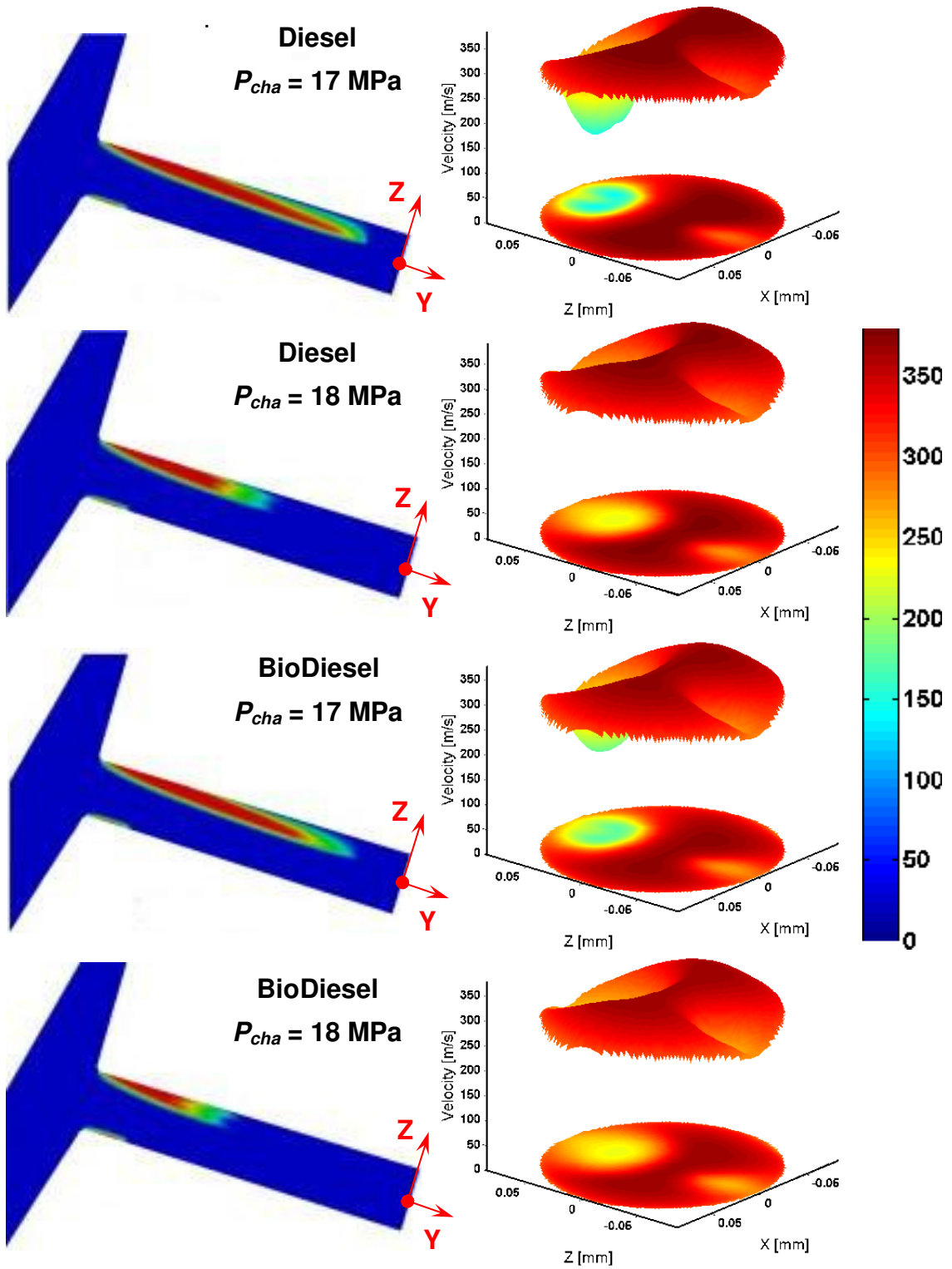


Figure 5-18: Time-averaged vapor field in the internal nozzle and the velocity profile at the nozzle outlet compared between Diesel and BioDiesel ($P_{inj} = 80$ MPa and different chamber pressure of 17 and 18 MPa respectively, cases Ca12, Ca14, Ca16, and Ca18).

Figure 5-19 shows the spray penetration results of four case studies. It can be observed that there is a slightly change between the chamber pressure of 18 and 17 MPa. Nevertheless, there is almost no difference between BioDiesel and Diesel fuel. The lower chamber pressure results a higher level of penetration. Similarly, the axial velocity on the centerline depicts the similar trend in Figure 5-20, the only different is for BioDiesel with higher chamber pressure. In this figure, a little strange in the centerline axial velocity close to the nozzle exit for the high chamber pressure and BioDiesel fuel, but the general behavior is similar to others.

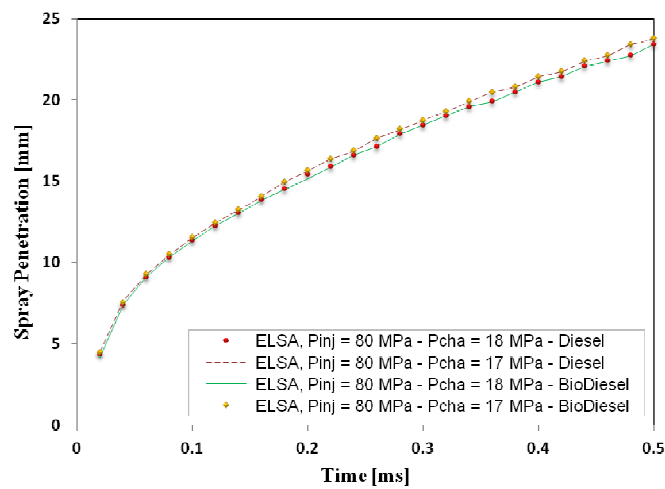


Figure 5-19: Spray penetration with different types of fuel and changing the chamber pressures (Diesel vs. BioDiesel, $P_{inj} = 80$ MPa, $P_{inj} = 17$ and 18 MPa, cases Ca12, Ca14, Ca16, and Ca18).

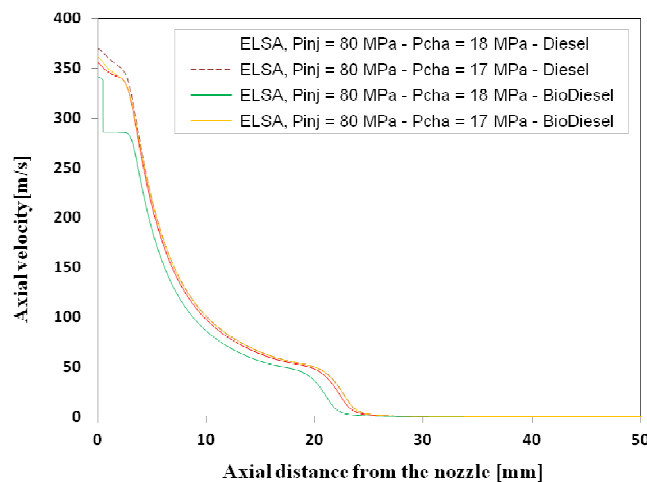


Figure 5-20: Centerline axial velocity with different types of fuel and changing the chamber pressures (Diesel vs. BioDiesel, $P_{inj} = 80$ MPa, $P_{inj} = 17$ and 18 MPa, cases Ca12, Ca14, Ca16, and Ca18).

Detailed effects amongst computed case are clearly in Figure 5-21 and Figure 5-22. The simulated spray spreading angles are almost identical for Diesel and BioDiesel fuels. Generally, the spray spreading angle in case with $P_{inj} = 17$ MPa chamber pressure (averaged angle are 19.62° , and 19.60°) is higher than $P_{inj} = 18$ MPa (18.96° , and 19.12°) for Diesel and BioDiesel respectively. As the higher centerline axial velocity obtained in the lower chamber pressure plotted in Figure 5-20. This also can be seen in Figure 5-22 where the averaged droplet diameter is examined. Diesel fuel produces smaller droplet size than BioDiesel, and the slower chamber pressure generated a larger droplet size.

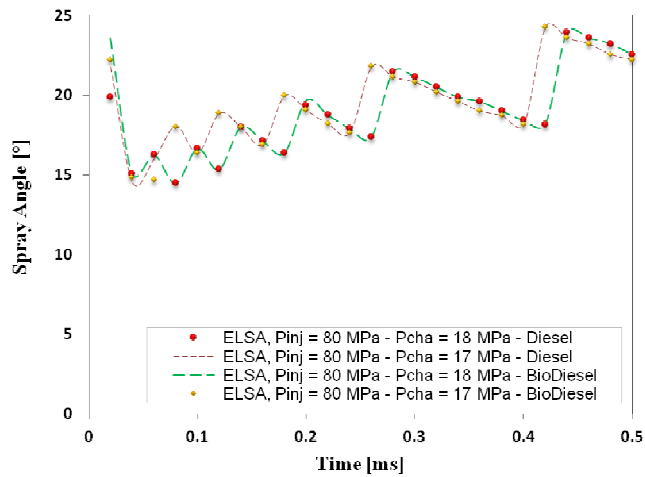


Figure 5-21: Spray spreading angle with different types of fuel and changing the chamber pressures ($P_{inj} = 80$ MPa, Diesel vs. BioDiesel, $P_{inj} = 17$ and 18 MPa; cases Ca12, Ca14, Ca16, and Ca18).

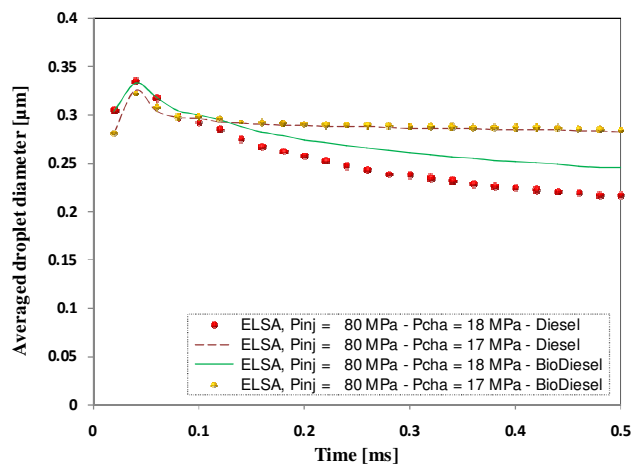


Figure 5-22: Averaged droplet diameter with different types of fuel and changing the chamber pressures (Diesel vs. BioDiesel, $P_{inj} = 80$ MPa, $P_{inj} = 17$ and 18 MPa, cases Ca12, Ca14, Ca16, and Ca18).

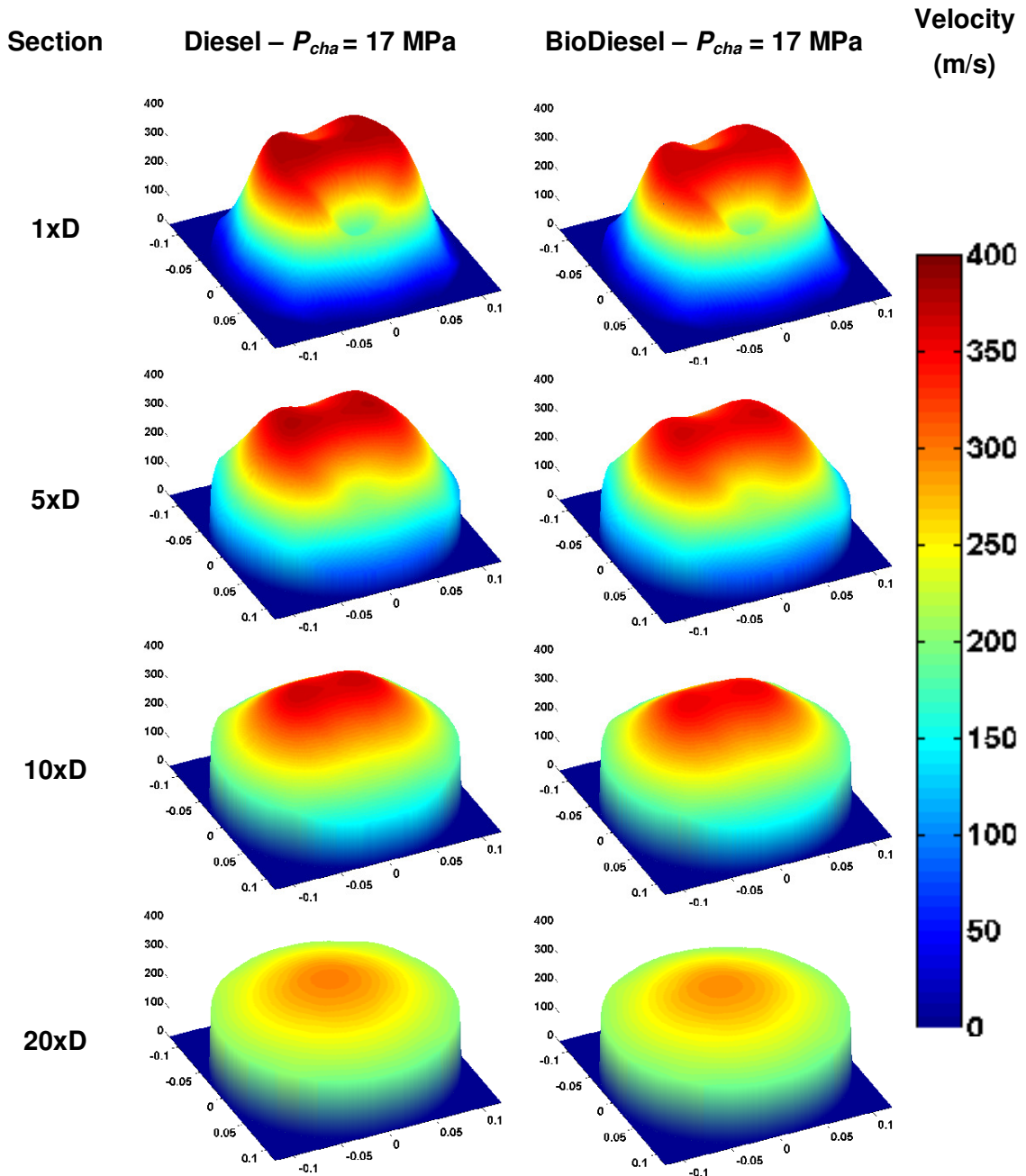


Figure 5-23: Compared spray profile in term of velocity between Diesel and BioDiesel for different cross-sections at 0.5 ms.

In Figure 5-23, the 3D plot showing axial velocity at various cross sections. From these figures the spray evolution and the effects of nozzle cavitation is clearly observed. At the distance close to the nozzle hole, it is heavily influence by the cavitating nozzle. Diesel results a slightly stronger magnitude rather than with BioDiesel.

Table 5-6: The example of typical CPU time in coupling modeling.

Case	Mesh	Total cells	Total vertices	Time step	Paralleling Processors	Transient time	CPU time (h)
Ca01	Coarse	259200	268327	1e ⁻⁸	6	0.5 ms	1111
Ca07	Coarse	259200	268327	1e ⁻⁸	6	0.37 ms	653
Ca10	Fine	518400	534877	1e ⁻⁸	6	0.31 ms	806

It is possible to extend much more parametric studies, and also necessary to validate with experiment. However, more powerful machines, more processors, and computing time will be needed for the computation in of 3D cylindrical mesh and especially under evaporative conditions. The extremely time consume of those simulations is presented in Table 5-6.

REFERENCES

- [1] Salvador, F.J.; Romero, J.V.; Roselló, M.D.; Martínez-López, J. *Validation of a code for modeling cavitation phenomena in Diesel injector nozzles*. Mathematical and Computer Modelling, Vol. 52, Issues 7–8, pp. 1123-1132, ISSN 0895-7177, October **2010**.
- [2] Salvador, F.J; Hoyas, S.; Novella, R.; Martínez-Lóper, J. *Numerical simulation and extended validation of two-phase compressible flow in Diesel injector nozzles*. Proceedings of the Institution of Mechanical Engineers, Part D: Journal of Automobile Engineering, Vol. 225, no. 4 545-563, April **2011**.
- [3] Salvador, F.; Martinez-Lopez, J.; Romero, J.V.; Rosello, M.D. *Influence of biofuels on the internal flow in Diesel injector nozzles*. Mathematical and Computer Modelling, Vol. 54(7-8), pp. 1699 – 1705, **2011**.
- [4] Salvador, F; Martinez-Lopez, J; Romero, J.V; Rosello, M.D. *Computational study of the cavitation phenomenon and its interaction with the turbulence developed in Diesel injector nozzles by Large Eddy Simulation (LES)*. Mathematical and Computer Modelling, ISSN 0895-7177, **2011**.
- [5] Payri, F.; Payri, R.; Salvador, F.J.; Martínez-López, J. *A contribution to the understanding of cavitation effects in Diesel injector nozzles through a combined experimental and computational investigation*. Computers & Fluids, Vol. 58, pp. 88-101, ISSN 0045-7930, 15 April **2012**.
- [6] Tamaki, N.; Shimizu, M.; Hiroyasu, H. *Enhancement of the atomisation of a liquid jet by cavitation in a nozzle hole*, Atom. And Sprays, Vol. 11, pp. 125-137, **2001**.

- [7] Payri, F.; Margot, X.; Patouna, S. *A CFD Study of the Effect of the Needle Movement on the Cavitation Pattern of Diesel Injectors*. SAE Technical Paper, **2009**.
- [8] Margot, X.; Patouna, S.; Payri, F.; Ravet, F.; Funk, M. *A CFD study of the effect of the needle movement on the cavitation pattern of Diesel injectors*. 9th International Conf. on Engines and Vehicles, Naples, Italy, paper number 09ICE-0194, **2009**.
- [9] Hespel, C.; Blaisot, J.-B.; Margot, X.; Patouna, S.; Cessou, A.; Lecordier, B. *Influence of Nozzle geometry on spray shape, particle size, spray velocity and Air entrainment of high pressure Diesel spray*. THIESEL 2010 - Conference on Thermo- and Fluid Dynamic Processes in Diesel Engines, Valencia, Spain, **2010**.
- [10] Patouna, S. *A CFD Study Of Cavitation In Real Size Diesel Injectors*. Universitat Politècnica de València, **2011**.
- [11] Margot, X.; Hoyas, S.; Gil, A.; Patouna, S. *Numerical Modelling of Cavitation: Validation and Parametric Studies*, Engineering Applications of Computational Fluid Mechanics, 6, **2012**.
- [12] Hoyas, S.; Gil, A.; Fajardo, P.; Khuong-Anh, D.; Ravet, F. (2012). *Evaluation and validation of ELSA model in Diesel sprays: 3D cavitating nozzles case*. International Conference on Liquid Atomization and Spray Systems, Germany, Sept **2012**.
- [13] Payri, R.; Salvador, F.; Gimeno, J.; Zapata, L. *Diesel nozzle geometry influence on spray liquid-phase fuel penetration in evaporative conditions*. Fuel, Vol. 87(7), pp. 1165 – 1176, **2008**.
- [14] Payri, R.; Salvador, F.; Gimeno, J.; la Morena, J.D. *Influence of injector technology on injection and combustion development - Part 1: Hydraulic characterization*. Applied Energy, Vol. 88(4), pp. 1068 – 1074, ISSN 0306-2619, 10.1016/j.apenergy.2010.10.012, **2011**.
- [15] R. Payri, F.J. Salvador, J. Gimeno, J. de la Morena. *Study of cavitation phenomena based on a technique for visualizing bubbles in a liquid pressurized chamber*. International Journal of Heat and Fluid Flow; Vol. 30, Issue 4, Pages 768-777, ISSN 0142-727X, **2009**.
- [16] Hoyas, S.; Pastor, J. M.; Khuong-Anh, D.; Mompó-Laborda, J. M.; Ravet, F. *Evaluation of the Eulerian-Lagrangian Spray Atomization (ELSA) in spray simulations*. International Journal of Vehicle Systems Modelling and Testing, Vol. 6, Nos. 3/4, pp. 187-201, **2011**.

Chapter 6 - Conclusions and Recommendations

6.1 Conclusions

In order to present the main conclusions of this thesis, we want to stress what it is and what is not. The main idea behind this thesis is to validate the ELSA model, implemented for the first time in a commercial code. Please note that this work is about the application of the ELSA model for DI ICE, not about the ELSA model itself. The most important system validated has been the spray coming from a cavitating injector whose internal flow was previously computed.

The validation has been made over a large amount of cases, comparing fuels, profiles at the inlet, different pressures at the injection system and chamber, temperatures and so on. The total amount of CPU-hours used in the last two years is around half a million. The main conclusion is that ELSA is able of simulate the spray in the hardest case: evaporative spray with the flow coming from a cavitating nozzle. This conclusion is supported by:

- The agreement with the experimental data, mostly coming from SANDIA, ECN network and CMT-Motores Térmicos, is in general excellent. However, as the pressure is increased, the precision decrease. Probably, this is an effect of the grid resolution, and better results can be achieved with a finer mesh.

Chapter 6 – Conclusions and Recommendations

- Particularizing, a good agreement in penetration has been obtained again in almost all the cases. A similar trend was observed in the axial velocity. The cone angle was not so well described, but the difference was not significant in most of the situations.
- The number of droplets necessary to create a parcel, N_{parcel} , gives a total amount of droplets that is consistent with the experiment, but in the case of high values. It should not be higher than 100.
- The time step, t_h depends mostly on the inlet boundary condition and evaporative conditions. Usually, $t_h = 1e^{-7}$ is enough for most of the cases. However, if the former situation applies, i.e., the inlet flow comes from a cavitating nozzle or there exists evaporation, it is necessary to move down t_h until $1e^{-8}$. This number has been enough for all the cases.
- About the coalescence model, all the results seem to be coherent. Spray penetration and spray spreading angle are almost independent of coalescence. Of course, the number of droplets is reduced when there exists coalescence.
- Three secondary breakup models: Reitz-Diwakar, Hsiang-Faeth, and Pilch-Erdman models for analyzing the fuel sprays were investigated. The Hsiang-Faeth model took less time than the other two, but its results were also different. The best option is the Reitz-Diwakar model.
- The last implementation of ELSA model provides reasonably accurate results under evaporating conditions. This is particularly true when using a standard single-component fuel described in a built-in library, in our case, n-dodecane. Others fuels, such as DF2, BioDiesel, n-heptane (C_7H_{16}), n-decane ($C_{10}H_{22}$), 2,2,4,4,6,8,8-heptamethylnonane (HMN) ($C_{16}H_{34}$), n-hexadecane ($C_{16}H_{34}$) and so forth are needed to further investigated to provide acceptable results. It is necessary to improve the

sub-models of heat and mass transfer, and correct routine to describe fuel properties.

- Concerning the temperature influence on the spray behavior, the change of gas temperature in the chamber is generally well captured. However, the results obtained changing the injector temperature do not show the same variation that the experimental ones.

6.2 Recommendations of future work

In the CFD simulations of a Diesel sprays using ELSA methodology, there are quite a number of areas where improvements can take place, just to name a few hereafter.

- Due to the short time length of the project, the author was limited by the lack of computational power and licensing constraints, which did not allow running many calculations at the same time. To provide a comprehensive validation and thus be able to identify problems that may arise when using this embedded model, it is necessary a more detailed parametric study of 3D evaporative sprays.
- The ELSA spray model shows to be generally successful for non-evaporating conditions. However, it is not really stable under evaporating conditions. It is hard to investigate in the origin of this problem, due to the lack of information about the implementation of the fuel chemistry and its physical properties.
- Other problem arises when the input profile shows severe oscillations either in the mass flux or in the velocity profile. This is particular true when the data is taken directly from experiments. In order to tackle this matter, a separated filtering or fitting processes were performed to

Chapter 6 – Conclusions and Recommendations

stabilize the oscillation. This should be directly incorporated in the CFD code by adding a special treatment at the inlet boundary condition input.

- ELSA model presents another problem: it is really expensive. Simulating an evaporative spray coming from a cavitating nozzle can take several months using eight cores. A few-month computing case is not worthy to be utilized within the RANS approach. To conduct a detailed parametric study can take years, so it is almost useless. There has not been possible to perform a detailed study of the speed-up of the code. Still, in the case of having 64 cores, for instance, we are talking about weeks.
- In summary, the ELSA model implemented in Star-CD has been able of reasonably simulate one liquid spray under very difficult conditions. Taking into account the intricate physical phenomena that happen in just 3 ms, the results of this implementation can only be described as brilliant.

Chapter 7 - List of papers

The work and results has been published in the following papers:

- Paper I - On the boundary condition setup of Large Eddy Simulation of Diesel sprays**
- Paper II - Application and Evaluation of the Eulerian-Lagrangian Spray Atomization (ELSA) Model on CFD Diesel Spray Simulations**
- Paper III - A large-eddy simulation of Diesel-like gas jets**
- Paper IV - Evaluation of the Eulerian-Lagrangian spray atomization (ELSA) in spray simulations**
- Paper V - Evaluation of the Eulerian–Lagrangian Spray Atomization (ELSA) model in spray simulations: 2D cases**
- Paper VI - A Recent Eulerian-Lagrangian CFD Methodology For Modelling Direct Injection Diesel Sprays**
- Paper VII - Evaluation and Validation of ELSA Model in Diesel Sprays: 3D Cavitating Nozzles Case**

On the boundary condition setup of Large Eddy Simulation of Diesel sprays.*

S. Hoyas[†], A. Gil, J. M. Mompó-Laborda, D. Khuong-Anh

CMT - Motores Térmicos,
Universidad Politécnica de Valencia,
Edificio 6D,46022, Valencia, Spain.

October 10, 2010

1 Introduction

For engine designers insight in the behaviour of an evaporating fuel spray is of great importance. Improvements in injection equipment reduce emissions and increase power by a more effective combustion process. Therefore, a deep understanding of the physics of Diesel spray will provide some fundamental knowledge for the design of more efficient, less consuming and cleaner engines.

During the last years great advances on the comprehension of several physical phenomena in liquid jets and sprays have been achieved, both by means of diagnosis experimental tests and CFD techniques mainly based on RANS (Reynolds Averaged Navier-Stokes) to simulate turbulence. These computational methods are very useful to study the averaged flow, but they do not provide any information neither about the turbulent fluctuations nor about the flow on the jet boundary. In this paper we present an implementation of a LES (Large Eddy Simulations) method in an non-reactive sprays. LES methods are computationally more expensive than RANS, but modelling required by RANS is reduced, and therefore they are more accurate. Furthermore, a detailed study of the flow characteristics in zones where turbulent fluctuations are significant is allowed by means of LES, while RANS, by definition, cannot model these features. For a comprehensive description of both methods, the book of Pope [1] is an excellent starting point.

Regarding Diesel spray injection, the most commonly used codes in the automotive industry, until very recently, are based on the RANS approach because of their reasonably accurate results and relatively lower computational cost. However as the RANS approach

*This research was funded by the Spanish Government (ENE2010-18542), the Universidad Politécnica de Valencia (PAID-2759) and the Generalitat Valenciana (GV/2010/039)

[†]Corresponding author.

has the highest level of modelling it can be seen as a successful interpolation between experimental data sets. On the contrary, direct numerical simulation (DNS) methods solve all the significative scales of the flow, so no modelling is require and it provides the highest level of description of the flow. Since the smallest structures of the flow have to be solved, the computational cost increases as $Re^{9/4}$ and the resources required for most practical cases are above current computer hardware limitations (and will probably be in the next 20 years). While the use of LES increases the computational cost, these methods are able to consistently simulate the complex structures related with turbulent mixing, which is decisive in the injection and combustion processes and invisible for RANS solvers ([2], and [3]).

The main goal of this work is to numerically investigate the influence of the inlet boundary conditions on a LES of the flow in a Diesel fuel spray evaporation system. This is the first part of a research project where the idea is to obtain a LES solver able to reproduce the different turbulent patterns that appear in the free shear flow of Diesel sprays, as well as the velocities profiles. In this paper we limited ourselves to the numerical simulation of Diesel spray with the isothermal, isodense and non-vaporizing conditions. Following the characteristic features of this congress, the paper concentrates on the mathematical aspects of the simulation. Thus, the chemical and physical analysis have also not discussed in this article and will be published elsewhere. The results are compared with the classical numerical RANS method with both Eulerian-Eulerian and Lagrangian-Eulerian approaches and are simultaneously validated with experimental data. Our algorithm has been implemented in the free all-purposes CFD code OpenFOAM © 2004-2010 OpenSource Ltd.

2 Numerical Technique

As mentioned above, the RANS approach has been traditionally used in order to model Diesel spray injections[4]. The RNG (Renormalization Group Theory) k-epsilon turbulence model with the default coefficients for the turbulent dissipation rate equation and turbulent viscosity is used for both Euler – Euler and Lagrangian – Euler spray calculations. Previous works [5] showed that RANS accurately predicts average velocity profiles and average spray's shape (i.e. dispersion rate, penetration), since the mean velocity profile and the spreading rate are independent of Re . Nevertheless, RANS is not valid if higher level of turbulence structure description is required during the calculations [3]. Table 1 resume the main characteristics of RANS models compared to LES formulation. Differences are based on the statistical treatment of the turbulence (RANS) and the use of the self-similarity theory of Kolmogorov (LES). Also differences can be found on the time-averaging of the Navier-Stokes equations and the spatial filtering for the RANS and LES respectively, see Table 2.

Application of the filtering operation to the continuity and momentum equations [1] yields:

Table 1: Comparison between RANS and LES.

RANS	LES
Reynolds-averaged Navier-Stokes	Large Eddy Simulation
Statistical phenomena	Kolmogorov theory of self similarity ¹
Time-averaged NS ²	Spatial filtered NS
k - ϵ model (Jones and Launder, 1972)	Smagorinsky (Smagorinsky, 1963)
RNG k - ϵ model (Yakhot, 1992)	One Equation model (Yoshizawa, 1985)
Less computationally demanding	Predict transient flows better

¹Large eddies of the flow are dependent on the flow geometry, while smaller eddies are self similar and have a universal character.

²NS: Navier-Stokes Equations

$$\nabla \cdot \bar{u} = 0 \quad (1)$$

$$\frac{\partial \bar{u}}{\partial t} + \nabla \cdot \overline{uu} = -\frac{1}{\rho} \nabla \bar{p} + \nu \nabla^2 \bar{u} - \nabla \tau \quad (2)$$

where \bar{u} is the filtered velocity field, t is the time, \bar{p} is the filtered pressure, ρ is the fuel density, ν is the uniform kinematic viscosity and τ is the stress-like tensor ($\tau = \overline{uu} - \bar{u}\bar{u}$). Eqs. (1) and (2) govern the evolution of the large (energy-carrying) scales of motion and the modelled stress term is τ . Also, this SGS stress tensor provides the communication between the resolved scales and the dissipation scales [6].

Closure is obtained by modelling the residual-stress tensor. The Smagorinsky [7] model is used for the sub-grid scale tensor:

$$\tau_{ij}^d = -2\mu_{SGS} S_{ij} \quad (3)$$

where τ_{ij}^d is the deviatoric SGS stress with $\mu_{SGS} = \bar{\rho} (C_S \Delta^2) \left\| \widetilde{S}_{ij} \right\|$. C_S is the Smagorinsky constant, a theoretical value (0.065–0.2) and $\left\| \widetilde{S}_{ij} \right\|$ is the Frobenius norm $\left\| \widetilde{S}_{ij} \right\| = \sqrt{2\widetilde{S}_{ij}\widetilde{S}_{ij}}$ of the filtered strain tensor, $\widetilde{S}_{ij} = \frac{1}{2} \left(\frac{\partial \bar{u}_i}{\partial \bar{x}_j} + \frac{\partial \bar{u}_j}{\partial \bar{x}_i} \right)$. Δ is the filter width, here assigned to be the cube root of the local cell volume.

3 Boundary conditions

Experimental results have confirmed the hypothesis that spray evolution is controlled by fuel-air mixing rates and thus they can be analysed in the same way as a gas jets [5]. Besides

Table 2: Time Averaging vs. Spatial Filtering.

Instantaneous = Average + Fluctuations ($u = \bar{u} + u'$)	
Averaging or filtering of NS equations gives identical equations for the averaged/filtered variables plus averaged fluctuation terms.	
Time Averaging	Spatial Filtering
$u_i(x) = \frac{1}{T} \int_t^{t+T} \bar{u}_j(x, s) ds.$	$u(x_0) = \int_{\Omega} u(x, t) G(x_0, x, \Delta) \text{ }^{\text{3}} dx.$
$\overline{u'_i} = 0, \text{ and } \overline{\bar{u}_i} = \bar{u}_i.$	$\overline{u'_i} \neq 0, \text{ and } \overline{\bar{u}_i} \neq \bar{u}_i.$
Reynolds Stress Tensor	SGS ⁴ Stress Tensor
$\tau_{ij}^R = \overline{u'_j u'_i}$	$\tau_{ij}^S = -(\overline{\bar{u}_i u'_j} + \overline{u'_i \bar{u}_j} + \overline{u'_i u'_j}) = \overline{u_i u_j} - \bar{u}_i \bar{u}_j$

³Spatial filter $G(x_0, x, \Delta)$ with filter size Δ

⁴Subgrid Scale

the simplifications brought by the experimental researches, CFD still remains limitations in term of the modelling of the atomisation process of the nearby zone which is not the goal of the present study. In addition, the present work can be seen as a previous approach to the inclusion of droplets (Lagrangian term) as a source of mass and momentum. Hence, to keep the same computational domain will provide a better application of present conclusions to future Lagrangian-Eulerian LES calculation and a more suitable framework for further comparison between them. Consequently, the simplification of the computational domain presented by Vuorinen [8] is also assumed. In his work the inlet boundary condition is set far enough from the nozzle avoiding the problems of the void fraction limits which grid resolution required by LES makes it more restrictive. As presented below, turbulent gas jet theory will be applied to set the fields in the inlet boundary conditions of the domain.

Studies show how under certain conditions, for any section perpendicular to the spray axis in the steady region of the gas jet or diesel spray, momentum flux is conservative, and thus equal to that existing at the nozzle exit ([9], [10]). Therefore, a proper implementation of the inlet boundary condition would perform the same spray development independent of where it would be placed. Consequently, the inlet boundary condition must be perpendicular to the spray axis, contain the whole spray and the same momentum flux as at the nozzle exit and in order to ensure a more realistic development of the flow the boundary inlet has to reproduce the same profile of the fields as in a steady spray.

Since momentum flux can be obtained from experimental data, the unknown factors to set up the BC. can be identified by integrating momentum over the whole spray section:

$$\begin{aligned}
 \dot{M}_0 &= \frac{\pi}{2\alpha} \cdot \rho_a \cdot \tan^2\left(\frac{\theta_u}{2}\right) \\
 &\cdot x^2 \cdot U_{axis}^2 \cdot \sum_{i=0}^{\infty} \frac{1}{\left(1 + i \frac{S_C}{2}\right)} \\
 &\cdot \left[\left(\frac{U_{axis}}{U_0}\right) \left(\frac{1 + S_C}{2}\right) \left(\frac{\rho_f - \rho_a}{\rho_f}\right) \right]^i
 \end{aligned} \tag{4}$$

Desantes et al. obtain the previous expression for the spray momentum [11] assuming a Gaussian radial profile [12] for fuel concentration and axial velocity. Here the Schmidt number (S_C) represents the relative rate of momentum and mass transport and θ_u is the spray cone angle. The point of interest for the present work can be seen in Figure 1 where the axis velocity equals the injected velocity ($U_{axis} = U_0$) and a Gaussian radial profile can be assumed. The spray injected under the physical conditions shown in Table 3 has been simulated [13]. In these conditions the end of the non-perturbed zone for the isodense case is located at 4.073mm, approximately $8d_{eq}$ from the nozzle exit (with $d_{eq} = d_0 \sqrt{\rho_f / \rho_a}$) and the spray diameter is 2.07mm which is set as the inlet boundary condition diameter. Since LES calculation requires perturbed inlet boundary conditions, the velocity and concentration reference profiles at the inlet boundary condition are Gaussian profiles randomly perturbed a 10% as a first simplify approximation. The discussion of the convenience of this hypothesis will be discussed in the followings sections.

Table 3: Definition of experimental and gas jet CFD simulation $\dot{M} = 1.11N$.

	reference[13]	simulation
Fuel	$C_{13}H_{28}(l)$	fuel (N_2)
Air	N_2	N_2
P_{inj} (MPa)	73.995	-
$P_{a,\infty}$ (MPa)	3.5	3.55
$T_{f,0}$ (K)	307.58	307.58
$T_{a,\infty}$	307.58	307.58
$\rho_{f,0} / \rho_{a,\infty}$	21.26	1
U_0 m/s	373.27	373.27
d_{inlet} μm	112	2070
d_{eq} μm	516	516

The computational domain is a cylindrical volume ($d = 40mm$, $L = 70mm$) that represents the shape of the injection test rig chamber. The meshing methodology is fairly the same for the RANS and LES calculations, with different grid densities depending on

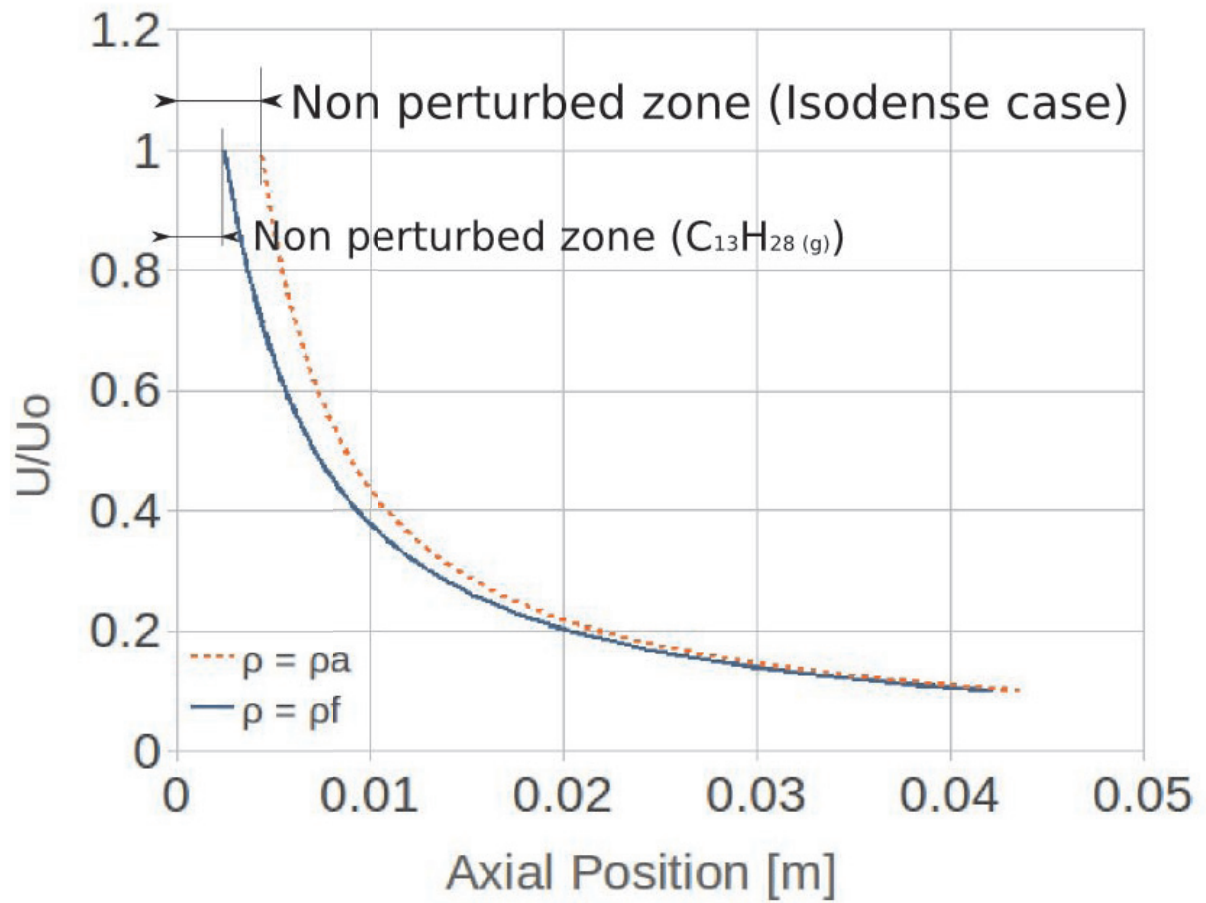


Figure 1: Axis velocity. Red line: Isodense case, Blue line: C₁₃H₂₈(g) case

Table 4: Definition of gas jet CFD boundary conditions.

Surface	Boundary type	Defining variables
Spray inlet diameter	Velocity turbulent inlet	$U_0(r) & C(r), T_f$
Wall	rigid wall, non-slip condition	–
outlet	constant pressure, wave Transmissive boundary	$P_{a,\infty}$; $T_{a,\infty}$

the turbulence formulation. Hexahedral cells have been preferred for the grid generation, since they provide better accuracy and stability than tetrahedral cells. The computational domain has been decomposed into hexahedral subparts in order to get a semi-structured topology mesh, as shown in Figure 2(a). Cells are concentrated around the spray diameter ($d = 2.07\text{mm}$) to get a cell size of $60 \mu\text{m}$ and $20 \mu\text{m}$ for the RANS and LES meshes respectively. Downstream the nozzle the mesh is progressively adapted to the shape of the computational domain in order to obtain a homogeneous cell size at sections located downstream the inlet boundary condition, see circular sections on the right of Figure 2(a) & (b). The number of cells is around 4×10^5 and 5.5×10^6 for the RANS and LES formulation respectively. Also, an evolution on the LES mesh has been performed in order to optimize skewness, uniformity and number of cells (reduced to 4.9×10^6 elements) of the mesh along the fluid zone occupied by the spray. Previous studies performed on RANS Euler – Euler [14] in similar spray conditions show that the structure of the mesh and cell size are enough to get a grid independent solution. Also, the meshes used for the LES formulation have comparable and also smaller cell sizes than recent LES studies [8] for sprays characterization where the grid independence is proved. Finally, three boundary conditions are assigned in the computational domain as depicted in Table 4.

4 Numerical results

The obtained numerical results are contrasted with those predicted by classical RANS models and compared with experimental data. Experimental results have been obtained from previously published data from the authors' research group [10], [15], [13].

Temporal evolution of the axial velocity at 25mm of the virtual nozzle has been used to justify the beginning for the statistical measurements. In Figure 3 (first of temp ev.) the criteria of a constant spray angle was used to set the radial position range of the probes. It is also shown the velocity value imposed in the center of the inlet boundary condition (4.073mm from the virtual nozzle under the isodense conditions). The difference in both the frequency content and the width of the velocity signals in the inlet boundary condition and the axis velocity at 25mm show a lack of precision of the spray fields simulated at the inlet boundary condition and justify the transient period needed for the turbulent

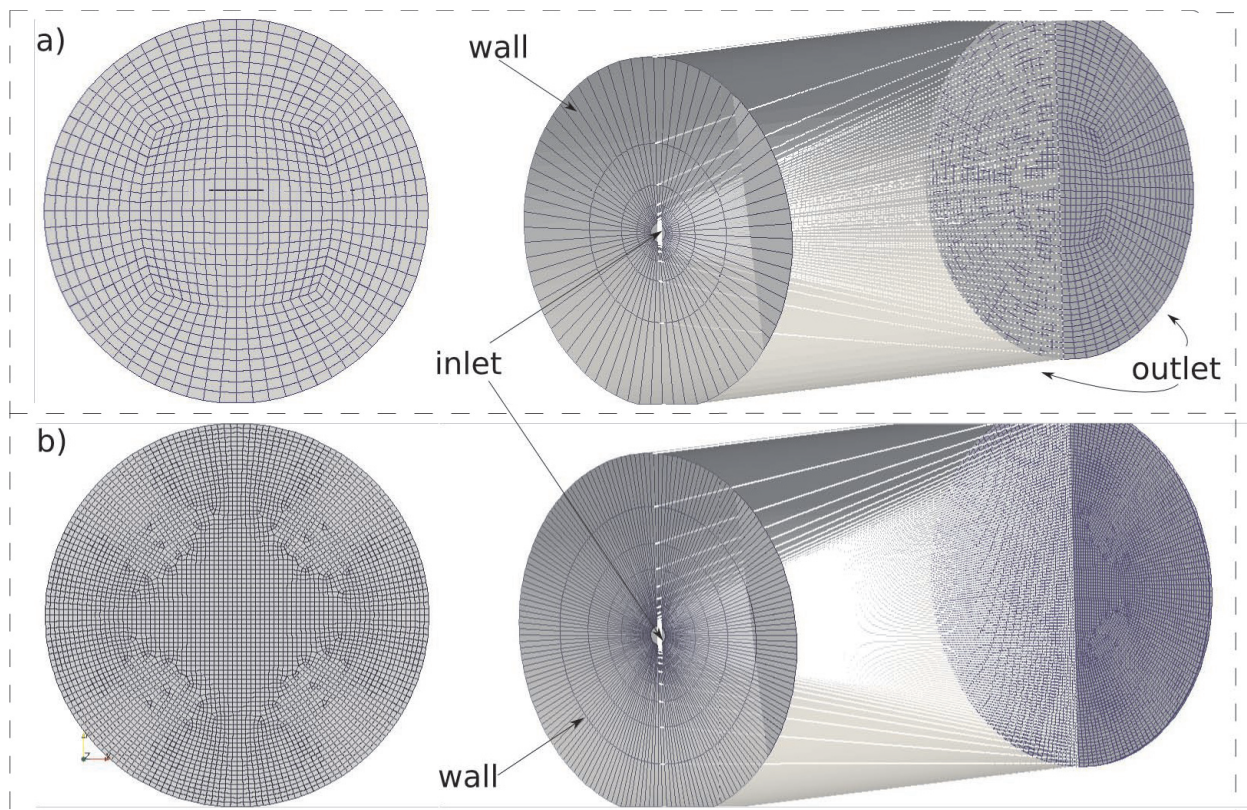


Figure 2: Calculation domain and boundary conditions. a) RANS case, b) LES case

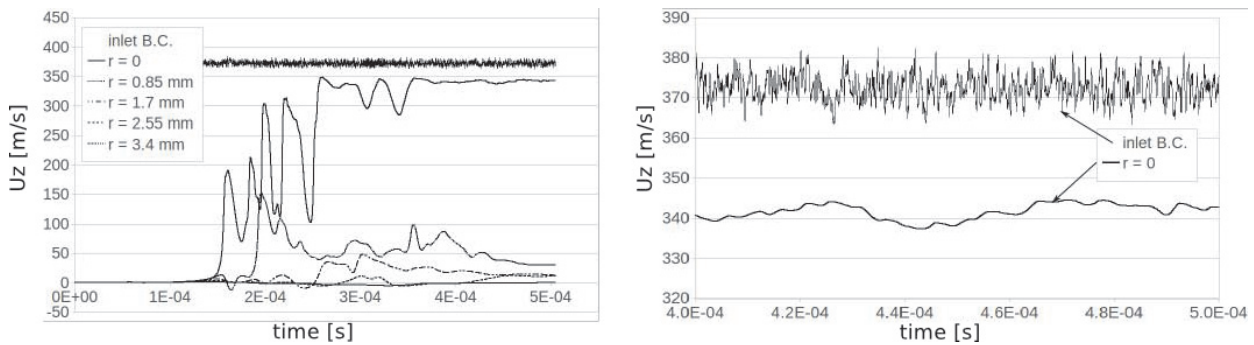


Figure 3: Measurements of radial probes ($x=25\text{mm}$)

evolution. Its effect in LES in terms of the classical parameters to characterize the spray is decisive as shown in Figures 4 and 5

The maximum axial distance for a 1% fuel concentration is the criteria used to define the penetration at Figures 4. Notice that this distance is located at the edge of the spray for theoretical and RANS calculations but not necessarily for LES simulations as shown in Figures 5. RANS and LES (E-E) calculations correspond to isodense cases detailed in previous sections and to obtain the RANS (L-E) penetration a Lagrangian formulation is coupled with an Eulerian one to track the particle dispersion and solve the gas phase variables.

The over prediction of both the RANS and LES Eulerian-Eulerian penetration at is affected by: the different injection mass flow rate shape, the fact that spray is more effective in transferring injection momentum to the ambient than the gas jet [16] and the non-fulfilment of the isodense hypothesis up to $30d_{eq}$. Furthermore, for the LES calculation, the first 5mm can be seen as a length required to develop turbulence Figure 5. Thus, the first assumption of a 1% of velocity fluctuation at the inlet boundary condition is not a good enough turbulent initialization of the flow. Although the inlet is placed at the end of an not well-known zone, authors think a more realistic turbulent conditions can be achieved by applying more realistic measured or calculated profiles of velocity variation [17], [18]. The Figure 5 show iso-surfaces of fuel concentration for the LES simulation at 0.3ms. The red line and the green line mark the stoichiometric iso-surface for LES and RANS (E-E) simulations respectively. These areas have a relevant importance in combustion processes. The upper part of the figure plots the radial distance of these surfaces where detached surfaces far from the jet can be found.

A comparison with the Gaussian radial profiles is shown in Figure 6. In both the axial velocity has been normalized with the axis velocity. In Figure 6(left) the radial distance is normalized with the jet's half-width as defined by Pope [1] where in Figure 6(right) is normalized with the axial distance. A spatial average at 25mm of the nozzle of the axial velocity ($t=0.5\text{ms}$) shows a good agreement with the theoretical Gaussian profile from the edge to the 30% of the axis speed Figure 6(left). Differences in simulated profiles at 20

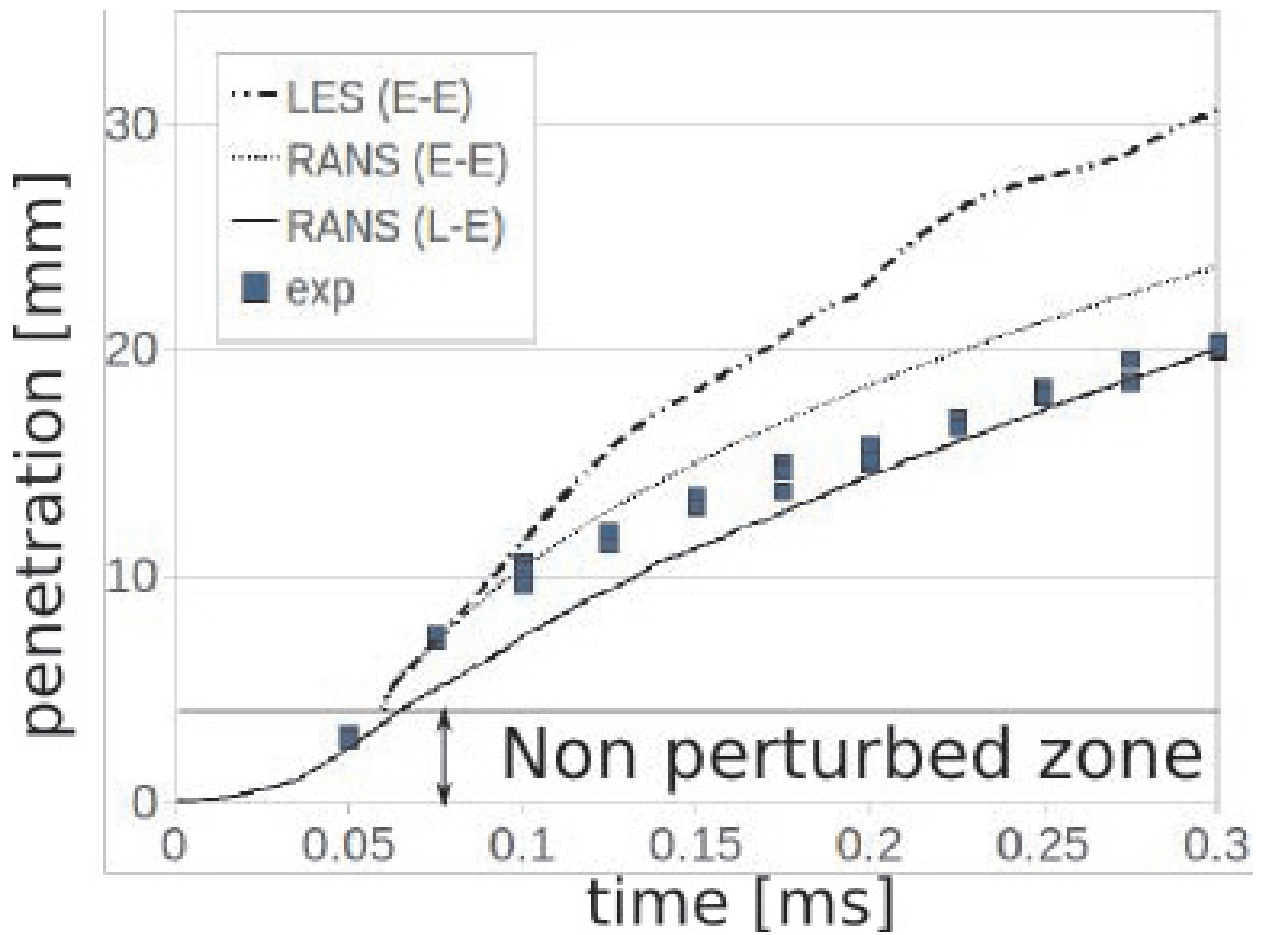


Figure 4: Comparison between experimental spray tip penetration (symbols) and CFD simulations (lines). The time axis is referred to the start of injection.

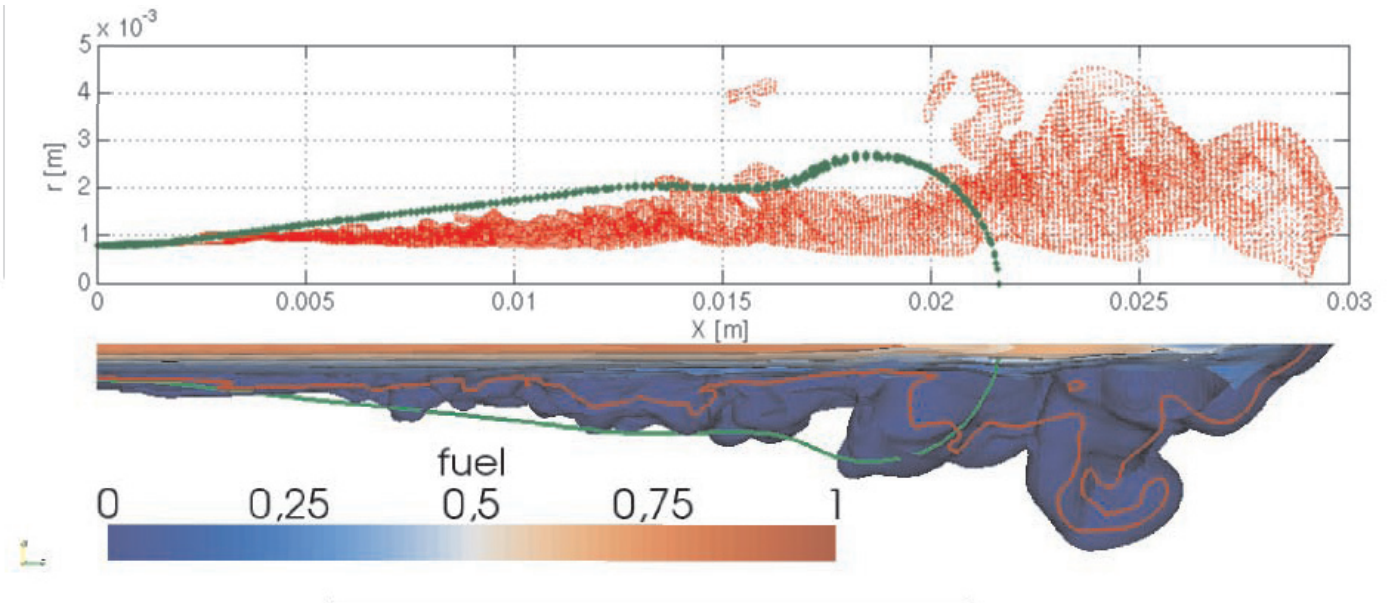


Figure 5: Comparison between RANS and LES concentration iso-surfaces $t=0.3\text{ms}$. Lower part: longitudinal clip of fuel concentration contours, Upper part: Radial coordinates of stoichiometric iso-surfaces

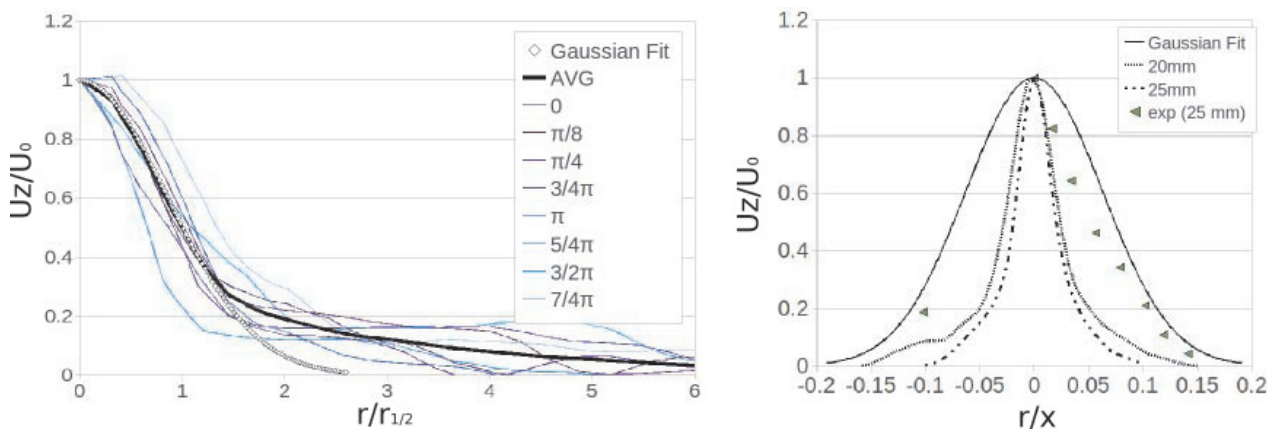


Figure 6: Radial velocity profiles ($t=0.5\text{ms}$). Left: Spatial average of eight different angles, Right: Time-averaged.

and 25 mm in Figure 6(right) can be affected by the amount of statistics for each location (around 0.05ms of data less at 25mm). Experimental data is close to LES simulated profile near the edge of the spray but moves to the Gaussian one as r increases.

5 Conclusions

Using the OpenFOAM code, the authors have performed a completed simulation of diesel spray in LES. Even the results do not match completely with the experimental results and RANS simulation, however; it performs a correct trend of spray simulation. These depict the complicate of modelling of spray processes with many direct or indirect parameters involved. Some specific needs are presented in our paper as challenges to overcome. The future research is now focusing on identifying the important parameters that affect the model and on improving the stability and accuracy of algorithms within OpenFOAM code. By so doing, the better spray simulation will be performed and a reliable tool will be used in modelling the spray simulation in the near future. Hence, LES modelling can become the practical tool in both industry and academic in the design process of combustion systems.

References

- [1] Pope S. B., Turbulent Flows, Cambridge University Press, 2000. 771 pp.
- [2] J.J. Riley, Review of large-eddy simulation of non-premixed turbulent combustion, *J Fluids Eng* 128 (2006), pp. 209-215.
- [3] Pitsch, H., Large-Eddy Simulation of Turbulent Combustion, *Annual Review of Fluid Mechanics*, Vol. 38, No. 1, 2006, pp. 453-482.
- [4] Fabian Peng-Krrholm, Numerical modelling of diesel spray injection, turbulence and combustion, Ph.D. Thesis, Chalmers Uni. of Technology, 2008.
- [5] J.M. Desantes and J.V. Pastor and J.M. García-Oliver and J.M. Pastor, A 1D model for the description of mixing-controlled reacting diesel spray, *Combustion and Flame*, 2009, 156, pp 234 - 249.
- [6] R. Payri and B. Tormos and J. Gimeno and G. Bracho, The potential of Large Eddy Simulation (LES) code for the modeling of flow in diesel injectors, *Mathematical and Computer Modelling*, Volume 52, Issues 7-8, 2010, Pages 1151-1160.
- [7] J.S. Smagorinsky, General circulation experiments with the primitive equations. I. The basic experiment, *Mon. Weather Rev.* 91 (1963), pp. 99-164.
- [8] Ville Vuorinen, LES of Certain Droplet Size Effects in Fuel Sprays, PhD Thesis, the Aalto University School of Science and Technology, 2010.

- [9] Desantes JM, Payri R, Salvador FJ, Gimeno J. Measurements of spray momentum for the study of cavitation in diesel injection nozzles. SAE Paper 2003-01-0703; 2003.
- [10] R. Payri, J.M. García, F.J. Salvador and J. Gimeno, Using spray momentum flux measurements to understand the influence of Diesel nozzle geometry on spray characteristics, *Fuel* 84 (2005), pp. 551–561.
- [11] J.M. Desantes, R. Payri, J.M. Garcí
a and F.J. Salvador, A contribution to the understanding of isothermal diesel spray dynamics, *Fuel* 86 (2007), pp. 1093–1101.
- [12] Correas D. Theoretical and experimental study of isothermal Diesel free sprays (In Spanish), PhD Thesis, Universidad Politcnica de Valencia; 1998.
- [13] D. Jaime Gimeno Garca, Desarrollo y aplicacin de la medida del flujo de cantidad de movimiento de un chorro diesel, PhD thesis, Universidad Politécnica de Valencia, 2008.
- [14] Abraham J, What is Adequate Resolution in the Numerical Computations of Transient Jets? SAE 970051 pp 81-95
- [15] L. Araneo, V. Soare, R. Payri, J. Shakal, Setting up PDPA system for measurement in a diesel spray, *Journal of Physics*, 45, 2006, 85-93.
- [16] Abraham J, Magi V, Macinnes J, Bracco FV. Gas versus Spray Injection: Which Mixes Faster? SAE paper 940895; 1994, pp163-177
- [17] Hussein HJ, Capp and George WK. Velocity measurements in a high-Reynolds-number, momentum-conserving, axisymmetric, turbulent jet, *J Fluid Mech* (1994). 258, 31-75.
- [18] Levy Y, Lockwood FC, *Combust. Flame* 40, 333 (1981)

Application and Evaluation of the Eulerian-Lagrangian Spray Atomization (ELSA) Model on CFD Diesel Spray Simulations

2011-37-0029

Published
06/09/2011Sergio Hoyas, Jose M. Pastor, Dung Khuong-Anh and Juan Manuel Mompó-Laborda
CMT, Universidad Politécnica de ValenciaFrederic Ravet
Renault

Copyright © 2011 SAE International

doi:10.4271/2011-37-0029

ABSTRACT

During the last fifteen years Computational Fluid Dynamics (CFD) has become one of the most important tools to both understand and improve the Diesel spray development in Internal Combustion Engine (ICE). Most of the approaches and models used pure Eulerian or Lagrangian descriptions to simulate the spray behavior. However, each one of them has both advantages and disadvantages in different regions of the spray, it can be the dense zone or the downstream dilute zone. One of the most promising techniques, which has been in development since ten years ago, is the Eulerian-Lagrangian Spray Atomization (ELSA) model. This is an integrated model for capturing the whole spray evolution, including primary break-up and secondary atomization.

In this paper, the ELSA numerical modeling of Diesel sprays implementation in Star-CD (2010) is studied, and simulated in comparison with the Diesel spray which has been experimentally studied in our institute, CMT-Motores Térmicos. Since many of the most important characteristics of the spray development, as the penetration or the axial velocity, can be captured using 2D simulations, in this preliminary validation of ELSA model only two-dimensional simulations have been performed. Moreover, the main objective of the paper is to: firstly, obtain mesh independency for further analysis and secondly, improve the classic $k - \epsilon$ RANS model for ELSA model. Apart from this, several characteristics of the spray as can be the droplet formation of the liquid penetration are also showed.

INTRODUCTION

Fuel injection process and subsequent fuel-air mixing formation play a major role on combustion and pollutant emissions in internal combustion engines. It is one of the most important phenomena in internal combustion engines which is still under development and with high concerns from both academic and scientific researchers, due to the complex interrelated phenomena taking place (See for instance Lefebvre, 1989 [17]). Still now, some of them, such as primary atomization or nozzle cavitation, are not fully understood.

In order to enhance Computational Fluid Dynamics (CFD) spray simulations, the ELSA model (Vallet et al., 2001 [24]) has been developed in recent years. It has been integrated very recently into the Star-CD CFD code by RSA. ELSA model is based on an Eulerian approach for the description of the dense spray region, where standard Discrete Droplet Model (DDM) method is not able to describe the flow. Within the diluted spray region, the ELSA model could switch to the traditional Lagrangian description of the liquid phase, taking advantage from well established and previously developed submodels.

The goal of the ELSA model is to realistically describe the dense zone of the spray and the spray atomization. Since the seminal work of Vallet et al. [24] it has been under development by several authors, including Blokkeel et al., 2003 [6], Beau, 2006 [5], Lebas, 2007 [15], De Lucas M., 2007 [9] or Ning W., 2007 [19]. As we have said, the ELSA model takes advantages of the Eulerian description of the

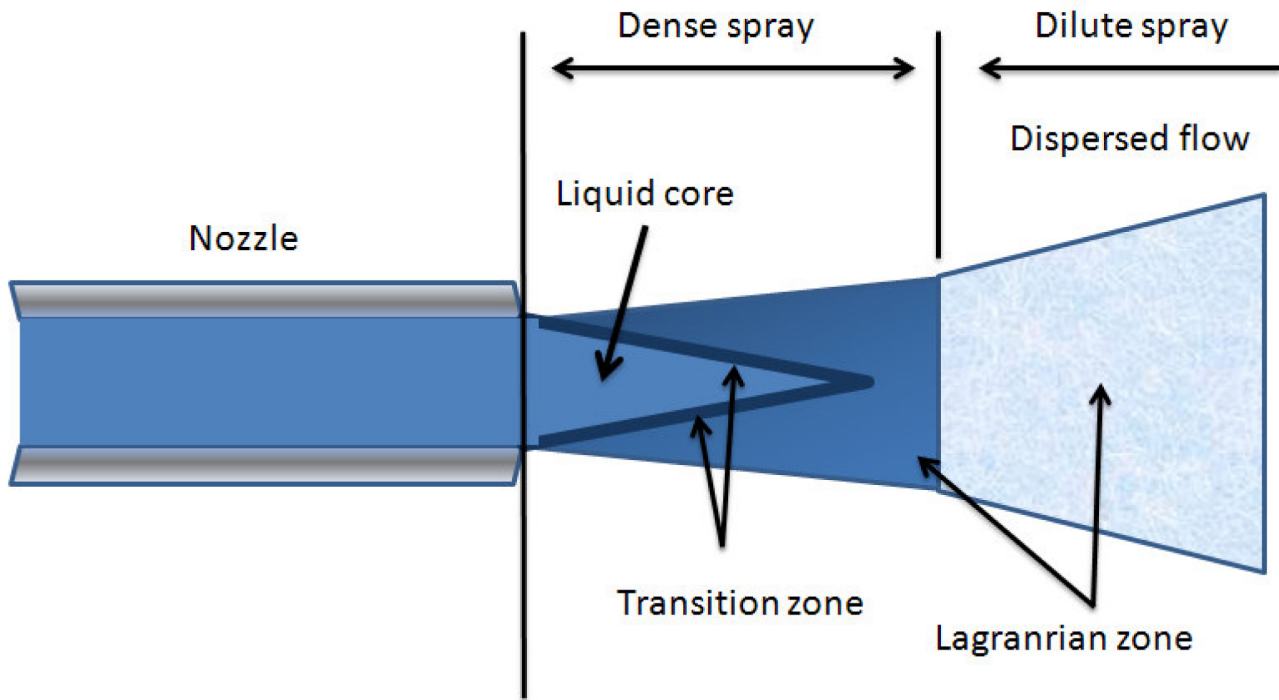


Figure 1. Illustration of the spray structure in the atomization regime (adapted from Faeth et al., 1995 [10]).

near nozzle flow where some assumptions of standard spray models based on discrete droplet method (DDM) shows strong limitations. This approach is valid only when the liquid volume fraction is small inside the computational cells and when the drops are homogeneously distributed in the computational space, neither of them is satisfied in the near field of the spray. In order to keep a low void fraction and assure numerical stability, it is necessary to use grid sizes larger than orifice diameter, which cannot adequately resolve the flow structures in this region. Additionally, it is also not required to assume any particular shape to represent drops and liquid ligaments on ELSA model, where the average area of the liquid-gas interface is introduced as a measure of the atomization extent. Moreover, the DDM method applies isolated drop based models in this region with strong interaction within the liquid phase, where its validity is hardly justified.

Basically, we have three separated zones in the ELSA model as shown in the following figure:

- **Eulerian mixture zone:** In this region (liquid core), liquid and gas phase are considered as a unique mixture flow. The classical Eulerian model is used to solve this single phase flow.
- **Transition zone:** switch from Eulerian to Lagrangian calculation.
- **Lagrangian zone:** classical Lagrangian tracking for droplets in the diluted spray zone and some regions of the Dense spray zone

The main hypothesis of ELSA, is that the flow must be a high-speed turbulent spray, where Reynolds bulk number and Weber number should be high (See Beau, 2006 [5] for a detailed study). In the case of Reynolds number, it must be at least $Re > 10^4$, (A. Doudou, 2005 [3]), whereas for Weber number, $We \sim 350$ (Lee and Reitz, 2001 [16] and Tanner, 2004 [23]). On the other hand, the main problem is that the turbulent mixing process between the liquid and surrounding gaseous phase is simulated as a single-phase turbulent fluid flow with mean properties, so it does not give a detailed information about both phases separately in the near nozzle region.

According to the previous statements, the purpose of the present study is to do a preliminary validation of the ELSA spray model implement in the Star-CD code. This work is part of a more ambitious project, with the general objective of developing and validating this spray model implementation for real-life applications on CFD engine calculations.

The structure of the paper is as follows. In the second section the model equations are written down. In the third section the geometry and the setup of the simulation are explained. Fourth section is devoted to the analysis of the results and conclusions are explained in the last section.

MODEL EQUATIONS

As we have said, the ELSA model was first described in an article of Vallet et al., 2001 [24]. Several other works as A.

Desportes et al., 2010 [2] Beau, 2006 [5], and Ning et al., 2007 [19] also discussed this set of equations, that we write down here in shake of completeness of the paper and a logical explanation of the ELSA model. These equations covered the several regions of the ELSA model, changing from one to another but, from now on and in all the regions, the subscript l stands for liquid and g stands for gas, whereas i, j are the direction in space. In order to facilitate the reading of the manuscript, we have added a symbol table at the end of the document.

a). Eulerian Mixture Zone

We define the mean liquid mass fraction, \tilde{Y}_l as

$$\tilde{Y}_l = \frac{\overline{\rho Y_l}}{\bar{\rho}}, \quad (1)$$

where ρ is the density and Y_l is the liquid mass fraction. Intuitively, mean density is defined as

$$\bar{\rho} = \rho_l \bar{Y}_l + \rho_g (1 - \bar{Y}_l), \quad (2)$$

which is expressed in terms of \tilde{Y}_l as

$$\frac{1}{\bar{\rho}} = \frac{\tilde{Y}_l}{\rho_l} + \frac{1 - \tilde{Y}_l}{\rho_g} \quad (3)$$

Favre averaged mean velocity is defined as

$$\tilde{U}_i = \tilde{Y}_l U_{l,i} + (1 - \tilde{Y}_l) U_{g,i} \quad (4)$$

and mean pressure \bar{P} is given by the equation of state

$$\bar{P} = \frac{(1 - \tilde{Y}_l) \bar{\rho} R_g T_g}{1 - \tilde{Y}_l \cdot \bar{\rho} / \rho_l} \quad (5)$$

In this equation R_g is the gas constant and T_g is the mixture temperature.

Then, the classical transport equations are solved for these mean variables:

$$\frac{\partial \bar{p}}{\partial t} + \frac{\partial \bar{\rho} \tilde{U}_j}{\partial x_j} = S_{EL}^{\tilde{Y}_l} \quad (6)$$

$$\frac{\partial \bar{\rho} \tilde{U}_i}{\partial t} + \frac{\partial \bar{\rho} \tilde{U}_j \tilde{U}_i}{\partial x_j} = - \frac{\partial \bar{P}}{\partial x_i} - \frac{\partial \overline{\rho u_i'' u_j''}}{\partial x_j} \quad (7)$$

Her, $S_{EL}^{\tilde{Y}_l}$ are some source terms that are activated during the transition from Eulerian to Lagrangian when there exist droplet generation. It should be noticed that the last equation does not contain any momentum exchange terms between liquid and gaseous phases. In order to model the liquid dispersion, this set of equations is completed by the transport equation for the liquid mass fraction:

$$\frac{\partial \bar{\rho} \tilde{Y}_l}{\partial t} + \frac{\partial \bar{\rho} \tilde{U}_j \tilde{Y}_l}{\partial x_j} = - \frac{\partial \overline{\rho u_j'' y''}}{\partial x_j} \quad (8)$$

In equations (6) and (7), there are two turbulent fluxes unknown. The turbulent stress tensor is modeled with a classical $k - \epsilon$ model closure, which is discussed below. Concerning the liquid turbulent diffusion flux, a gradient law approximation is applied:

$$\overline{\rho u_j'' y''} = - \bar{\rho} \frac{\nu_l}{Sc_t} \frac{\partial \tilde{Y}_l}{\partial x_j} \quad (9)$$

In this equation ν_l is the liquid viscosity and Sc_t is the turbulent Schmidt number.

b). Liquid/Gas Interface Density

In order to characterize the size of liquid fragments resulted from the jet atomization, the notion of liquid surface density is introduced. This variable is defined as the quantity of

liquid/gas interface per unit of volume $\bar{\Sigma} (m^{-1})$. Using this new variable, we can obtain the Sauter Mean Diameter of droplet, D_{32} and the drop number density (drop number per unit of volume), n (Lebas R., 2005 [14]):

$$D_{32} = \frac{6 \bar{\rho} \tilde{Y}_l}{\rho_l \bar{\Sigma}}$$

$$n = \frac{\rho_l^2 \bar{\Sigma}^3}{36 \pi \bar{\rho} \tilde{Y}_l^2} \quad (10)$$

A transport equation for liquid surface density, $\tilde{\Omega}$, is postulated by analogy with the flame surface density.

$$\frac{\partial \bar{\rho} \tilde{\Omega}}{\partial t} + \frac{\partial \bar{\rho} \tilde{\Omega} \tilde{U}_j}{\partial x_j} = \frac{\partial}{\partial x_j} \left(\bar{\rho} \frac{v_t}{Sc_t} \frac{\partial \tilde{\Omega}}{\partial x_j} \right) + \bar{\rho} \cdot \left(\tilde{\Omega}_{init} + \tilde{\Omega}_{mean} + \tilde{\Omega}_{turb} + \tilde{\Omega}_{coll} + \tilde{\Omega}_{coal} \right) + S_{EL}^{\tilde{\Omega}} \quad (11)$$

Where $\tilde{\Omega}_{init}$, $\tilde{\Omega}_{mean}$, $\tilde{\Omega}_{turb}$, $\tilde{\Omega}_{coll}$, and $\tilde{\Omega}_{coal}$, are the initial, mean, turbulence, collision and coalescence value of liquid/gas surface density respectively; $S_{EL}^{\tilde{\Omega}}$ is the source term of the liquid/gas interface. Beau, 2006 [5] introduced other notion of liquid/gas interface per unity of mass that is defined as $\tilde{\Omega} = \tilde{\Sigma} / \bar{\rho}$ (m²/kg).

The production and destruction of liquid surface are accounted for the five liquid/gas surface densities. The first term source $\tilde{\Omega}_{init}$ in Eq. (11) permits to initialize the calculations since all other terms source are proportional to $\tilde{\Omega}$:

$$\tilde{\Omega}_{init} = \begin{cases} 2 \frac{v_t}{Sc_t} \frac{6\bar{\rho}}{\rho_l \rho_g L_t} \frac{\partial \tilde{Y}_l}{\partial x_i} \frac{\partial \tilde{Y}_l}{\partial x_i}, & \text{if } \tilde{Y}_l (1 - \tilde{Y}_l) \leq 0.001 \\ 2 \frac{v_t}{Sc_t} \frac{\tilde{\Omega}}{(1 - \tilde{Y}_l) \tilde{Y}_l} \frac{\partial \tilde{Y}_l}{\partial x_i} \frac{\partial \tilde{Y}_l}{\partial x_i}, & \text{otherwise} \end{cases} \quad (12)$$

L_t is the turbulent length scale.

Three next terms correspond to the production of liquid surface density due to the mean or turbulent stresses and due to the collisions:

$$\tilde{\Omega}_{mean} = \frac{\overline{\rho u_i'' u_j''}}{\bar{\rho} k} \frac{\partial \tilde{U}_i}{\partial x_j} \tilde{\Omega};$$

$$\tilde{\Omega}_{turb} = \frac{\tilde{\Omega}}{\tau_{turb}}; \quad \text{and}$$

$$\tilde{\Omega}_{coll} = \frac{\tilde{\Omega}}{\tau_{coll}}$$

(13)

τ_{turb} and τ_{coll} are the characteristic time scale of turbulence and collisions respectively and k is the turbulent kinetic energy.

The last term on the right hand side of Eq. (11) deals with destruction of surface density due to coalescence, $\tilde{\Omega}_{coal}$:

$$\tilde{\Omega}_{coal} = - \frac{1}{\tau_{coll}} \frac{\tilde{\Omega}^2}{\tilde{\Omega}_{crit}} \quad (14)$$

c). Transition Zone

We rely on a critical value of the Eulerian liquid volume fraction to decide whether it should turn from Eulerian to Lagrangian formulation (Beau, 2006 [5]). The Lagrangian droplets are formed where spray is assumed to be diluted enough. It follows the below equation.

$$\tilde{\Phi}_l = \tilde{Y}_l \frac{\bar{\rho}}{\rho_l} \leq \tilde{\Phi}_l^{crit} \quad (15)$$

where $\tilde{\Phi}_l^{crit}$ is the critical value of the Eulerian liquid volume fraction.

The transitional criterion is based on the value of liquid volume fraction that is linked to the ratio of mean free path between two droplets and mean equivalent radius of the droplets in the cell. In our calculation, the transition is done when the liquid volume fraction becomes lower than 0.01 [2]. The transition zone is composed of the computational cells that form the border with the dense zone (i.e. zone where the liquid volume fraction is greater than 0.01) and only one parcel is generated per transition cell and per time step.

The velocity of the droplets is defined as

$$\bar{U}_{l,i} = \tilde{U}_i + \frac{\overline{\rho u_i'' y''}}{\bar{\rho} \tilde{Y}_l} \quad (16)$$

The diameter of the droplet is equal to the Sauter Mean Diameter

$$D_{32} = \frac{6\tilde{Y}_l}{\rho_l \tilde{\Omega}} \quad (17)$$

The number of droplets per generated parcel n_{drop} is obtained from mass conservation

$$n_{drop} = \frac{\bar{\rho} \tilde{Y}_l V_{cell}}{\pi/6 \rho_l D_{32}^3} \quad (18)$$

where V_{cell} is the volume of one transitional cell

Table 1. Basis Parameters

Ambient pressure	Injection pressure	Ambient Temperature	Fuel Density
3.53 MPa	80 MPa	293 K	822.10 kg/m ³

MODEL VALIDATION SETUP

GEOMETRY AND BOUNDARY CONDITIONS

The geometry is to simulated an outflow of a non-cavitating single-hole injector (tapered nozzle), with an outlet diameter of 112 μm . The chamber has a size of 80×25mm. Some physical key parameters of chamber and spray are depicted in [table 1](#).

This nozzle presents a variable velocity profile input at the nozzle exit that is showed in [Figure 2](#). This is an average measure, not an instantaneous realization. The great irregularity showed in this picture seems to be an effect of wave reflections inside the nozzle (see R. Payri et al., 2008 [22] or J. Gimeno, 2008 [8] for more details about this issue).

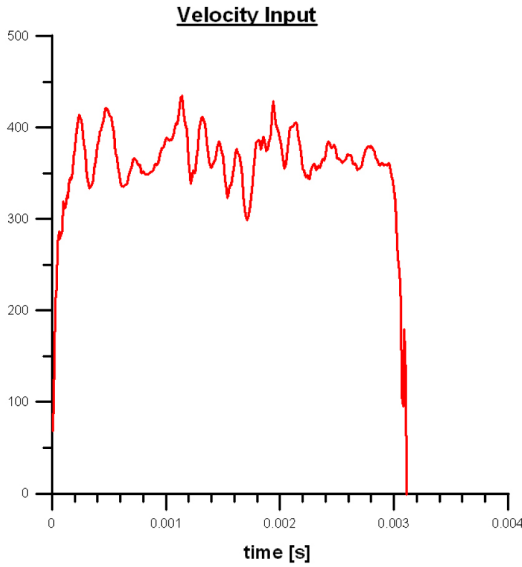


Figure 2. Velocity Profile (m/s).

In our computational cases we simulate the maximum time of 2ms, as the measurement obtained in CMT are matched well with our computational cases and velocity as explicitly shown in the later results. Moreover, the most important reason is the computational time is quite long especially once many droplets formed in ELSA modeling when time increased.

As this is axis-symmetric nozzle, a first approximation to this sort of problems is to perform 2D simulations. Of course, turbulence and engines are always 3D, but, as a first approximation to the real problem, 2D simulation can model reasonably the spray behavior. In our calculation, 2D

simulations are actually a 3D simulation with only a cell in the azimuthal direction, modeling a 5° sector of the spray. This is showed in the rightmost part of [Figure 4](#), where we also show the boundary conditions imposed on the spray and chamber. [Figure 3](#) depicts the front view of two typical meshes.

Generally, the requirements for mesh structure are especially important at the nozzle, where the mesh size has to be small enough to capture the spray structure and droplets. The criterion used in this paper is to define the size of the first cell and then extrude the mesh, fixing the axial and radial ratio. The six cases studied in this paper are showed in [table 2](#).

In [table 3](#) we have the main formula based on the successive ratio used in constructing our meshes are showed. In these equations: l_1 is length of the first interval of the edge, l_n is length of the n interval of the edge, R is the interval length ratio, n is the number of intervals and L stands for the total edge length [11]. The sixth case is a little bit different. Instead of using first/last ratio of 72 on the axial direction, and the last/first ratio equal to 0.006 on the radial direction, we have taken the first segment of the mesh with $\Delta x_1 = \Delta z_1 = l_1 = 0.2R_{inj} = 0.1D_{inj} = 11.1 (\mu\text{m})$, and have used the same number of segments in the axial edge and radial edge, 218 and 25, respectively.

For the completeness, three different configurations with 3-, 5-, and 10-cell at the half of the nozzle are used (note that only half of the nozzle is simulated). In all of these cases we have fixed Δt in 10^{-8} , obtaining Courant numbers below 0.3. Mesh structures can be seen in [Figure 3](#) with a zoom of the near nozzle region.

The RANS turbulent model chosen for our validation is the $k - \varepsilon$ /High Reynolds Number, those equations are

$$\frac{\partial \tilde{k}}{\partial t} + \tilde{u}_j \frac{\partial \tilde{k}}{\partial x_j} = C_\mu \frac{\tilde{k}^2}{\tilde{\varepsilon}} \left(\frac{\partial \tilde{u}_i}{\partial x_j} + \frac{\partial \tilde{u}_j}{\partial x_i} \right) \frac{\partial \tilde{u}_i}{\partial x_j} + \frac{\partial}{\partial x_j} \left(\frac{C_\mu \tilde{k}^2}{\sigma_k \tilde{\varepsilon}} \frac{\partial \tilde{k}}{\partial x_j} \right) - \tilde{\varepsilon} \quad (19)$$

and

$$\frac{\partial \tilde{\varepsilon}}{\partial t} + \tilde{u}_j \frac{\partial \tilde{\varepsilon}}{\partial x_j} = C_{\varepsilon_1} C_\mu \tilde{k} \left(\frac{\partial \tilde{u}_i}{\partial x_j} + \frac{\partial \tilde{u}_j}{\partial x_i} \right) \frac{\partial \tilde{u}_i}{\partial x_j} + \frac{\partial}{\partial x_j} \left(\frac{C_\mu \tilde{k}^2}{\sigma_\varepsilon \tilde{\varepsilon}} \frac{\partial \tilde{\varepsilon}}{\partial x_j} \right) - C_{\varepsilon_2} \frac{\tilde{\varepsilon}^2}{\tilde{k}} \quad (20)$$

The constants of the model are listed in [table 4](#). We are using the classical constants used in most of the spray calculation. However, as it is also known few decades back by Pope,

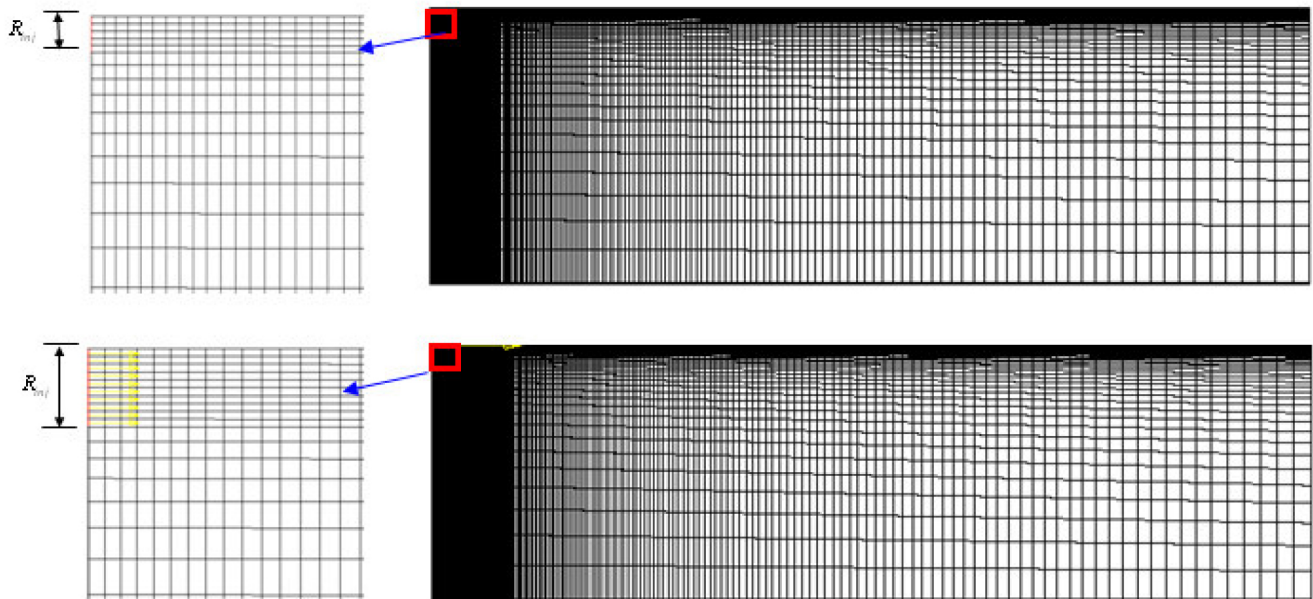


Figure 3. Computational meshes and detailed views (on the left side), for 5 cells and 10 cells at the same nozzle radius.

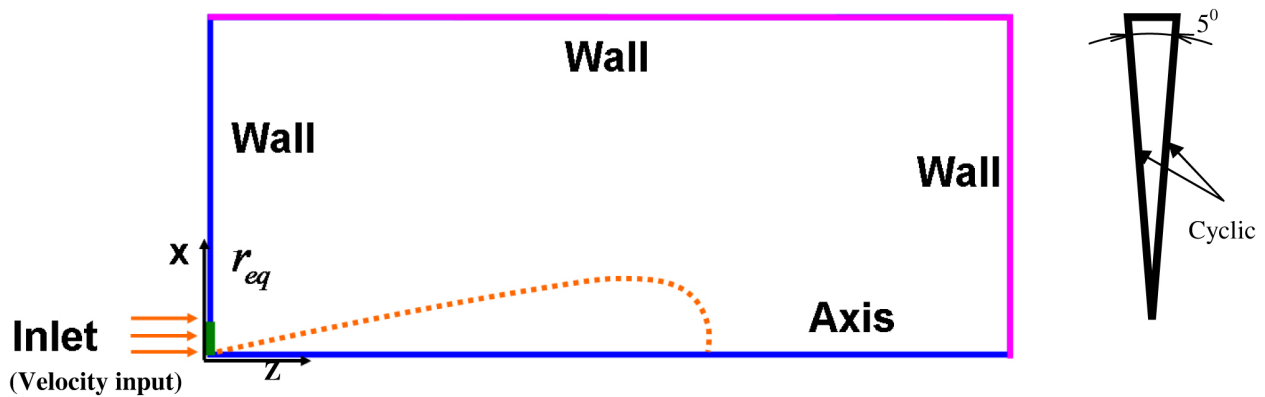


Figure 4. Geometry (front view and side view) & Boundary Condition.

1978 [20], the classical value of C_{ϵ_1} causes an overprediction of the spreading and decay of rate of a round jet flow.

The C_{ϵ_1} constant modifications are based on the suggestion of (J. Janicka et al., 1982 [13] and Dally B.B., 1998 [7]). Thus, we have used classical value $C_{\epsilon_1}=1.44$ the suggested value $C_{\epsilon_1}=1.60$ and an average value of 1.52 that in some cases give a better approximation. The turbulent Prandtl number has been set to 1 in order to produce similar solutions for the conservation equations of axial momentum, fuel mass and energy. Noting that the Prandtl (K.E.) in table 4 is another Prandtl constant which is only used for solving the k- ϵ equations which is well-known in CFD calculation and

mentioned again in Diesel spray by Lebas and Blokkeel et al., 2005 [14].

Experimental Validation

The numerical results are compared with experimental data at CMT-Motores Térmicos. Experimental results have been obtained from quiescent vessel tests previously published in R. Payri et al., 2008 [22], and J. Gimeno, 2008 [8].

The injection velocity profile comes from measurements of mass and momentum fluxes performed in a pressurized test rig with nitrogen. Mass flow rate for the velocity inlet was measured by means of Bosch's method (Bosch, 1966 [4]) The momentum flux measuring principle of this technique is explained in two references of R. Payri et al., 2005 [21], and J. Gimeno, 2008 [8], and consists of measuring the impact

Table 2. Mesh parameters

Case No.	No cells at the half of nozzle	No. axial cells	Axial ratio (First/Last ratio)	No. radial cells	Radial ratio (Last/First ratio)	Total Vertices	Total Cells
1	3	218	72	45	0.006	19929	9810
2	5	218	72	25	0.006	11,169	5450
3	5	218	72	45	0.006	19,929	9,810
4	5	435	72	90	0.006	78,916	39,150
5	10	250	143	50	0.003	25,351	12,500
			First length		First length		
6	5	218	11.1 μm	25	11.1 μm	11,169	5450

Table 3. Successive Ratio of Mesh edges

Successive Ratio	Last/First ratio	First/Last ratio	First Length
Formula	$R = \left(\frac{l_n}{l_1}\right)^{1/(n-1)}$	$R = \left(\frac{l_1}{l_n}\right)^{-1/(n-1)}$	$\sum_{i=1}^n R^{i-1} = \frac{L}{l_1}$

Table 4. Turbulence Models

	C_μ	C_{ε_1}	C_{ε_2}	C_{ε_3}	C_{ε_4}	Prandtl (K.E.)	Prandtl (Eps)
Turb 1	0.09	1.44	1.92	1.44	-0.33	1	1.219
Turb 2	0.09	1.52	1.92	1.44	-0.33	1	1.219
Turb 2	0.09	1.60	1.92	1.44	-0.33	1	1.219

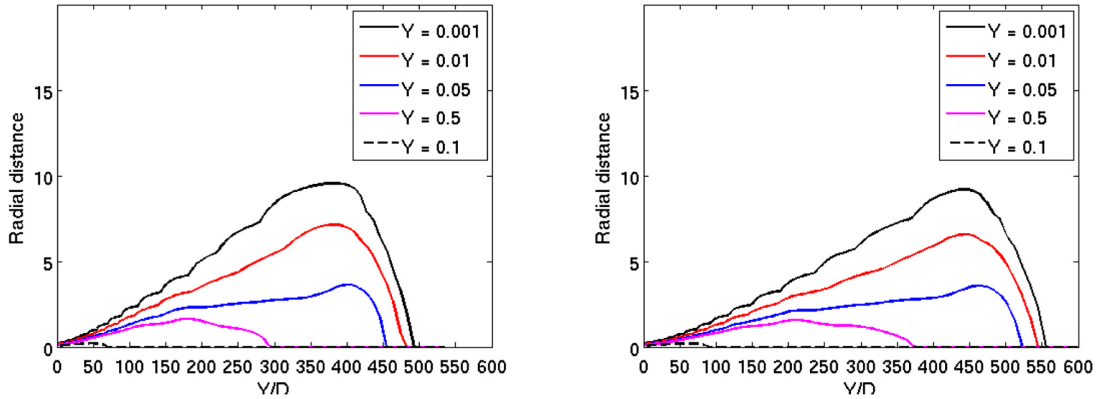


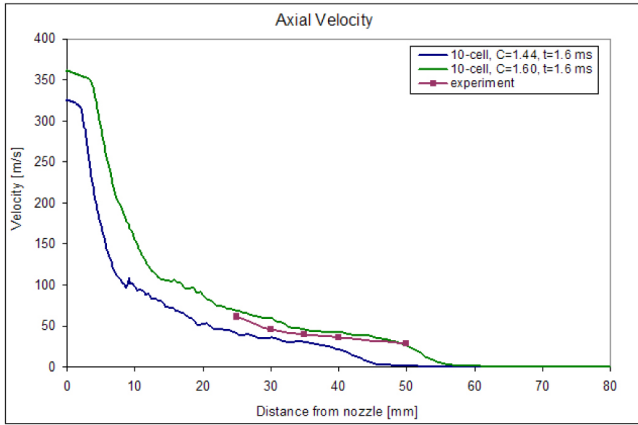
Figure 5. Comparison of iso-surfaces of 5-cell at 2ms, case 2 with $C_{\varepsilon_1} = 1.52$ (left figure) and $C_{\varepsilon_1} = 1.60$ (right figure).

force of the spray in a surface with a piezo-electric sensor. As long as the whole cross-section of the spray impacts on the sensor, the measured force equals to the momentum flux at that cross section. If the measurement position is close to the nozzle exit, the time evolution of the impact force is equal to the nozzle (hole) momentum flux, M_o .

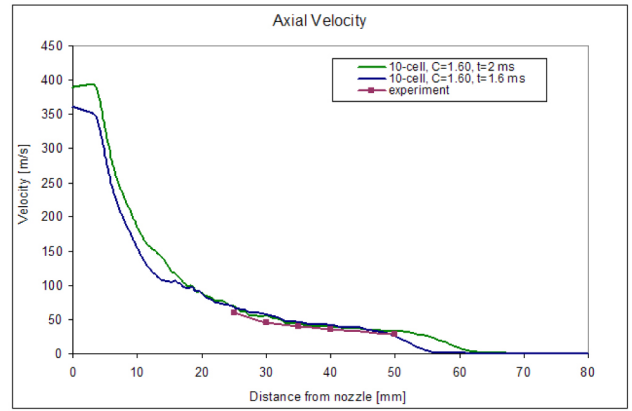
NUMERICAL RESULTS

The C_{ε_1} effect of the penetration can be clearly seen in Figure 5, where several iso-surfaces of liquid mass fraction are shown. The longer axial distance of approximately 570 is obtained with $C_{\varepsilon_1} = 1.60$, while it is only 490 with $C_{\varepsilon_1} = 1.52$.

It is clear from the figures, the effect of C_{ε_1} reduces spray dispersion and consequently increases spray penetration.

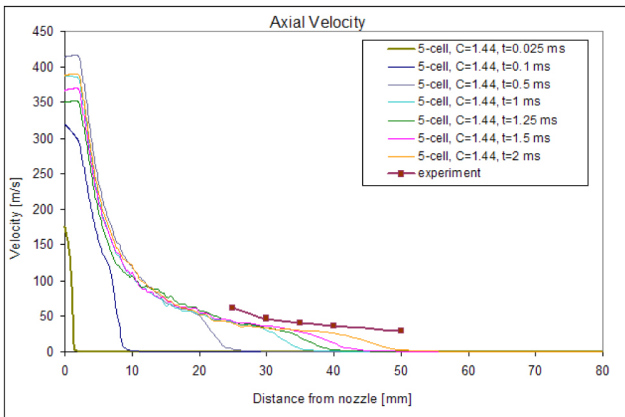


(a)

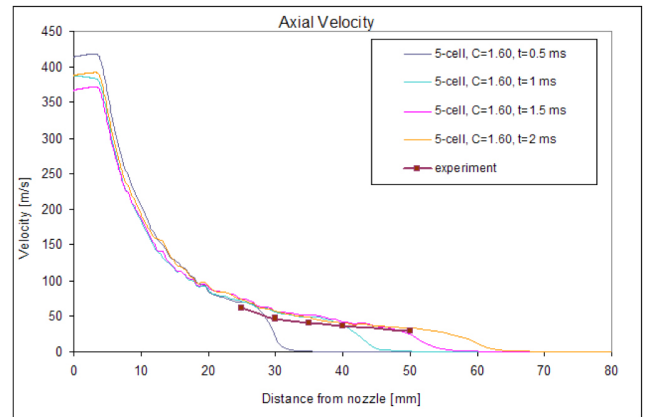


(b)

Figure 6. Axial velocity for $0.1 R_{inj}$ cases: (a) Changes in C_{ϵ_1} , (b) Changes in time.



(a)



(b)

Figure 7. Comparisons of Axial velocity: (a) $C_{\epsilon_1} = 1.44$; (b) $C_{\epsilon_1} = 1.60$.

In the case of axial velocity, this effect is also very clear as can be seen in Figure 6, where the comparison of axial velocity for 10-cell case corresponding to two turbulent constants (1.44 and 1.60) at $t=1.6$ ms are illustrated. The matching of $C_{\epsilon_1}=1.60$ is better than in the case of $C_{\epsilon_1}=1.44$. Moreover, it seems to be clear from the figure that in the latter case, spray penetration is not enough to show an appreciable axial velocity at 50 mm from the nozzle. This result is also clear in the Figure 7, where we only have 5 cells at the nozzle. Clearly, $C_{\epsilon_1}=1.44$ is underpredicting the axial velocity, whereas the 1.60 value gets more accurate results.

In Figure 8, a full view of droplet profile combined with the velocity in the same plot and a detailed view of the dense zone are depicted for 5-cell case (case no. 3), with turbulent constant equal to 1.60 at $t = 2$ ms. The first three figures on the left hand side are only depicted the velocity profile, and the last figure is illustrated both droplets and velocity. As it is

expected, it confirms that velocity magnitude is highest in the zone next to the nozzle/inlet boundary and in the liquid core zone where the Eulerian approach is used. The farther distance from axial and radial edge, the less velocity we obtained. The last figure on the right hand side captures both velocity profile and the droplets, which are generated in regions where the velocity are approximately below 150 m/s.

The droplet formation is showed in Figure 9. According to the above description, the droplet formation starts at the transition zone and continue to develop in the farther zone (Lagrangian zone). As it was also expected, there is no droplet in the Eulerian mixture zone (regions contained the red color and its closed surroundings). These figures confirm that the initial setting and formulae for ELSA model are correctly captured in the final result. The Sauter Mean Diameters range from $8.88e-9 \mu\text{m}$ to $4.896 \mu\text{m}$ in our computational cases, which is smaller than the smallest cell as stated in the previous part.

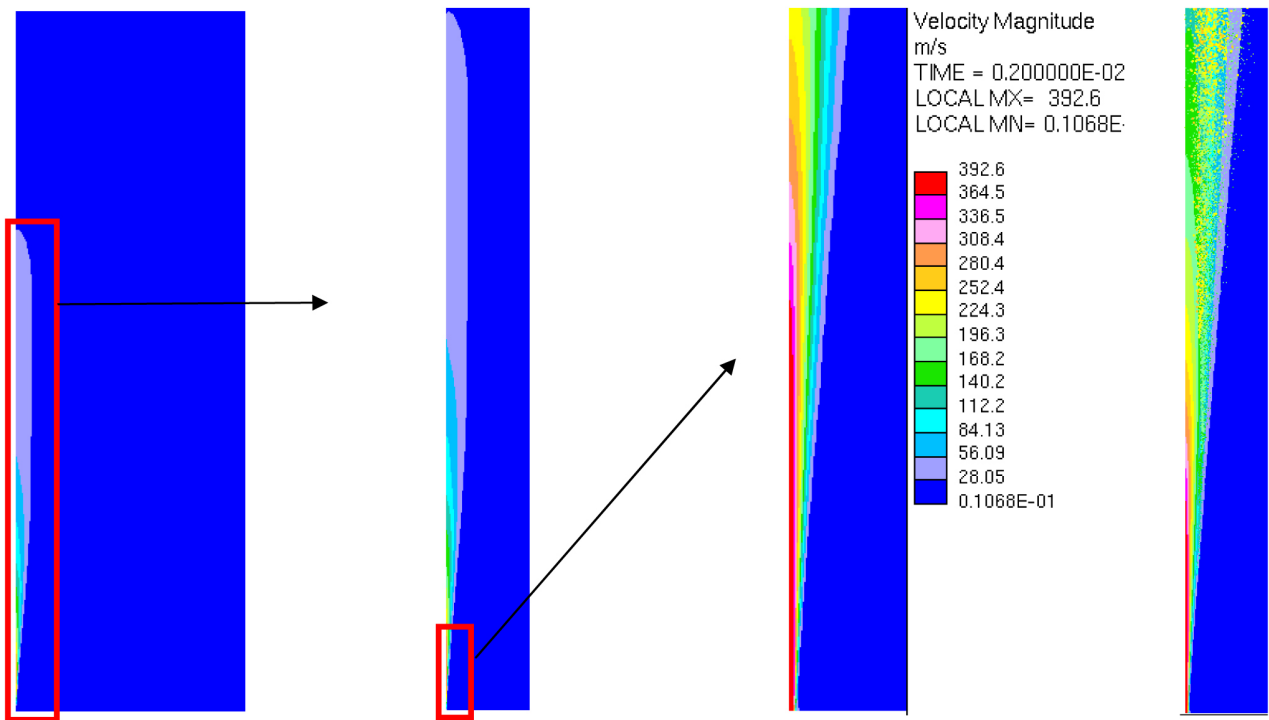


Figure 8. Velocity profile and droplet formation.

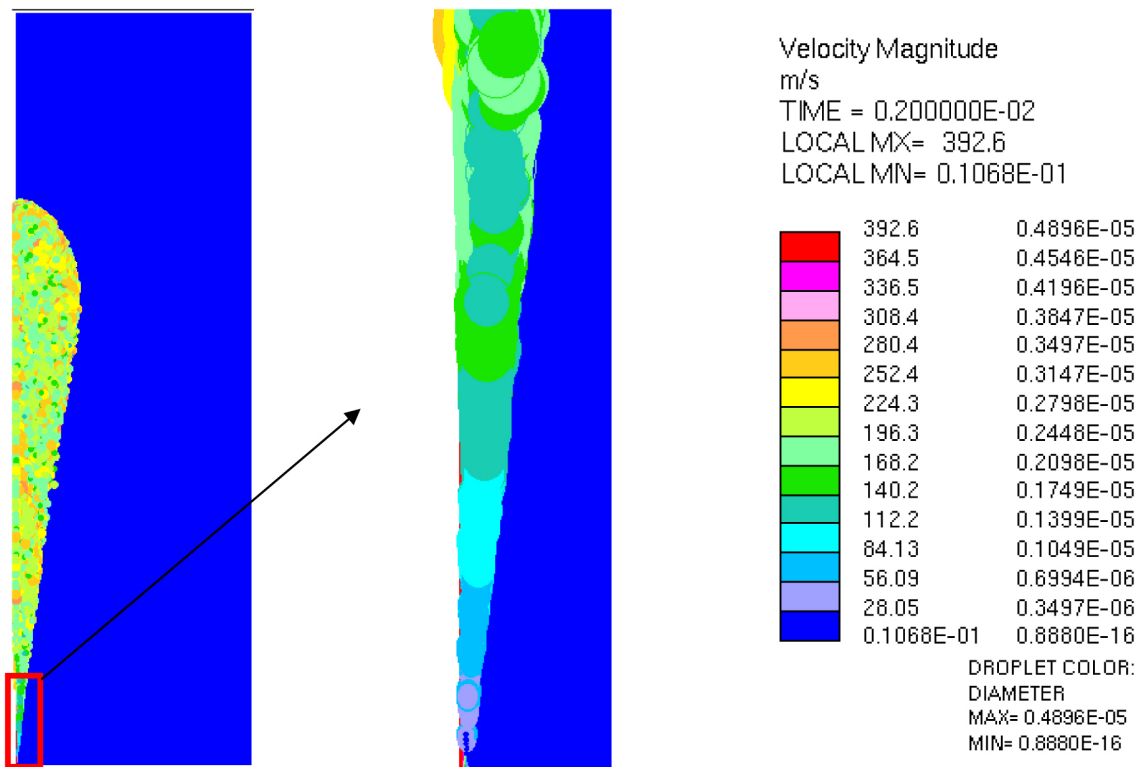


Figure 9. Droplet profile.

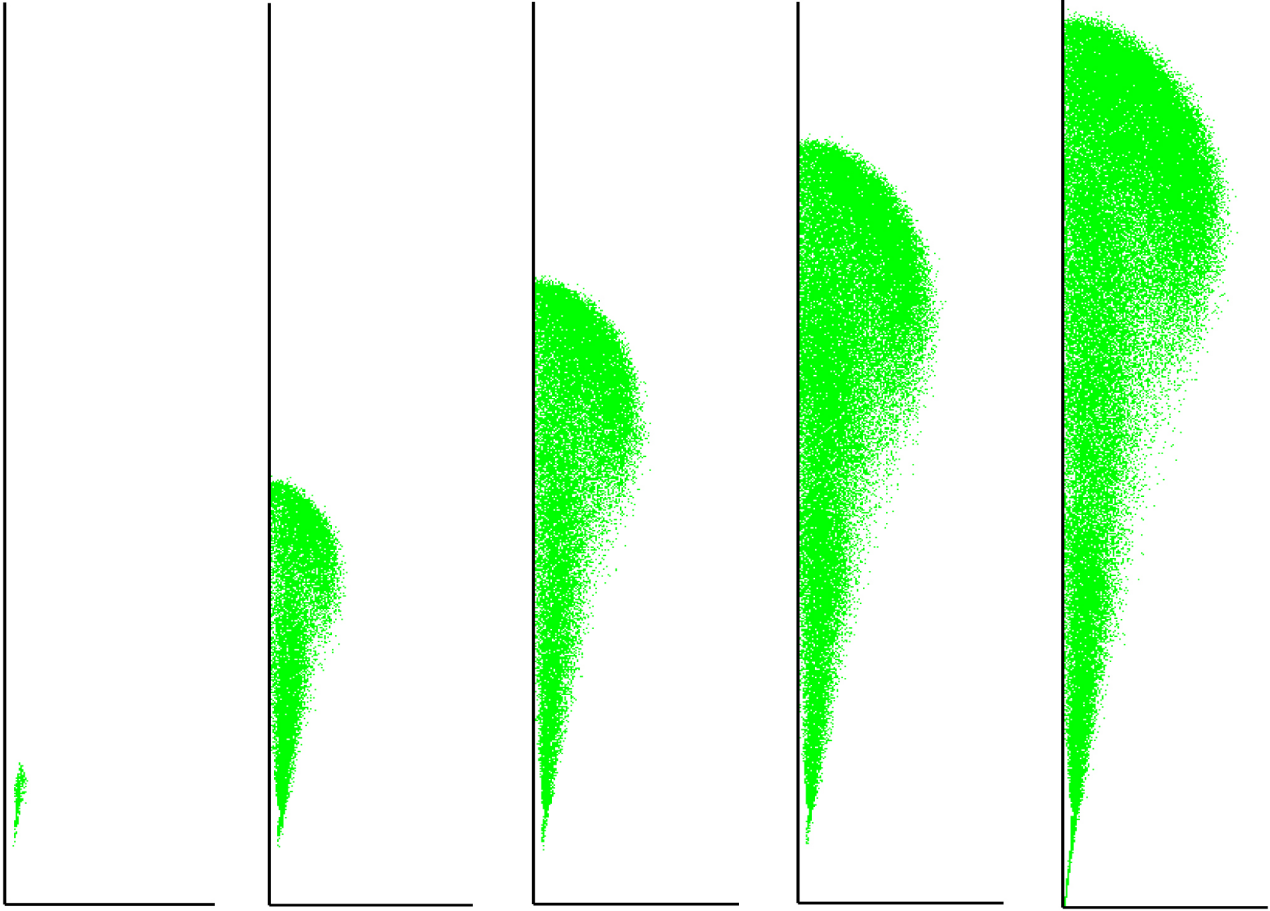


Figure 10. Droplet profiles at different time of 0.1, 0.5, 1, 1.5, and 2 ms (from left to right) for case 3, $C_{\varepsilon_1} = 1.44$.

Table 5. Droplet Information

	Time (ms)	Active Droplets	Evaporated / Disappeared / Absorption Droplets	Total Droplets
5-cell, $C_{\varepsilon_1} = 1.44$	2	69101	422,994	492,095
5-cell, $C_{\varepsilon_1} = 1.60$	2	125,739	529,320	655,059
10-cell, $C_{\varepsilon_1} = 1.44$	1	706	3,734	4,440
10-cell, $C_{\varepsilon_1} = 1.44$	1.5	78,894	398,061	476,955
10-cell, $C_{\varepsilon_1} = 1.44$	1.75	87,969	440,249	528,218
10-cell, $C_{\varepsilon_1} = 1.60$	2	107,549	630,334	737,883

Figure 10 shows the evolution of droplets in various time steps of 0.1, 0.5, 1, 1.5, 2 ms respectively for the case with 5 cells at nozzle radius. In those plots, all the droplets have the same size for the sake of visibility, independently of their actual diameter as already shown in Figure 9. A summary of the active and inactive droplets are shown in table 5. The total number of generated droplets increase rapidly after each time step for all the C_{ε_1} values. As an example, the case with 10-

cell, $C_{\varepsilon_1} = 1.44$, for $t = 1, 1.5,$ and 1.75 in table 5 accumulated 4440, 476955, and 528218 droplets respectively. Several reasons could lead to the disappearance of droplets such as the evaporation due to the high temperature or their absorption into the Eulerian zone, where the flow is treated as a monophasic fluid.

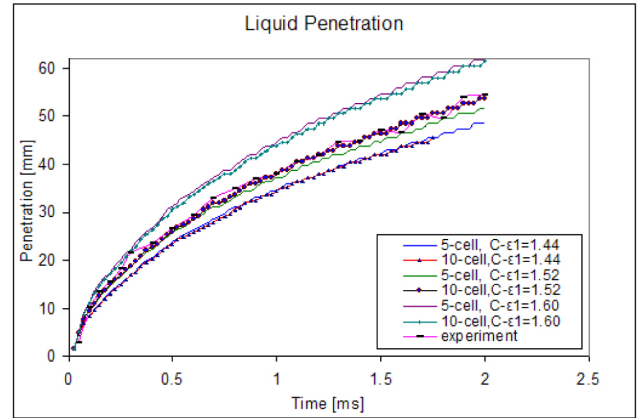
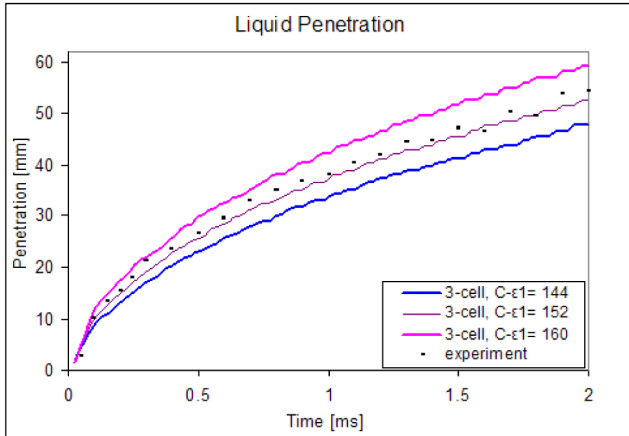
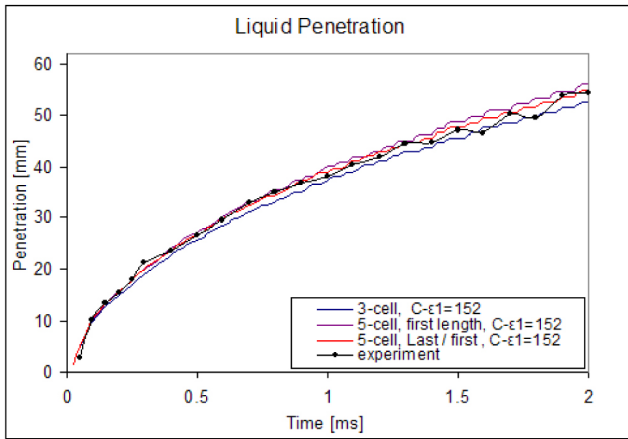
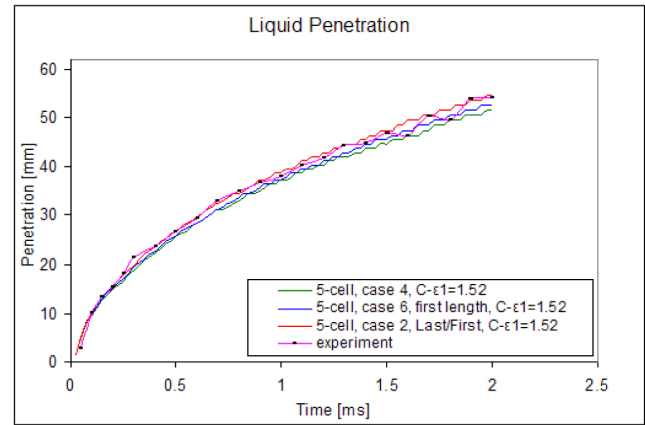


Figure 11. Spray penetration of the case with 3 cells and 5 cells.



(a)



(b)

Figure 12. Comparison of spray penetration.

Penetration rates also show a great dependency on the value of C_{ϵ_1} . Results on the penetration are showed in Figure 11 and 12. In this case, it is clear that the value of 1.60 is overpredicting the penetration, while 1.44 is underpredicting in Figure 11, and for all the meshes has been tested so far. Hence, we have used a third value of 1.52 and we obtain the best fit with various meshes.

While the Figure 12 (a) illustrate the difference between 3- and 5-cell meshes, the averaged numerical errors of 3-cell case (case 1) is 0.9% whereas the 5-cell case with the first length equal to $11.1 \mu\text{m}$ (case 6) is 1%, and 5-cell case with last/first ratio (case 2) is only 0.42% as plotted in Figure 12 (b) and the detailed difference of representative errors are depicted in the Figure 13. The variance between 3-cell case and 5-cell case as in Figure 12 (a) is quite large in comparison with the discrepancy from 5-cell to 10-cell cases in Figure 11 (b). Using the same constant $C_{\epsilon_1} = 1.52$, it only

takes **138451** seconds (~ 39 hours) to complete one parallel calculation consisted of 6 processors for 5-cell case (case no. 3), while it must need **517741** seconds (~ 144 hours) to complete one parallel calculation consisted of 12 processors for 10-cell case (case no. 5). Hence, the 5-cell mesh with last/first ratio consisted of 25 radial cells, and $C_{\epsilon_1} = 1.52$ is the optimal setup, it should be enough for using the future RANS calculation of this nozzle diameter.

SUMMARY/CONCLUSIONS

In this study, several test cases are employed to have an initial validation of the ELSA model implemented in Star-CD. Mesh independency and the effect of changing C_{ϵ_1} constant are explored. All the simulations have been made in 2D meshes, considering axis-symmetric problems and have been validated against experimental data of a well characterized nozzle.

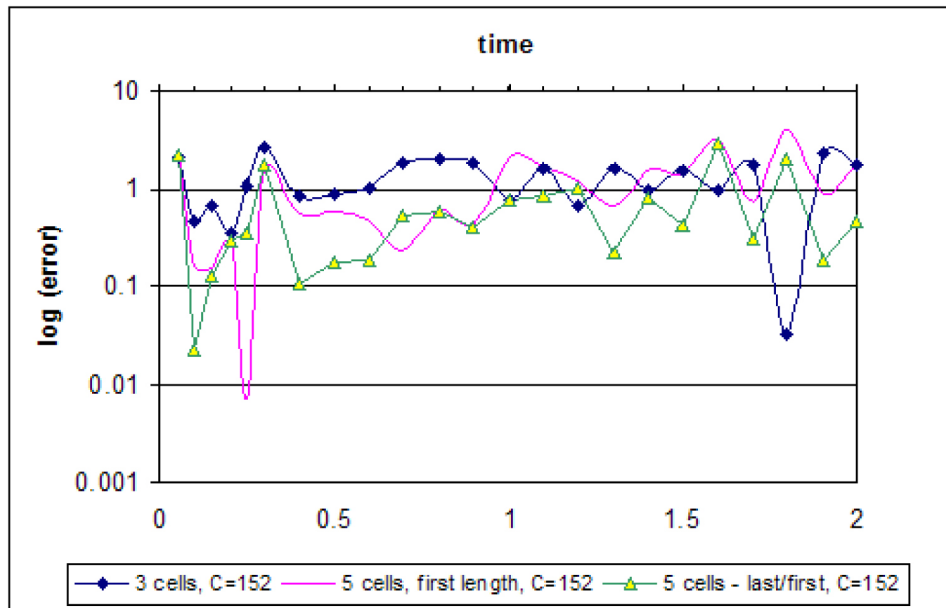


Figure 13. Numerical errors of 3-cell and 5-cell cases with turbulent constant = 1.52.

Two major conclusions are obtained from this work. Firstly, the classical value of C_{ϵ_1} , 1.44, leads to an overpredicting of the penetration, while the typical value used in sprays, 1.60, causes overprediction. Secondly, mesh independency is obtained with only 5-cell at the nozzle radius, which satisfies the reasonable result, permits a considerable saving in computational time and storage space. The best fit in the penetration curve is obtained for $C_{\epsilon_1} = 1.52$.

Obviously, a couple of 2D simulations are not a completed validation of the code. It is planned to continue with two other experimental cases analyzed in our institute, a full 3D simulation of the three nozzles, and last but not least, the effect of a cavitating nozzle.

REFERENCES

1. Araneo, L, Soare, V, Payri, R, Shakal, J (2006). Setting up a PDPA system for measurements in diesel spray. J Phys: Conf Ser 2006; 45:85-93.
2. Hoyas, S., Pastor, J., Khuong-Anh, D., Mompó-Laborda, J. et al., "Application and Evaluation of the Eulerian-Lagrangian Spray Atomization (ELSA) Model on CFD Diesel Spray Simulations," SAE Technical Paper [2011-37-0029](https://doi.org/10.4271/2011-37-0029), 2011.
3. Doudou, A., Turbulent flow study of an isothermal diesel spray injected by a common rail system, Fuel, Volume 84, Issues 2-3, January-February 2005, Pages 287-298.
4. Bosch, W., "The Fuel Rate Indicator: A New Measuring Instrument For Display of the Characteristics of Individual Injection," SAE Technical Paper [660749](https://doi.org/10.4271/660749), 1966, doi: [10.4271/660749](https://doi.org/10.4271/660749).
5. Beau, PA (2006). Modelisation de l'atomisation d'un jet liquide - Application aux sprays diesel. Ph.D. Thesis, University of Rouen.
6. Blokkeel, G., Barbeau, B., and Borghi, R., "A 3D Eulerian Model to Improve the Primary Breakup of Atomizing Jet," SAE Technical Paper [2003-01-0005](https://doi.org/10.4271/2003-01-0005), 2003, doi: [10.4271/2003-01-0005](https://doi.org/10.4271/2003-01-0005).
7. Dally, B.B.: Flow and Mixing Fields of Turbulent Bluff-Body Jets and Flames, Combust.Theory Modelling, Band 2, S. 193-219 (1998).
8. García, D. Jaime Gimeno (2008). Desarrollo y aplicación de la medida del flujo de cantidad de movimiento de un chorro Diesel, PhD thesis, Universidad Politécnica de Valencia.
9. De Lucas, M (2007). Contribution a la modelisation de la pulverisation d'un liquide phytosanitaire en vue de reduire les pollutions. Ph.D. Thesis, University of Aix-Marseille II.
10. Faeth, G., Hsiang, L.-P., and Wu, P.-K. (1995). Structure and breakup properties of sprays. Int. J. Multiphase Flow, 21:99-127.
11. Fluent, Gambit manual 13, Fluent, Inc. 05/03/00.
12. Faeth, G. M., Hsiang, L. -P., Wu, P. -K., Structure and breakup properties of sprays, International Journal of Multiphase Flow, Volume 21, Supplement 1, December 1995, Pages 99-127.
13. Janicka, J., Peters, N., Prediction of turbulent jet diffusion flame lift-off using a PDF transport equation, in: Symposium (International) on Combustion, vol. 19, 1, 1982, pp. 367-374.

14. Lebas, R., Blokkeel, G., Beau, P., and Demoulin, F., "Coupling Vaporization Model With the Eulerian-Lagrangian Spray Atomization (ELSA) Model in Diesel Engine Conditions," SAE Technical Paper [2005-01-0213](#), 2005, doi: [10.4271/2005-01-0213](#).

15. Lebas, R. (2007). Modelisation Eulerienne de l'Atomisation haute pression - Influences sur la vaporisation et la combustion induite. Ph.D. Thesis, University of Rouen.

16. Lee, S. and Reitz, R. (2001). Effect of liquid properties on the breakup mechanism of high-speed liquid drops. *Atomization and Sprays*, 11:1-19.

17. Lefebvre, A.H. (1989). *Atomization and sprays*, Taylor and Francis.

18. Naber, J. and Siebers, D., "Effects of Gas Density and Vaporization on Penetration and Dispersion of Diesel Sprays," SAE Technical Paper [960034](#), 1996, doi: [10.4271/960034](#).

19. Ning, W, Reitz, RD, Lippert, AM and Diwakar, R (2007). Development of a next generation spray and atomization model using an Eulerian-Lagrangian methodology. 17th Int. Multidimensional Engine Modeling User's Group Meeting, Detroit, MI.

20. Pope, S.: An explanation of the turbulent round-jet/plain-jet anomaly. *AIAA J.* 16, 279-281 (1978).

21. Payri, R., García, J.M., Salvador, F.J. and Gimeno, J. (2005). Using spray momentum flux measurements to understand the influence of Diesel nozzle geometry on spray characteristics, *Fuel* 84, pp. 551-561.

22. Payri, R., Tormos, B., Salvador a, F.J., Araneo, L. (2008). Spray droplet velocity characterization for convergent nozzles with three different diameters. *Fuel* 87, pp 3176-3182.

23. Tanner, F. (2004). Development and validation of a cascade atomization and drop breakup model for high-velocity dense sprays. *Atomization and sprays*, 14:20-32.

24. Vallet, A, Burluka, AA and Borghi, R (2001). Development of a Eulerian model for the atomization of a liquid jet. *Atomization and sprays*, vol. 11, pp. 619-642.

CONTACT INFORMATION

Sergio Hoyas, J.M. Pastor, Dung Khuong-Anh, Juan Manuel Mompó-Laborda

CMT - Motores Térmicos (Department of thermal engine)
Universidad Politécnica de Valencia.

Camino de Vera S/N, 46022
Valencia, Spain

E-mail: (serhocal, jopasen, ankh2, juamomla) @mot.upv.es

F. Ravet

Renault

1 Avenue du golf 78288

Guyancourt, France

frederic.ravet@renault.com

ACKNOWLEDGMENTS

The authors would like to thank the referee for his/her comments, which have greatly improved the article. This work has been granted by Renault and VECOM (Vehicle Concept Modeling) - EU FP7 Marie Curie Initial Training Network (ITN) Grant Agreement 213543 (from October 1st, 2008 to September 30, 2012). The aim of the proposed training network is to provide dedicated research training in the emerging field of vehicle concept modeling for up-front pre-CAD functional performance engineering, bridging between industry and academia across Europe. Authors also acknowledge the support of the Spanish Government in the frame of the Project "Métodos LES para la simulación de chorros multifásicos", Ref.ENE2010-18542, the Universidad Politécnica de Valencia under the contract Reference PAID-2759 and the Generalitat Valenciana, under the contract GV/2010/039.

DEFINITIONS/ABBREVIATIONS

CAD

Computer-aided Design

CMT

CMT Motores Térmicos

CFD

Computational Fluid Dynamics

DDM

Discrete Droplet Model

ICE

Internal Combustion Engine

ELSA

Eulerian-Lagrangian Spray Atomization

ITN

Initial Training Network

PDDPA

Phase Doppler Particle Analyzer

SMD
Sauter Mean Diameter

VECOM
Vehicle Concept Modeling

NOMENCLATURE

l
liquid

g
gas

i, j
direction in space

k
turbulent kinetic energy

$\bar{\Sigma}$
quantity of liquid/gas interface per unit of volume

D_{32}
Sauter Mean Diameter

n
drop number density (drop number per unit of volume)

n_{drop}
number of droplets per generated parcel

ρ
density

$\bar{\rho}$
mean density

Sc_t
turbulent Schmidt number

τ_{turb}
characteristic time scale of turbulence

τ_{coll}
characteristic time scale of collision

ν_t
liquid viscosity

\bar{P}
the mean pressure

L_t
turbulent length scale

R_g
the gas constant

$S_{EL}^{\tilde{Y}_l}$
source term when droplet generation during the transition from Eulerian to Lagrangian formulation

$S_{EL}^{\bar{\Omega}}$
source term of the liquid/gas interface

T_g
the mixture temperature

$\tilde{\Phi}_l^{crit}$
critical value of the Eulerian liquid volume fraction

\tilde{U}_i
Favre averaged mean velocity

\tilde{Y}_l
mean liquid mass fraction

$\tilde{\Omega}$
liquid/gas interface per unity of mass

$\tilde{\Omega}_{mean}$
mean value of liquid/gas surface density

$\tilde{\Omega}_{turb}$
turbulence value of liquid/gas surface density

$\tilde{\Omega}_{coll}$	collision value of liquid/gas surface density
$\tilde{\Omega}_{coal}$	coalescence value of liquid/gas surface density
$\tilde{\Omega}_{init}$	first source term
V_{cell}	volume of one transitional cell
l_1	length of the first interval of the edge
l_n	length of the n interval of the edge
R	the interval length ratio
n	the number of intervals
L	the total edge length

The Engineering Meetings Board has approved this paper for publication. It has successfully completed SAE's peer review process under the supervision of the session organizer. This process requires a minimum of three (3) reviews by industry experts.

All rights reserved. No part of this publication may be reproduced, stored in a retrieval system, or transmitted, in any form or by any means, electronic, mechanical, photocopying, recording, or otherwise, without the prior written permission of SAE.

ISSN 0148-7191

Positions and opinions advanced in this paper are those of the author(s) and not necessarily those of SAE. The author is solely responsible for the content of the paper.

SAE Customer Service:

Tel: 877-606-7323 (inside USA and Canada)

Tel: 724-776-4970 (outside USA)

Fax: 724-776-0790

Email: CustomerService@sae.org

SAE Web Address: <http://www.sae.org>

Printed in USA

A large-eddy simulation of diesel-like gas jets

Sergio Hoyas*, Antonio Gil,
Juan Manuel Mompó-Laborda and
Dung Khuong-Anh

CMT – Motores Térmicos,
Universidad Politécnica de Valencia,
Camino de Vera S/N, 46022 Valencia, Spain
E-mail: serhocal@mot.upv.es
E-mail: angime@mot.upv.es
E-mail: juamomla@mot.upv.es
E-mail: ankh2@mot.upv.es
*Corresponding author

Abstract: Some aspects of the transient evolution of diesel-like gas jets by means of large-eddy simulation (LES) are discussed in this work. In order to understand the relationship between the inlet boundary condition and the development of the turbulent motions of the diesel sprays, a 3D injection chamber is simulated. The main assumption of the setup is the turbulent gas jet theory hypothesis applied to the inlet boundary conditions. Validation of the results is achieved by comparing with both experimental diesel spray measurements and trusted Reynolds-averaged Navier-Stokes (RANS) simulations. Results show that reasonable simulation of turbulent patterns from one diameter distant from the inlet boundary condition is achieved.

Keywords: LES methods; diesel sprays; biphasic flows.

Reference to this paper should be made as follows: Hoyas, S., Gil, A., Mompó-Laborda, J.M. and Khuong-Anh, D. (2011) 'A large-eddy simulation of diesel-like gas jets', *Int. J. Vehicle Systems Modelling and Testing*, Vol. 6, Nos. 3/4, pp.268–282.

Biographical notes: Sergio Hoyas is an Associate Professor of Aerospace Engineering at the Universidad Politécnica de Valencia, and is also serving as a CFD Coordinator of the CMT-Motores Térmicos Research Institute. He holds a PhD in Applied Mathematics, and his expertise includes supercomputation and wall turbulence.

Antonio Gil is a Senior Lecturer of Civil Engineering at the Universidad Politécnica de Valencia, and is also a researcher at the CMT-Motores Térmicos Research Institute. He holds a PhD in Civil Engineering and has been working also in the industry for several years.

Juan Manuel Mompó Laborda finished his degree in Engineering (2009) with a six-month stay at the Yacht Research Unit (University of Auckland) and with the first Promoe scholarship to New Zealand that has been managed by the Polytechnic University of Valencia (Spain). In November 2009, he joined the CMT-Motores Térmicos for his doctoral thesis on LES of diesel sprays with OpenFOAM. Previously, he has participated in three R&D projects in his institute as a Research Fellow.

Dung Khuong-Anh graduated with a degree in Mechanical Engineering in 2005. He obtained his dual Master in Computational Mechanics from the Universitat Politècnica de Catalunya (2008) and École centrale de Nantes (2009), and his Master in Internal Combustion Engine from the Universidad Politécnica de Valencia (2011). His research interests are computational mechanics, FE, CFD and CAx. Currently, he works as a researcher for European Commission Marie Curie FP7 ITN 'VECOM' at UPV. His research activities include CFD simulation of direct injection diesel sprays within the framework of the Eulerian Lagrangian spray atomisation model in order to develop and validate a numerical tool for spray modelling in engine simulation and calculation.

1 Introduction

For engine designers, insight in the behaviour of an evaporating fuel spray is of great importance. Improvements in injection equipment reduce emissions and increase power by a more effective combustion process. Therefore, a deep understanding of the physics of diesel spray will provide some fundamental knowledge for the design of more efficient, less consuming and cleaner engines.

During the last years great advances on the comprehension of several physical phenomena in liquid jets and sprays have been achieved, both by means of diagnosis experimental tests and computational fluid dynamics (CFD) techniques. Simulation of turbulence is still one of the most challenging problems in physics and there is a general agreement that this simulation can be done within three levels of accuracy. The most used approaches to simulate turbulence are based on Reynolds-averaged Navier-Stokes (RANS). These computational methods are very useful to study the averaged flow, but they do not provide any information either about the turbulent fluctuations or about the flow on the jet boundary. Regarding diesel spray injection, the most commonly used codes in the automotive industry, until very recently, are based on this approach because of their reasonably accurate results and relatively lower computational cost. However, as the RANS approach has the highest level of modelling it can be seen as a successful interpolation between experimental datasets, and without a careful check of the results against experiments, little can be said. On the contrary, direct numerical simulation (DNS) methods solve all the significative scales of the flow, so no modelling is required and it provides the highest level of description of the flow. Since the smallest structures of the flow have to be solved, the computational cost increases as $Re^{9/4}$ and the resources required for most practical cases are above current computer hardware limitations (and will probably be in the next 20 years) (Jiménez, 2003; Hoyas and Jiménez, 2006). In this paper, we present an implementation of the third method: LES. It is computationally more expensive than RANS, but modelling required by RANS is reduced, and therefore it is more accurate. Furthermore, a detailed study of the flow characteristics in zones where turbulent fluctuations are significant is allowed by means of large-eddy simulation (LES), while RANS, by definition, cannot model these features. For a comprehensive description of these methods, the book of Pope (2000) is an excellent starting point.

As it has been said, LES increases the computational cost, but these methods are able to consistently simulate the complex structures related with turbulent mixing, which is

decisive in the injection and combustion processes and invisible for RANS solvers (Riley, 2006; Pitsch, 2006). A good knowledge of this part of the spray is crucial in order to reduce the diesel emissions. Apart from the turbulence modelling, the spray behaviour itself comprises a range of complex physical and chemical processes which are difficult to incorporate in the engine design or computer models. The nozzle internal flow greatly affects the fuel atomisation characteristics and so the subsequent engine combustion and exhaust emissions (Desantes et al., 2010; Payri et al., 2009b). The transient nature of the flow is greatly affected by the needle movement which associated with cavitation has dominated recent studies as the key phenomenon connecting internal flow and spray behaviour (Payri et al., 2009a; Margot et al., 2010). Thus, simulating the transient behaviour inside the nozzle (Payri et al., 2010) and predicting the real spray characteristics is of great importance.

Experimental information [refereed by Pastor et al. (2008)] shows that diesel sprays under both non-evaporising and vaporising conditions can be properly described with a mixing-controlled approach, and thus they can be analysed in the same way as a gas jets. However, since fuel-air mixing process is significantly influenced by fuel atomisation, breakup and collision, the idea to approximate the spray evolution using gas injection cannot be completely acceptable for LES due to its degree of physical description. LES was originally developed to deal with turbulence in single phase flows. Therefore, different approaches have been recently implemented in LES, in order to deal with this a priori complicated two-phase problem. The Eulerian-Eulerian (E-E) approach for two-phase flow has based models like the mesoscopic (Fevrier et al., 2005) or the volume of fluid (VOF) (Befrui et al., 2008). Regarding the Lagrangian-Eulerian (L-E) approach, a direct use in LES can be performed by taking into account the models needed for the sub-grid two-phase interaction (viscous work, dissipation rate, turbulent viscosity, heat flux, and species flux) (Bharadwaj and Rutland, 2010). Each of them has both advantages and disadvantages in the various regions of spray consisting of the dense zone and the downstream dilute zone. Hence, the Eulerian-Lagrangian spray atomisation (ELSA) is an integrated model for capturing the whole spray evolution in RANS calculations (Deportes et al., 2010). Consequently, LES of atomisation seems to be a necessary step forward as depicted by Chesnel et al. (2010).

The main goal of this work is to numerically investigate the influence of the inlet boundary conditions on a LES of the flow in a diesel fuel spray evaporation system. Therefore, in this paper, we limited ourselves to the numerical simulation of diesel-like gas jet in a combustion chamber. By including in future works those phenomena and conditions omitted here, the effect of more complex/realistic hypothesis on the physical behaviour of the spray will be noticed and its contribution on the fuel-air mixing process could be quantified. The results are compared with the classical numerical RANS method with both E-E and L-E approaches and are simultaneously validated with experimental data. Our algorithm has been implemented in the free all-purposes CFD code OpenFOAM.

The paper is structured as follows: after the introduction, the basis of the LES methodology and the main differences with RANS provide the needed mathematical background. In a subsequent section, the detailed description of the assumptions to set the boundary conditions together with the computational domain is presented. Finally, the numerical results with the main conclusions are exposed.

2 Numerical technique

As we said in the introduction, there are basically three types of methods to solve a CFD problem depending on the modelling and the description of turbulence: RANS, LES and DNS. DNS was the first developed method, but it is inapplicable in most practical cases. Both RANS and LES methods were developed more or less at the same time in the sixties. LES methods were first described by Smagorinsky in 1963 (Launder and Spalding, 1974) but, due to the computational resources required, it has not been widely applied in engineering until very recently.

Pope (2000), in his book gives an excellent introduction to LES that we are going to follow here. There are three conceptual steps in LES. First, define a filtering operation to decompose the velocity field as:

$$u(x, t) = \bar{u}(x, t) + u'(x, t). \quad (1)$$

Here, the filtered component \bar{u} represents the motion of the large scales while the small scale motions that occur on length scales smaller than the mesh spacing are included in the residual component u' . The motion of these sub-grid scales (SGSs) cannot be captured and therefore their effect on the large scales is modelled in a subsequent step.

In a second stage, the Navier-Stokes equations are spatially filtered assuming that the filtering operator is commutative with the differential operator. The filtering operation is defined as:

$$\bar{f}(x, t) = \int_{\Omega} G(x - x'; \Delta(x)) f(x', t) dx', \quad (2)$$

where G is the filter function and Δ is the filter width, here assigned to be the cube root of the local cell volume. As the isodense condition was set, the introduction of density filter quantities $\bar{f} = \overline{\rho f} / \bar{\rho}$ is negligible. A deep explanation can be found in Payri et al. (2010). In this study, the conservation equations governing the filtered velocity field $\bar{u}(x', t)$ are obtained by applying the filtering operation to the Navier-Stokes equation, for an incompressible flow of a Newtonian fluid. Thus, the filtered continuity equation and the filtered momentum equation become:

$$\nabla \cdot \bar{u} = 0, \quad (3)$$

$$\frac{\partial \bar{u}}{\partial t} + \nabla \cdot \overline{uu} = -\frac{1}{\rho} \nabla \bar{p} + \nu \nabla^2 \bar{u} - \nabla \tau, \quad (4)$$

where \bar{u} is the filtered velocity field, t is the time, \bar{p} is the filtered pressure, ρ is the fuel density, ν is the uniform kinematic viscosity and τ is the stress-like tensor ($\tau = \overline{uu} - \bar{u}\bar{u}$).

Notice that the filtered product \overline{uu} differs from the product of the filtered velocities $\bar{u}\bar{u}$. Equations (3) and (4) govern the evolution of the large (energy-carrying) scales of motion and the modelled stress term is τ . Also, this SGS stress tensor provides the communication between the resolved scales and the dissipation scales (Payri et al., 2010).

In the last step, closure is obtained by modelling the residual-stress tensor. The Smagorinsky (1963) model is used for the SGS tensor:

$$\tau_{ij}^d = -2\mu_{SGS}S_{ij}, \quad (5)$$

where τ_{ij}^d is the deviatoric SGS stress with:

$$\mu_{SGS} = \bar{\rho}(C_S\Delta^2)\|\widetilde{S}_{ij}\|$$

CS is the Smagorinsky constant, with a theoretical value in the interval (0.065–0.2) and $\|\widetilde{S}_{ij}\|$ is the Frobenius norm $\|\widetilde{S}_{ij}\| = \sqrt{2\widetilde{S}_{ij}\widetilde{S}_{ij}}$ of the filtered strain tensor,

$$\widetilde{S}_{ij} = \frac{1}{2}\left(\frac{\partial\overline{u}_i}{\partial x_j} + \frac{\partial\overline{u}_j}{\partial x_i}\right).$$

The Smagorinsky constant varies with both grid mesh aspect ratio as pointed out by Scotti et al. (1993) and the mean shear (Horiuti, 1993; Yakhot et al., 1989). Although some dynamic implementations of the Smagorinsky model allow to determine CS as a function of time and position (Piomelli and Liu, 1995; Germano, 1992), there is little to be gained by the use of more complex SGS models in the case of high Reynolds number free flows of the type considered. As it was shown clearly in the previous results (Jones et al., 2010), the standard Smagorinsky model and even more simple models (Vuorinen, 2010) give good results for free flows.

The time derivative terms in equations (3) and (4) are discretised using a first order Euler scheme. The discretisation scheme for the diffusive term in equation (4) is a second order Gaussian integration interpolated linearly by a centred scheme. The convection term in equations (3) and (4) is discretised implicitly using a second order Gaussian limited linear differencing scheme. The PISO (Barton, 1998) method is used to solve the pressure correction equation.

As mentioned above, the RANS approach has been traditionally used in order to model diesel spray injections (Peng-Krrholm, 2008). The renormalisation group theory (RNG) k-epsilon turbulence model with the default coefficients for the turbulent dissipation rate equation and turbulent viscosity is used for both Euler-Euler and Lagrangian-Euler spray calculations. Previous works (Pastor et al., 2008) showed that RANS accurately predicts average velocity profiles and average spray's shape (dispersion rate, penetration), since the mean velocity profile and the spreading rate are independent of Reynolds number. Nevertheless, RANS is not valid if higher level of turbulence structure description is required during the calculations (Pitsch, 2006).

Table 1 summarises the main characteristics of RANS models compared to LES formulation. Differences are based on the statistical treatment of the turbulence (RANS) and the use of the self-similarity theory of Kolmogorov (LES). Consequently, differences can be found on the time-averaging of the Navier-Stokes equations and the spatial filtering for the RANS and LES respectively, see Table 2.

Solutions schemes for the E-E spray simulations with the RANS formulation are exactly the same to those used and described in the previous section for the LES E-E spray calculations.

Table 1 Comparison between RANS and LES

<i>RANS</i>	<i>LES</i>
Statistical phenomena	Kolmogorov theory of self similarity ^a
Time-averaged NS ^b	Spatial filtered NS
k – ε model	Smagorinsky (1963)
RNG k – ε model	One equation model
Less computationally demanding	Predict transient flows better

Notes: ^aLarge eddies of the flow are dependent on the flow geometry, while smaller eddies are self similar and have a universal character.

^bNS: Navier-Stokes equations

Table 2 Time averaging vs. spatial filtering

<i>Instantaneous = Average + Fluctuations (u = \bar{u} + u')</i>	
<i>Averaging or filtering of NS equations gives identical equations for the averaged/filtered variables plus averaged fluctuation terms.</i>	
<i>Time averaging</i>	<i>Spatial filtering</i>
$\bar{u}_i(x) = \frac{1}{T} \int_0^{+T} \bar{u}_j(x, s) ds.$	$u(x_0) = \int_{\Omega} u(x, t) G(x_0, x, \Delta)^3 dx.$
$\bar{u}'_i = 0, \text{ and } \bar{\bar{u}}_i = \bar{u}_i.$	$\bar{u}'_i \neq 0, \text{ and } \bar{\bar{u}}_i \neq \bar{u}_i.$
<i>Reynolds stress tensor</i>	<i>SGS^d stress tensor</i>
$\tau_{ij}^R = \overline{u'_j u'_i}$	$\tau_{ij}^S = -\left(\overline{u'_i u'_j} + \overline{u'_i \bar{u}'_j} + \overline{u'_i \bar{u}'_j}\right) = \overline{u'_i u'_j} - \overline{u'_i \bar{u}'_j}$

Notes: ³Spatial filter $G(x_0, x, \Delta)$ with filter size Δ

⁴SGS

3 Boundary conditions

In diesel engines, the fuel is injected into a cylinder by a high pressure atomiser with a nozzle hole diameter d_0 which creates the fuel spray. In terms of computational difficulty, the flow is not statistically stationary and has three directions of statistical inhomogeneity. Those conditions together with the two phases appearing in the fuel at high velocity sets the spray evolution as one of the most complicated turbulent flows to simulate (Pope, 2000; Chesnel et al., 2010). As depicted at the introduction, besides the simplifications brought by the experimental researches, CFD still presents limitations in term of the modelling of the atomisation process of the nearby zone which is not the goal of the present study. Consequently, the simplification of the computational domain presented by Vuorinen (2010) is also assumed. In this work, the inlet boundary condition is set far enough from the nozzle avoiding the problems of the void fraction limits which grid resolution required by LES makes it more restrictive. In addition, the present work can be seen as a previous approach to the inclusion of droplets (Lagrangian term) as a source of mass and momentum. These particle-laden gas jets are considered by the

authors as the logical following step as it has been widely used to analyse dilute sprays (Faeth, 1987, 1996). As it can be inferred from the description of the computational domain this is the region of the spray where the research is focused. Furthermore, by keeping the same computational domain will provide a better application of present conclusions to future L-E LES calculation and a more suitable framework for further comparison between them. As presented below, turbulent gas jet theory will be applied to set the fields in the inlet boundary conditions of the domain.

Studies show how under certain conditions, for any section perpendicular to the spray axis in the steady region of the gas jet or diesel spray, momentum flux is conservative, and thus equal to that existing at the nozzle exit (Desantes et al., 2003; Payri et al., 2005). Therefore, a proper implementation of the inlet boundary condition would perform the same spray development independent of where it would be placed. Hence, the inlet boundary condition must be perpendicular to the spray axis, contain the whole spray and the same momentum flux as at the nozzle exit and in order to ensure a more realistic development of the flow the boundary inlet has to reproduce the same profile of the fields as in a steady spray.

Since momentum flux can be obtained from experimental data, the unknown factors to setup the boundary condition can be identified by integrating momentum over the whole spray section:

$$\dot{M}_0 = \dot{M}(x) = \int_0^R 2\pi\rho(x, r)U(x, r)rU(x, r)dr, \quad (6)$$

where the x -coordinates coincides with the spray axis and the r -coordinate is the radial position (perpendicular to the spray axis), ρ is the local density in the diesel spray and U is the axial velocity. Writing the density at an internal point of the spray in terms of local concentration and assuming a Gaussian radial profile (Correas, 1998) for fuel concentration and axial velocity, Desantes et al. (2007) obtained the following expression for the spray momentum:

$$\begin{aligned} \dot{M}_0 &= \frac{\pi}{2\alpha} \cdot \rho_a \cdot \tan^2\left(\frac{\theta_u}{2}\right) \cdot x^2 \cdot U_{axis}^2 \\ &\cdot \sum_{i=0}^{\infty} \frac{1}{\left(1+i\frac{S_C}{2}\right)} \cdot \left[\left(\frac{U_{axis}}{U_0}\right)\left(\frac{1+S_C}{2}\right)\left(\frac{\rho_f - \rho_a}{\rho_f}\right)\right]^i. \end{aligned} \quad (7)$$

Here, the Schmidt number (S_C) represents the relative rate of momentum and mass transport and θ_u is the spray cone angle. The point of interest for the present work can be seen in Figure 1 where the $U_{axis} = U_0$. The spray injected under the physical conditions shown in Table 3 has been simulated (Correas, 1998). In these conditions, the end of the non-perturbed zone for the isodense case is located at 4.073 mm, approximately $8d_{eq}$ from the nozzle exit (with $d_{eq} = d_0\sqrt{\rho_f / \rho_a}$) and the gas jet diameter is 2.07 mm which is set as the inlet boundary condition diameter. The velocity and concentration reference profiles are defined as:

$$U(x, r) = U_{axis}(x) \cdot \exp\left(-\alpha\left(\frac{r}{R}\right)^2\right), \quad (8)$$

$$C(x, r) = C_{axis}(x) \cdot \exp\left(-\alpha \cdot S_C \cdot \left(\frac{r}{R}\right)^2\right), \quad (9)$$

with ($\alpha = 4.6$) the shape factor of the Gaussian distribution. Since LES calculation requires perturbed inlet boundary conditions, the reference signal is randomly perturbed a 10% as a first approximation. The discussion of the convenience of this hypothesis will be overcome in the followings sections.

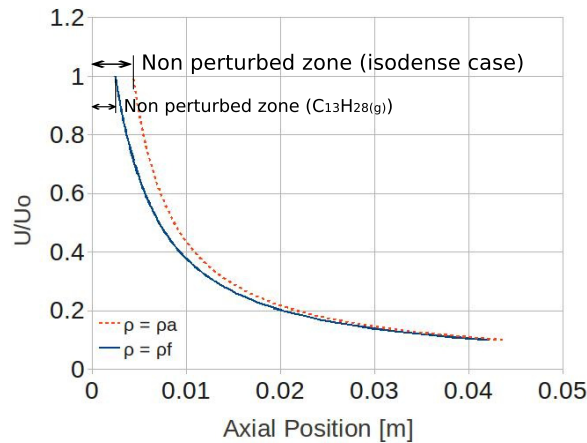
Table 3 Definition of experimental and gas jet CFD simulation

	Exp. (Correas, 1998; Gimeno García, 2008) ($M = 1.11 N$)	Simulation
Fuel	$C_{13}H_{28}$ (l)	Fuel (N_2)
Air	N_2	N_2
P_{inj} (MPa)	73.995	-
$P_{a,\infty}$ (MPa)	3.5	3.55
$T_{f,0}$ (K)	307.58	307.58
$T_{a,\infty}$ (K)	307.58	307.58
$\rho_{f,0} / \rho_{a,\infty}$	21.26	1
U_0 (m/s)	373.27	373.27
d_{inlet} (μm)	112 ^a	2,070 ^b
d_{eq} (μm)	516	516

Notes: ^aNozzle diameter

^bJet diameter at the end of the non-perturbed zone

Figure 1 Axis velocity (see online version for colours)



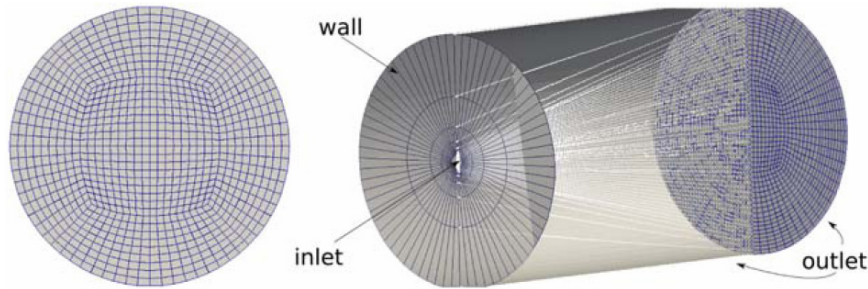
Notes: Red dot line: isodense case; Blue solid line: $C_{13}H_{28}$ (g) case

The computational domain is a cylindrical volume ($d = 40$ mm, $L = 70$ mm) that represents the shape of the injection test rig chamber. The meshing methodology is fairly the same for the RANS and LES calculations, with different grid densities depending on the turbulence formulation. Hexahedral cells have been preferred for the grid generation,

since they provide better accuracy and stability than tetrahedral cells. The computational domain has been decomposed into hexahedral subparts in order to get a semi-structured topology mesh, as shown in Figure 2(a). Cells are concentrated around the spray diameter ($d = 2.07$ mm) to get a cell size of $57.5 \mu\text{m}$ and $22.5 \mu\text{m}$ for the RANS and LES meshes respectively. Downstream the nozzle the mesh is progressively adapted to the shape of the computational domain in order to obtain a homogeneous cell size at sections located downstream the inlet boundary condition, see circular sections on the right of Figure 2. The numbers of cells are 4.05×10^5 and 4.9×10^6 for the RANS and LES formulation respectively.

In this mesh, the circular faces of the cylinder are split into four parts and then meshed with a non-structured hexahedral mesh using the same cell size as that described above. Previous studies performed on RANS Euler-Euler (Abraham, 1997) in similar spray conditions show that the structure of the mesh and cell size are enough to get a grid independent solution. Also, the meshes used for the LES formulation have comparable and also smaller cell sizes than recent LES studies (Vuorinen, 2010) for sprays characterisation where the grid independence is proved. Finally, three boundary conditions are assigned in the computational domain as depicted in Table 4.

Figure 2 Calculation domain and boundary conditions for the RANS case (see online version for colours)



Note: LES grid is a finer version of this one.

Table 4 Definition of gas jet CFD boundary conditions

<i>Surface</i>	<i>Boundary type</i>	<i>Defining variables</i>
Inlet	Turbulent velocity inlet	$U_0(r)$ and $C(r), T_f$
Wall	Rigid wall, non-slip cond.	-
Outlet	Constant pressure, wave transmissive	$P_{a,\infty} T_{a,\infty}$

4 Numerical results

The obtained numerical results are contrasted with those predicted by classical RANS models and compared with experimental data. Experimental results have been obtained from previously published data from the authors' research group. Momentum flux data was achieved by measuring the impact force of the spray in a surface with a piezo-electric sensor (Payri et al., 2005). The droplet velocity measurements have been performed under non-vaporising conditions inside a SF₆ (a dense gas) atmosphere at

room temperature (298 K). The environmental density at low pressure (0.5 MPa) was 40 kg/m^3 , close to the reference case (Araneo et al., 2006).

Temporal evolution of the axial velocity at 25 mm of the virtual nozzle has been used to justify the beginning for the statistical measurements. In Figure 3, the criteria of a constant spray angle was used to set the radial position of the probes. Thus, the first probe in the isodense calculation is located at the edge of the spray and the last at 4.25 mm from the edge. Since no significant velocity variation was detected by the most far-off probe, its measurements do not appear. It is also shown the velocity value imposed in the centre of the inlet boundary condition (4.073 mm from the virtual nozzle under the isodense conditions).

Differences in both the frequency content and the width of the velocity signals in the inlet boundary condition and the axis velocity at 25 mm show a lack of precision of the spray fields simulated at the inlet boundary condition. Its effect in LES in terms of the classical parameters to characterise the spray is decisive as shown in Figure 4.

Figure 3 Measurements of radial probes ($x = 25 \text{ mm}$)

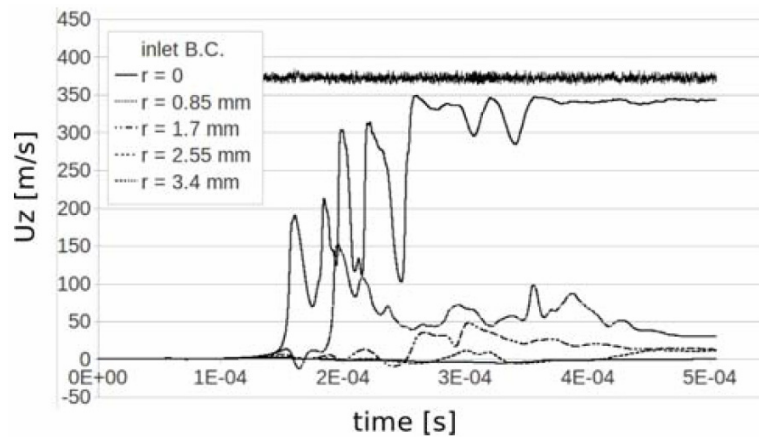
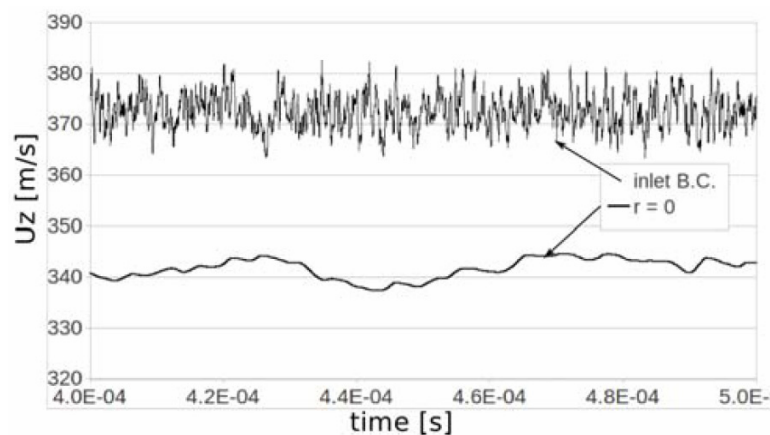


Figure 4 Measurements of axial velocity

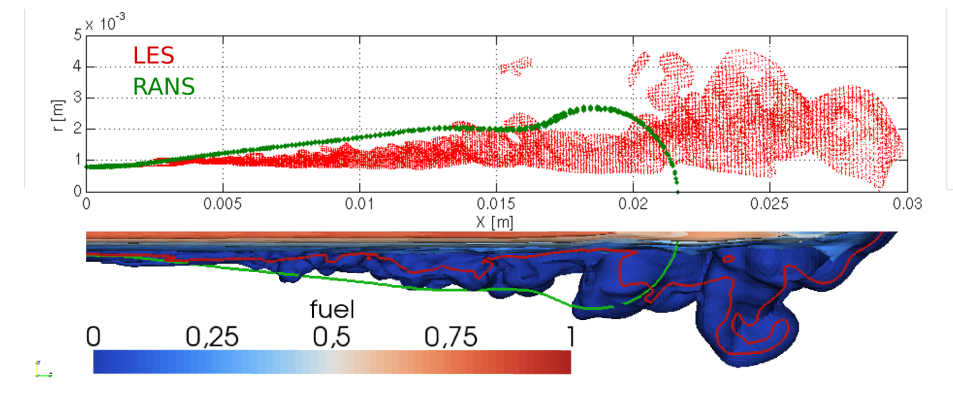


The maximum axial distance for a 1% fuel concentration is the criterion used to define the penetration. Notice that this distance is located at the edge of the spray for theoretical and RANS calculations but not necessarily for LES simulations as shown in Figure 5 (solid red line). RANS and LES (E-E) calculations correspond to isodense gas jets cases detailed in previous sections. A description of the L-E approach will be done in future works when comparing RANS with LES L-E calculations. This approach is outside of the scope of the present paper and has been shown as a reference of a good experimental estimation to compare with.

The over prediction of both the RANS and LES E-E penetration is highly affected by the different injection mass flow rate shape. The L-E injection follows the experimental progressive evolution while the E-E injection is a constant value, simplified in this way to avoid disguising the first stages of the jet with this variable.

The over prediction of both the RANS and LES E-E penetration at is also affected by the fact that spray is more effective in transferring injection momentum to the ambient than the gas jet (Abraham et al., 1994). In the L-E approach, the Lagrangian term carries the 45% of the momentum at $8d_{eq}$ of the nozzle.

Figure 5 Comparison between RANS and LES concentration iso-surfaces ($t = 0.3$ ms) (see online version for colours)



Notes: Lower part: longitudinal clip of fuel concentration contours. Upper part: Radial coordinates of stoichiometric iso-surfaces.

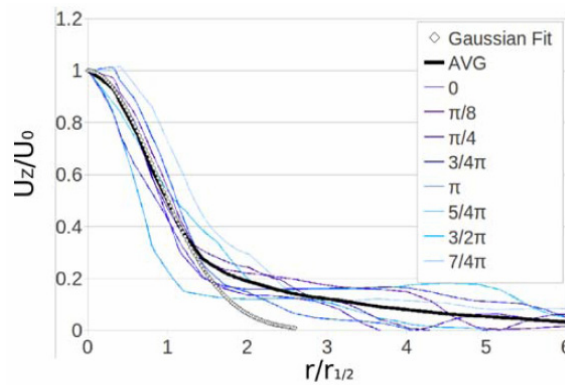
Furthermore, in this initial part of the spray the local density is far from the assumption of constant density of the gas jets. Therefore, the isodense hypothesis that allows to compare the gas jet with the diesel spray is so restrictive from the actual boundary condition placed at $8d_{eq}$. The assumption is acceptable beyond the developing region ($x / d_{eq} > 30$) where differences in axis velocity under turbulent gas jet theory are less than 3%.

Moreover, for the LES calculation, the first 5 mm can be seen as a length required developing turbulence Figure 5. Thus, the first assumption of a 10% of velocity fluctuation at the inlet boundary condition is not a good enough turbulent initialisation of the flow. Given that the inlet is placed at the end of a not well-known zone, authors think a more realistic turbulent condition can be achieved by applying measured or more accurate calculated profiles of velocity variation (Hussein et al., 1994; Levy and Lockwood, 1981). Figure 5 shows iso-surfaces of fuel concentration for the LES simulation at 0.3 ms. The red line and the green line mark the stoichiometric iso-surface

for LES and RANS (E-E) simulations respectively. These areas have a relevant importance in combustion processes. The upper part of the figure plots the radial distance of these surfaces where detached surfaces far from the jet can be found.

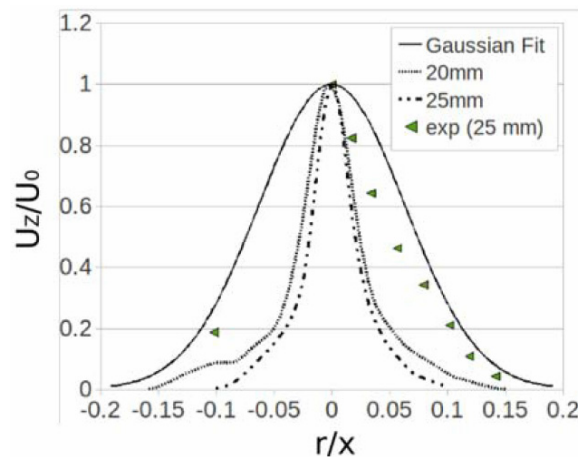
A comparison with the Gaussian radial profiles is shown in Figure 6 and Figure 7. In both the axial velocity has been normalised with the axis velocity. In Figure 6, the radial distance is normalised with the jet's half-width as defined by Pope (2000) where in Figure 7 is normalised with the axial distance. A spatial average at 25 mm of the nozzle of the axial velocity ($t = 0.5$ ms) shows a good agreement with the theoretical Gaussian profile from the edge to more than the half of the jet radius (up to 30% of the axis speed) Figure 6. Differences in simulated profiles at 20 and 25 mm in Figure 7 can be affected by the amount of statistics for each location (around 0.05 ms less data at 25 mm). Experimental data is close to LES simulated profile near the edge of the spray but moves to the Gaussian one as r increases.

Figure 6 Radial velocity profiles ($t = 0.5$ ms) (see online version for colours)



Note: Spatial average of eight different angles

Figure 7 Radial velocity profiles ($t = 0.5$ ms) (see online version for colours)



Note: Time-averaged

5 Conclusions

Using the OpenFOAM code, the authors have performed a completed simulation of diesel spray in LES. A comparison between the proposed method and trusted (E-E) RANS sprays simulations has been performed, obtaining a very good agreement. Configuration and turbulent boundary conditions election have been justified and validated. Internal structure of the spray has been deeply studied, showing some characteristics of the spray. LES results have been also validated against experimental measurements of the velocity field. Some specific needs are presented in our paper as challenges to overcome. LES modelling can become the practical tool in both industry and academic in the design process of combustion system. The future research is now focusing on identifying the important parameters that affect the model and on improving the stability and accuracy of algorithms within OpenFOAM code. By so doing, the better spray simulation will be performed and a reliable tool will be used in modelling the spray simulation in the near future.

Acknowledgements

This research has been funded by the Spanish Government in the frame of the Project ‘Métodos LES para la simulación de chorros multifásicos’, Ref. ENE2010-18542. The authors also acknowledge the financial support of the Universidad Politécnica de Valencia under the contract Reference PAID-2759 and the Generalitat Valenciana, under the contract GV/2010/039. We are also grateful to Dr. Francisco Javier Salvador and Dr. José Manuel Pastor for providing experimental data and fruitful advices. In addition, we gratefully acknowledge helpful discussions with many researchers in CMT-Motóres Térmicos, especially Ms. Palma González and Ms. Mariany Chávez.

References

- Abraham, J. (1997) ‘What is adequate resolution in the numerical computations of transient jets?’, SAE 970051, pp.81–95.
- Abraham, J., Magi, V., Macinnes, J. and Bracco, F.V. (1994) ‘Gas versus spray injection: which mixes faster?’, SAE paper 940895, pp.163–177.
- Araneo, L., Soare, V., Payri, R. and Shakal, J. (2006) ‘Setting up PDPA system for measurement in a diesel spray’, *Journal of Physics*, Vol. 45, pp.85–93.
- Barton, I.E. (1998) ‘Comparison of simple- and piso-type algorithms for transient flows’, *International Journal for Numerical Methods in Fluids*, Vol. 26, No. 4, pp.459–483.
- Befrui, B., Corbinelli, G., Robart, D. and Reckers, W. (2008) ‘LES simulation of the internal flow and near-field spray structure of an outward-opening GDI injector and comparison with imaging data’, SAE paper 2008-01-0137, pp.163–177.
- Bharadwaj, N. and Rutland, C.J. (2010) ‘A large-eddy simulation study of sub-grid two-phase interaction in particle-laden flows and diesel engine sprays’, *Atomization and Spray*, Vol. 20, No. 8, pp.673–695.
- Chesnel, J., Réveillon, J., Ménard, T., Berlemont, A. and Demoulin, F.X. (2010) ‘Large eddy simulation of liquid atomization: from the resolved scales to subgrid spray’, *International Conference on Multiphase Flow (ICMF)*.

- Correas, D. (1998) 'Theoretical and experimental study of isothermal diesel free sprays', (in Spanish), PhD thesis, Universidad Politécica de Valencia.
- Deportes, A., Zellat, M., Desoutter, G., Liang, Y. and Ravet, F. (2010) 'Application of the Eulerian-Lagrangian spray atomization (ELSA) model for the diesel injection simulation', *THIESEL (2010)*.
- Desantes, J.M., Payri, R., García-Oliver, J.M. and Salvador, F.J. (2007) 'A contribution to the understanding of isothermal diesel spray dynamics', *Fuel*, Vol. 86, Nos. 7–8, pp.1093–1101.
- Desantes, J.M., Payri, R., Salvador, F.J. and de la Morena, J. (2010) 'Influence of cavitation phenomena on primary break-up and spray behaviour at stationary conditions', *Fuel*, Vol. 89, No. 10, pp.3033–3041.
- Desantes, J.M., Payri, R., Salvador, F.J. and Gimeno, J. (2003) 'Measurements of spray momentum for the study of cavitation in diesel injection nozzles', SAE Paper 2003-01-0703.
- Faeth, G.M. (1987) 'Mixing, transport and combustion in sprays', *Prog. Energy Combust. Sci.*, Vol. 13, pp.293–345.
- Faeth, G.M. (1996) 'Spray combustion phenomena', *26th International Symposium on Combustion*, pp.1596–1612.
- Fevrier, P., Simonin, O. and Squires, K.D. (2005) 'Partitioning of particle velocities in gas-solid turbulent flows into a continuous field and a spatially uncorrelated random distribution: theoretical formalism and numerical study', *J. Fluid Mech.*, Vol. 533, pp.1–46.
- Germano, M. (1992) 'Turbulence: the filtering approach', *J. Fluid Mech.*, Vol. 238, pp.325–336.
- Gimeno García, D.J. (2008) Desarrollo y aplicación de la medida del flujo de cantidad de movimiento de un chorro diesel, PhD thesis, Universidad Politécica de Valencia.
- Horiuti, K. (1993) 'A proper velocity scale for modelling subgrid-scale eddy viscosities in large eddy simulation', *Physics of Fluids*, Vol. 5, No. 1, pp.146–157.
- Hoyas, S. and Jiménez, J. (2006) 'Scaling of the velocity fluctuations in turbulent channels up to $Re_{\tau} = 2000$ ', *Phys. Fluids*, Vol. 18, No. 1, pp.1–4.
- Hussein, H.J., Capp, S.P. and George, W.K. (1994) 'Velocity measurements in a high-Reynolds-number, momentum-conserving, axisymmetric, turbulent jet', *J. Fluid Mech.*, Vol. 258, pp.31–75.
- Jiménez, J. (2003) 'Computing high-Reynolds-number turbulence: will simulations ever replace experiments?', *Journal of Turbulence*, Vol. 4, Art no. 22.
- Jones, W.P., Lyra, S. and Marquis, A.J. (2010) 'Large eddy simulation of evaporating kerosene and acetone sprays', *International Journal of Heat and Mass Transfer*, May, Vol. 53, Nos. 11–12, pp.2491–2505.
- Lauder, B.E. and Spalding, D.B. (1974) 'The numerical computation of turbulent flows', *Computer Methods in Applied Mechanics and Engineering*, March, Vol. 3, No. 2, pp.269–289.
- Levy, Y. and Lockwood, F.C. (1981) 'Velocity-measurements in a particle laden turbulent free jet', *Combustion and Flame*, Vol. 40, No. 3, p.333–339.
- Margot, X., Hoyas, S., Fajardo, P. and Patouna, S. (2010) 'A moving mesh generation strategy for solving an injector internal flow problem', *Mathematical and Computer Modelling*, Vol. 52, Nos. 7–8, pp.1143–1150.
- Pastor, J.V., López, J.J., García, J.M. and Pastor, J.M. (2008) 'A 1D model for the description of mixing-controlled inert diesel sprays', *Fuel*, Vol. 87, No. 8, pp.2871–2885.
- Payri, F., Margot, X., Patouna, S., Ravet, F. and Funk, M. (2009a) 'A CFD study of the effect of the needle movement on the cavitation pattern of diesel injectors', *Proceedings ICE2009*, SAE Naples Section 2009-24-0025.
- Payri, R., Salvador, F.J., Gimeno, J. and de la Morena, J. (2009b) 'Effects of nozzle geometry on the direct injection diesel engine combustion process', *Appl. Therm. Eng.*, Vol. 29, No. 10, pp.2051–2060.

- Payri, R., García-Oliver, J.M., Salvador, F.J. and Gimeno, J. (2005) 'Using spray momentum flux measurements to understand the influence of diesel nozzle geometry on spray characteristics', *Fuel*, Vol. 84, No. 5, pp.551–561.
- Payri, R., Tormos, B., Gimeno, J. and Bracho, G. (2010) 'The potential of large eddy simulation (LES) code for the modeling of flow in diesel injectors', *Mathematical and Computer Modelling*, Vol. 52, Nos. 7–8, pp.1151–1160.
- Peng-Krrholm, F. (2008) 'Numerical modelling of diesel spray injection, turbulence and combustion', PhD thesis, Chalmers Uni. of Technology.
- Piomelli, U. and Liu, J. (1995) 'Large-eddy simulation of rotating channel flows using a localized dynamic model', *Phys. Fluids*, Vol. 7, No. 4, pp.839–848.
- Pitsch, H. (2006) 'Large-eddy simulation of turbulent combustion', *Annual Review of Fluid Mechanics*, Vol. 38, No. 1, pp.453–482.
- Pope, S.B. (2000) *Turbulent Flows*, p.771, Cambridge University Press, UK.
- Riley, J.J. (2006) 'Review of large-eddy simulation of non-premixed turbulent combustion', *J. Fluids Eng.*, Vol. 128, No. 2, pp.209–215.
- Scotti, A., Meneveau, C. and Lilly, D.K. (1993) 'Generalized Smagorinsky model for anisotropic grids', *Phys. Fluids A*, Vol. 5, No. 9, pp.2306–2308.
- Smagorinsky, J.S. (1963) 'General circulation experiments with the primitive equations. I. The basic experiment', *Mon. Weather Rev.*, Vol. 91, pp.99–164.
- Vuorinen, V. (2010) 'LES of certain droplet size effects in fuel sprays', PhD Thesis, the Aalto University School of Science and Technology.
- Yakhot, A., Orszag, S., Yakhot, V. and Israeli, M. (1989) 'Renormalization group formulation of large-eddy simulations', *J. Sci. Comput.*, Vol. 4, No. 2, pp.139–158, USA.

Evaluation of the Eulerian-Lagrangian spray atomisation (ELSA) in spray simulations

Sergio Hoyas*, J.M. Pastor,
Dung Khuong-Anh and
Juan Manuel Mompó-Laborda

CMT – Motores Térmicos,
Universidad Politécnica de Valencia,
Camino de Vera S/N, 46022 Valencia, Spain

E-mail: serhocal@mot.upv.es

E-mail: jopasen@mot.upv.es

E-mail: ankh2@mot.upv.es

E-mail: juamomla@mot.upv.es

*Corresponding author

Frederic Ravet

Renault,
1 Avenue du Golf 78288, Guyancourt, France
E-mail: frederic.ravet@renault.com

Abstract: Many approaches have been used to simulate the spray structure especially in modelling fuel sprays, i.e., Eulerian, Lagrangian, Lagrangian-Eulerian, Eulerian-Eulerian and Eulerian-Lagrangian approaches. The present study uses an Eulerian-Lagrangian spray atomisation (ELSA) method which is an integrated model for capturing the whole spray evolution starting directly from injector nozzle still the end.

Our goal in this study is to evaluate the ELSA model which is implementing into the commercial software Star-CD, for numerical modelling of diesel sprays. There are two key studies in these validations, at first we examine the turbulent parameters through the three different scenarios and then we study mesh dependency. The results show in form of liquid penetrations, droplet velocity, and axial velocity profiles. All numerical results are compared with experimental data from our research institute, CMT-Motores Térmicos.

Keywords: spray penetration; droplet; injection; Eulerian-Lagrangian spray atomisation; ELSA; atomisation; turbulence.

Reference to this paper should be made as follows: Hoyas, S., Pastor, J.M., Khuong-Anh, D., Mompó-Laborda, J.M. and Ravet, F. (2011) 'Evaluation of the Eulerian-Lagrangian spray atomisation (ELSA) in spray simulations', *Int. J. Vehicle Systems Modelling and Testing*, Vol. 6, Nos. 3/4, pp.187–201.

Biographical notes: Sergio Hoyas is an Associate Professor of Aerospace Engineering at the Universidad Politécnica de Valencia, where is also serving as a CFD Coordinator of CMT-Motores Térmicos Research Institute. He holds a PhD in Applied Mathematics, and his expertise includes supercomputation and wall turbulence.

J.M. Pastor obtained his PhD in Mechanical Engineering in 2003. He is currently a Senior Researcher at CMT-Motores Térmicos, Universidad Politécnica de Valencia. His research fields are analysis and modelling of engine combustion processes, and CFD applied to simulations of internal combustion engines and sprays.

Dung Khuong-Anh graduated with a degree in Mechanical Engineering (2005) and obtained his dual Master in Computational Mechanics from the Universitat Politècnica de Catalunya (2008) and École centrale de Nantes (2009), and his Master in Internal Combustion Engine from the Universidad Politécnica de Valencia (2011). His research interests are computational mechanics, FE, CFD and CAx. Currently, he works as a researcher for European Commission Marie Curie FP7 ITN 'VECOM' at UPV. His research activities include CFD simulation of direct injection diesel sprays within the framework of the Eulerian Lagrangian spray atomisation model in order to develop and validate a numerical tool for spray modelling in engine simulation and calculation.

Juan Manuel Mompó Laborda finished his degree in Mechanical Engineering (2009) with a six-month stay at the Yacht Research Unit (University of Auckland) with the first Promoe scholarship to New Zealand that has been managed by the Polytechnic University of Valencia (Spain). In November 2009, he joined the CMT-Motores Térmicos for his doctoral thesis on LES of diesel sprays with OpenFOAM. Previously, he participated in three R&D projects in his institute as a Research Fellow.

Frederic Ravet is an Engineer and a Specialist in combustion systems. He joined Renault in 2004 after working for ten years in aeronautics industry. He graduated from CORIA (Rouen University) as a Doctor in Energy. He is in charge of combustion designing.

1 Introduction

Everybody knows the auto world has shifted. New efficiency standards are requiring a fleet-wide fuel economy. Within this purpose, car manufacturers have paid more attention to enhance the improvement of R&D resources in automotive industry. There is a variety of research fields including noise, vibration and harshness (NVH), simulation of vehicle performance, dynamics, safety, durability, etc. Even though there have been big advances over the last decade in the efficiency of the diesel engine, automakers insist there is still much to improve about the humble combustion engines, especially in the diesel injection simulation.

In the 1980s, Lefebvre (1989) described the complexity of spray structure and its related theories. Fuel injection process and subsequent fuel-air mixing formation play a major role in combustion and pollutant emissions from internal combustion engines. As the development of a spray is dependent on many parameters and coefficients, simulation studies try to assess the impact of complex phenomena. It is characterised by orifice diameter, nozzle shape, pressure, density, temperature, physical chemistry components, contraction coefficient, discharge coefficient, vaporisation, etc.

Thus an accurate prediction of these processes is required in order to perform reliable engine combustion and pollutants formation simulations. Fuel spray injection is one of the most important phenomena in internal combustion engine which is still under

development and it has been attracted high concerns from both academic and scientific researchers. Diesel fuel injection and spray formation modelling is still a challenging task due to the complex interrelated phenomena taking place. Still now some of them such as primary atomisation or nozzle cavitation are not fully understood.

Even though many models are mentioned in the abstract but each of them has both advantages and disadvantages in the various regions of spray consisting of the dense zone and the downstream dilute zone or atomisation.

In order to enhance CFD spray simulations, the Eulerian-Lagrangian spray atomisation (ELSA) model has been developing in recent years and integrated into the Star-CD CFD code by Renault. This model is based in an Eulerian approach for the description of the dense spray region, where standard discrete droplet model (DDM) method is not suited for. Hence, the ELSA is an integrated model for capturing the whole spray evolution. Within the diluted spray region the ELSA model could switch to the traditional Lagrangian description of the liquid phase, taking advantage from well established previously developed submodels.

The theoretical aspects of the model have been developing in the last decade, however we need to make it real and stable for engineering applications. The ELSA model has been implementing into Star-CD code. Through the toughest structuring period, we continued to validate and evaluate heavily to ensure the prompt correction in preliminary stage.

Targeting this general objective, it is included to evaluate and validate the different parameters, improve the simple model for computation and identify the well-described phenomena involved in diesel spray formation and development from nozzle outflow to complete fuel vaporisation. As a result, we form the set of correct models for producing a diesel engine simulation in real-life operation. This work is part of a more ambitious project, with the general objective of developing and validating a new spray model tool for practical applications on CFD engine calculations.

2 The ELSA model

In this section, the ELSA approach is described. The goal of the ELSA model is to realistically describe the dense zone of the spray. The ELSA model has been developed from 2001 ignited by Vallet et al. and during the time has been under development (Beau, 2006; Lebas, 2007; De Lucas, 2007; Ning, 2007; Blokkeel et al., 2003).

The ELSA model is used for situations when it assumes the following hypotheses:

- in the situation of high-speed turbulent sprays where Reynolds and Weber numbers are high
- and it proposes a turbulent mixing process between the liquid and surrounding gaseous phases as a single-phase turbulent fluid flow with mean properties.

Basically, we can divide ELSA approach into three broad zones:

- *Eulerian mixture zone*: in the first part, single phase CFD code to describe the liquid/gas mixture in the dense part of the spray. In this region, liquid and gas phase are considered as a unique mixture flow. The classical Eulerian model is used to solve this single phase flow.

- *Transition zone*: switch from Eulerian to Lagrangian calculation.
- *Lagrangian zone*: classical Lagrangian tracking for droplets in the diluted spray zone.

Once the difference of velocity of a liquid jet with respect to the surrounding gas is very strong, atomisation of the jet occurs, and droplets are formed (atomisation regime).

In the two papers of Desportes et al. (2010a, 2010b), the author had summarised the key formulae as following, and we include here for completeness. Mean liquid mass fraction \tilde{Y}_l

$$\tilde{Y} = \frac{\overline{\rho Y}}{\bar{\rho}} \quad (1)$$

where \bar{Y} is the mean liquid volume fraction,

The mean properties of this effective fluid or mixture (like mean density $\bar{\rho}$ or Favre averaged mean velocity \tilde{U}_i) are defined with the following relationships:

The state equation is obtained as

$$\bar{\rho} = \rho_l \bar{Y} + \rho_g (1 - \bar{Y}) \quad (2)$$

ρ_l is the liquid density and ρ_g is the gas density, which is expressed in terms of \tilde{Y}_l as

$$\frac{1}{\bar{\rho}} = \frac{\tilde{Y}_l}{\rho_l} + \frac{1 - \tilde{Y}_l}{\rho_g} \quad (3)$$

$$\tilde{U}_i = \tilde{Y}_l U_{l,i} + (1 - \tilde{Y}_l) U_{g,i} \quad (4)$$

and the equation of state

$$\bar{P} = \frac{(1 - \tilde{Y}_l) \bar{\rho} R_g T_g}{1 - \tilde{Y}_l \cdot \bar{\rho} / \rho_l} \quad (5)$$

In the equation of state (5), we take into account the volume occupied by liquid.

Then, the classical transport equations are solved for these mean variables:

$$\frac{\partial \bar{\rho}}{\partial t} + \frac{\partial \bar{\rho} \tilde{U}_j}{\partial x_j} = S_{EL}^{\tilde{Y}_l} \quad (6)$$

$$\frac{\partial \bar{\rho} \tilde{U}_i}{\partial t} + \frac{\partial \bar{\rho} \tilde{U}_j \tilde{U}_i}{\partial x_j} = - \frac{\partial \bar{P}}{\partial x_i} - \frac{\partial \overline{\rho u_i'' u_j''}}{\partial x_j} + S_{EL}^{\tilde{U}_i} \quad (7)$$

It should be noticed that the last equation does not contain any momentum exchange terms between liquid and gaseous phases. In order to model the liquid dispersion, this set of equations is completed by the transport equation for the liquid mass fraction:

$$\frac{\partial \bar{\rho} \tilde{Y}_l}{\partial t} + \frac{\partial \bar{\rho} \tilde{U}_j \tilde{Y}_l}{\partial x_j} = - \frac{\partial \overline{\rho u_j'' y''}}{\partial x_j} + S_{EL}^{\tilde{Y}_l} \quad (8)$$

where $S_{EL}^{\tilde{Y}_l}$ and $S_{EL}^{\tilde{U}_i}$ are the sink or source terms due to the droplet generation or absorption when the transition from Eulerian to Lagrangian formulation is activated.

In equations (5) and (6), there are two turbulent fluxes to be closed. The turbulent stress tensor is modelled with a classical $k - \varepsilon$ model closure. Concerning the liquid turbulent diffusion flux, the gradient law approximation is applied:

$$\overline{\rho u_j'' y''} = -\bar{\rho} \frac{v_t}{Sc_t} \frac{\partial \tilde{Y}_l}{\partial x_j} \quad (9)$$

2.1 Liquid/gas interface density

In order to characterise the size of liquid fragments resulted from the jet atomisation, the notion of liquid surface density is introduced. This variable is defined as the quantity of liquid/gas interface per unit of volume $\bar{\Sigma}$ (m^{-1}). Using this new variable, we can obtain the Sauter mean diameter of droplet (Lebas et al., 2005):

$$D_{32} = \frac{6\bar{\rho}\tilde{Y}_l}{\rho_l\bar{\Sigma}} \quad (10)$$

$$n = \frac{\rho_l^2\bar{\Sigma}^3}{36\pi\rho\tilde{Y}_l^2}$$

A transport equation for liquid surface density is postulated by analogy with the flame surface density.

$$\frac{\partial \bar{\rho}\tilde{\Omega}}{\partial t} + \frac{\partial \bar{\rho}\tilde{\Omega}\tilde{U}_j}{\partial x_j} = \frac{\partial}{\partial x_j} \left(\bar{\rho} \frac{v_t}{Sc_t} \frac{\partial \tilde{\Omega}}{\partial x_j} \right) + S_{EL}^{\tilde{\Omega}} \quad (11)$$

$$\bar{\rho} \cdot \left(\dot{\tilde{\Omega}}_{init} + \dot{\tilde{\Omega}}_{mean} + \dot{\tilde{\Omega}}_{turb} + \dot{\tilde{\Omega}}_{coll} + \dot{\tilde{\Omega}}_{coal} \right)$$

Here, Beau (2006) introduced the other notion of liquid/gas interface per unity of mass that is defined as $\tilde{\Omega} = \bar{\Sigma}/\bar{\rho}$ (m^2/kg).

The production and destruction of liquid surface are accounted for with source terms detailed below. The first term source $\tilde{\Omega}_{init}$ in equation (8) permits to initialise the calculations since all other terms source are proportional to $\tilde{\Omega}$:

$$\dot{\tilde{\Omega}}_{init} = \begin{cases} 2 \frac{v_t}{Sc_t} \frac{6\bar{\rho}}{\rho_l\rho_g L_t} \frac{\partial \tilde{Y}_l}{\partial x_i} \frac{\partial \tilde{Y}_l}{\partial x_i} \text{ if } \tilde{Y}_l(1-\tilde{Y}_l) \leq 0.001 \\ 2 \frac{v_t}{Sc_t} \frac{\tilde{\Omega}}{(1-\tilde{Y}_l)\tilde{Y}_l} \frac{\partial \tilde{Y}_l}{\partial x_i} \frac{\partial \tilde{Y}_l}{\partial x_i}, \text{ otherwise} \end{cases} \quad (12)$$

The second term in the right hand side stands for a general definition that was obtained by the phenomenological considerations for the spray formed of the droplets with a

constant diameter. In the region closed to the injector $\tilde{Y}_l \rightarrow 1$, the scale of the first liquid fragments is assumed to be proportional to the turbulent length scale, L_t .

The three next terms correspond to the production of liquid surface density due to the mean or turbulent stresses and due to the collisions:

$$\begin{aligned}\dot{\tilde{\Omega}}_{mean} &= \frac{\overline{\rho u_i'' u_j''}}{\bar{\rho} \tilde{k}} \frac{\partial \tilde{U}_i}{\partial x_j} \tilde{\Omega} \\ \dot{\tilde{\Omega}}_{turb} &= \frac{\tilde{\Omega}}{\tau_{turb}} \quad \text{and} \quad \dot{\tilde{\Omega}}_{coll} = \frac{\tilde{\Omega}}{\tau_{coll}}\end{aligned}\tag{13}$$

The last term in the right hand of equation (8) deals with destruction of surface density due to coalescence:

$$\dot{\tilde{\Omega}}_{coal} = -\frac{1}{\tau_{coll}} \frac{\tilde{\Omega}^2}{\tilde{\Omega}_{crit}}\tag{14}$$

with τ_{coll} and $\tilde{\Omega}_{crit}$ are the characteristic time scale of collisions and the critical value of liquid/gas surface density.

3 Experiments for comparison

The obtained numerical results are compared with experimental data at CMT Motores Térmicos. Experimental results have been obtained from previously published data from the authors' research group (Payri et al., 2008; Gimeno García, 2008).

The injection velocity profile comes from measurements of mass and momentum fluxed performed in a pressurised test rig with nitrogen. The momentum flux measuring principle of this technique is explained in two references of Payri et al. (2005) and Gimeno Garcia (2008), and consists of measuring the impact force of the spray in a surface with a piezo-electric sensor. As long as the whole cross-section of the spray impacts on the sensor, the measured force equals to the momentum flux at that cross section. If the measurement position is close to the nozzle exit, the time evolution of the impact force is equal to the nozzle (hole) momentum flux, \dot{M}_o .

4 Geometry and boundary conditions

These cases have been simulated as axis-symmetric boundary-value problems. We study 2D axis-symmetric meshes (five-degree cylindrical segment along the axis). A 2D view, boundary conditions and coordinate system are shown in Figure 1.

Within this work, we used a data as similar as CMT diesel-type single-hole injector experiments for a diameter of 112 μm with variable velocity profile input at the injector as depicted in Figure 2 and some key parameters in Table 1.

Figure 1 Boundary conditions (see online version for colours)

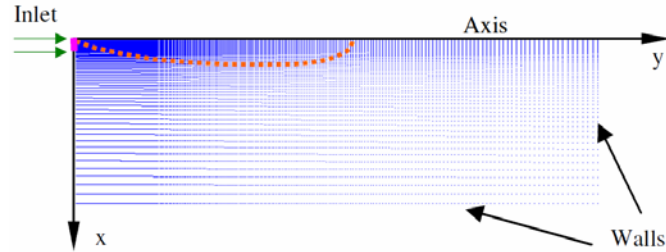


Figure 2 Starting velocity profile (see online version for colours)

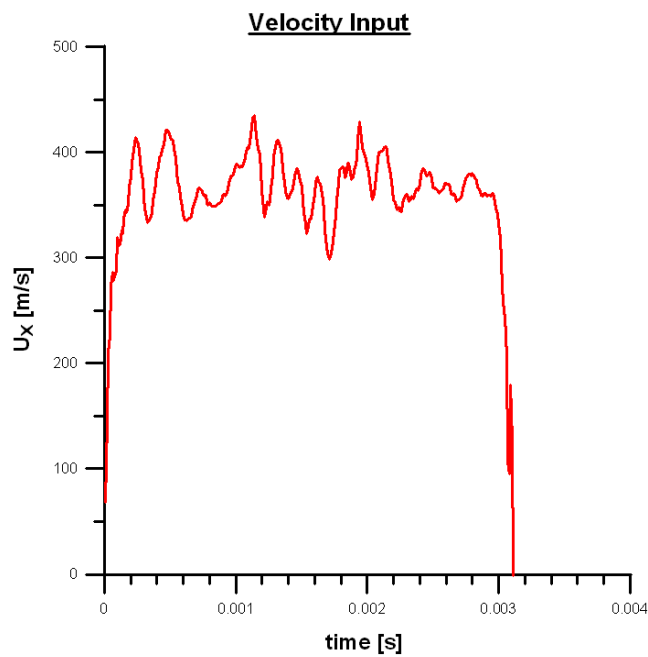


Table 1 Basis parameters

<i>Ambient pressure</i>	<i>Injection pressure</i>	<i>Temperature</i>	<i>Fuel density</i>
3.53 MPa	80 MPa	307.58 K	822.10 kg/m ³

Generally, the requirement for mesh structure is especially at the nozzle where the mesh size has to be small enough to capture the spray structure and the small droplets at the injector and surroundings. Our current mesh structure is based on the following criteria:

$$\Delta x \sim 0.05 - 0.1 D_{inj} \Rightarrow \Delta t \approx 10^{-8} \text{ s}$$

Hence, two different configurations with 10, and 20 cells at the nozzle are used. The computational domains with the size of 80 × 25 mm are shown in Figure 3 according to the mesh structures in Table 2.

Figure 3 Geometry (see online version for colours)

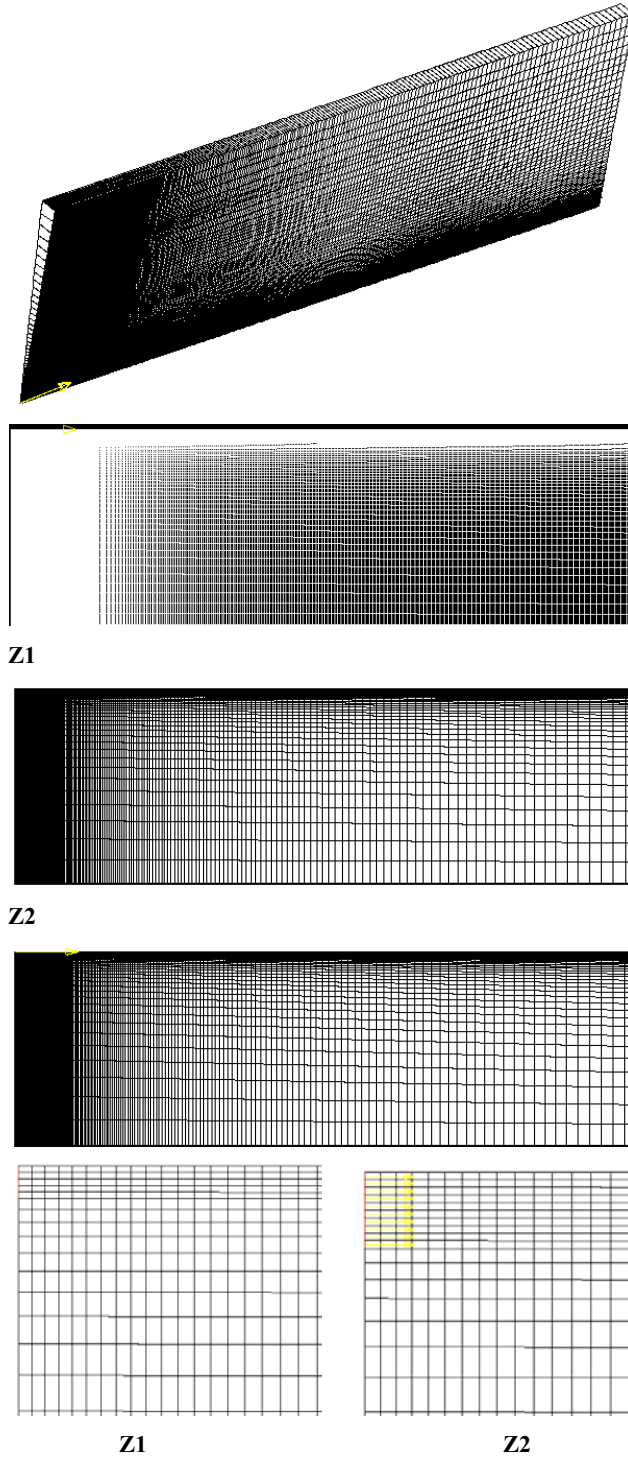


Table 2 Mesh structures

<i>No cells at the nozzle</i>	<i>No. axial cells</i>	<i>Axial ratio (first/last ratio)</i>	<i>No. radial cells</i>	<i>Radial ratio (last/first ratio)</i>
10	435	72	90	0.006
10	218	72	45	0.006
20	250	143	50	0.003

The first two graphs in Figure 3 are for the ten cells with fine meshes in isometric and side views respectively, the third one is for ten cells with coarse mesh. The fourth figure from downward position is for the case with 20 cells at the nozzle. The detailed views of two types of meshes are also showed in pairs.

We used the $k - \varepsilon$ high Reynolds number turbulent model with the following constants in Table 3 that are usually accepted in most of the spray calculation where $C-\varepsilon 1 = 1.44$ is the standard value, and we also use the suggested value $C-\varepsilon 1 = 1.60$ in order to improve predictions on round jets modelling, moreover we examine the behaviour of the simulation with $C-\varepsilon 1 = 1.52$. The turbulent Prandtl number has been set to 1 in order to produce similar solutions for the conservation equations of axial momentum, fuel mass and energy. We notice that the Prandtl (K.E.) in Table 3 is another Prandtl constant which is only used for solving the $k - \varepsilon$ equations.

Table 3 Turbulent parameters

	<i>C-Mu</i>	<i>C-ε1</i>	<i>C-ε2</i>	<i>C-ε3</i>	<i>Prandtl (K.E.)</i>	<i>Prandtl (Eps)</i>
Turb 1	0.09	1.44	1.92	1.44	1	1.219
Turb 2	0.09	1.52	1.92	1.44	1	1.219
Turb 3	0.09	1.60	1.92	1.44	1	1.219

Combining the above descriptions, we finalise six main cases in total:

Table 4 Computational cases

<i>Case no.</i>	<i>Cells at nozzle</i>	<i>Turbulent constant</i>	<i>Vertices</i>	<i>Cells</i>
Case 1	10	C = 1.60	78,916	39,150
Case 2	10	C = 1.44	19,929	9,810
Case 3		C = 1.52		
Case 4		C = 1.60		
Case 5	20	C = 1.44	25,351	12,500
Case 6		C = 1.60		

5 Numerical results

Figure 4 shows the comparison of the liquid penetrations using different meshes vs. time. At first, the plot for only 20 cells at nozzle diameter with the experimental result is depicted on top. With the constant equal to 1.44, the numerical result prone to the right hand side of the experimental results meanwhile with the value of 1.60, the spray

penetration tends to the other side of experimental results. This similar behaviour remains for the comparison with 10 cells. For the second plot, the critical changes are observed between the three turbulent constants. In the last plot, we could see the dramatic change in the fine mesh case where the penetration curve moves far way in comparison with the coarse mesh. Thus, the choice of this parameter must be considered for each numerical simulation.

Figure 4 Liquid penetrations (see online version for colours)

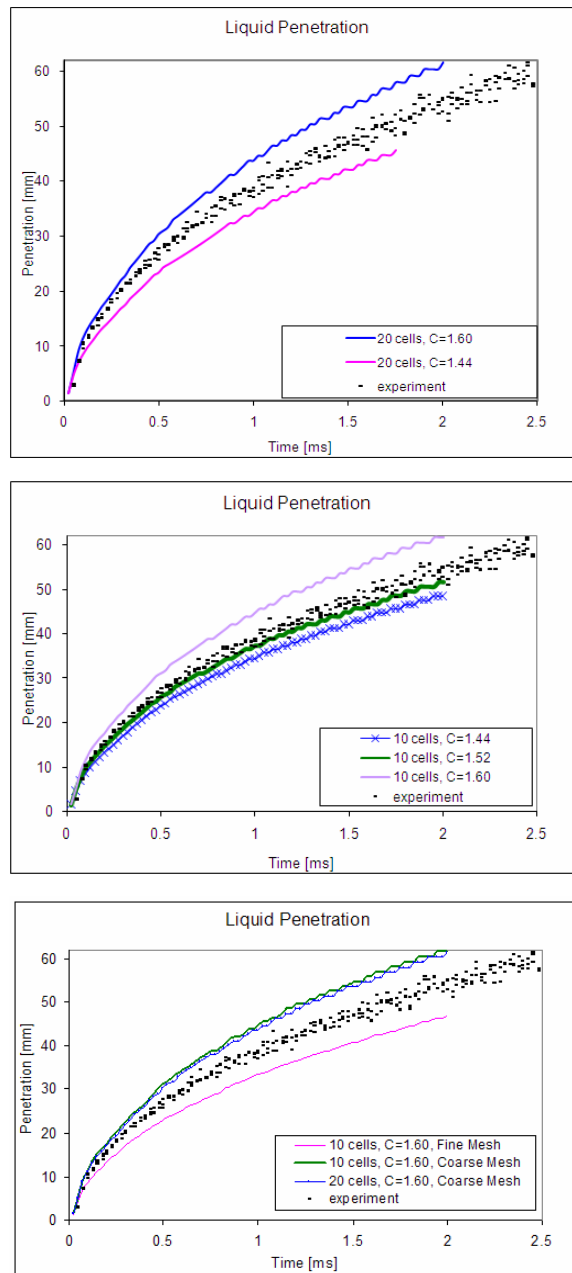
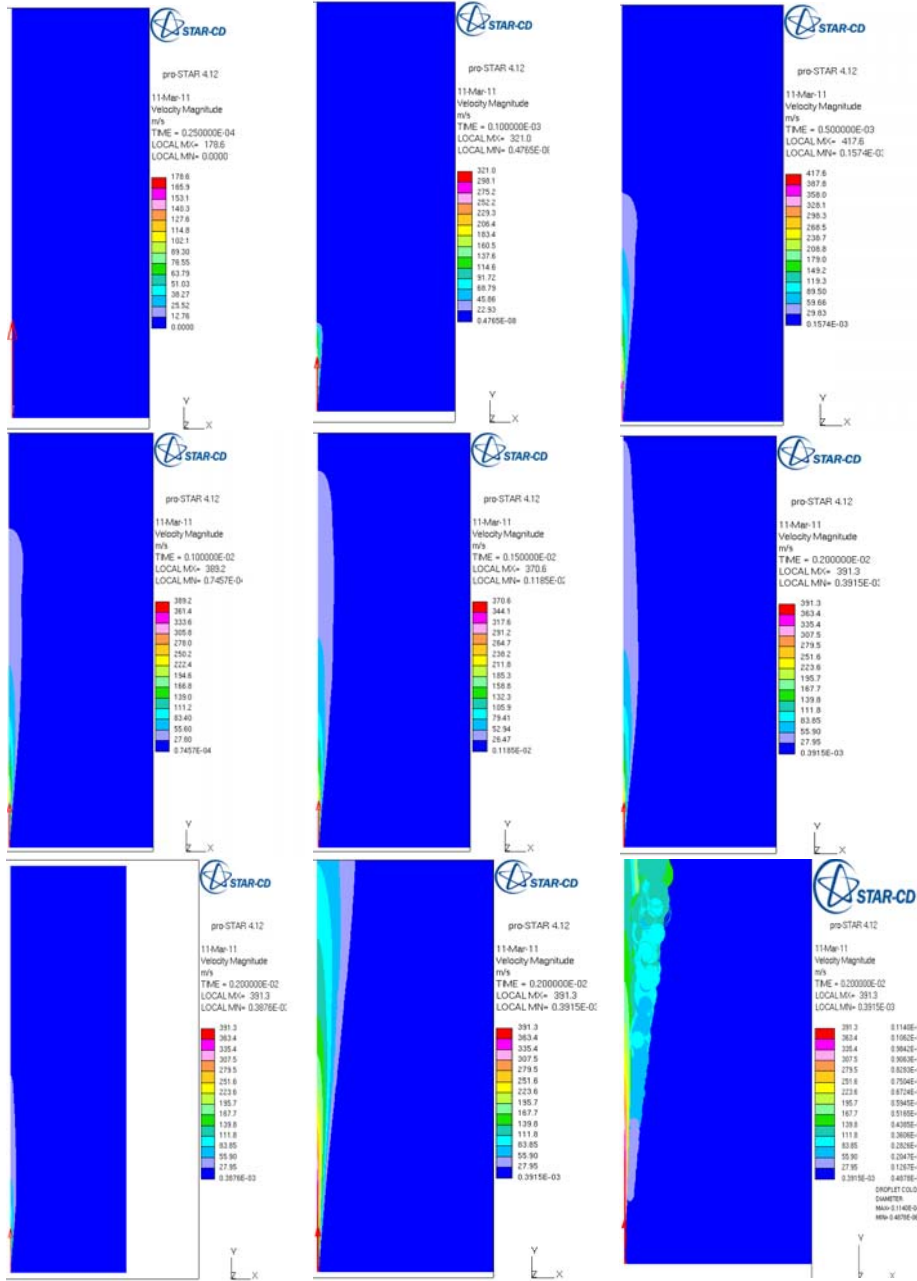


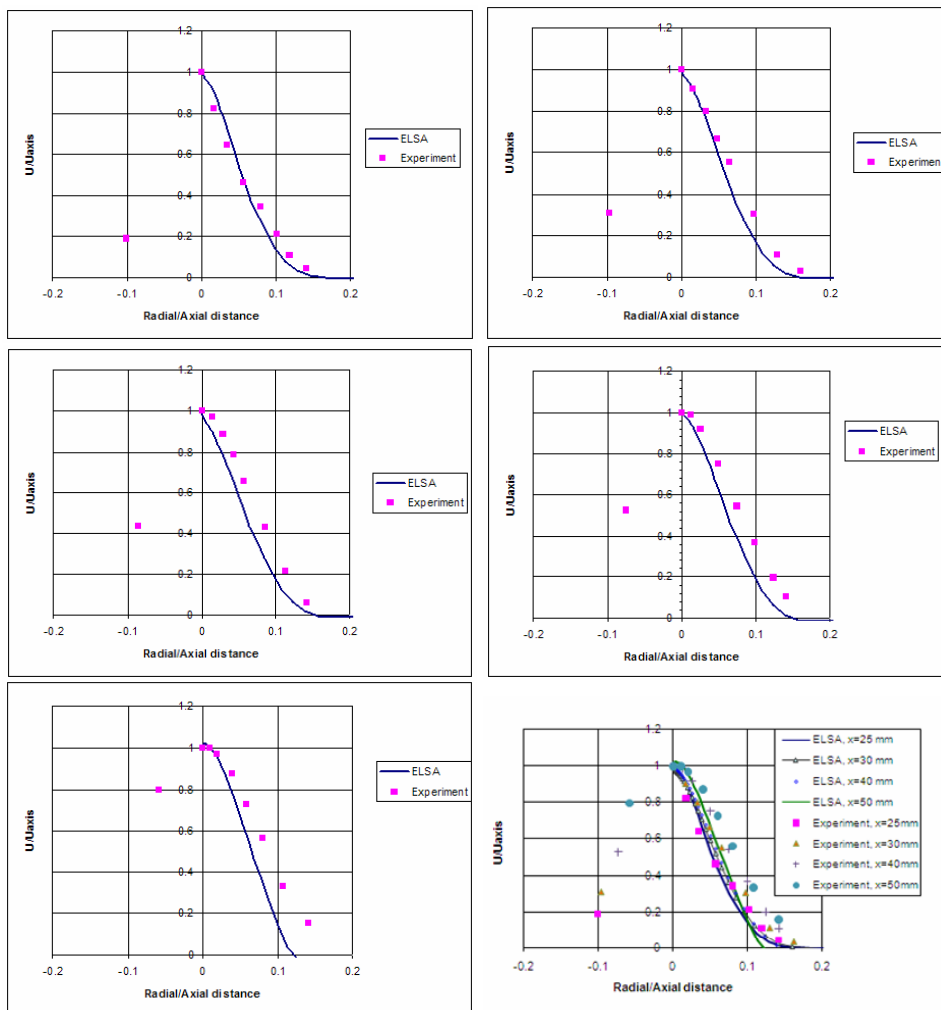
Figure 5 Spray structure and droplet formation (see online version for colours)



As visual presentation in Figure 5, it can be easily imagined the evolution of velocity profiles in various time steps of 0.025, 0.01, 0.5, 1, 1.5, 2 ms respectively, the structure of spray is represented for the number of cell size of 10 at the nozzle diameter and fine mesh case (case 1). It can be seen that velocity magnitude is highest in the zone surrounding the nozzle and in the liquid core zone where the Eulerian approach is used and lowest in

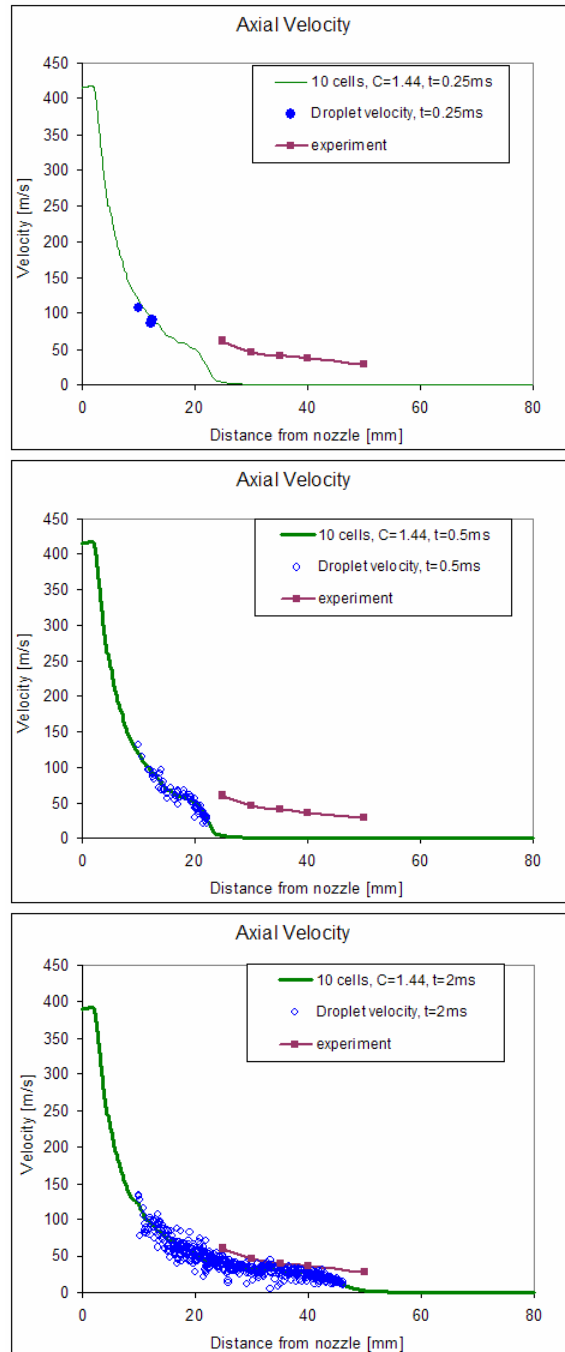
the droplet peak in the axial direction. The droplet figure describes how the droplet formation is produced starting from the transition zone and continues to develop in the farther zone (Lagrangian zone) continuously. It is the combined plot where the contours profile represents for the velocity and the round circles show the droplet diameter but it shows in the same colour scale. Here, droplet diameter is in mm and the velocity unit as m/s. Definitely, there is no droplet in the Eulerian mixture zone. It confirms our initial setting and formulae for ELSA model. Mean velocities and droplet velocities in different radial and axial position are shown in Figure 5 and Figure 6. Generally, the velocity profiles in the numerical calculation are in line with the experiments.

Figure 6 Velocity profiles of spray (10 cells, $C-\epsilon_1 = 1.60$) (see online version for colours)



In Figure 6, we plot velocity profiles in different sections with five sections at round number of distance equal to 25 30, 35, 40, and 50 mm respectively in order to compare with the available experiments from R. Payri et al. (2008). It can be seen that the velocity profiles decrease according to the penetration distance.

Figure 7 Droplet velocity profiles (see online version for colours)



In Figure 7, the droplet velocity along axial direction and total number of droplets are sketched. To bear in mind that we only take into account total droplets which contain within the closest cells from the axial line.

We can see the number of droplets increases through each time step and their velocity also changes accordingly and along the mean velocity curve.

6 Conclusions

In this report we brought out some key differences amongst those computational models and typical plots for certain cases. For the rest of figures which resulted similar behaviour, and do not add much value to the report are not showed here. As stated in our target, we showed the relationships or discrepancy among key elements of penetration, velocity, turbulent parameters and different in position or number of time step and mesh effects.

In sum, mean velocity profile and droplet velocity is staying very close with the experiment index especially in the highest time step. Liquid penetration is totally depend on the mesh size, topology and of course turbulent model and parameters which we used for our simulation. Grid sensitivity is shown in our calculations, thus for 2-D RANS (Reynolds-averaged Navier-Stokes) simulations, we can use meshes as much fine as possible if time simulation and computing power allowed in order to get nearly grid independent results. We have to do more test and computations to know exactly which value should be best fit to each case.

The diesel spray performed with ELSA model produced a good accuracy even with the 2D axisymmetric meshes, the numerical results indicated the similar prediction in conjunction with the real experimental results conducted at CMT in 2008. Designers often focus on performance areas, thus our liquid sprays analysis and design using computational fluid dynamics (CFD) simulations were performed on the diesel spray and validated the ELSA model with the latest experimental results with almost the same configuration are very useful for them to refer to.

Acknowledgements

This work has been granted by Renault and vehicle concept modelling (VECOM) – EU FP7 Marie Curie Initial Training Network (ITN) Grant Agreement 213543 (from 1 October 2008 to 30 September 2012). The aim of the proposed training network is to provide dedicated research training in the emerging field of vehicle concept modelling for up-front pre-CAD functional performance engineering, bridging between industry and academia across Europe.

References

- Beau, P.A. (2006) 'Modelisation de l'atomisation d'un jet liquide – application aux sprays diesel', PhD thesis, University of Rouen.
- Blokkeel, G., Barbeau, B. and Borghi, R. (2006) 'A 3D Eulerian model to improve the primary breakup of atomizing jet', SAE Technical Paper 2003-01-0005.
- De Lucas, M. (2007) 'Contribution a la modelisation de la pulverisation d'un liquide phytosanitaire en vue de reduire les pollutions', PhD thesis, University of Aix-Marseille II.

- Desportes, A., Zellat, M., Desoutter, G., Abouri, D., Liang, Y. and Ravet, F. (2010) 'Validation and application of the Eulerian-Lagrangian spray atomization (ELSA) model for the diesel injection simulation', SAE.
- Desportes, A., Zellat, M., Desoutter, G., Abouri, D., Liang, Y. and Ravet, F. (2010) 'Application of the Eulerian-Lagrangian spray atomization (ELSA) model for the diesel injection simulation', *THIESEL 2010 Conference*.
- Gimeno García, D.J. (2008) 'Desarrollo y aplicación de la medida del flujo de cantidad de movimiento de un chorro diesel', PhD thesis, Universidad Politécnica de Valencia.
- Lebas, R. (2007) 'Modélisation Eulerienne de l'atomisation haute pression – influences sur la vaporisation et la combustion induite', PhD thesis, University of Rouen.
- Lebas, R., Blokkeel, G., Beau, P-A. and Demoulin, F-X. (2005) 'Coupling vaporization model with the Eulerian-Lagrangian spray atomization (ELSA) model in diesel engine conditions', SAE100, 2005-01-0213.
- Lefebvre, A.H. (1989) *Atomization and Sprays*, Taylor and Francis, USA.
- Ning, W., Reitz, R.D., Lippert, A.M. and Diwakar, R. (2007) 'Development of a nextgeneration spray and atomization model using an Eulerian-Lagrangian methodology', *17th Int. Multidimensional Engine Modeling User's Group Meeting*, Detroit, MI.
- Payri, R., García, J.M., Salvador, F.J. and Gimeno, J. (2005) 'Using spray momentum flux measurements to understand the influence of diesel nozzle geometry on spray characteristics', *Fuel*, Vol. 84, No. 5, pp.551–561.
- Payri, R., Tormos, B., Salvador, F.J. and Araneo, L. (2008) 'Spray droplet velocity characterization for convergent nozzles with three different diameters', *Fuel*, Vol. 87, Nos. 15–16, pp.3176–3182.
- Vallet, A., Burluka, A.A. and Borghi, R. (2001) 'Development of an Eulerian model for the atomization of a liquid jet', *Atomization and Sprays*, Vol. 11, No. 6, pp.619–642.

Definitions/abbreviations

CAD	computer-aided design
CMT	CMT Motores Térmicos
CFD	computational fluid dynamics
DDM	discrete droplet model
ELSA	Eulerian-Lagrangian spray atomisation
ITN	initial training network
PDPA	phase doppler particle analyser
RANS	Reynolds-averaged Navier-Stokes
SMD	Sauter mean diameter
VECOM	vehicle concept modelling
R&D	research and development
NVH	noise, vibration and harshness
FE	finite element
CAX	computer-aided x
UPV	Universidad Politécnica de Valencia



Contents lists available at SciVerse ScienceDirect

Mathematical and Computer Modelling

journal homepage: www.elsevier.com/locate/mcm

Evaluation of the Eulerian–Lagrangian Spray Atomization (ELSA) model in spray simulations: 2D cases

Sergio Hoyas^{a,*}, Antonio Gil^a, Xandra Margot^a, Dung Khuong-Anh^a, Frederic Ravet^b

^a CMT-Motores Térmicos, Universitat Politècnica de València, Valencia 46022, Spain

^b Renault, 1 Avenue du Golf 78288, Guyancourt, France

ARTICLE INFO

Article history:

Received 4 October 2011

Received in revised form 28 October 2011

Accepted 2 November 2011

Keywords:

Spray models

CFD

ELSA

ABSTRACT

The aim of this paper is the evaluation and validation of the Eulerian–Lagrangian Spray Atomization (ELSA) model implemented in a CFD code by Renault. ELSA is an integrated model for capturing the whole spray evolution, in particular including primary break-up and secondary atomization. Two-dimensional simulations have been performed during the study, which is in fact enough to capture some of the main features of the spray, such as the spray penetration and the axial velocity. A mesh independence study has also been carried out in order to characterize the lowest mesh size that can be used to correctly characterize the spray. Furthermore, the two-equation $k-\varepsilon$ turbulence model has been adjusted by changing some of the parameters of the dissipation rate transport equation in order to accurately characterize the spray. Finally some analyses of the results obtained, in terms of penetration, liquid mass fraction and droplet number and size, are presented in the last section of the paper.

© 2011 Elsevier Ltd. All rights reserved.

1. Introduction

During the past fifteen years, computational fluid dynamics (CFD) has become one of the most important tools for both understanding and improving diesel spray development in the internal combustion engine (ICE). Fuel injection process and subsequent fuel–air mixing formation play a major role in combustion and pollutant emissions in the ICE. Even now, some of the processes involved in these phenomena, such as primary atomization and nozzle cavitation, are not fully understood [1–3], even taking into account that the full set of equations describing the physical situation are known [4,5].

The goal of the Eulerian–Lagrangian Spray Atomization (ELSA) model is to realistically describe the dense zone of the spray and its atomization. Since the seminal work of Vallet et al. [6] it has been under development by several authors, including Blokkeel et al. [7], Beau [8], Lebas [9], De Lucas [10], and Ning [11]. The ELSA model takes advantages of the Eulerian description of the near nozzle flow where some assumptions of standard spray models based on the discrete droplet method (DDM) show strong limitations. The DDM approach is valid only when the liquid volume fraction is small inside the computational cells and when the drops are homogeneously distributed in the computational space; neither of these requirements is satisfied in the near field of the spray. Therefore, in order to keep a low void fraction and assure numerical stability, it is necessary to use grid sizes larger than the orifice diameter, which cannot adequately resolve the flow structures in this region by means of the DDM. Additionally, it is also not required to assume any particular shape to represent drops and liquid ligaments in the ELSA model, where the average area of the liquid–gas interface is introduced as a measure of

* Corresponding author.

E-mail addresses: serhocal@mot.upv.es (S. Hoyas), angime@mot.upv.es (A. Gil), xmargot@mot.upv.es (X. Margot), ankh2@mot.upv.es (D. Khuong-Anh), frederic.ravet@renault.com (F. Ravet).

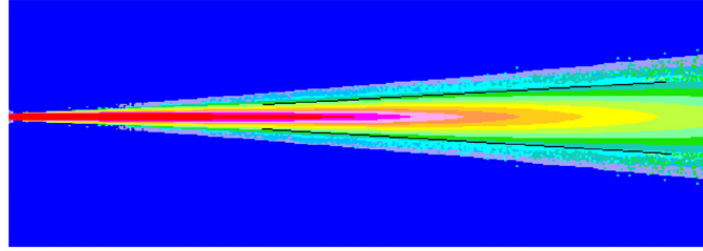


Fig. 1. Near nozzle region of a spray. The bulk of the spray is treated as an Eulerian fluid. For the outer region, where droplets appear, a Lagrangian formulation is used. A thin transition layer is also sketched (black line).

the extent of the atomization. Moreover, the DDM method applies isolated drop based models in this region with strong interaction within the liquid phase, where its validity is hardly justified.

Fig. 1 shows the three separate regions considered in the ELSA model:

- Eulerian mixture zone: in this region (the liquid core), the liquid and gas phases are considered as a unique mixture flow. The classical Eulerian model is used to obtain this single-phase flow.
- Transition zone: the switch from Eulerian to Lagrangian calculation.
- Lagrangian zone: classical Lagrangian tracking for droplets in the diluted spray zone and some regions of the dense spray zone.

The main hypothesis of ELSA, is that the flow must be a high-speed turbulent spray, where the Reynolds bulk number and Weber number should be high (see the Ph.D. thesis of [8] for a detailed study). The Reynolds number should be greater than 1500 [6], and the Weber number should be $We > 350$ [12,13]. Values of these numbers in actual diesel injectors are far greater than these thresholds. The second hypothesis is that the turbulent process of mixing between the liquid and surrounding gaseous phase is simulated as a single-phase turbulent fluid flow with mean properties. From this second hypothesis comes the main concern about the ELSA model, which is that it does not give detailed information about the two phases separately in the near nozzle region.

According to the previous statements, the purpose of the present study is to perform a 2D preliminary validation of the ELSA spray model implemented in the Star-CD code. This work is part of a more ambitious project, with the general objective of developing and validating this spray model implementation for real-life applications in CFD engine calculations, including cavitating nozzles. There also exists a growing interest in such nozzles [14–16], due to the general perception that cavitation can increase the turbulence level, thus improving the mixture of the spray and its combustion. As the DDM cannot resolve the near nozzle region, ELSA, which effectively resolves the vicinities of the nozzle, can be the right tool for coupling the internal flow and the spray.

The structure of the paper is as follows. In Section 2 the model equations and variables are written out. In Section 3 the geometry and the setup of the simulation are explained, including the onset of the experimental validation. Section 4 is devoted to the analysis of the results. Conclusions and future works are explained in the last section.

2. The ELSA model

As commented before, the ELSA model was described first by Vallet et al. [6]. Several subsequent works such as [17,8,11] also discussed this set of equations, which are written out here for the sake of completeness of the paper and to give a logical explanation of the ELSA model.

These equations solve for the spray as a whole, but there are terms that are activated or deactivated depending of the region. From now on, the subscripts l and g denote the liquid and gas zones of the flow, while $i, j = 1, 2, 3$ denote directions in space. As usual, for any magnitude σ , the Reynolds average is denoted as $\bar{\sigma}$ and the fluctuation as σ' . The mass weighted Favre mean is denoted as $\tilde{\sigma} = \overline{\rho\sigma}/\bar{\rho}$, and the Favre fluctuation as σ'' . In this definition, ρ is the density, and the velocity will be denoted as $\mathbf{u} = (u_1, u_2, u_3)$.

The mean density is defined in terms of the liquid fraction, \bar{Y}_l , as

$$\bar{\rho} = \rho_l \bar{Y}_l + \rho_g (1 - \bar{Y}_l) \quad (1)$$

which is expressed in terms of Favre means as

$$\frac{1}{\bar{\rho}} = \frac{\tilde{Y}_l}{\rho_l} + \frac{1 - \tilde{Y}_l}{\rho_g}. \quad (2)$$

The Favre averaged Navier–Stokes equations are given by

$$\partial_t \bar{\rho} \tilde{u}_i + \partial_j \bar{\rho} \tilde{u}_j \tilde{u}_i = -\partial_i \bar{p} - \partial_j R_{ij}. \quad (3)$$

In this equation, $R_{ij} = \overline{\rho u_i'' u_j''}$ is the Favre–Reynolds tensor, which needs a closure model. Classically, the standard k – ε model has been used and this tensor can be modeled as

$$R_{ij} = -\mu_t \left(\partial_j \tilde{u}_i + \partial_i \tilde{u}_j - \frac{2}{3} \partial_k \tilde{u}_k \delta_{ij} \right) + \frac{2}{3} \bar{\rho} \tilde{k} \delta_{ij}. \quad (4)$$

Here δ_{ij} is the Kronecker δ and μ_t is the turbulent viscosity, which is computed as

$$\mu_t = C_\mu \bar{\rho} \frac{\tilde{k}^2}{\tilde{\varepsilon}}. \quad (5)$$

The k – ε model is completed with the classical transport equations:

$$\partial_t \bar{\rho} \tilde{k} + \partial_j \bar{\rho} \tilde{u}_j \tilde{k} = \partial_j \left(\bar{\rho} \frac{\nu_t}{Pr_k} \partial_j \tilde{k} \right) - \bar{\rho} R_{ij} \partial_i \tilde{u}_j - \overline{u_j'' \partial_j \tilde{k}} - \bar{\rho} \tilde{\varepsilon} \quad (6)$$

$$\partial_t \bar{\rho} \tilde{\varepsilon} + \partial_j \bar{\rho} \tilde{u}_j \tilde{\varepsilon} = \partial_j \left(\bar{\rho} \frac{\nu_t}{Pr_\varepsilon} \partial_j \tilde{\varepsilon} \right) \quad (7)$$

$$+ C_{\varepsilon_1} \frac{\tilde{\varepsilon}}{\tilde{k}} \left(-\bar{\rho} R_{ij} \partial_i \tilde{u}_j - \overline{u_j'' \partial_j \tilde{\varepsilon}} \right) - C_{\varepsilon_2} \bar{\rho} \frac{\tilde{\varepsilon}^2}{\tilde{k}}. \quad (8)$$

There are still some terms in these equations that need to be modeled. The Reynolds averaged form of the Favre fluctuation is exactly related to the turbulent liquid mass flux R_{iY_l} as follows:

$$\overline{u_i''} = \bar{\rho} \left(1/\rho_l - 1/\rho_g R_{iY_l} \right), \quad (9)$$

where

$$R_{iY_l} = \frac{\overline{\rho u_i'' Y_l''}}{\bar{\rho}}. \quad (10)$$

In this model, the gas and liquid phase are considered as species, so the corresponding transport equation is quite important [9]:

$$\partial_t \bar{\rho} \tilde{Y}_l + \partial_j \bar{\rho} \tilde{u}_j \tilde{Y}_l = \partial_j \bar{\rho} R_{jY_l} - \rho \dot{m}_{v,ELSA} \tilde{\Omega}. \quad (11)$$

The first RHS term of this equation is usually modeled as

$$R_{jY_l} = \frac{\nu_t}{Sc_t} \partial_j \tilde{Y}_l, \quad (12)$$

but in this case, it is possible to get a closed expression:

$$R_{jY_l} = \tilde{Y}_l \left(1 - \tilde{Y}_l \right) \left(\tilde{u}_j|_l - \tilde{u}_j|_g \right) = \tilde{Y}_l \left(\tilde{u}_j|_l - \tilde{u}_j \right). \quad (13)$$

See [9], for instance, for a detailed account of Eq. (13).

The second RHS term of this equation represents the effects of the liquid–gas surface density. The transport equation most commonly used for Ω , which is the quantity of the liquid/gas interface per unit of mass, is

$$\partial_t \bar{\rho} \tilde{\Omega} + \partial_j \bar{\rho} \tilde{u}_j \tilde{\Omega} = \partial_j \left(\bar{\rho} \frac{\nu_t}{Sc_t} \partial_j \tilde{\Omega} \right) + \bar{\rho} \left(\Omega_{terms} \right) + S_{EL}^{\tilde{\Omega}} \quad (14)$$

where

$$\Omega_{terms} = \tilde{\Omega}_{init} + \tilde{\Omega}_{mean} + \tilde{\Omega}_{turb} + \tilde{\Omega}_{coll} + \tilde{\Omega}_{coal}. \quad (15)$$

These five different terms represent the production and destruction of the liquid surface due to its initial value, mean, turbulent, collision and coalescence effects respectively. There are no closed representations for these terms, so all of them must be modeled.

The first source term in Eq. (15) permits us to initialize the calculations, since all other source terms are proportional to $\tilde{\Omega}$. It is defined as

$$\tilde{\Omega}_{init} = \begin{cases} 2 \frac{\nu_t}{Sc_t} \frac{6\bar{\rho}}{\rho_l \rho_g L_t} \left(\partial_i \tilde{Y}_l \right) \left(\partial_i \tilde{Y}_l \right), & \text{if } \tilde{Y}_l \left(1 - \tilde{Y}_l \right) \leq 0.001 \\ 2 \frac{\nu_t}{Sc_t} \frac{\tilde{\Omega}}{\tilde{Y}_l \left(1 - \tilde{Y}_l \right)} \left(\partial_i \tilde{Y}_l \right) \left(\partial_i \tilde{Y}_l \right), & \text{otherwise,} \end{cases} \quad (16)$$

where L_t is the turbulent scale. The three next terms are modeled as

$$\dot{\tilde{\Omega}}_{mean} = \frac{R_{ij}}{\rho k} \partial_j U_i \tilde{\Omega}, \quad (17)$$

$$\dot{\tilde{\Omega}}_{turb} = \frac{\tilde{\Omega}}{\tau_{turb}}, \quad (18)$$

$$\dot{\tilde{\Omega}}_{coll} = \frac{\tilde{\Omega}}{\tau_{coll}}. \quad (19)$$

In these equations, τ_{turb} and τ_{coll} are the turbulent and collision characteristic times. The last term deals with the coalescence of droplets and is modeled as

$$\dot{\tilde{\Omega}}_{coal} = -\frac{1}{\tau_{coll}} \frac{\tilde{\Omega}^2}{\tilde{\Omega}_{crit}} \quad (20)$$

where

$$\tilde{\Omega}_{crit} = \frac{6\tilde{Y}_l}{\rho_l d_{crit}}, \quad (21)$$

d_{crit} being the critical diameter of the droplets. Details concerning Eqs. (16)–(21) are given in [8].

As was stated (Fig. 1), the ELSA model uses the Eulerian formulation close to the nozzle and the Lagrangian when the spray is sufficiently diluted. The main parameter controlling this transition is the Eulerian liquid volume fraction, defined as

$$\tilde{\Phi}_l = \tilde{Y}_l \frac{\bar{\rho}}{\rho_l} \leq \tilde{\Phi}_l^{crit}. \quad (22)$$

The transition is complete when the liquid volume fraction becomes lower than 0.01 [17]. The transition zone is composed of the computational cells that form the border with the dense zone (i.e. the zone where the liquid volume fraction is greater than 0.01) and only one parcel is generated per transition cell and per time step.

Furthermore, the ELSA model can be used to compute the diameter of the droplets. It is calculated as the Sauter mean diameter, given by

$$D_{32} = \frac{6\tilde{Y}_l}{\rho_l \tilde{\Omega}}. \quad (23)$$

The number of droplets per generated parcel is obtained from mass conservation:

$$n_{drop} = \frac{\bar{\rho} \tilde{Y}_l V_{cell}}{\pi / 6 \rho_l D_{32}^3}, \quad (24)$$

where V_{cell} is the volume of each transitional cell. The droplet velocity is given by

$$\tilde{u}_{l,j} = \tilde{u}_j + \frac{R_{iY_l}}{\bar{\rho} \tilde{Y}_l}. \quad (25)$$

3. The model validation setup

In order to perform this 2D validation of the ELSA model, data obtained from an injection experimental test facility [19] are used for the process of validation of the 2D-ELSA calculations presented in this work. The geometry reproduces a chamber of 80×25 mm. In this chamber, one diesel spray develops, coming from a non-cavitating single-hole injector (tapered nozzle), with an outlet diameter of $112 \mu\text{m}$. An inert gas is considered to be enclosed in the chamber at an initial ambient pressure (P_A) and temperature (T_A) of 3.53 MPa and 293 K respectively. The fuel injection pressure is $P_i = 80$ MPa and the fuel density is $\rho = 822 \text{ kg/m}^3$.

This nozzle presents an averaged velocity profile input at the nozzle exit that is shown in Fig. 2. The great irregularity shown in this picture seems to be an effect of wave reflections inside the nozzle (see [18,19] or [20] for more details concerning this issue).

The simulations are actually 3D simulations with only a cell in the azimuthal direction, and modeling a 5° sector of the spray. This is shown in Fig. 3, where the boundary conditions imposed on the spray and chamber are also depicted. The key zone in simulations of this sort is the vicinity of the nozzle, where the mesh size has to be small enough to capture the spray structure and droplets. The criterion used in this paper is to define the size of the first cell and then extrude the mesh, fixing the axial and radial ratios. The last to first ratio, $R = (l_1/l_n)^{-1/(n-1)}$, is fixed in all cases at 0.006. In this formula, l_1 and l_n are the lengths of the first and last cells, and n is the number of cells in the radial direction.

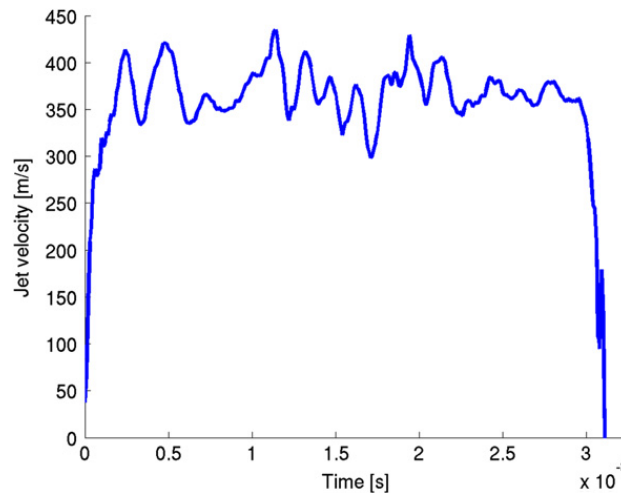


Fig. 2. Nozzle velocity profile at the nozzle exit. See [18] for details.

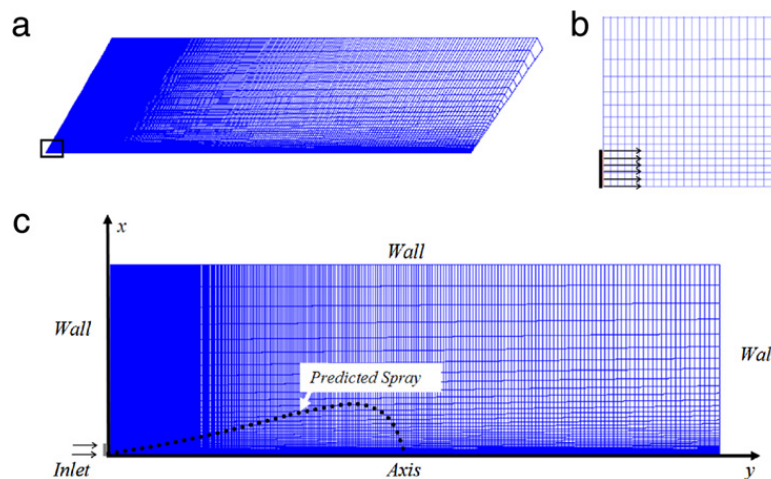


Fig. 3. 3D mesh used for the simulation (a) with a zoom of the near nozzle region (b), and the boundary conditions used (c).

As was stated before, turbulence is modeled using a $k-\varepsilon$ model. The model constants used are the classical ones apart from $C_{\varepsilon 1}$, which is well known [21] to cause an overprediction of the spreading and decay of rate of a round jet flow. The constant modifications are based on the suggestion of [22,23]. Thus, three values—classical, suggested and averaged (1.44, 1.60 and 1.52, respectively)—are used.

4. Numerical results

A typical calculation of a diesel injection, around $t_{inj} = 2$ ms, using the ELSA model takes approximately one week on 8–12 last generation cores. So, it is crucial to choose the mesh as coarse as possible to reduce the computational time, as we need to validate many different factors afterwards. Actually, mesh size is only one of the criteria used, due to the value of $C_{\varepsilon 1}$ greatly affecting the spray penetration. The numerical results are depicted in Figs. 4–7.

Fig. 4 shows typical information on the spray penetration and axial velocity. In Fig. 4a penetration is plotted against experimental values for different meshes and $C_{\varepsilon 1} = 1.52$ (see [20] for details). From this figure it seems that $n = 326$ would be the right choice. Nevertheless, as we can see in Fig. 4b, axial velocity is not well represented. Despite this underestimation, if for any reason one is only interested in penetration, this election can save a significant amount of time.

The challenge now is to find the ultimate setup for minimizing the gap between experiments and our calculated cases in both velocity and spray penetration. In order to do this, the number of cells either along the axial axis or along the radial axis is kept constant, and the value is changed on the other axis. After testing a variety of setups with different radial and axial cells, the most appropriate criterion is obtained, providing not only the more accurate calculation but also reducing the time spent. Some other computations, not shown, allow us to be certain that we already have mesh independence. Fig. 5 shows the final mesh chosen, $n = 500$, $m = 50$, which can be used to accurately represent the experimental results and eliminate the weakness described in the case with $C_{\varepsilon 1} = 1.52$ above. In this case, $C_{\varepsilon 1} = 1.60$ is used, as Pope [21] suggested, for capturing the jet from the round nozzle. This results in a better curve in terms of axial velocity (see Fig. 5b), while the

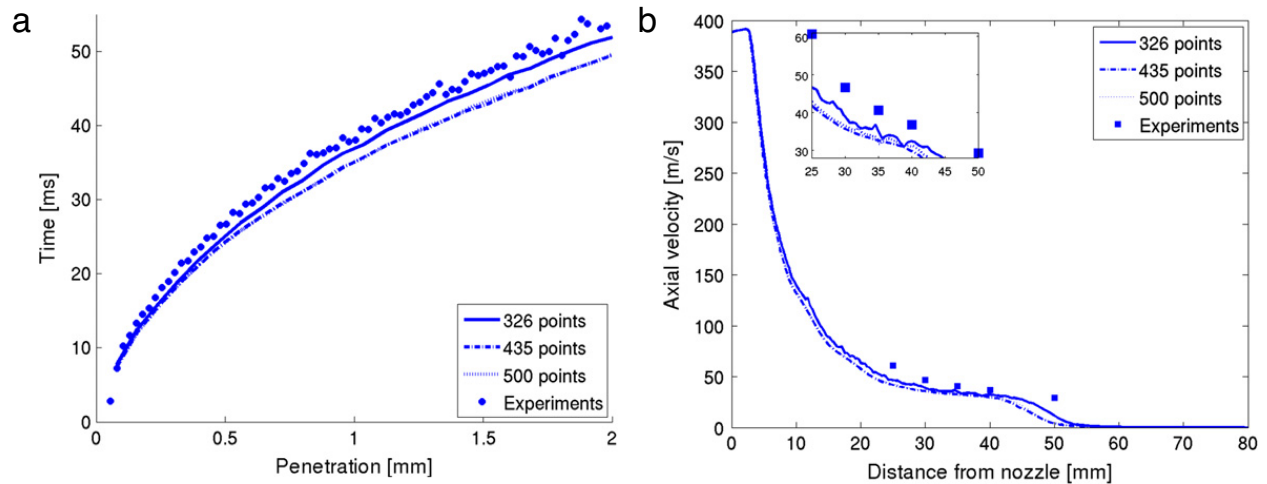


Fig. 4. Penetration and axial velocity, varying the number of cells in the axial direction. Although the results for the penetration are a little bit overestimated, the axial velocity presents a tight fit.

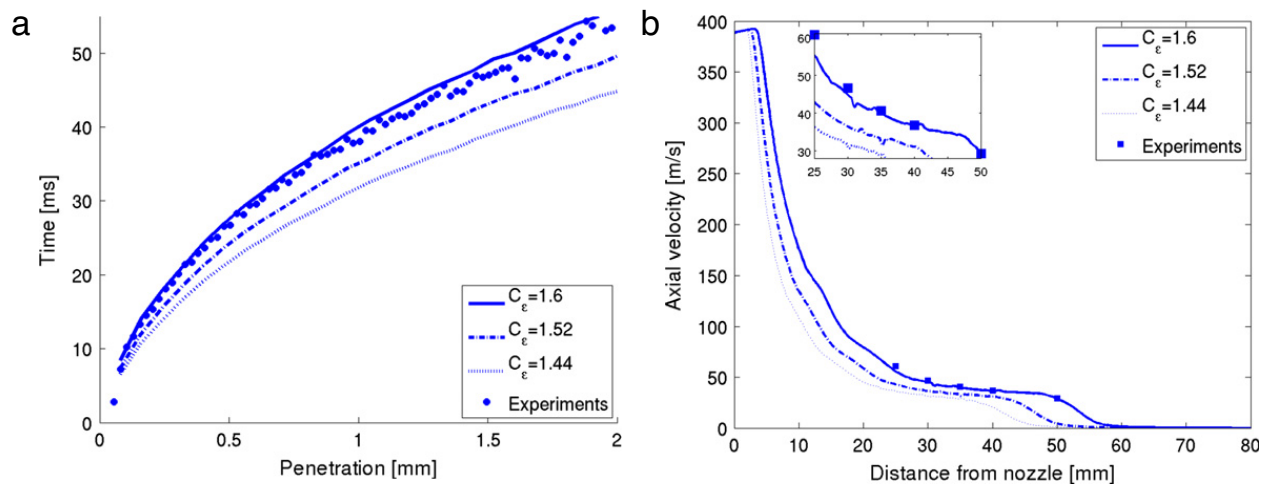


Fig. 5. Penetration and axial velocity, varying the diffusion coefficient $C_{\epsilon_1} = 1.60$. Although the results concerning penetration are a little overestimated, the axial velocity presents an almost perfect adjustment.

spray penetration curve is slightly overestimated over the experimental result, but is still highly acceptable in the numerical calculation. Furthermore, it creates a lesser error in comparison with Fig. 4.

Droplet formation and its distribution along the axial axis are represented in Fig. 6. In this figure, the same mesh and boundary condition as were plotted and mentioned in Fig. 5 are used. The actual number of droplets and their size in each time step are not shown—just those at $t = 2$ ms. Each point represents a droplet that is obtained in this case. In order to reduce the discrepancy in the scatter plot and to predict the trend of average droplet size along the axis, a high order polynomial curve fitting is obtained, drawn as a continuous line.

In the last figure, Fig. 7, the spray evolution in combination with droplets is visualized. In Fig. 6, the numbers of droplets formed in each time step are not shown, but can be observed. The consistency of the spray structure is plotted in these figures where the vapor mass fraction is also shown. The relative importance and main features of the ELSA model can also be found in this figure, where we can observe the dense zone without droplets, and the other two zones in which the droplets are produced gradually.

5. Conclusions

In this study, a pre-validation study of the ELSA model, implemented in Adapco's Star-CD software from Renault, has been performed. The several advantages of the ELSA model, compared to the traditional DDM method, and its mathematical characterization are described in the paper. Selection of the right setup and appropriate method for determining the relative importance of a few parameters was dealt with; the best case, which we suggest using, in this article gives results very similar in profile to the results obtained from diesel spray experiments. The coarser mesh is able to provide an accurate description of the penetration and axial velocity, with a corrected value of the $k-\epsilon$ constant $C_{\epsilon_1} = 1.60$. Besides this, the droplet generation and spray angle and shape show that the ELSA model can provide an accurate description of these features.

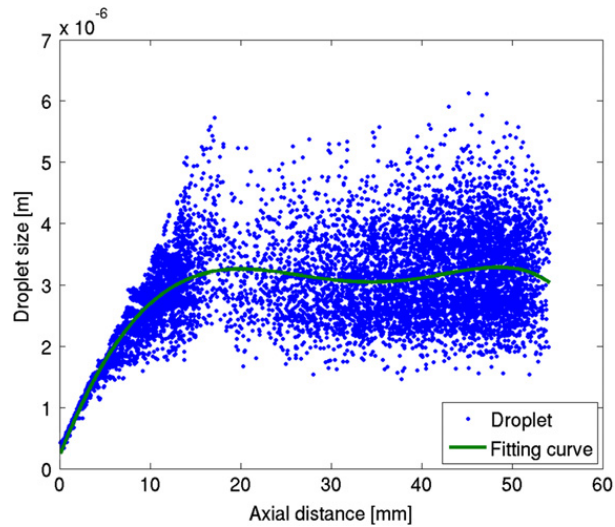


Fig. 6. Droplet size distribution against axial distance.

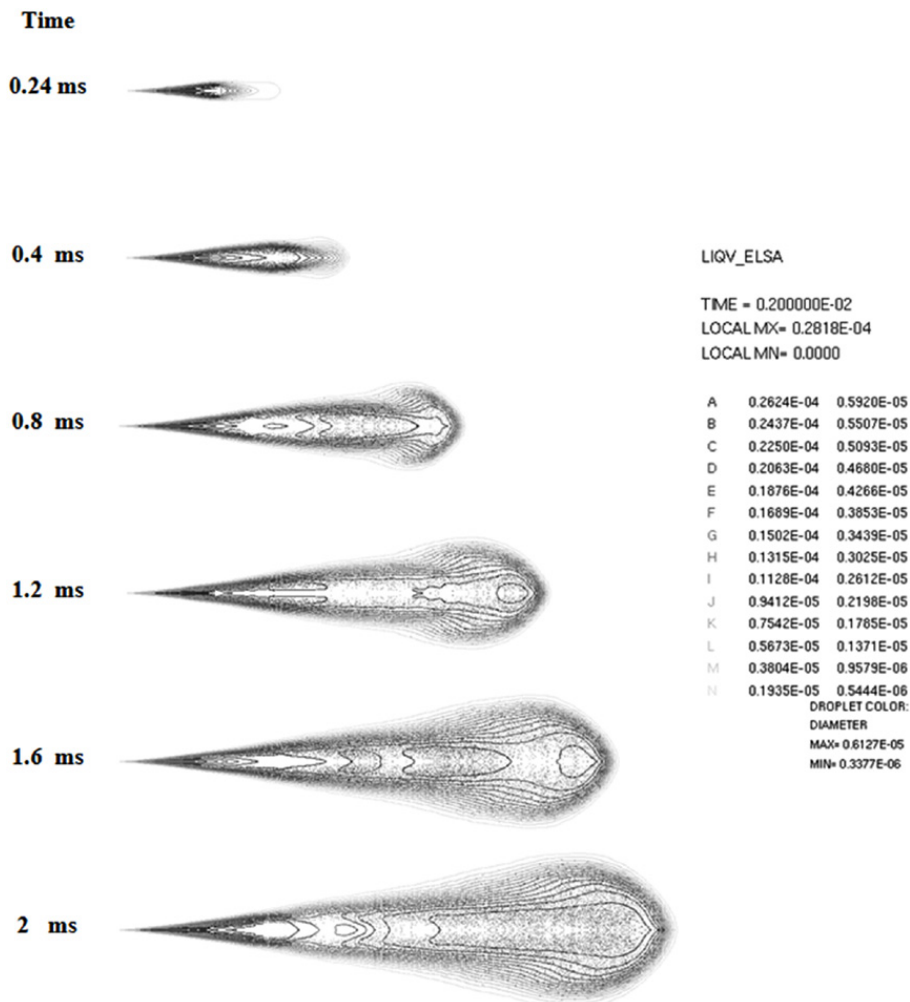


Fig. 7. Spray development against time. Every cell showing droplets is plotted.

There are three major drawbacks in continuing the validation. Firstly, it is necessary to increase the temperature in the chamber in order to take into account the evaporation of diesel droplets. Secondly, 2D cases are special simulations, and do not reflect the 3D structure and development of real-life sprays. Last, but by no means least, it is necessary to consider cavitating nozzles, as it seems that cavitation is present in nozzles now and will remain so for the foreseeable future.

Acknowledgments

This work was supported by Renault and VECOM (Vehicle Concept Modeling) EU FP7, under the Marie Curie Initial Training Network (ITN) Grant Agreement 213543. The authors also acknowledge the support of the Generalitat Valenciana, under the contract GV/2010/039.

References

- [1] A.H. Lefebvre, *Atomization and Sprays*, Taylor and Francis, 1989.
- [2] R. Lebas, G. Blokkeel, P. Beau, F. Demoulin, Coupling vaporization model with the Eulerian–Lagrangian Spray Atomization (ELSA) model in diesel engine conditions, SAE Technical Paper 2005-01-0213, 2005.
- [3] R. Lebas, T. Menard, P.A. Beau, A. Berlemont, F.X. Demoulin, Numerical simulation of primary break-up and atomization: DNS and modelling study, *Int. J. Multiphase Flow* 35 (2009) 247–260.
- [4] M. Ishii, *Thermo-Fluid Dynamic Theory of Two-Phase Flow*, second ed., Springer, New York, 2011.
- [5] I. Kataoka, Local instant formulation of two-phase flow, *Int. J. Multiphase Flow* 12 (1986) 745–758.
- [6] A. Vallet, A.A. Burluka, R. Borghi, Development of a Eulerian model for the atomization of a liquid jet, *Atom. Sprays* 11 (2001) 619–642.
- [7] G. Blokkeel, B. Barbeau, R. Borghi, A 3D Eulerian model to improve the primary breakup of atomizing jet, SAE Technical Paper 2003-01-0005.
- [8] P.A. Beau, *Modelisation de l'atomisation d'un jet liquide—application aux sprays diesel*, Ph.D. Thesis, University of Rouen, 2006.
- [9] R. Lebas, *Modelisation Eulerienne de l'atomisation haute pression—influences sur la vaporisation et la combustion induite*, Ph.D. Thesis, University of Rouen, 2007.
- [10] M. De Lucas, *Contribution a la modelisation de la pulverisation d'un liquide phytosanitaire en vue de reduire les pollutions*, Ph.D. Thesis, University of Aix-Marseille II, 2007.
- [11] W. Ning, R.D. Reitz, A.M. Lippert, R. Diwakar, Development of a next generation spray and atomization model using an Eulerian–Lagrangian methodology, in: 17th Int. Multidimensional Engine Modeling User's Group Meeting, Detroit, MI, 2007.
- [12] S. Lee, R. Reitz, Effect of liquid properties on the breakup mechanism of high-speed liquid drops, *Atom. Sprays* 11 (2001) 1–19.
- [13] F. Tanner, Development and validation of a cascade atomization and drop breakup model for high velocity dense sprays, *Atom. Sprays* 14 (2004) 20–32.
- [14] F.J. Salvador, S. Hoyas, R. Novella, J. Martinez-Lopez, Numerical simulation and extended validation of two-phase compressible flow in diesel injector nozzles, *Proc. Inst. Mech. Eng. Part D—J. Automob. Eng.* 225 (D4) (2011) 545–563.
- [15] X. Margot, S. Hoyas, P. Fajardo, S. Patouna, A moving mesh generation strategy for solving an injector internal flow problem, *Math. Comput. Modelling* 52 (2010) 1143–1150.
- [16] X. Margot, S. Hoyas, P. Fajardo, S. Patouna, CFD study of needle motion influence on the exit flow conditions of single-hole injectors, *Atom. Sprays* 21 (2011) 31–40.
- [17] A. Desportes, M. Zellat, G. Desoutter, D. Abouri, Y. Liang, F. Ravet, Validation and application of the Eulerian–Lagrangian Spray Atomization (ELSA) model for the diesel injection simulation, SAE, 2010.
- [18] R. Payri, F.J. Salvador, J. Gimeno, A. Garcia, Flow regime effects over non-cavitating diesel injection nozzles, *Int. J. Heat Fluid Flow* 32 (2011) 273–284.
- [19] R. Payri, J.M. García, F.J. Salvador, J. Gimeno, Using spray momentum flux measurements to understand the influence of diesel nozzle geometry on spray characteristics, *Fuel* 84 (2005) 551–561.
- [20] R. Payri, B. Tormos, F.J. Salvador, L. Araneo, Spray droplet velocity characterization for convergent nozzles with three different diameters, *Fuel* 87 (2008) 3176–3182.
- [21] S. Pope, An explanation of the turbulent round-jet/plain-jet anomaly, *AIAA* 16 (1978) 279–281.
- [22] J. Janicka, N. Peters, Prediction of turbulent jet diffusion flame lift-off using a PDF transport equation, in: *Symposium International on Combustion*, 19, 1982 pp. 367–374.
- [23] B.B. Dally, Flow and mixing fields of turbulent bluff-body jets and flames, *Combust. Theory Model.* 2 (1998) 193–219.

A RECENT EULERIAN-LAGRANGIAN CFD METHODOLOGY FOR MODELLING DIRECT INJECTION DIESEL SPRAYS

José M. Desantes¹, Sergio Hoyas², Antonio Gil³, Dung Khuong-Anh⁴
and Frédéric Ravet⁵

^{1,2,3,4} CMT-Motores Térmicos, Universitat Politècnica de València, Valencia 46022, Spain
e-mail: ¹ jmdesant@mot.upv.es, ² serhocal@mot.upv.es, ³ angime@mot.upv.es,
⁴ ankh2@mot.upv.es

⁵ Renault
1 Avenue du Golf 78288, Guyancourt, France
e-mail: frederic.ravet@renault.com

ABSTRACT

The global objective of this work is to show the capabilities of the Eulerian-Lagrangian Spray Atomization (ELSA) model for the simulation of Diesel sprays in cold starting conditions. Our main topic is to focus in the analysis of spray formation and its evolution at low temperature 255K (-18°C) and non-evaporative conditions. Spray behaviour and several macroscopic properties, included the liquid spray penetration, and cone angle are also characterized. This study has been carried out using different ambient temperature and chamber pressure conditions. Additionally, the variations of several technical quantities, as the area coefficient and effective diameter are also studied. The results are compared with the latest experimental results in this field obtained in our institute. In the meantime, we also compare with the normal ambient temperature at 298 K (25°C) where the numerical validation of the model has shown a good agreement.

Key words: *CFD, ELSA, Eulerian, Lagrangian, Diesel spray, Non-evaporating, Atomization.*

1. INTRODUCTION

Efficiency standards, emission control and fuel economy have been and are nowadays an immense challenge in the automotive industry. Even though automotive world have made big advances during the last decades in the efficiency of both the gasoline and diesel engines, there are many processes and mechanism that should be improved. These include the necessity of a better understanding of noise generation, physics of turbulent flows, combustion processes and pollutant formation and transport. In the field of numerical simulation, Computational Fluid Dynamics (CFD) has established its roles in the car industry to take advantage of its relatively easy implementation, low time consuming and lower cost investment.

The understanding of spray and atomization of diesel spray in the internal combustion engine is very difficult in either experimental or theoretical studies (See for instance the complex phenomena presented by Lefebvre, 1989 [1]). Fuel spray occurs in a small chamber inside the combustion engine. Fuel comes from a tiny nozzle cross section (hundred micrometers) at very high pressure and everything happens at an extremely short time (few milliseconds). Regardless the reactive part of the processes, diesel spray study includes several fundamentals, and not totally resolved topics, as can be the spray structure itself, break-up and atomization processes, or the behaviour of two-phase turbulent flows.

As Direct Numerical Simulation (DNS) is impossible in the daily product design, due to its massive computational cost, Large Eddy Simulation (LES) model has been applied gradually in studying specific problems in engine simulation together with the continuously increasing powerful computer technology. LES schemes, however, need still a further theoretical development, due to some problems close to walls and that the grid resolution must be adjusted correctly with each particular flow problem and boundary conditions. Thus, the Reynolds-averaged Navier–Stokes (RANS) turbulence models are still the most used methods modelling turbulence due to its relatively good accuracy at a very low computational cost.

RANS approaches in spray modelling using both Eulerian and Lagrangian descriptions are being used in industry for decades. However, each of them has both advantages and disadvantages in modelling the various regions of spray consisting of the dense zone and the downstream dilute zone. Typically the Eulerian description presents better results in the first part of the spray, whereas Lagrangian description is the most widely used in the diluted zone. In the framework of this numerical research, we have used a coupled method for spray and atomization simulation: ELSA model. The original idea was ignited by Vallet *et al.* in 2001 [2], Blokkeel *et al.* added an overview in 3D [3], Beau formed many source terms and simulation in his thesis [4], and so on. This algorithm is able to describe the primary break-up and the secondary atomization of the spray, and switches automatically from one description to the other.

This algorithm has been implemented in CD-Adapco Star-CD CFD code, conducted together with Renault S.A. The code has been previously validated, showing an excellent agreement with experimental data ([5], [6], and [7]). As stated before, spray simulations on cold starting conditions are performed by means of the ELSA model are presented in this paper.

2. COMPUTATIONAL METHOD

As mentioned previously, the ELSA model was first initiated in an article of Vallet *et al.*, 2001 [2]. Several other continuous works, including Beau, 2006 [8], Lebas, 2007 [9], De Lucas M., 2007 [10] and Ning *et al.* [11] also additionally contributed to the development of the model. A detail description of governing equations and methodology were presented in Hoyas *et al.*, 2011 ([6] and [7]), and Desportes *et al.*, 2010 ([12], and [13]). In this subsection, the main equations are summarized hereafter in

shake of completeness of the paper and a logical explanation of the ELSA model. These equations cover the several regions of the ELSA model, changing from one to another, from now on and in all the sections, the subscript l stands for liquid and g stands for gas, whereas i, j are the direction in space.

2.1. Eulerian Mixture Zone

The mean liquid mass fraction, \tilde{Y}_l is

$$\tilde{Y}_l = \frac{\overline{\rho Y_l}}{\bar{\rho}} \quad (1)$$

where ρ is the density and Y_l is the liquid mass fraction. Intuitively, mean density, $\bar{\rho}$ is defined as

$$\bar{\rho} = \rho_l \bar{Y}_l + \rho_g (1 - \bar{Y}_l) \quad (2)$$

which is expressed in terms of \tilde{Y}_l as

$$\frac{1}{\bar{\rho}} = \frac{\tilde{Y}_l}{\rho_l} + \frac{1 - \tilde{Y}_l}{\rho_g} \quad (3)$$

Favre averaged mean velocity is then

$$\tilde{U}_i = \tilde{Y}_l U_{l,i} + (1 - \tilde{Y}_l) U_{g,i} \quad (4)$$

2.2. Liquid/Gas Interface Density

A transport equation for liquid surface density, $\tilde{\Omega}$, is postulated by analogy with the flame surface density.

$$\frac{\partial \bar{\rho} \tilde{\Omega}}{\partial t} + \frac{\partial \bar{\rho} \tilde{\Omega} \tilde{U}_j}{\partial x_j} = \frac{\partial}{\partial x_j} \left(\bar{\rho} \frac{v_t}{Sc_t} \frac{\partial \tilde{\Omega}}{\partial x_j} \right) + \bar{\rho} \cdot \left(\tilde{\Omega}_{init} + \tilde{\Omega}_{mean} + \tilde{\Omega}_{turb} + \tilde{\Omega}_{coll} + \tilde{\Omega}_{coal} \right) + S_{EL}^{\tilde{\Omega}} \quad (5)$$

Where $\tilde{\Omega}_{init}$, $\tilde{\Omega}_{mean}$, $\tilde{\Omega}_{turb}$, $\tilde{\Omega}_{coll}$ and $\tilde{\Omega}_{coal}$ are the initial, mean, turbulence, collision and coalescence value of liquid/gas surface density respectively; $S_{EL}^{\tilde{\Omega}}$ is the source term of the liquid/gas interface. Beau, 2006 [8] introduced other notion of liquid/gas interface per unity of mass that is defined as $\tilde{\Omega} = \bar{\Sigma} / \bar{\rho}$ (m²/kg).

2.3. Transition Zone

The model relies on a critical value of the Eulerian liquid volume fraction to decide whether it should turn from Eulerian to Lagrangian formulation (Beau, 2006 [8]). The Lagrangian droplets are formed where spray is assumed to be diluted enough. It follows the below relationship.

$$\tilde{\Phi}_l = \tilde{Y}_l \frac{\bar{\rho}}{\rho_l} \leq \tilde{\Phi}_l^{crit} \quad (6)$$

with $\tilde{\Phi}_l^{crit}$ stands for the critical value of the Eulerian liquid volume fraction.

The transitional criterion is based on the value of liquid volume fraction that is linked to the ratio of the mean free path between two droplets and mean equivalent radius of the droplets in the cell. In our calculations, the transition is done when the liquid volume fraction becomes lower than 0.01 [12]. The transition zone is composed of the computational cells that form the border with the dense zone (i.e. zone where the liquid volume fraction is greater than 0.01) and only one parcel is generated per transition cell and per time step.

The velocity of the droplets is defined as

$$\bar{U}_{l,i} = \tilde{U}_i + \frac{\overline{\rho u_i'' y''}}{\bar{\rho} \tilde{Y}_l} \quad (7)$$

3. EXPERIMENTAL DATA AND SETUP

The experimental results used in this paper were conducted in a test rig installed at CMT Motores Térmicos Institute. The facility has been used to investigate the influence of diesel spray under cold starting conditions [14]. This set of experiments, were intended only for studying the macroscopic characteristics of the diesel spray.

3.1. Nozzle Geometry and Liquid Fuel

For this study, a conical nozzle, $D = 112 \mu\text{m}$ was used. Macián et al., 2003 [15] developed the silicone methodology to determine the internal geometry of the injector as shown in Figure 1. Its main parameters are depicted in Table 1.

Table 1: Nozzle parameters

Nozzle	r	D_e (inlet diameter)	D_0 (out diameter at the nozzle exit)	k-factor
	[μm]	[μm]	[μm]	[-]
N1	42	140	112	2.8

Where the k-factor, a measure of the conicity, is calculated based on the following formula:

$$k - factor = \frac{D_e - D_0}{10\mu\text{m}} \quad (8)$$

Nitrogen was used to fill the pressurised vessel. ARCTIQUE fuel (ARCT from now on), was investigated. These results were used in order to validate the simulation, and once

trusted, another fuel, ELITE – Repsol (REF) has been used. The properties of those fuels are tabulated in Table 2.

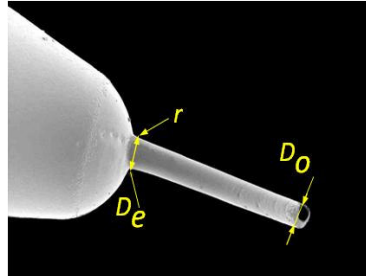


Figure 1: Nozzle geometry and the definition of some basic parameter

Table 2: Fuel properties

Fuel type	Liquid Density (kg/m ³)	Kinematic Viscosity (mm ² /s)	Dynamic Viscosity (kg/ms)	Surface Tension (N/m)
ARCTIQUE (ARCT)	825	2.34	0.00193050	0.0205
ELITE – Repsol (REF)	812	2.06	0.00167272	0.022

3.2. Measurement of the Injection Rate

Bosch, 1966 [16] developed the test rig using Injection Rate Discharge Curve Indicator (IRDCI) to measure the mass flow rate based on the Bosch method. The mass flow rate test rig operates relied on the principle the pressure wave propagation in the liquid column. The pressure wave created a pressure variation, these quantities is then recorded by a piezoelectric sensor located near the nozzle tip.

Using Allievi equation ([17], and [18]) for a simple pressure wave in a steady flows, the pressure increment with respect to the steady pressure, ΔP_m is linearly proportional to the liquid flow velocity:

$$\Delta P_m = a \rho_l u \quad (9)$$

Where a stands for the fuel speed of sound, u stands for the liquid fuel velocity.

Finally, the injection rate \dot{m} is obtained using the following equation:

$$\dot{m}(t) = \frac{A_{tub} \Delta P_m}{a} \quad (10)$$

where A_{tub} is the cross section area of the tube.

4. BOUNDARY CONDITIONS AND GEOMETRY

In previous articles, a detailed study of the number of cells in the nozzle diameter, axial,

radial cells, successive ratio of mesh edges, etc., were performed ([5], [6], and [7]). Hence, the mesh dependency is not considered in this study. Similar scales and ratios obtained from these previous works have been applied to build the grid for this nozzle.

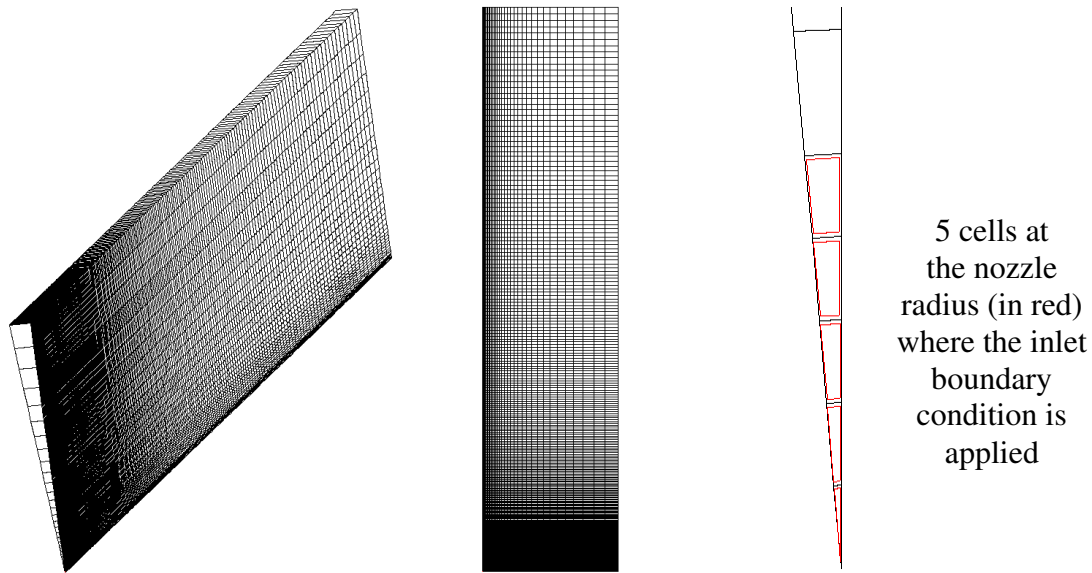


Figure 2: (from the left to the right) Isometric view of the whole computational domain, side view and zoom of front view at nozzle cross section

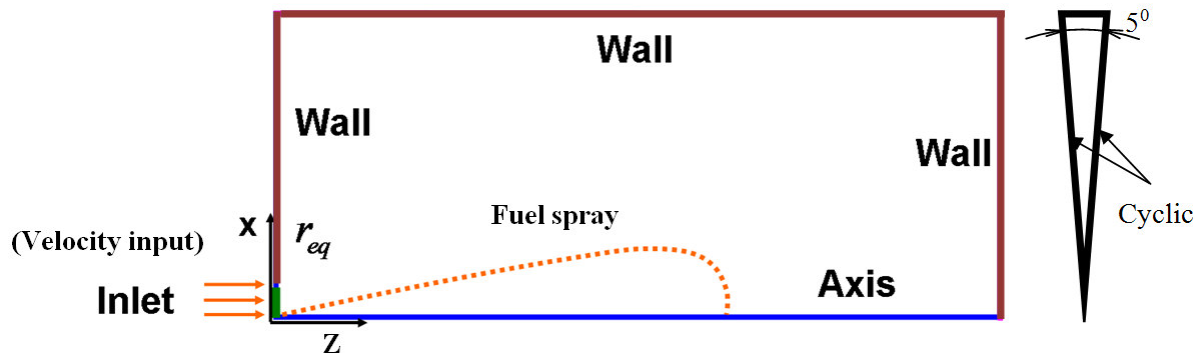


Figure 3: Geometry (front view and side view) & boundary conditions

The computational domain is a wedge of area $12 \times 80 \text{ cm}^2$ and an angle of 5° which contains 40,581 vertices and 20,000 cells, plotted in Figure 2. The mesh structure is built in such a way that the smallest cells are in the spray region (where gradients are high) and grows continuously until the end of the grid domain.

Figure 2 and Figure 3 show all boundary conditions for the computational domain. The input velocity at the nozzle exit is directly calculated from the real mass flow rate (injection rate). The velocity radial profile is constant spatially, and an effective diameter has been used instead of real diameter ($D = 112 \mu\text{m}$). This detail is explained

more carefully later. The injection rate was measured by León [14] using current available test rig at CMT Motores Térmicos Institute. This injection rate is plotted in Figure 4, corresponding to an injection pressure $P_{inj} = 30$ MPa, and an injection temperature equal to 293 K.

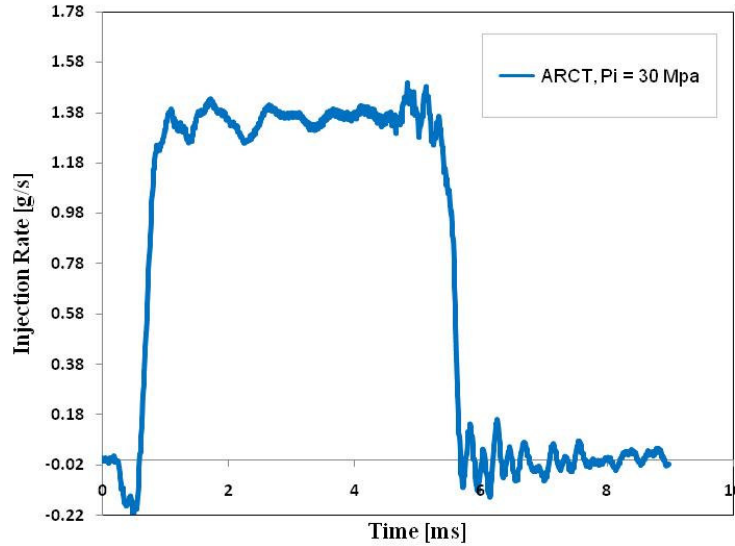


Figure 4: Injection rate of ARCT fuel at $P_{inj} = 30$ MPa, the ambient temperature $T = 255$ K, and ambient pressure 2.1 MPa

5. RESULTS AND DISCUSSION

In this section, numerical results are presented and several comparisons with the measured data are performed. For the sake of identically validated results, a spray tip penetration figure and axial velocity along the axis is plotted for all cases hereafter.

As far as the spray tip penetration $S(t)$ is concerned, the theoretical spray tip penetration applied the Buckingham π theorem [19] is formulated as:

$$S(t) = k \cdot \rho_g^{-0.25} \cdot M_0^{-0.25} \cdot t^{0.5} \cdot \tan^{-0.5} \left(\frac{\theta}{2} \right) \quad (11)$$

Where M_0 is theoretical spray momentum flux, k adjustment constant is obtained from experimental test, t at the specific time; $\theta/2$ is the experimental semi-cone angle. The different injected fuel are examined using the same effective diameter equal to 100 μm , nitrogen ambient pressure with the vessel temperature equal to 255 K and the vessel pressure equal to 2.1 MPa. Using the same injection rate, there is very little change in the input velocity due to the different liquid fuel density between those fuels, as a result, there are a slightly discrepancy one moving from REF and ARCT at the beginning as shown in Figure 5, but this small variation were sooner eliminated in the vessel conditions at further distance from nozzle exit since the chamber conditions remained the same in both cases.

As can be seen in Figure 6, a very good agreement between the experimental data and the simulation results in term of spray tip penetration is observed in the plot. For the normal operating temperature ($\sim 25\text{ }^{\circ}\text{C}$), the model showed extremely fit with the experiment results, there is a very slightly different for the lower vessel temperature levels ($-18\text{ }^{\circ}\text{C}$), however, it is very small and can be considered the very good prediction of the experimental trend.

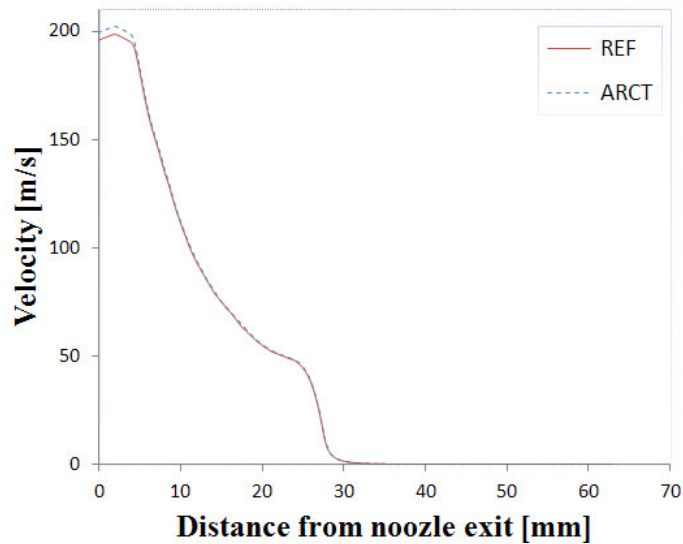


Figure 5: Axial velocity profiles of two types of fuels at the same ambient temperature $T = 255\text{ K}$, and ambient pressure 2.1 MPa

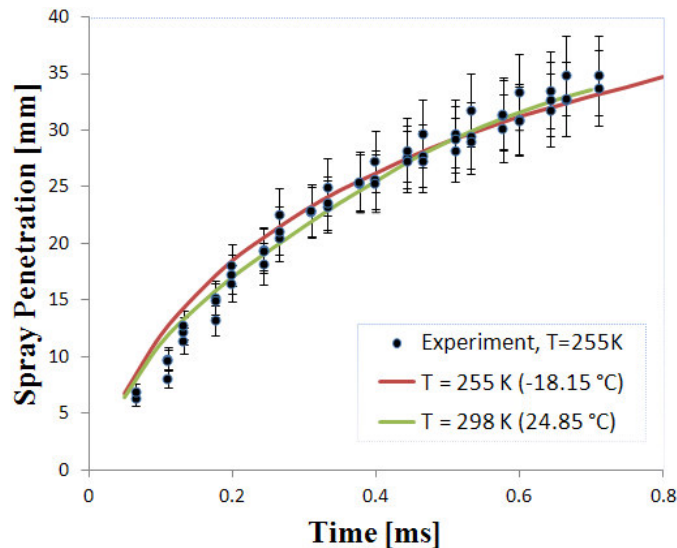


Figure 6: Comparison of the spray tip penetration at the gas ambient temperature of 255 K , 298 K and $P_{\text{amb}} = 2.1\text{ MPa}$, $P_{\text{amb}} = 2.4\text{ MPa}$ respectively, $P_{\text{inj}} = 30\text{ MPa}$. The experiment is shown only for the low ambient temperature at 255 K

The comparison of the velocity profile along the axial axis, where the set of highest value of velocity are produced, was made. In Figure 7, the velocity in the spray axis is showed. Obviously, for the low ambient temperature, a lower velocity is obtained during the whole injection process; on the other hand, the normal temperature produced a higher axial velocity profile. In the theoretical approach, the velocity along the axis can be calculated using the following equation:

$$U_{axis}(x) = \frac{\dot{M}_0^{1/2}}{\rho_{amb}^{1/2} \left(\frac{\pi}{2\omega} \right)^{1/2} x \tan \frac{\theta}{2}} \quad (12)$$

Where ω is the shape factor of the Gaussian distribution, it is equal to 4.6 referred to [20].

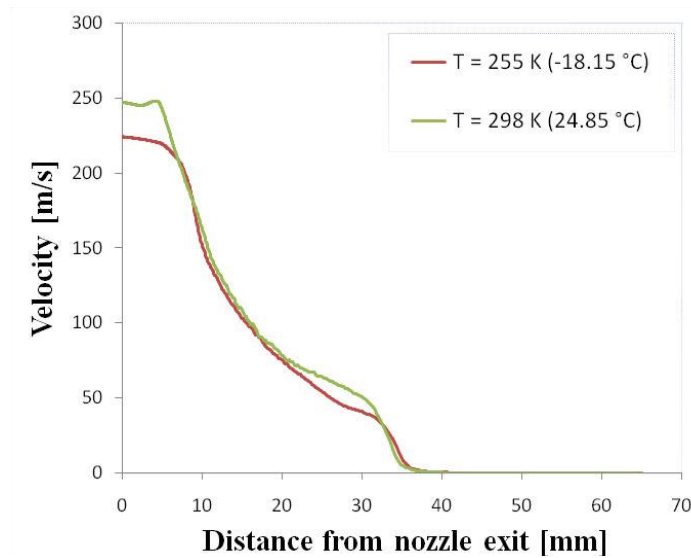


Figure 7: The comparison of the velocity along the axial axis at the gas ambient temperature of 255 K, 298 K and $P_{amb} = 2.1$ MPa, $P_{amb} = 2.4$ MPa respectively, and $P_{inj} = 30$ MPa

As already mentioned in the previous section, since we used the convergent orifice, there is almost no or very less cavitation in the internal nozzle flow. Thus the area coefficient C_a is approach to 1, to take into account a small effect of the area coefficient equal to 0.98 are used. Eqs. (13) – (15) depicted the relation of C_a and cross-sectional area, diameter of the desired nozzle.

$$C_a = \frac{A_{eff}}{A_0} \quad (13)$$

With

$$A = \pi \cdot r^2 \quad (14)$$

where A_0 is the real nozzle exit diameter.

$$C_a = \frac{D_{eff}^2}{D_0^2} \quad (15)$$

With a fixed geometry convergent nozzle, when the area coefficient is moved toward 1, the effective diameter also increased accordingly as seen in Table 3.

Table 3: Area coefficient and effective diameter

D_0 (nozzle exit diameter) [μm]	C_a (area coefficient) [-]	D_{eff} (effective diameter) [μm]
112	0.98	111
112	0.9	106
112	0.8	100

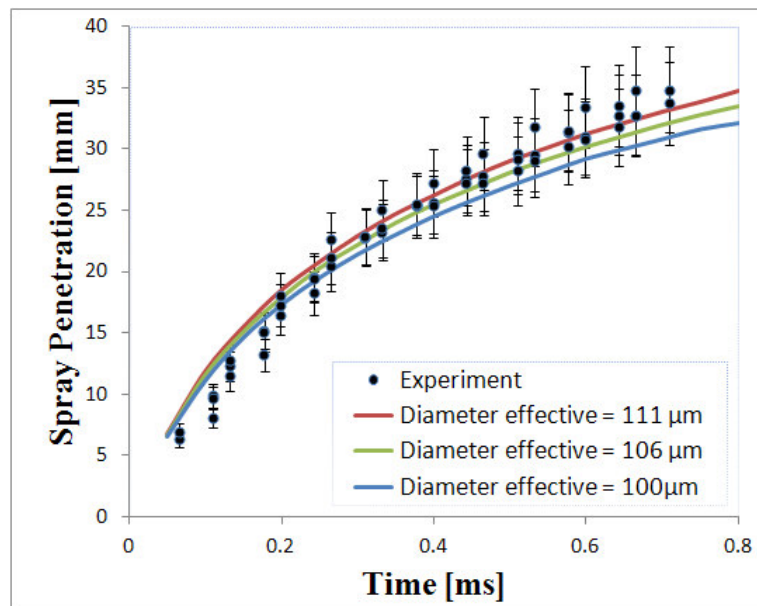


Figure 8: The effect of different effective diameter at 100 μm , 106 μm , and 111 μm on the spray tip penetration at the gas ambient temperature of 255 K

The spray penetration is again investigated in Figure 8 in order to study the influence of the effective diameter. In this figure the higher effective diameter gave the better commitment with the effective diameter equal to 111 μm , for the lower effective diameter, the results are a bit underestimate. It is understandable as the conical nozzle has been used.

To provide a detailed view and further understanding of spray structure, the vapour mass fraction of both cases with diameter of 100 μm , and 111 μm are shown in Figure 9. For each case, the comparison between two time steps is shown at 0.6 and 0.7 ms respectively. It depicts the evolution of those values at different computing time. This figure shows different degree of vapour mass fraction inside the spray structure, the

scale is fitted in both cases, the maximum value is approximately 0.2231. It presents the vapour mass fraction contours coloured with the fraction magnitude in range from 0 to 0.2231. As plotted in Figure 8, the spray penetration for the case with $D_{\text{eff}}=111\mu\text{m}$ is higher than the case with $D_{\text{eff}}=100\mu\text{m}$, the similar trend can be also seen in Figure 9. The nozzle geometry not only affects the spray penetration, it also changes the other parameters. The highest fraction is observed near the axial axis. As radial distance from the axial axis increases, the vapour mass fraction decreases. Obviously, the value is higher at 0.7ms.

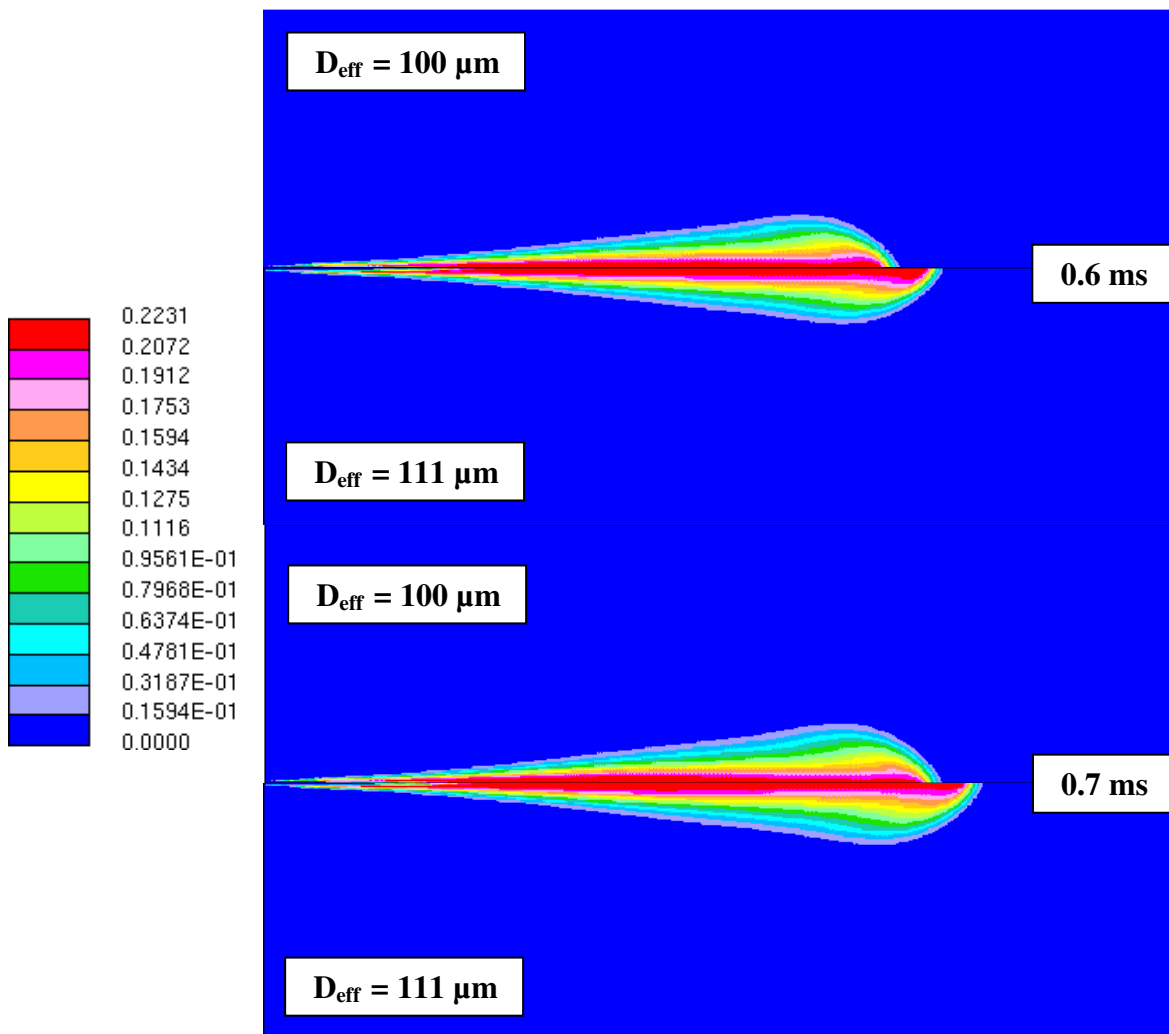


Figure 9: The vapour mass fraction contours of different effective diameter at $100\mu\text{m}$, and $111\mu\text{m}$ at the gas ambient temperature of 255 K. The comparison is made at 0.6 and 0.7 ms respectively. The size of a rectangle area (in blue) is 12x42 millimeters

Similarly, the velocity profiles along the axis for three different effective diameters are plotted in Figure 10. As shown in the plot, the velocity at the nozzle exit is identical for three cases, then taking into account the effect of nozzle diameter; the velocity is higher for the larger effective diameter and smaller for the lower effective diameter, though the

trend is observed to be the same. It also proved that the simulation and ELSA model is stable from the beginning to the end of the computed time. The only effect is on the change of particular setup or parameter.

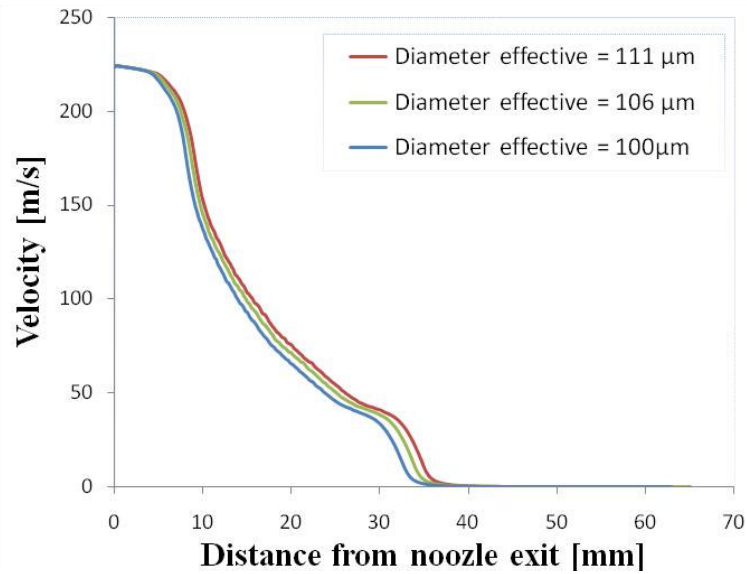


Figure 10: The effect of different effective diameter at 100μm, 106 μm, and 111μm on the velocity along the axial axis at the gas ambient temperature of 255 K

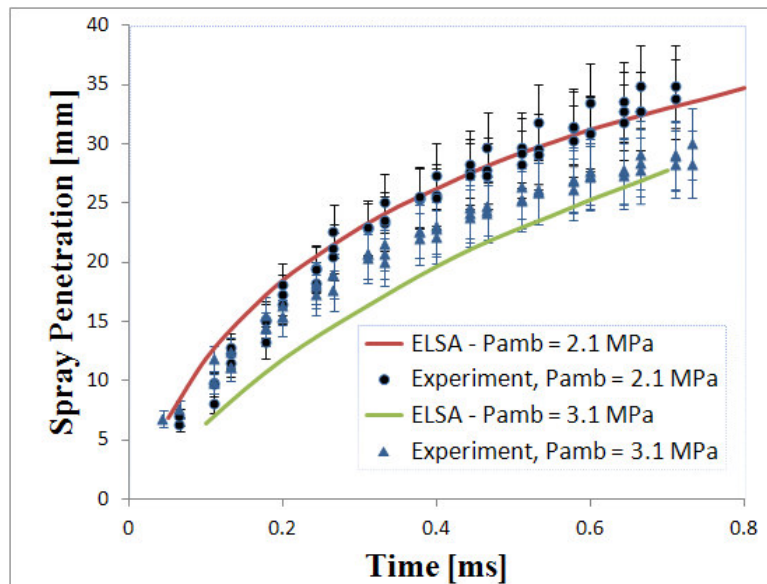


Figure 11: Comparison of spray tip penetration between different ambient pressure 2.1 MPa and 3.1 MPa at the gas ambient temperature of 255 K

As shown in Figure 11, the results obtained for both ambient pressure is acceptable in the two computational cases. It is remarkable that the study of spray tip penetration is fitted well with the lower ambient pressure of 2.1 MPa. For the higher ambient pressure of 3.1 MPa, the computational model show a small difference below 0.4 ms, but still remains within a acceptable range. For the higher computational time after 0.5 ms, the experimental results and simulated case can be properly compared. Since the spray penetration mostly concern at the stable value above 0.6 ms, thus the value at 0.7 ms shown in the plot is very good.

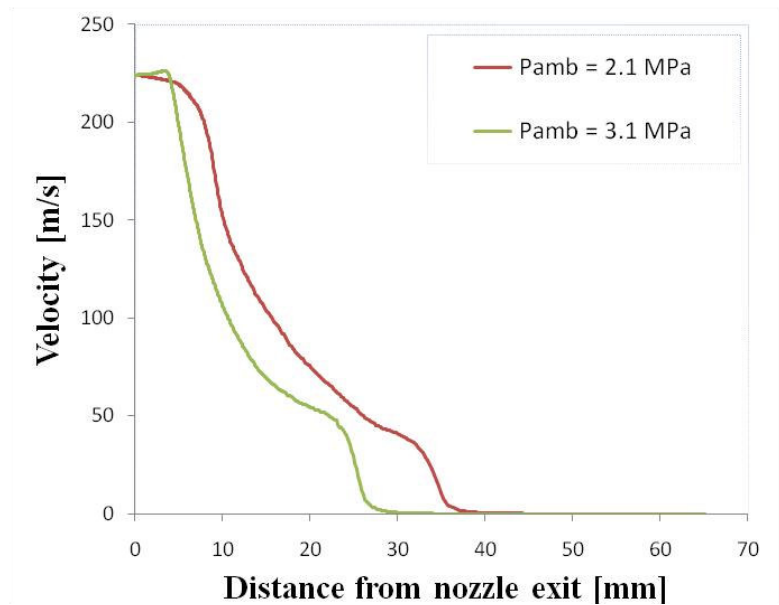


Figure 12: Comparison of velocity profile along the axial axis between different ambient pressure 2.1 MPa and 3.1 MPa at the gas ambient temperature of 255 K

In Figure 12, the assessment of the impact of gas ambient composition variations on the performance of velocity is studied. For the case with ambient pressure of 3.1 MPa, under the higher ambient pressure or in other words, the higher ambient density (as the same temperature and ambient gas are used) the velocity obtained is lower than the case with gas ambient pressure equal to 2.1 MPa.

Cone angle proposed by Hiroyasu & Arai, 1990 [21] are as following:

$$\theta = 83.5 \left(\frac{1}{d} \right)^{-0.22} \left(\frac{d}{D_o} \right)^{0.15} \left(\frac{\rho_g}{\rho_l} \right)^{0.26} \quad (16)$$

In Figure 13, the spray cone angle depends on time is reported. The simulated results show a close connection with the experimental scatter plot. There is a gap at the beginning of the injection, it happens due to the effect of the fluctuation in mass flow rate and momentum flux measurement from experimental test.

6. CONCLUSIONS AND DISCUSSION

This paper is focused on the assessment of the Eulerian - Lagrangian Spray Atomization (ELSA) model for the simulation of Diesel sprays in cold starting conditions.

Using the same nozzle, injection pressure and injection temperature, the various vessel parameters have been evaluated in this work by means of CFD-ELSA and compared to some experimental data. Similar results have been observed when comparing ELSA modelling results and experiments. Furthermore, all the spray behaviour and its properties are explainable and in line with the theoretical physical approach of the diesel spray in the internal combustion engine.

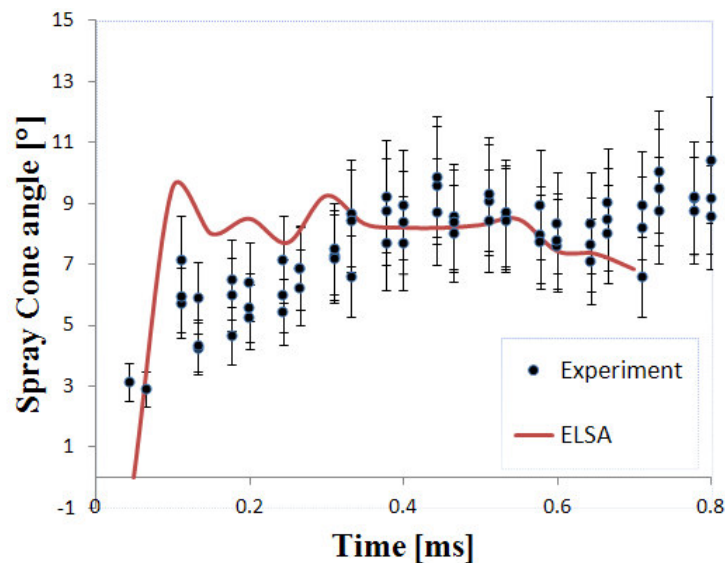


Figure 13: Spray cone angle in the case with $P_{amb} = 3.1$ MPa, $T_{amb} = 255$ K, $D_{eff} = 111\mu\text{m}$

By using the larger area coefficient, as a linear relation the effective area and effective diameter are increased accordingly. Once we have the higher volume of liquid across the nozzle exit section, the spray tip penetration as well as the velocity increases their magnitude. For the conical nozzle the cavitation phenomena in the internal nozzle flow can be ignored. This occurs not only in the low temperature simulation, but it is true for any ambient temperature.

The computational results obtained under very low temperature show good concordance with the experiment data and macroscopic properties of the diesel spray. The change in ambient pressure and ambient density resulted in a slightly different during the first few milliseconds of injection process at the higher ambient pressure, but it tends to reach experimental data above 0.5 ms.

Taking into account the commented positive results, it can be concluded that the ELSA model can be used to simulate diesel spray in those conditions. There is still more research to be done and more parameters to be evaluated. Probably, the most important

is the temperature, in order to have high evaporative conditions. Simulations at real engine conditions are being performed at this moment in order to prove the stability and the capability of the code for working in all conditions.

Acknowledgment – This work was supported in part by the Spanish Government in the frame of the Project ‘Métodos LES para la simulación de chorros multifásicos’, Ref. ENE2010-18542 and by Renault. Dung Khuong-Anh has been supported in part by the VECOM (Vehicle Concept Modelling), EU FP7 Marie Curie Initial Training Network (ITN) Grant Agreement 213543 and in conjunction with Renault SA., France.

REFERENCES

- [1] A.H. Lefebvre. *Atomization and sprays*. Taylor and Francis, 1989.
- [2] A. Vallet, A.A. Burluka, R. Borghi. Development of a Eulerian model for the atomization of a liquid jet. *Atomization and sprays* 2001; **11**: 619-642.
- [3] G. Blokkeel, B. Barbeau, R. Borghi. A 3D Eulerian model to improve the primary breakup of atomizing jet. *SAE Technical Paper* 2003; 2003-01-0005.
- [4] P.A. Beau. *Modelisation de l'atomisation d'un jet liquide – Application aux sprays diesel*. Ph.D. Thesis. University of Rouen, 2006.
- [5] S. Hoyas, J.M. Pastor, D. Khuong-Anh, J.M. Mompó-Laborda, F. Ravet. Evaluation of the Eulerian-Lagrangian Spray Atomization (ELSA) in spray simulations. *International Journal of Vehicle Systems Modelling and Testing* 2011; **6**(3-4): 187-201.
- [6] S. Hoyas, J.M. Pastor, D. Khuong-Anh, J.M. Mompó-Laborda, F. Ravet. Application and evaluation of the Eulerian-Lagrangian Spray Atomization (ELSA) model on CFD Diesel spray simulations. *SAE Paper* 2011; 2011-37-0029.
- [7] S. Hoyas, A. Gil, X. Margot, D. Khuong-Anh, F. Ravet. Evaluation of the Eulerian-Lagrangian Spray Atomization (ELSA) in spray simulation: 2D cases. *Mathematical and Computer Modelling* 2011; In Press.
- [8] P.A. Beau. *Modelisation de l'atomisation d'un jet liquide – Application aux sprays diesel*. Ph.D. Thesis. University of Rouen, 2006.
- [9] R. Lebas R. *Modelisation Eulerienne de l'Atomisation haute pression – Influences sur la vaporisation et la combustion induite*. Ph.D. Thesis. University of Rouen, 2007.
- [10] M. De Lucas. *Contribution a la modelisation de la pulverisation d'un liquide phytosanitaire en vue de reduire les pollutions*. Ph.D. Thesis. University of Aix-Marseille II, 2007.
- [11] W. Ning, R.D. Reitz, A.M. Lippert, R. Diwakar. Development of a next generation spray and atomization model using an Eulerian-Lagrangian methodology. *17th Int. Multidimensional Engine Modeling User's Group Meeting, Detroit, MI*, 2007.
- [12] A. Desportes, M. Zellat, G. Desoutter, D. Abouri, Y. Liang. Validation and Application of the Eulerian-Lagrangian spray atomization. (ELSA) model for the Diesel injection simulation. *SAE Technical Paper*, 2010.
- [13] A. Desportes, M. Zellat, G. Desoutter, Y. Liang, F. Ravet. Application of the Eulerian-Lagrangian spray atomization. (ELSA) model for the Diesel injection simulation. *Conference on Thermo- and Fluid Dynamic Processes in Diesel Engines*, 2010.
- [14] G.B. León. *Experimental and theoretical study of the direct diesel injection process at low temperatures*. PhD Thesis. Universidad Politécnica De Valencia, 2011.
- [15] V. Macian, V. Bermudez, R. Payri, J. Gimeno. New technique for determination of internal geometry of a diesel nozzle with the use of silicone methodology. *Experimental Techniques* 2003; **27**(2): 39-43.
- [16] B. Wilhelm. The fuel rate indicator: a new measuring instrument for display of the characteristics of individual injection. *SAE Paper* 660749, 1966.
- [17] L. Allievi. Teoria generale del moto perturbato dell'acqua nei tubi in pressione (colpo d'ariete). (General theory of the variable motion of water in pressure conduits.) *Annali della Società degli Ingegneri ed Architetti Italiani* 1902; **17**(5): 285-325, Milan, Italy (in Italian).

- [18] L. Allievi. Teoria del colpo d'ariete. (Theory of water-hammer.) Nota I-V. *Atti dell'Associazione Elettrotecnica Italiana* 1913; **17**: 127-150, 861-900 + plates, 1129-1145 + plates, 1235-1253 + plates, and Supplement No 1, 1-35 + plates (in Italian).
- [19] E. Buckingham. Model experiments and the forms of empirical equations. *Trans Am Soc Mech Eng* 1915; **37**: 263–296.
- [20] J.M. Desantes, R. Payri, J.M. Garcia, F.J. Salvador. A contribution to the understanding of isothermal diesel spray dynamics. *Fuel* 2007; **86**: 1093-1101.
- [21] H. Hiroyasu, M. Arai. Structure of fuel sprays in diesel engines. *SAE paper 900475*,1990.

LIST OF ABBREVIATIONS

ARCT	ARCTIQUE	VECOM	Vehicle Concept Modelling
CFD	Computational Fluid Dynamics	amb	Ambient
DNS	Direct Numerical Simulation	inj	Injection
ELSA	Eulerian-Lagrangian Spray Atomization	eff	Effective
ITN	Initial Training Network	g	Gas
LES	Large Eddy Simulation	l	Liquid
REF	ELITE – Repsol		

Evaluation and Validation of ELSA Model in Diesel Sprays: 3D Cavitating Nozzles Case

Sergio Hoyas[†], Antonio Gil[†], Pablo Fajardo[†], Dung Khuong-Anh^{†*}, and Frederic Ravet[‡]

[†] CMT-Motores Térmicos, Universitat Politècnica de València, Valencia 46022, Spain
[serhocal, angime, pabfape, ankh2]@mot.upv.es

[‡] Renault, 1 Avenue du Golf 78288, Guyancourt, France
frederic.ravet@renault.com

Abstract

Computational Fluid Dynamic (CFD) techniques have become one of the main tools in the design and development of diesel engines. There exist, however, some drawbacks and problems that must be overcome in the next years. One of the challenges is to predict accurately the couple between the flow inside the nozzle and the spray, including the primary break-up and the secondary atomization. In the last years, several authors have been developed the Eulerian-Lagrangian Spray Atomization (ELSA) model. ELSA model combines an Eulerian and Lagrangian descriptions by coupling these two methods properly. ELSA model also accounts for the modeling of droplets and their formation process, particularly in the dense spray region. The ELSA model for diesel spray modeling has been recently implemented and developed into Star-CD CFD commercial code. Author's effort was focused on a detailed validation and evaluation of the fuel injection in diesel engines using this last implementation. Spray atomization, spray formation and macroscopic characteristics of diesel spray behavior were investigated. The overall work has been conducted in non-evaporative conditions. As cavitation greatly affects to spray behavior and it is thought that cavitating nozzles will be present in most of close future engines, this sort of configuration has been chosen for validation. Velocity profiles at the section area of the nozzle exit obtained from trusted and experimentally validated RANS internal flow simulation were used. Results have been validated against experimental data, mostly coming from CMT-Motores Térmicos institute. It was found that the ELSA model reproduces accurately the experimental results.

Introduction

The primary break-up and secondary atomization of liquid sprays are up to now not totally understood. In the case of diesel engines, the fuel spray occurs in a small chamber inside the combustion engine. The fuel comes from a tiny nozzle cross section (hundred micrometers) at very high pressure and everything happens at an extremely short time (few milliseconds). Regardless the reactive part of the processes, diesel spray study includes several fundamentals, and not totally resolved topics, as can be the spray structure itself, break-up and atomization processes, or the behavior of two-phase turbulent flows. Probably, one of the main problems is the lack of experimental techniques which can be used in the vicinities of the nozzle.

Computational Fluid Dynamic (CFD) techniques have become one of the main tools in the design and development of diesel engines. There exists, however, some drawbacks and problem that must be overcome in the next years. One of the challenges is to predict accurately the couple between the flow inside the nozzle and the spray, including the primary break-up and the secondary atomization. Fuel injection and spray characterization have been investigated thoroughly during the last decades and there exist many techniques to model diesel spray. Each one of these methods has its own advantages and disadvantages, mainly due to the fact that they focus in a particular region of the spray. The traditional Eulerian method performs well in the liquid phase while the Lagrangian drop method describes accurately the dispersed region. Transition between both zones is not particularly well resolved, mainly due to time and computational power restrains. The ELSA model combines Eulerian and Lagrangian descriptions by coupling these two methods properly. It accounts for the modeling of droplets and their formation process, particularly in the dense spray region. In the last years several authors have been developed the ELSA model [1], [2], and [3]. This algorithm has been recently implemented in CD-adapco Star-CD CFD code conducted together with Renault SA in the version 4.12 and it has been continuously enhanced since then.

Spray modeling are commonly applied in ideally non-cavitating condition. The code has been pre-validated previously under non-evaporative and non-cavitating conditions, showing an excellent agreement with experimental data [4], [5], and [6]. However, nowadays nozzles cavitate, and this plays a critical role in real applications, affecting heavily on the spray behavior. In the next section the cavitating nozzles used for this validation are presented, together with the experimental data characteristics. The numerical methods are presented in the following section and after that discussed. Last section is devoted to conclusions.

Experimental setup

The experimental data used in this project were obtained as part of a broader collaboration between Renault and CMT-Motores Térmicos. The only cavitating diesel injection nozzle characterized in this project was a Bosch injector, reference no., DLLA 145 PV3 192 805. A microscopic characterization of this nozzle is presented at Figure 1.

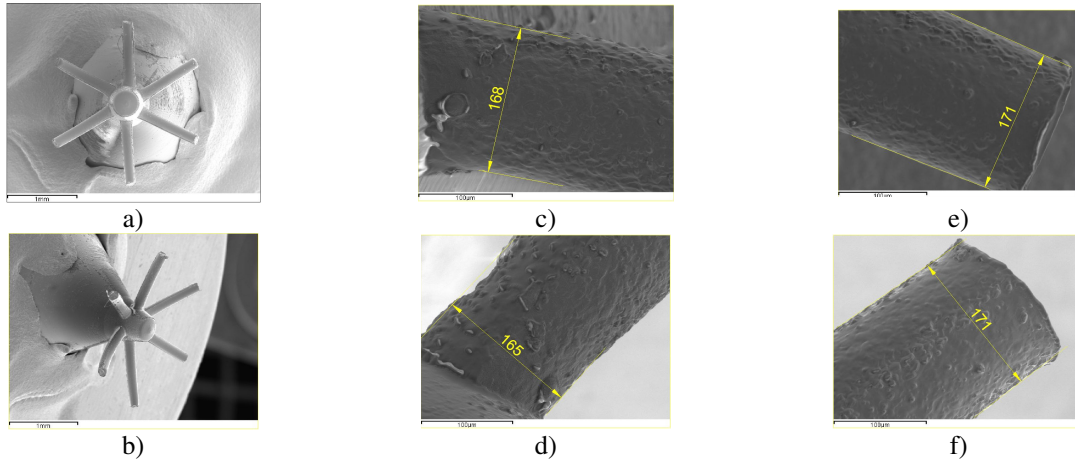


Figure 1: Detailed view of internal nozzle geometry.

Slightly differences in diameters were found amongst the six holes (Figure 1c, d, e, and f) so the mean diameter of the orifices has been used for the numerical analysis. This mean value is $D_{Bosch} = 0.170$ mm, 145° cone angle, $HE = 13.5$, and nozzle conicity, $k\text{-factor} = 0$.

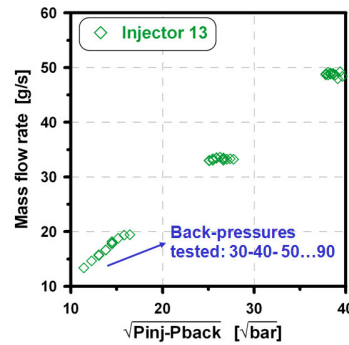


Figure 2: Mass flow rate vs. the variation between injection pressure and ambient pressure in the cavitating injection nozzle (Injector 13).

The correlation amongst different injection pressure, back pressure vs. the mass flow rate obtained from experimental study is plotted in Figure 2. In this paper, the mass flow rate corresponded to a test case with the 30 MPa injection pressure and 7 MPa ambient pressure.

Computing the liquid length

The parameters linking the flow at the nozzle with the spray liquid length under evaporative condition were presented in [7], [8], [9] and [10]. According to the turbulent spray theory, in a quasi-steady spray, the fuel penetration is modeled by the following Eq.:

$$x = K_p \dot{M}_f^{\frac{1}{4}} \rho_a^{-\frac{1}{4}} t^{\frac{1}{2}} \quad (1)$$

Where ρ_a is the ambient density, t is the time since the start of the injection (SOI). K_p is a function of the spray cone angle, θ_u .

$$K_p = k \left(\tan \left(\frac{\theta_u}{2} \right) \right)^{\frac{1}{2}} \quad (2)$$

Where k is a universal constant, and K_p is the variable used in the fuel parcel penetration definition. The momentum flux, \dot{M}_f is given in Eq. (3).

$$\dot{M}_f = \dot{m}_f u_{eff} = C_a \frac{\pi}{4} D_0^2 \rho_l C_v^2 u_{th}^2 \quad (3)$$

$$C_v = \frac{u_{eff}}{u_{th}} \quad (4)$$

$$u_{th} = \sqrt{\frac{2\Delta P}{\rho_l}} \quad (5)$$

In these equations, u_{eff} is the effective velocity, \dot{m}_f is the fuel mass flow rate, C_a is the area coefficient, D_0 is the outlet diameter of the nozzle and ρ_l is the fuel density. The relationship between the effective velocity and the viscous-free theoretical velocity (u_{th} in Eq. (5)) is defined as C_v , (Eq. (4)). Delta pressure, ΔP is defined by $\Delta P = P_{inj} - P_{amb}$.

Substituting Eq. (3) into Eq. (1), the latter becomes

$$x = K_p \left(\frac{\pi}{4} \right)^{\frac{1}{4}} C_a^{\frac{1}{4}} C_o^{\frac{1}{2}} C_v^{\frac{1}{2}} u_{th}^{\frac{1}{2}} \rho_l^{\frac{1}{4}} \rho_a^{-\frac{1}{4}} t^{\frac{1}{2}} \quad (6)$$

The fuel parcel velocity in the axis, u_x is obtained deriving this equation, obtaining

$$u_x = \frac{\partial x}{\partial t} = K_p \frac{1}{2} \left(\frac{\pi}{4} \right)^{\frac{1}{4}} C_a^{\frac{1}{4}} C_o^{\frac{1}{2}} C_v^{\frac{1}{2}} u_{th}^{\frac{1}{2}} \rho_l^{\frac{1}{4}} \rho_a^{-\frac{1}{4}} t^{-\frac{1}{2}} \quad (7)$$

As spray momentum is a conserved magnitude:

$$\dot{M}_f = \dot{m}_f u_{eff} = (\dot{m}_f + \dot{m}_{a,x}) u_x \quad (8)$$

In this equation $\dot{m}_{a,x}$ is the air entrained by the spray. Defining C_m as the fuel mass fraction, from Eq. (8),

$$C_m = \frac{\dot{m}_f}{\dot{m}_f + \dot{m}_{a,x}} = \frac{u_x}{u_{eff}} \quad (9)$$

is obtaining. Replacing Eq. (7) to Eq. (9):

$$C_m = K_p \cdot \frac{1}{2} \cdot \left(\frac{\pi}{4} \right)^{\frac{1}{4}} \cdot C_a^{\frac{1}{4}} \cdot C_o^{\frac{1}{2}} \cdot C_v^{-\frac{1}{2}} \cdot u_{th}^{-\frac{1}{2}} \cdot \rho_l^{\frac{1}{4}} \cdot \rho_a^{-\frac{1}{4}} \cdot t^{-\frac{1}{2}} \quad (10)$$

Using this equation it is possible to define a new time scale, t_m , defined as the time needed by a fuel parcel moving along the spray axis in order to reach a certain value of fuel mass fraction, C_m :

$$t_m = \frac{K_p^2 \frac{1}{4} \left(\frac{\pi}{4}\right)^{\frac{1}{2}} C_a^{\frac{1}{2}} D_o \rho_l^{\frac{1}{2}}}{C_m^2 C_v u_{th} \rho_a^{\frac{1}{2}}} \quad (11)$$

Using t_m , it is easy to compute the penetration distance, x_m , defined as the axial position with a “ C_m ” value of the fuel mass fraction.

$$x_m = \frac{K_p^2 \left(\frac{1}{4}\right)^{\frac{1}{2}} \left(\frac{\pi}{4}\right)^{\frac{1}{2}} C_a^{\frac{1}{2}} D_o \rho_l^{\frac{1}{2}}}{C_m \rho_a^{\frac{1}{2}}} \quad (12)$$

The liquid length (penetration), LL , is defined as the distance from the nozzle exit to the farthest location where the fuel parcel on the spray axis has entrained enough higher-temperature gas to vaporize the injected fuel. In order to obtain an equation for LL , C_m is taken equal to C_{mv} – the value of mass concentration in the axis at which the injected fuel is totally vaporized by higher-temperature gas.

By replacing the defined value of C_{mv} at Eq.(12) the liquid-phase penetration, LL is computed as :

$$LL = \frac{K_p^2 \left(\frac{1}{4}\right)^{\frac{1}{2}} \left(\frac{\pi}{4}\right)^{\frac{1}{2}} C_a^{\frac{1}{2}} D_o \rho_f^{\frac{1}{2}}}{C_{mv} \rho_a^{\frac{1}{2}}} \quad (13)$$

Numerical Study

Cavitation phenomena depends strongly on the nozzle geometry. In this particular case, cavitation occurs mostly on the upper part of the nozzle wall (see Figure 3).

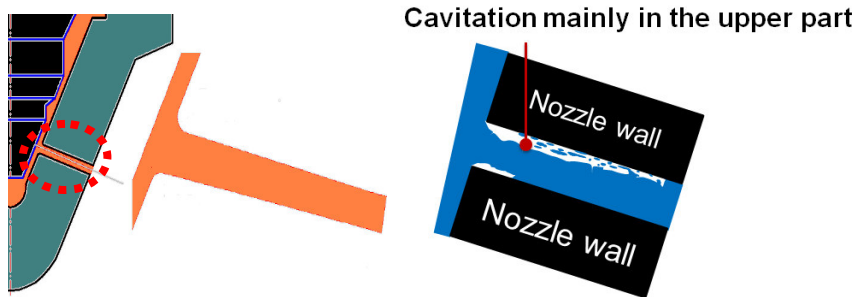


Figure 3: The nozzle, needle shape, and a zoom view of the internal nozzle flow (left) and the internal cavitation profile (right) produced by this type of injector.

The main physical parameters of the experimental set-up are tabulated in Table I.

Table I: The experimentally averaged parameters

Injection pressure	Ambient pressure	Momentum flow	Mass flow orifice	Effective velocity	Effective diameter	C_d	C_v	C_a
[MPa]	[MPa]	[N]	[g/s]	[m/s]	[μm]	[-]	[-]	[-]
30	7	0.540	18.79	172.5	166.9	0.706	0.733	0.963

To investigate the effects of diesel spray with the same cavitating nozzle, including or excluding cavitation phenomenon together with evaporative and non-evaporative conditions, three different cases, tabulated in table II, have been studied. In all cases, the injection pressure and ambient pressure were fixed to 30 MPa and 7 MPa respectively.

Table II: Computational cases

Case	D_0 (real diameter) [μm]	D^{eff} (effective diameter) [μm]	Nozzle cavitation	Inlet velocity [m/s]	Evaporation	Ambient Temperature [K]
Case 1	170	165	Yes/simplify	$V = 173$	No	307.7
Case 2	170	-	Yes	Figure 5	No	307.7
Case 3	170	-	Yes	Figure 5	Yes	935.0

Effective velocity was rounded up to 173 m/s as described in case 1 of table II. To compensate for this increment, an effective diameter of 165 μm was used in the excluded-cavitating case. Figure 4a shows the output parameters extracted from the case with cavitation (case 2, and 3), whereas Figure 4b illustrates a simplified output parameters using in case 1 in which the cavitating nozzle is used but excluding the cavitating effects in simulation by using the effective values.

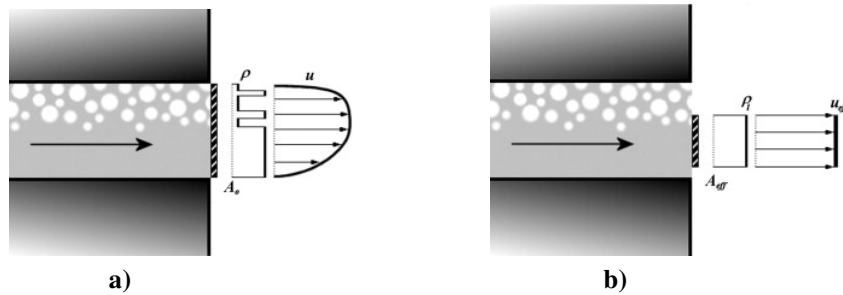


Figure 4: The cavitating nozzle and its density, velocity profile including or excluding cavitation phenomenon [8].

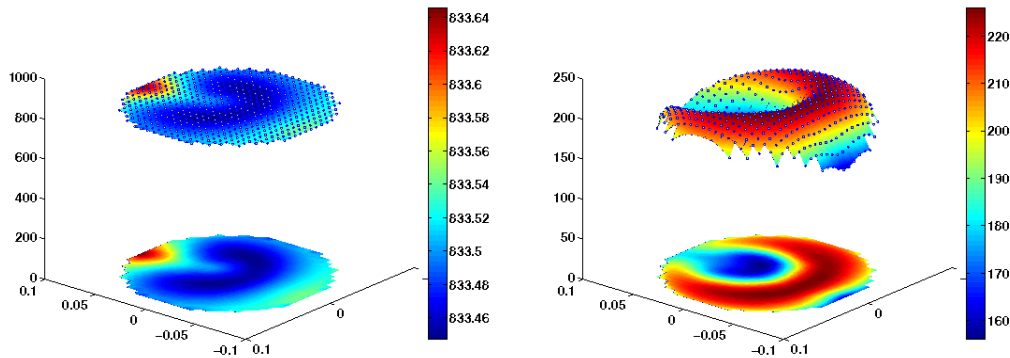


Figure 5: Density (on the left) and the velocity (on the right) at the nozzle exit ($P_{\text{inj}} = 30 \text{ MPa}$, $P_{\text{amb}} = 7 \text{ MPa}$, $T_{\text{amb}} = 935 \text{ K}$).

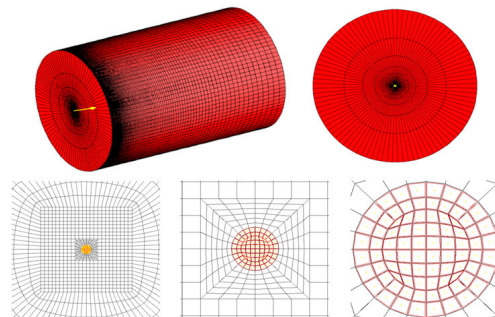


Figure 6: Computational mesh and detail of the grid structure near the nozzle exit (front view).

Taking into account the cavitating nozzle influence, the inlet boundary condition for case 2 and case 3 are shown in Figure 5. The cavitating modeling of the internal flow is seperately simulated by Salvador et al. using the open code, OpenFOAM. Thanks for the works of Salvador et al. 2010 [11] and 2011 [12]. A homogeneous

equilibrium model (HEM) was used and assumed that liquid and vapour phases are always perfectly mixed. Additionally, a barotropic equation of state was employed to model cavitation phenomenon (see more in [11] and [12]). The output data from internal flow calculation is extracted and interpolated in order to apply for the inlet boundary condition of the spray modeling. The effect of cavitation in the nozzle flow generated the variation at the cross-sectional nozzle exit as presented in Figure 5. The density and velocity profile distribution on the cross section are uneven.

About the geometry, in this study, only one nozzle of diameter $170\ \mu\text{m}$ was simulated. The mesh, previously tested, is made of 518400 cells and 534877 vertices with 300 segments along the spray axis. This computational mesh and its structure are shown in Figure 6. Noted that a really fine mesh was built near the nozzle exit, and in the region where the spray develops. In this figure, the nozzle exit is the circular area containing 84 cells and bolding in red in the last two views of Figure 6. In the first case, where the simulate diameter is $165\ \mu\text{m}$, the length of all segments was scaled down by a coefficient of $165/170$.

Results and Discussion

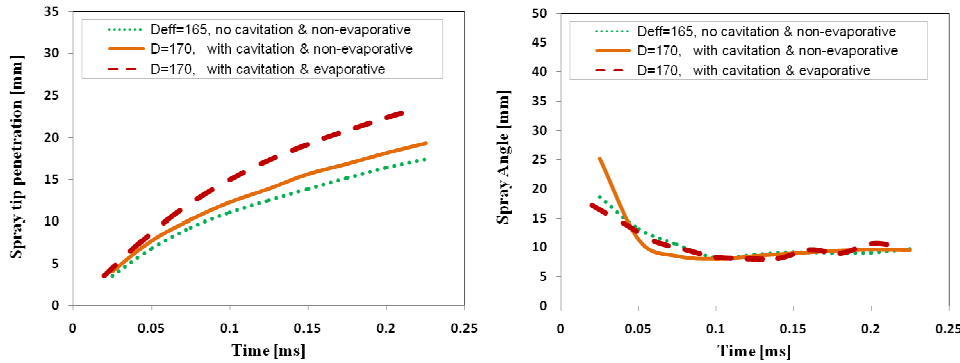


Figure 7: The comparison of the spray tip penetration and spray cone angle amongst three cases.

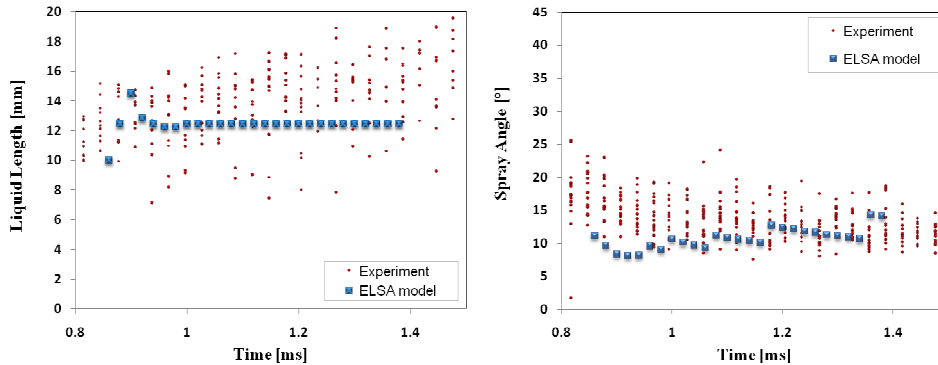


Figure 8: Comparison of experimental and numerical results in term of a) (left) liquid length and b) (right) spray cone angle under evaporative condition for the case with $D=170\ \mu\text{m}$, $P_{inj}=30\ \text{MPa}$, $P_{amb}=7\ \text{MPa}$, $T_{amb}=935\ \text{K}$.

In Figure 7, the spray tip penetration and spray cone angle of the three cases are shown. The spray tip penetration under cavitating and evaporative conditions – case 3 – was much higher than case 2, cavitating and non-evaporative conditions. It is also clear from these plots that the cavitation increases the spray penetration in comparison with the traditional simulation without cavitation, whereas the cone angle is similar in the three cases.

There also exist experimental results about the liquid length for the third case, showing an excellent agreement with the computed data, as it is shown in Figure 8a. Although there are a great dispersion in the data coming from the experimental (red dots) in Figure 8, the numerical results (blue dots) show a good agreement. As can be seen for the Figure 8b, the computed spray cone angle is a bit low at the beginning of the simulation, because we use as input the magnitudes coming from the steady region of nozzle, without simulating the transitory. The extracted data from the internal nozzle flow was taken only when the cavitation reached the certain stable value. That is also explained why we don't show the time before 0.8ms. Since the steady regime is reached, the agreement between experimental and numerical data is reasonably good.

Figure 9 expressed the effect of internal cavitating flow on the spray structure in both cross sections perpendicular to the spray axis as well as along the axial axis. The velocity contour at the cross section (perpendicular to the spray axis) taken at the position equal to one nozzle diameter from the nozzle outlet clearly shows the influence of cavitation phenomena on the spray formation. From this plot, the cavitation occurs mostly on the upper part of the nozzle wall (on the positive side of the Z axis) and there is very little variation on the X axis. As a consequent, the vapor mass fraction at the cross section along the spray axis on the XY plane is quite symmetric.

As depicted in the contour plots of the case 3 (Figure 10), two cross sections which are perpendicular to the spray axis at the distance of 5, and 10 mm has been extracted. The vapor mass fraction values were increased rapidly at the further distance. In every time step, there is a small vapor occurred in the area close to the nozzle diameter, that is at the section equal to 5 mm as liquid appears and the cavitating flow still heavily influent on the spray structure, however, the vapor mass fraction obtained much more higher, it occupied whole section area at the distance of 10 mm where there is no more liquid. Under cavitation effects, the vapor mass fraction are asymmetric as observed clearly at 5 mm distance, once the sprays develop and the cavitation influence reduces at a longer distance the vapor mass fraction value tends more symmetric (refer to 10 mm at 0.08 ms). For case 1, and 2, since it simulated under non-evaporative conditions, the vapor mass fraction value are almost equal to zero at all cross sections and in every times step, thus, no it is no need to put it herein.

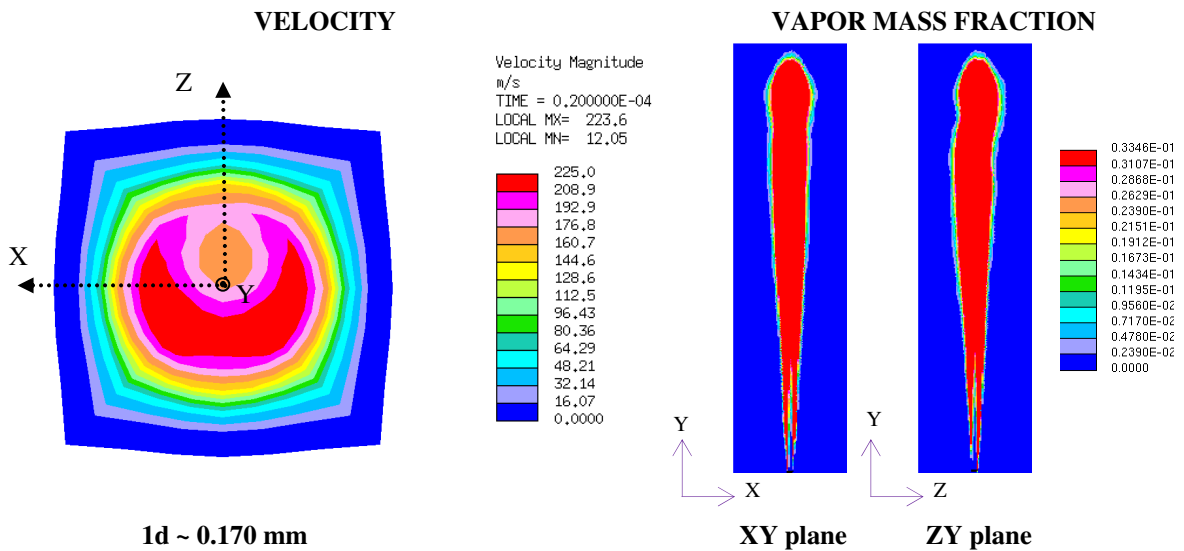


Figure 9: Velocity contour at 1D cross section (left), and vapor mass fraction profile along the spray axis in XY and ZY planes (two figures on the right hand side); contour plots of case 3 ($P_{inj} = 30$ MPa, $P_{amb} = 7$ MPa, $T_{amb} = 935$ K).

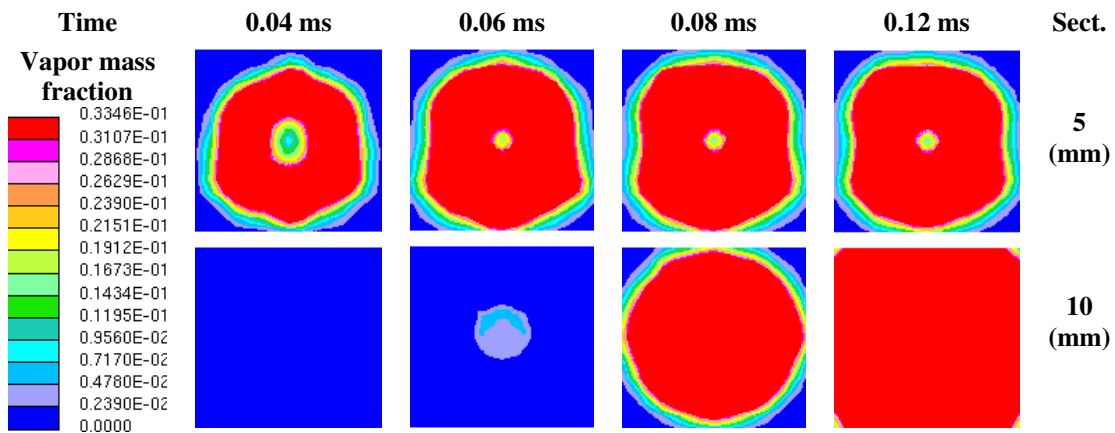


Figure 10: The vapor mass fraction at different cross sections [5, and 10 mm] along the spray axis and at different time steps [0.04, 0.06, 0.08, and 0.12ms] ($D = 170$ μ m, $P_{inj} = 30$ MPa, $P_{amb} = 7$ MPa, $T_{amb} = 935$ K).

Summary and Conclusions

In this work the authors have presented a validation of the ELSA method implemented very recently in STAR-CD software. This study comprises three cases, combining cavitating nozzles in evaporative and non evaporative conditions. When possible the results have been compared to experiments, showing an excellent agreement. It is also important to notice that the spray tip penetration and spray cone angle in the cavitating nozzle cases are larger than in the case excluding cavitation. This probably made the spray more effective in the combustion stage.

Although a RANS model has been used to simulate turbulence, in order to take into account the effect of cavitation, a fine mesh has been used. The model produces also many droplets, so computation take a long time to run, even in parallel machines. This limited parametric study. As a future work, a more detailed parametric study is planned, including variation in ambient and injection pressure, ambient density and ambient temperature.

Acknowledgements

This work was supported in part by the Spanish Government in the frame of the Project ‘Métodos LES para la simulación de chorros multifásicos’, Ref. ENE2010-18542 and by Renault S.A. Experimental data was the joined project between Renault S.A., and CMT- Motores Térmicos. Dung Khuong-Anh has been also supported by the VECOM, EU FP7 Marie Curie Initial Training Network (ITN) Grant Agreement 213543.

References

- [1] Vallet A, Burluka AA and Borghi R., *Atomization and sprays* 11: 619-642 (2001).
- [2] Blokkeel G, Barbeau B and Borghi R., *SAE Technical Paper*: 2003-01-0005 (2003).
- [3] Beau P.A. Modélisation de l'atomisation d'un jet liquide. Application aux sprays diesel. Ph.D. Thesis, *University of Rouen*: (2006).
- [4] Hoyas, S., Pastor, J. M., Khuong-Anh, D., Mompó-Laborda, J. M., and Ravet, F., *International Journal of Vehicle Systems Modelling and Testing* 6-3/4: 187-201 (2011).
- [5] Hoyas, S., Pastor, J. M., Khuong-Anh, D., Mompó-Laborda, J. M., and Ravet, F., *SAE Technical Paper*: 2011-37-0029 (2011).
- [6] Hoyas, S., Gil, A., Margot, X., Khuong-Anh, D., and Ravet, F., *Mathematical and Computer Modelling* (2011).
- [7] Payri, R., Salvador, F.J., Gimeno, J. and Zapata, L.D. *Fuel* 87: 1165-1176 (2008).
- [8] Payri, R., Salvador, F.J., Gimeno, J. and De la Morena, J., *International Journal of Heat and Fluid Flow* 30-4: 768-777 (2009).
- [9] Payri, F., Bermúdez, V., Payri, R., and Salvador, F., *Fuel* 83: 419 - 431 (2004).
- [10] Desantes, J.M., Payri, R., Garcia, J.M., and Salvador, F.J., *Fuel* 86: 1093-1101 (2007).
- [11] Salvador, F.J., Romero, J.V., Roselló, and M.D., Martínez-López, *Mathematical and Computer Modelling* 52, 1123-1132 (2010).
- [12] Salvador, F.J, Hoyas, S., Novella, and R., Martínez-Lóper, *Proceedings of the Institution of Mechanical Engineers, Part D: Journal of Automobile Engineering* 225, 545-563 (2011).
- [13] Hiroyasu H. and Arai M., *SAE Technical Paper*: 900475 (1990).

Appendix: Nomenclature

C_m	fuel mass concentration in the spray axis	t	time elapsed from the start of the injection
C_{mv}	fuel mass concentration in the spray axis to evaporate the fuel	T_a	temperature in the engine injection chamber
k -factor	nozzle conicity	u_{eff}	effective velocity at the outlet orifice
k	constant used in the fuel parcel penetration definition	u_{th}	theoretical velocity at the outlet orifice
K_p	variable used in the fuel parcel penetration definition	u_x	velocity of a fuel parcel in the axis of a stationary spray
LL	liquid-length	x	penetration of a fuel parcel in the axis of a stationary spray
\dot{M}_f	momentum flux at the nozzle outlet orifice	x_m	spray axial position where a mass fuel concentration equal to C_m is located
\dot{m}_a	mass flow rate of air entrained by the spray	Greek symbols	
\dot{m}_f	fuel mass flow rate	ΔP	Delta Pressure, $\Delta P = P_{inj} - P_{amb}$
P_{amb}	ambient pressure / back pressure	ρ	density
P_{inj}	injection pressure	ρ_a	ambient density
t_m	time needed for a fuel parcel in the axis of a stationary spray in order to reach a concentration equal to C_m	ρ_l	fuel density
		θ_u	spray cone angle

APPENDICES

Appendix A – A literature review on Atomization and break-up in Diesel sprays

A.1 An overview of Atomization and Break-up models

A thoughtfully comprehensive understanding of the spray break-up phenomena occurring within high-pressure sprays in diesel engine is extremely tough. A proper description of mechanisms of liquid jet breakup results an accurate predictions of droplet size distributions. Due to a complex phenomenon, a large variety of approaches have been studied and documented in literature.

Three different sources lead to the deformation of a spray structure are noted: creating a rotation in the spray (swirl), colliding liquid jets, and direct droplet creation from a turbulent liquid jet on leaving the nozzle (e.g. diesel spray). Figure A-1 shows the typical transformation processes from liquid to particles in Diesel sprays.

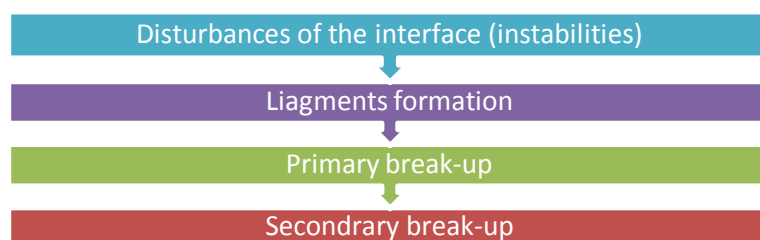


Figure A-1: The development of transformation processes from liquid to particles/drops.

Rayleigh, 1878 [1] pioneered theoretically the instability and breakup of liquid jets. A well-known Rayleigh mechanism (see in Figure A-2a) is still valid. Lefebvre, 1989 [2] mentioned the additional break-up mechanisms. Wavy sheets, ligaments and droplets formation are very complicated phenomena, modeling ligament formation demands to detail the instability. Breakup is caused by waviness of the jet at higher jet velocities (see in Figure A-2b).

Appendix A – A literature review on Atomization and break-up in Diesel sprays

Aerodynamic forces cause irregularities in the smooth liquid surface and amplify to tear of droplets at the leading edge of the sheet in Figure A-2c.

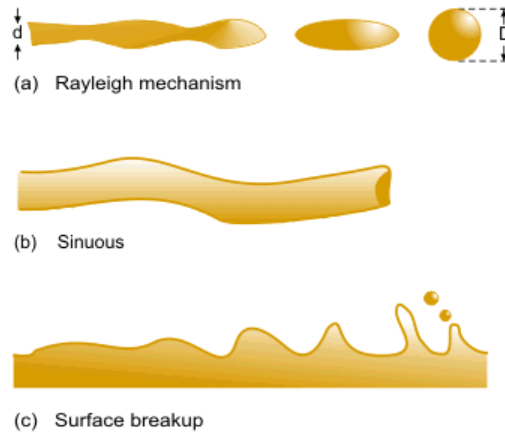


Figure A-2: Break-up of liquid jets [9].

Weber, 1931 [3] defined the Weber numbers, this dimensionless number became a criteria to group type of regimes in the turbulent breakup. Dombrowski & Johns, 1963 [4] studied the theory of the liquid-sheet breakup and atomization, the definition of liquid break-up is quite simple as shown in Figure A-3.

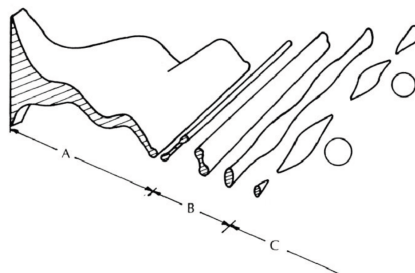


Figure A-3: The traditional description on liquid-sheet breakup and atomization (Dombrowski & Johns, 1963 [4]).

Reitz was among the first to study atomization in the round liquid jet in his thesis, 1978 [5] and then applied in automotive industry in the following years. Lefebvre, 2012 [2] and 1989 [6], deeply investigated on the spray break-up.

Villermaux et al. ([7] - [9]) experimentally studied the jet liquid break-up and theoretically described the different Rayleigh-related structures as shown in Figure A-4.

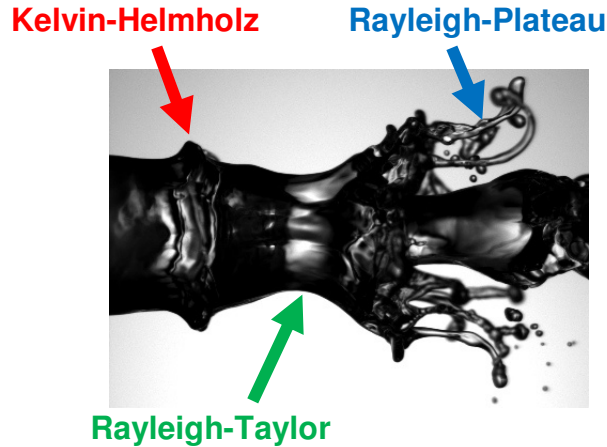


Figure A-4: Atomization of a liquid jet [7].

Three instabilities affect on the fluid flow path:

- Ishikawa et al., 1996 [10] showed that the Kelvin-Helmholz instabilities tend to grow going into the downstream forming vortexes. This instability occurs very close to the nozzle exit when the liquid firstly contact with gas. Von Helmholtz, 1868 [11] observed the effect of velocity discontinuity, meanwhile Kelvin focused on the gravity and surface tension effect.

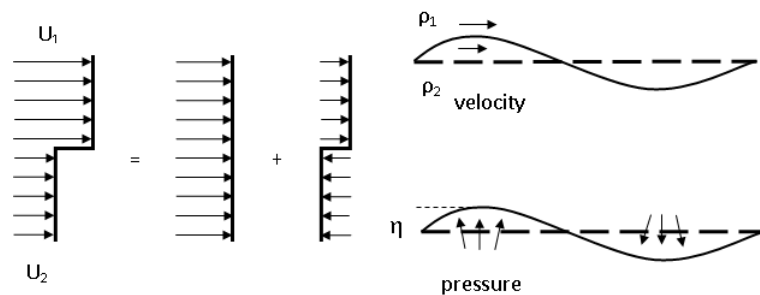


Figure A-5: Basic principle of the Kelvin-Helmholz instability [27].



Figure A-6: Schematic Pattern of the Kelvin-Helmholz instability (Dhainaut, 2002 [13]).

- The Raleigh-Taylor instabilities cause the catastrophic break-up.

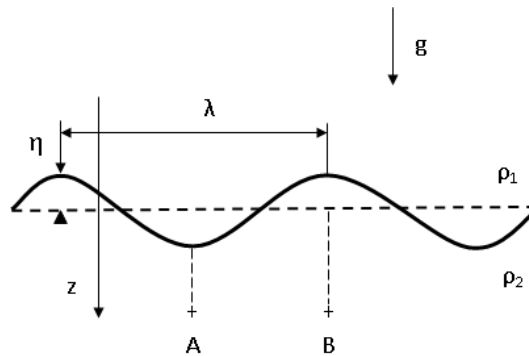


Figure A-7: Basic principle of the Rayleigh-Taylor instability [27].



Figure A-8: Schematic Pattern of the Rayleigh-Taylor instability (Dhainaut, 2002 [13]).

- The **Rayleigh-Plateau** instabilities cause a fluid stream to break up into smaller particles/droplets.

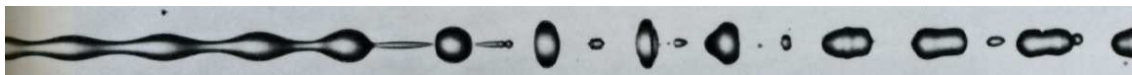


Figure A-9: Example of the Rayleigh-Plateau instability (Rutland and Jameson, 1970 [14] and 1971 [15]).

Reitz and Bracco ([16] - [20]), Corcione et al., 1999 [21], and Bianchi et al., 1999 [22] described the fundamental mechanisms of atomization and break-up of a liquid jet and round liquid jet and also contributed several theories for the controlling of the break-up phenomena such as aerodynamics liquid turbulence, cavitation-induced mechanisms.

In order to investigate five break-up regimes, the break-up length and the intact core length are defined as following:

- L_{BU} is the break-up length,
- L_{LC} is the intact core length as shown in Figure A-10.

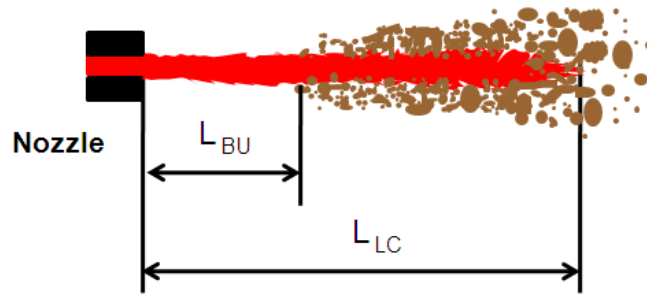


Figure A-10: Definition of the break-up length and the intact core length.

Hiroyasu and Arai, 1990 [23] built formulation for the break-up length as

$$L_{BU} = 15.8 \sqrt{\frac{\rho_l}{\rho_{cha}}} D_0 \quad (\text{A.1})$$

Where ρ_{cha} is the chamber gas density.

Ramos, 1989 [26] and Tanner and Weisser 1998 [27] named five break-up regimes, and Husted et al., 2004 [24] restated a clearer classification amongst five regimes:

- **Dripping flow regime (A)**: this regime only appears in the liquid jet with low velocity, thus most of authors ignore this regime in high speed spray-related definition.
- **Rayleigh regime (B)**: the flow in this region is the laminar flow. The droplet is only generated far away from the nozzle exit and the diameter of droplets are larger than the nozzle hole diameter.
- **The first wind-induced (FWI) liquid-jet break-up regime (C)**: this is the transition region. The droplets is formed several nozzle diameters downstream of the nozzle hole exit. The diameter of the droplets is about the same size of the nozzle hole diameter.

- **The second wind-induced (SWI) liquid-jet break-up regime (D):** the flow in this region is the turbulent flow. Droplet formation occurs a short distance downstream of the nozzle. The diameter of the droplets is smaller than the nozzle hole diameter.
- **The atomization regime (E):** this is the fully developed spray region. Droplet formation takes place at the exit from the nozzle. The diameter of the droplets is much more smaller than the diameter of the nozzle hole exit.

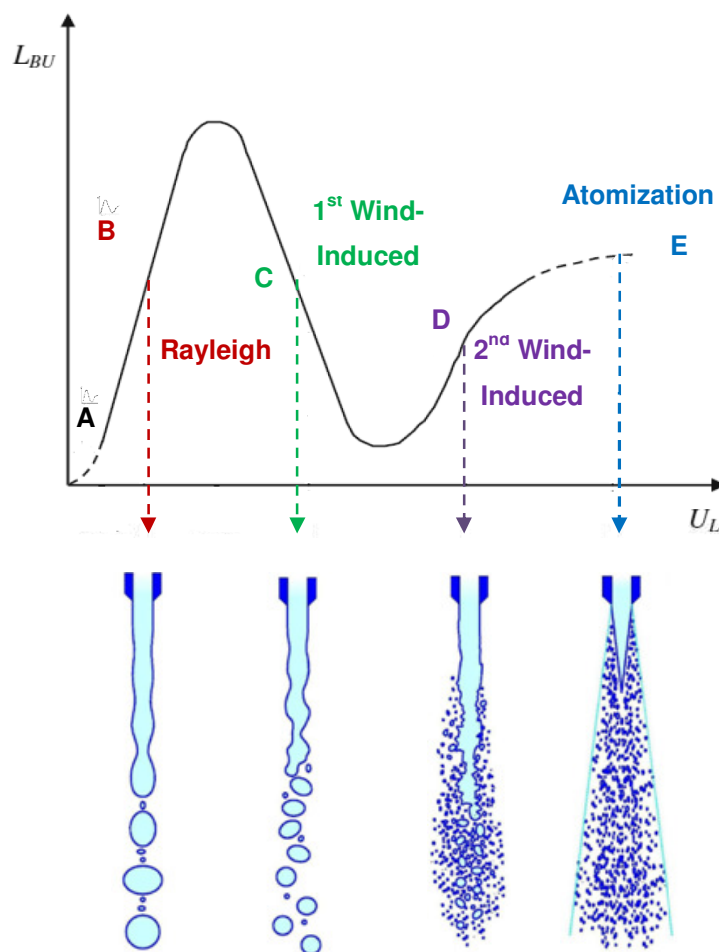


Figure A-11: Break-up regions expressed in term of liquid length and liquid velocity and its corresponding regimes (U_L is the velocity of liquid jet).

Different regimes of liquid fuel jet: (from left to right) Rayleigh, first wind-induced, second wind-induced and atomization (Adapted from Husted et al., 2004 [24] and Schneider, 2003 [25]).

According to Faeth, 1990 [28], the difference amongst each regimes can be analyzed based on the Weber number of gas We_g and Ohnesorge number (Oh) as shown in Figure A-12.

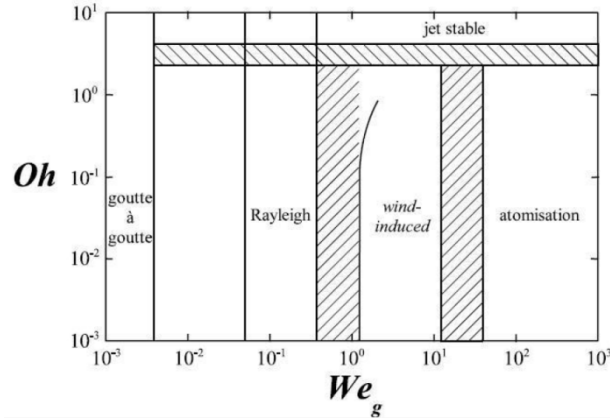


Figure A-12: Classification of each regime based on the Weber (We) and Ohnesorge (Oh) number Faeth [28].

The Weber number shows the relation with the surface tension σ , density ρ of both fluid and gas, d is the characteristic size of the jet (usual represent for the diameter).

$$We_g = \frac{\rho_g u^2 d}{\sigma} \quad (A.2)$$

And

$$Oh = \frac{\sqrt{We_l}}{Re_l} = \frac{\mu_l}{\sqrt{\sigma \rho_l d}} \quad (A.3)$$

Apart from the Weber number (We) and Ohnesorge number (Oh), Reitz, 1978 [5] suggested to take into account the influence of both gas and fluid density as presented in Figure A-13.

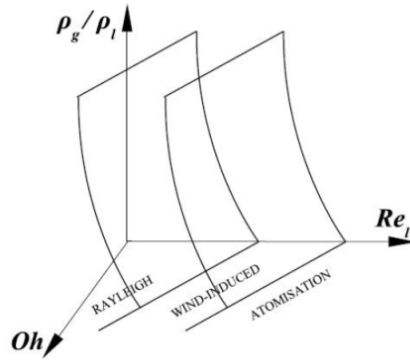


Figure A-13: Classification of each regime based on the Weber (We) and Ohnesorge (Oh) number, and the ratio between gas density and liquid density.

The atomization of the injection process is classically divided in two stages: the primary break-up and secondary break-up. The primary break-up that occurs in the dense zone of the spray starting from the nozzle exit, the secondary break-up occurs in the scatter zone of the spray as can be seen in Figure A-14. The liquid core belongs to the dense spray marked in red color in the dense spray.

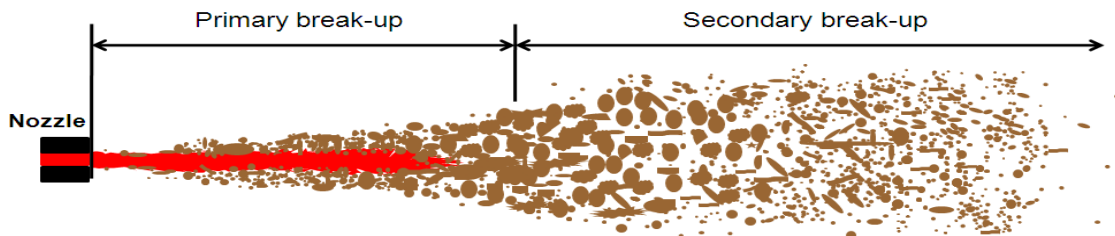


Figure A-14: Primary and secondary break-up in the liquid fuel diesel spray.

A.1.1 Primary break-up

Baumgarten's book, 2006 [29] proposed several mechanisms of the high-pressure injections that originally lead to the primary break-up in the dense spray regions as plotted in Figure A-15. The primary atomization can be produced by either the aerodynamic forces acting on the injected flow or internal nozzle flow structure itself such as the level of turbulence and the

cavitating phenomena of the internal flow. It is also shown that the inner cavitating flow may heavily affect the primary break-up.

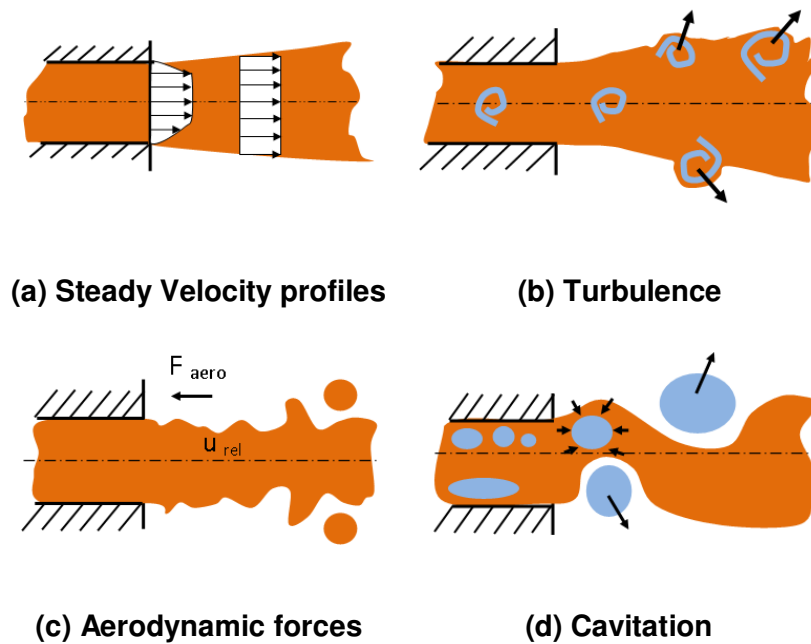


Figure A-15: Different mechanisms lead to the Primary break-up defined by Baumgarten, 2006 (Adapted from [29]).

A fully understanding of the physical phenomena in the near-nozzle region and analyzing the primary atomization at the exit of the nozzle is a great challenge for any spray modelers. Because the high-pressure spray in diesel engine results an extremely high velocity gradient of the liquid that has just left the injector nozzle. The fluid impacts with gas in the chamber thus it generates a high degree of turbulence. As a result, a two-phase turbulent problem needed to be solved in this zone. Practically, the liquid core does not directly break up into spherical droplets in the primary break-up. Indeed, the injected liquid subjects to aerodynamics instabilities that lead it to break up into ligaments. Modeling a large variety of leading edges are subject to aerodynamic induced surface break-up and the multiphase mixing layer at the transition zone close to liquid core and are a great challenge. Figure A-16 highlights the complexity of surface instabilities of liquid jet. The mechanisms of break-up of liquids are not well understood up-to-date. According to Saveliev and Gorokhovski, 2005 [30] atomization of liquid drops at high relative liquid-to-gas velocity is considered in

the framework of uncorrelated breakup events, and independent of the initial droplet size.

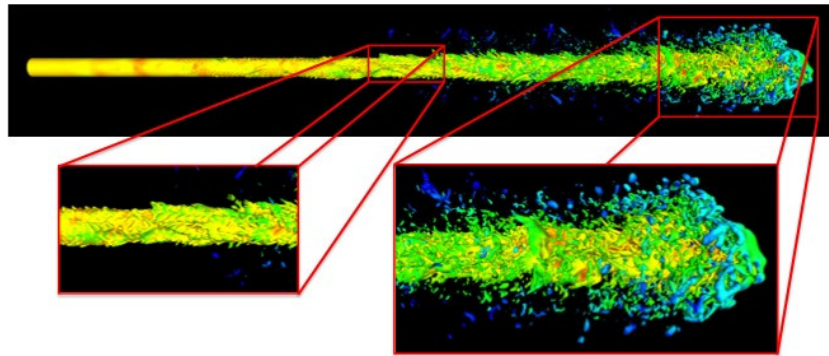


Figure A-16: Primary break-up of liquid jet. $D_0 = 0.2$ mm, Constant velocity equals to 200 m/s (ERC – Uni. Wisconsin-Madison [31]).

A.1.2 Secondary break-up

The secondary break-up is a consecutive process of the previous process in which the liquid core breaks into initial droplets. In this new process, the initial droplets continue to break up into new droplets in various size and properties. It causes by droplet deformation, bag break-up, stripping break-up, capillary wave stripping, and so on.

Dhainaut, 2002 [13] concluded that the practical bubbles/droplets break-up is caused by either one of the following mechanisms (see in Figure A-1)

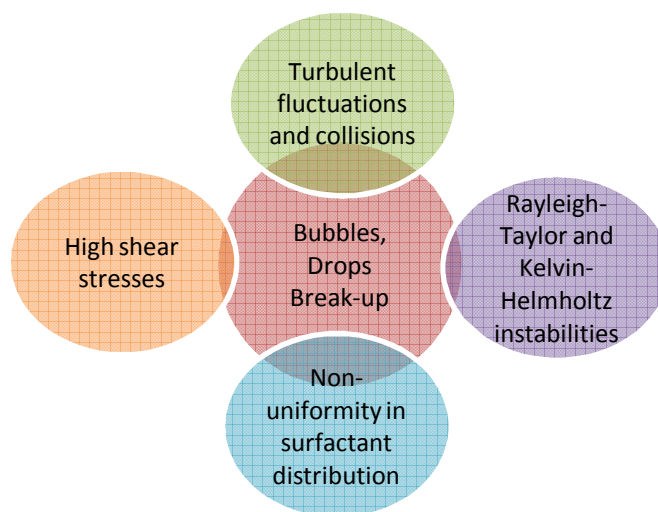


Figure A-17: Mechanisms that create the break-up of bubbles and drops.

A.1.3 Atomization / break-up models

A.1.3.1 Blob Method

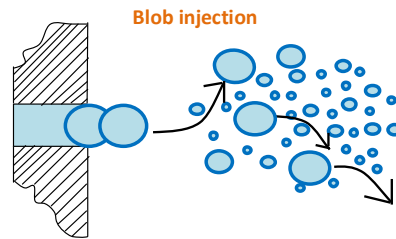


Figure A-18: Schematic of Blob Method.

Baumgarten et al. [32] presented an overview of several break-up models. Blob method assumes that the injected fluid at the nozzle exit is a spherical droplet with the diameter equals to the nozzle diameter. As a result, there is no primary break-up occurring, it directly enters in the secondary breakup (even the blob injection is classified as primary break-up by many authors). This break-up model associates with the framework of the DDM. The change in mass detachment rate causes the initial droplet diameter is subsequently reduced accordingly. Therefore, solving this problem is quite simple, however, one of the disadvantages is this assumption do not work for internal cavitating flow. Identifying this shortcoming, Kuensberg et al., 1999 [33] proposed a method based on Blob method to encounter the cavitating phenomena, namely enhanced blob method.

A.1.3.2 Linearized Instability Sheet Atomization

Senecal et al., 1999 [34] developed the Linearized Instability Sheet Atomization (LISA) model. For this approach, there are two main steps: the first step is the liquid film formation along the inner injector walls, and the second one is the sheet break-up and atomization. Thus, this model is not going to use in diesel spray simulations. The LISA model is widely used for predicting primary atomization for sprays produced through pressure-swirl atomizers,

hollow cone sprays, and gasoline spray in direct-injection spark ignition engines.

A.1.3.3 TAB model

O'Rourke and Amsden, 1987 [35] defined the Taylor Analogy Break-up (TAB) model based on the foundation of an analogy described in Taylor's work [36], its operation similar in the damp system where the oscillation of the drop caused by the external force [37].

The traditional equation of a damped harmonic oscillator:

$$\frac{d^2x}{dt^2} = \frac{F}{m} - \frac{k}{m}x - \frac{d}{m} \frac{dx}{dt} \quad (\text{A.4})$$

Where F is the external force analogous to aerodynamic forces, k is the stiffness, m is the mass, and x is the displacement of the droplet from its equilibrium position.

According to the Taylor's analogy, the following expressions defined some coefficients:

$$\frac{F}{m} = C_F \frac{\rho_g U_{rel}^2}{\rho_l r_0}, \quad \frac{k}{m} = C_k \frac{\sigma}{\rho_l r_0^3}, \quad \frac{b}{m} = C_b \frac{\mu_l}{\rho_l r_0^2} \quad (\text{A.5})$$

Where b is the viscous damping coefficient.

Setting $q = 2x/r_0$, the equation can be expressed as a function of q

$$\frac{d^2q}{dt^2} = C_F \frac{2\rho_g U_{rel}^2}{\rho_l r_0^2} - \frac{C_k \sigma}{\rho_l r_0^3} q - \frac{C_b \mu_l}{\rho_l r_0^2} \frac{dq}{dt} \quad (\text{A.6})$$

Where σ is the surface tension, μ_l is the dynamic viscosity of the liquid, ρ_l is the liquid density, ρ_g is the gas density, U_{rel} is the relative velocity between the gas and liquid drop. Those empirical coefficients are provided by experiment's work, the usual constants are used the following recommendation $C_F = 1/3$, and $C_k = 8$ and $C_b = 10$.

When $q > 1$ or the displacement is greater than $r_0/2$, then the drops are going to separate to smaller drops. Depending on the Weber number, it could be the bag atomization in case of the low value of Weber number or the stripping atomization if the Weber number is high.

$$t_{b,bag} = \pi \sqrt{\frac{\rho_l r_0^3}{8\sigma}} \quad (\text{A.7})$$

$$t_{b,stripping} = \sqrt{3} \sqrt{\frac{\rho_l}{\rho_g}} \frac{r_0}{U} \quad (\text{A.8})$$

However, those aforementioned equations only represent for the movement of drops in one direction, there is no angle. In order to fully describe it in the model, the relation of speed and angle is formulated as below.

$$\frac{dx}{dt} = \frac{1}{2} r_0 \frac{dq}{dt} \quad (\text{A.9})$$

The normal speed is given as:

$$V_{\perp} = \frac{C_v}{2} r_1 \frac{dq}{dt} \quad (\text{A.10})$$

Where r_0 , r_1 denotes the radius of the mother drops and of the drops obtained after break-up respectively and $C_v \approx 1$.

The spray spreading angle is defined:

$$\tan \frac{\theta}{2} = C_v \frac{\sqrt{3}}{3} \sqrt{\frac{\rho_g}{\rho_l}} \quad (\text{A.11})$$

Based on the conservation of energy, the following equation is derived:

$$\frac{r_0}{r_{32}} = 1 + \frac{8K}{20} + \frac{\rho_l r_0^3}{\sigma} \dot{q}^2 \left(\frac{6K-5}{120} \right) \quad (\text{A.12})$$

Where $K=10/3$ and r_{32} is a data model and is calculated as the ratio volume on the surface of all the drops injected. The drop size is determined by a random draw in a distribution type χ^2 .

A.1.3.4 Wave model

Reitz, 1987 [19] believed that the break-up of the drops is caused by the difference in velocity between the liquid and gas phases. The fragmentation is caused through the development of instabilities of Kelvin-Helmholtz hole which makes this model is also called model KH. The liquid column is discretized numerically by liquid particles, so-called "blobs" in diameter equal to that of the injection exit. In this approach, the break-up and the droplet size resulting are related to the most amplified wave provided by the linear theory of instabilities.

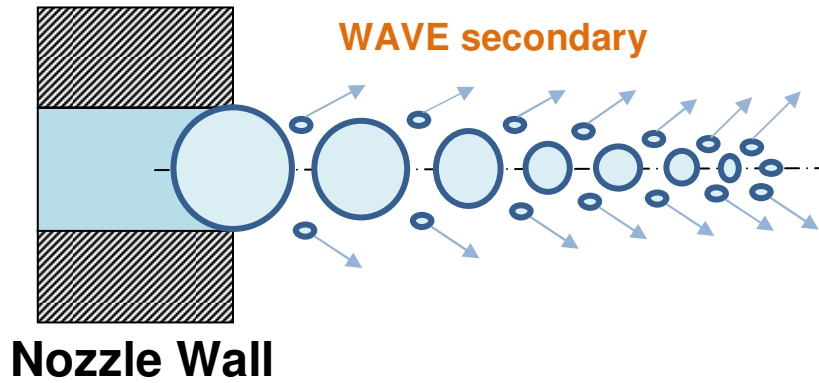


Figure A-19: Schematic of WAVE secondary break-up.

Reitz and Bracco, 1986 [20] denoted the wavelength (Λ) and its rate growth (Ω).

$$\frac{\Lambda}{r_0} = 9.02 \frac{(1 + 0.45Oh^{0.5})(1 + 0.4Ta^{0.7})}{(1 + 0.87We_g^{1.67})^{0.6}} \quad (\text{A.13})$$

$$\Omega \left(\frac{\rho_l r_0^3}{\sigma} \right)^{0.5} = \frac{0.34 + 0.38We_g^{1.5}}{(1 + Oh)(1 + 1.4Ta^{0.6})} \quad (\text{A.14})$$

Where r_0 is the radius of the “mother” drop, Oh is the Ohnesorge number of the liquid, which represents the ratio of the force of internal viscosity of the drop on the surface tension force.

The Weber number of the gas:

$$We_g = \frac{\rho_g U^2 r_0}{\sigma} \quad (\text{A.15})$$

The Taylor number:

$$Ta = Oh We_g^{0.5} \quad (\text{A.16})$$

Reitz uses these results to determine the radius r of new drops from splitting.

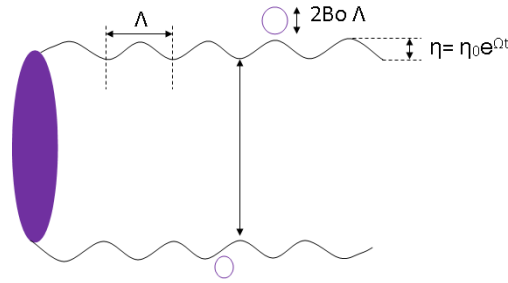


Figure A-20: Schematic of WAVE surface break-up to form the droplets.

$$r = B_0\Lambda \quad \text{if} \quad B_0\Lambda \leq r \quad (\text{A.17})$$

$$r = \min \left\{ \begin{array}{l} \left(\frac{3\pi r_0^2 U}{2\Omega} \right)^{0.33} \quad \text{if} \quad B_0\Lambda > r \text{ (only one time)} \\ \left(\frac{3r_0^2 \Lambda}{4} \right)^{0.33} \end{array} \right. \quad (\text{A.18})$$

Where B_0 equals to 0.61. The radius of the drops is assumed generating proportional to the length of the wave the more unstable. The second part of the expression above (which involves the minimum) only applies to larger drops and that the jet based on the assumption that the disturbance has a frequency of $\Omega/2\pi$ (a droplet is created each time). This particular case is checked for the Rayleigh regime.

The break-up times stated the following:

$$t_w = 3.726B_1 \frac{r_0}{\Lambda\Omega} \quad (\text{A.19})$$

B_1 is the constant depends on the geometry of the injector, the default value suggest by Reitz, $B_1 = 10$.

The “mother” drop size decreases during the time t_w as follows:

$$\frac{dr_0}{dt} = -\frac{r_0 - r}{t_w}, r \ll r_0 \quad (\text{A.20})$$

Unlike the TAB mode, the decrease of radius is continuous in time in WAVE model. This is illustrated in Figure A-21 below.

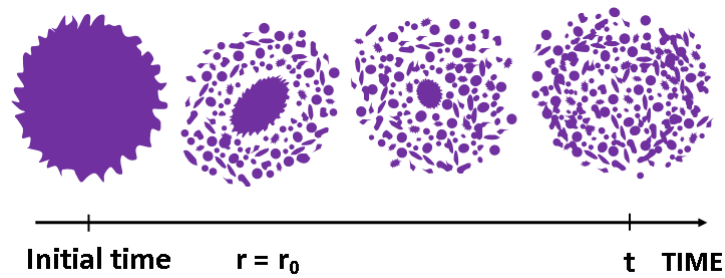


Figure A-21: Schematic of WAVE break-up to form the droplets.

The angle of the spray is given by:

$$\tan \frac{\theta}{2} = A_1 \Lambda \frac{\Omega}{U} \quad (\text{A.21})$$

Where A_1 is a constant depending on the design of the injector, taken equal to 0.188.

The radial velocity component is defined by:

$$V_0 = U \tan \left(\frac{\theta}{2} \right) \quad (\text{A.22})$$

A.1.3.5 Reitz-Diwakar

The work of Nicholls, 1972 [38], Reitz, 1986 [9], and Liu et al., 1993 [40] defined the break-up in form of bag and stripping break-up.

In the Reitz-Diwakar model, the break-up rate is expressed in [50].

$$\frac{dD_d}{dt} = -\frac{(D_d - D_{d,stable})}{\tau_b} \quad (A.23)$$

Where D_d stands for instantaneous droplet diameter.

In order to identify the two types of break-up, the Weber number and characteristic time are used.

Bag break-up



Figure A-22: The bag break-up.

$$We = \frac{\rho |u - u_d|^2 D_d}{2\sigma_d} \geq C_{b1} \quad (A.24)$$

Where σ_d is the surface tension coefficient and $|u - u_d|$ is the relevant velocity between the chamber gas and the velocity of the drop. Reitz, 1986 [9] suggested an empirical coefficient for bag break-up C_{b1} in the range of 3.6 to 8.4 (the usual value is 6).

The characteristic time of the bag break-up:

$$\tau_b = \frac{C_{b2} \rho_d^{\frac{1}{2}} D_d^{\frac{3}{2}}}{4\sigma_d^{\frac{1}{2}}} \quad (\text{with } C_{b2} \approx \pi) \quad (A.25)$$

Stripping break-up

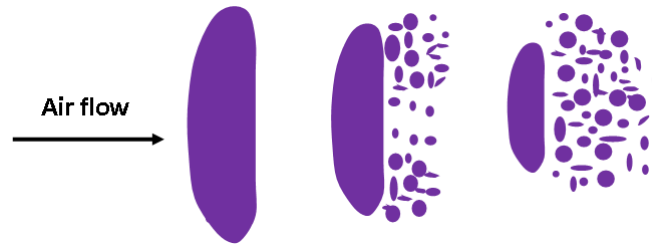


Figure A-23: The stripping break-up.

The criteria for stripping break-up:

$$\frac{We}{\sqrt{Re_d}} \geq C_{s1} \quad (\text{A.26})$$

Where Re_d is the droplet Reynolds number and C_{s1} is an empirical coefficient for bag break-up. Reitz, 1986 [9] suggested this value equals to 0.5. The characteristic time scale for this regime is:

$$\tau_b = \frac{C_{s2}}{2} \left(\frac{\rho_d}{\rho} \right)^{\frac{1}{2}} \frac{D_d}{|u - u_d|} \quad (\text{with } C_{s2} = 2 \div 20) \quad (\text{A.27})$$

A.1.3.6 Hsiang-Faeth

Hsiang and Faeth, 1992 [42] defined the new mathematical formulation for characteristic break-up time and the stable diameter, while the Weber expression is identical with the formula in Reitz-Diwakar bag break-up with $C_{b1} = 6$ and the droplet diameter changes according to the same break-up rate in Reitz-Diwakar model.

The characteristic break-up time and the stable diameter are given by the following equations:

$$\tau = \frac{5}{1 - \left(\frac{Oh}{7}\right)} \frac{D_d}{|u - u_d|} \sqrt{\frac{\rho_d}{\rho}} \quad (\text{A.28})$$

$$D_s = 6.2 D_d \left(\frac{\rho_d}{\rho}\right)^{\frac{1}{4}} \sqrt{\frac{\mu_d}{\rho_d D_d |u - u_d|}} \quad (\text{A.29})$$

A.1.3.7 Pilch-Erman

Pilch and Erdman, 1987 [43] found the relation of droplets break-up based on the Weber and Ohnesorge number (Oh).

$$We_{P-E} = 12(1 + 1.077 Oh^{1.6}) \quad (\text{A.30})$$

The Ohnesorge number characterizes the ratio of viscous forces to inertial and surface tension forces, is expressed as following:

$$Oh = \frac{\mu_l}{(\rho_l D_d \sigma_l)^{1/2}} \quad (\text{A.31})$$

The break-up rate is using the same as the Reitz-Diwakar model. The time scale in the regime:

$$\tau_{P-E} = T \frac{D_d}{|u - u_d|} \sqrt{\frac{\rho_l}{\rho_g}} \quad (\text{A.32})$$

Where T is the dimensionless total break-up times. Different T value corresponds to various modes of break-up as shown in the following formulae.

- Vibrational break-up:

$$T = 6(We - 12)^{-0.25}, 12 \leq We \leq 18 \quad (\text{A.33})$$

- Bag break-up:

$$T = 2.45(We - 12)^{0.25}, 18 < We \leq 45 \quad (\text{A.34})$$

- Bag-and-stamen break-up:

$$T = 14.1(We - 12)^{0.25}, 45 < We \leq 350 \quad (\text{A.35})$$

Appendix A – A literature review on Atomization and break-up in Diesel sprays

➤ Sheet stripping:



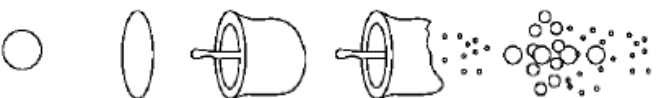
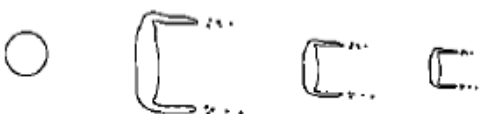


$$T = 0.766(We - 12)^{0.25}, \quad 350 < We \leq 2670 \quad (\text{A.36})$$

➤ Wave crest stripping:

$$T = 5.5, \quad We > 2670 \quad (\text{A.37})$$

The Weber criteria in Table A-1 are slightly different with the formulae mentioned above.

Table A-1: Pilch-Erdman break-up modes.

Modes	Schematic drawing	Weber criteria
Vibrational break-up		$We < 12$
Bag break-up		$12 < We < 50$
Bag and Jet break-up		$50 < We < 100$
Sheet Stripping		$100 < We < 350$
Wave crest stripping		$350 < We < 1000$
Catastrophic breakup		$1000 < We$

The stable droplet diameter is calculated from:

$$D_s = We_c \frac{\sigma_d}{\rho |u - u_d|^2} \left(1 - \frac{V_d}{|u - u_d|} \right)^{-2} \quad (\text{A.38})$$

With

$$V_d = |u - u_d| \left(\frac{\rho}{\rho_d} \right)^{\frac{1}{2}} (0.375T + 0.2274T^2) \quad (\text{A.39})$$

A.1.3.8 Other break-up models

There are much more break-up models have been proposed by many authors based on various approaches. Nevertheless, author did not investigate those models in this thesis, therefore no detailed description is carried out. To give few references of some additional models, it is worthy to list those additional models: Huh and Gosman, 1991 [44]; WAVE-FIPA model by Habchi et al., 1997 [45], and Lambert, 1996 [46]; Droplet Deformation and Break-up (DDB) model by Sung and Chang, 2004 [47]; KH-RT or called Patterson-Reitz model Patterson and Reitz, 1998 [48]; Gavaises-Arcoumanis [49] and [50]; the Cavitation Bubble Collapse Energy Breakup (CEB) model by Nishimura and Assanis [51].

A.2 Spray sub-models and droplet dynamics

In the reality, and in the DNS, or LES simulations, the break-up of liquid column generates particles with different shape and size. However, author is using RANS, ELSA approach, thus all particles are considered as spherical particles, called droplets from now on. Spray sub-models are required to properly represent droplet distortion, droplet deformation, droplet break-up, droplet collision, droplet coalescence, droplet splashing and turbulent

Appendix A – A literature review on Atomization and break-up in Diesel sprays

dispersion to model effects on different types of disperse sprays and under different conditions. Various sub-models of the Lagrangian Multiphase Module are detailed in [52] see more in Figure A-24.

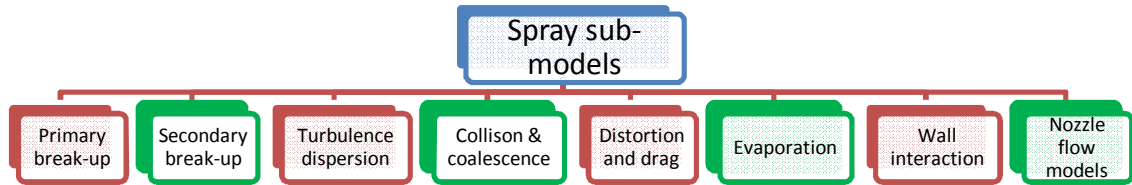


Figure A-24: Spray sub-models.

O'Rourke, 1981 [53] considered three possibilities incidence when the collision between drop occurred, that is bouncing, coalescence and separation. Ko and Ryou, 2005 [54] specified the boundaries amongst the regimes based on the impact parameter and the Weber number as in Figure A-26. Figure A-25 shows a diagram of four collision regimes consisted of bouncing, coalescence, reflexive separation, and stretching separation.

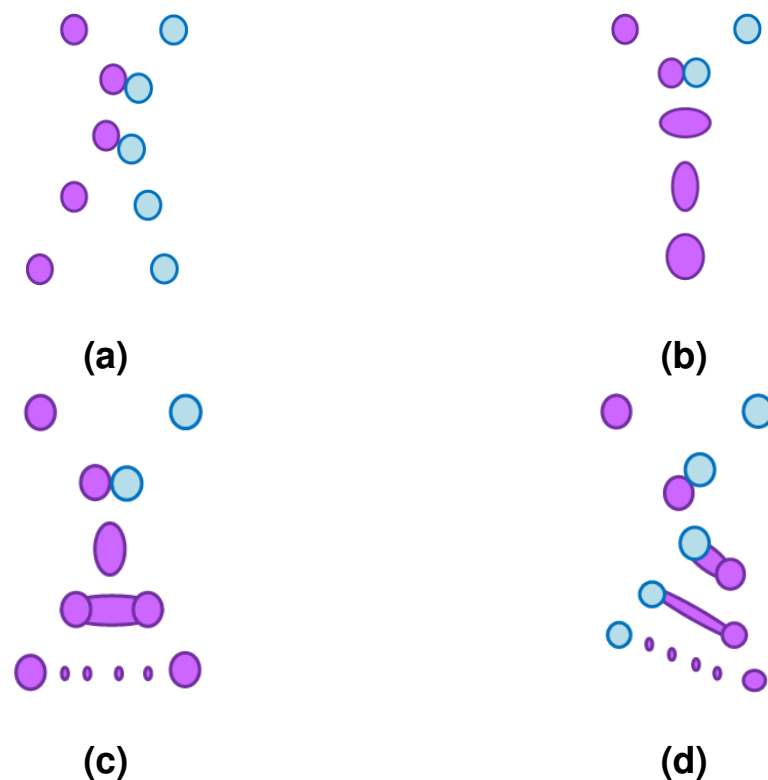


Figure A-25: Schematic of Droplet collision in case of (a) bouncing; (b) coalescence; (c) reflexive separation; (d) stretching separation (Ko and Ryou, 2005 [54]).

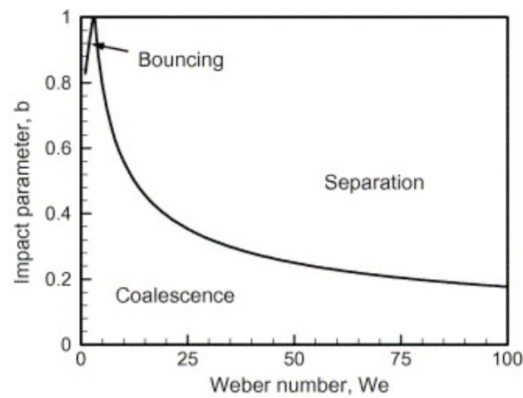


Figure A-26: Classification of three regimes: bouncing, coalescence and separation (Ko and Ryou, 2005 [54]).

A.2.1 Droplets distortion and drag

In this consideration, the individual droplet itself is deformed and distorted under the external force such as aerodynamic forces and the influence on the droplet drag coefficient.

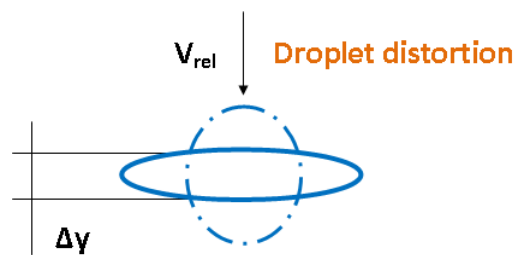


Figure A-27: Droplet deformation.

Hinze, 1955 [55] defined three basic type of deformation of drops and bubbles are lenticular, cigar-shaped and bulgy, that lead to the break-up.

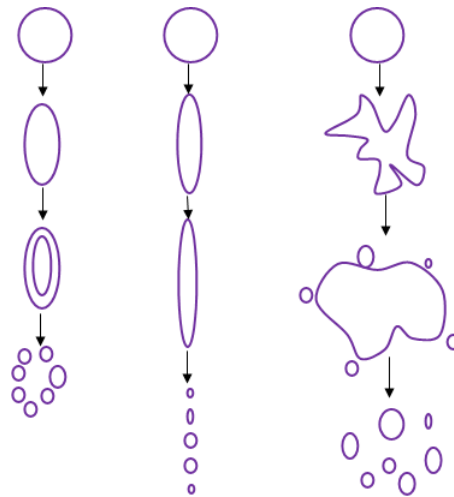


Figure A-28: Basic types of deformations led to the break-up: lenticular, cigar-shaped and bulgy respectively (Hinze, 1955 [55]).

A.2.2 Droplet interaction and motion

Unlike the droplet distortion and drag, the collision and coalescence models can solve the interaction amongst small particles and droplets. Under the collision effect, the group of initial droplets hit each other and forms a new group of droplets. Figure A-29a shows the schematic of droplets collision and break-up and Figure A-29b highlighted the droplets splashing.

Droplet coalescence takes place once two or many droplets merge together to form a new droplet as shown in Figure A-29c. Thomson et al., 1885 [56] initially studied the simple problem of the coalescence of droplets. Eggers, 1997 [57] investigated the effects of surface tension on the break-up of free-surface. Nevertheless, a drawback occurred due to the hydrodynamic singularities. Following works of Eggers et al., 1999 [58] and Duchemin et al., 2003 [59] have been able to capture the singularity problems.

Figure A-29d shows the individual turbulent eddy interacted droplets referred as turbulence dispersion. The turbulence dispersion model is used to better describe this interaction because the additional turbulence effects cannot be resolved by the flow field.

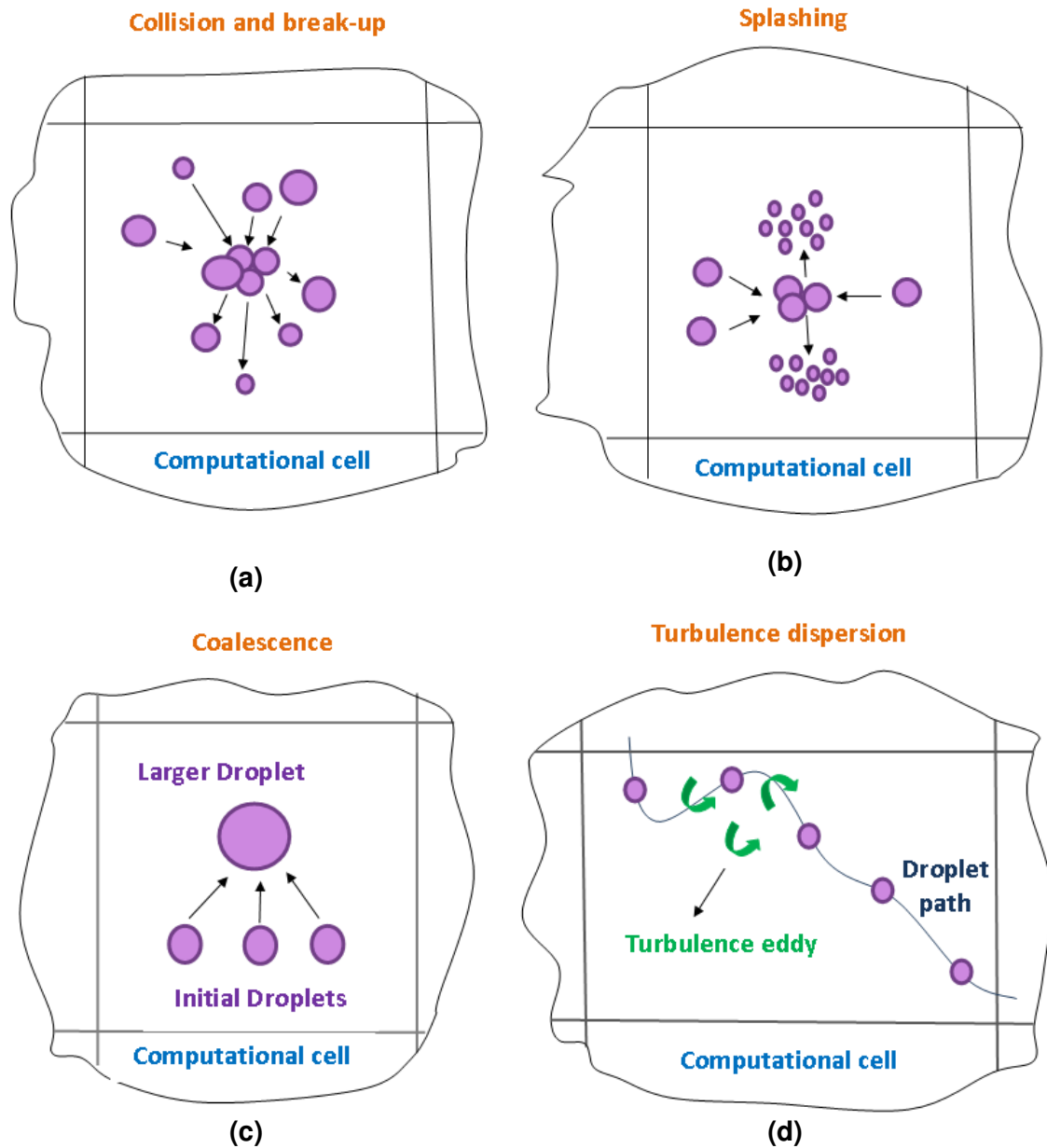


Figure A-29: Droplets: (a) Collision and break-up, (b) Splashing, (c) Coalescence, (d) Turbulence dispersion in a computational cell.

A.2.3 Wall Impingement

Wall interaction is another field of droplets dynamics studies where the droplets impinge on the chamber walls is detailed. The results depend on the droplets parameters and the wall surface roughness and wall temperature. Figure A-30 represents six types of wall interaction regimes.

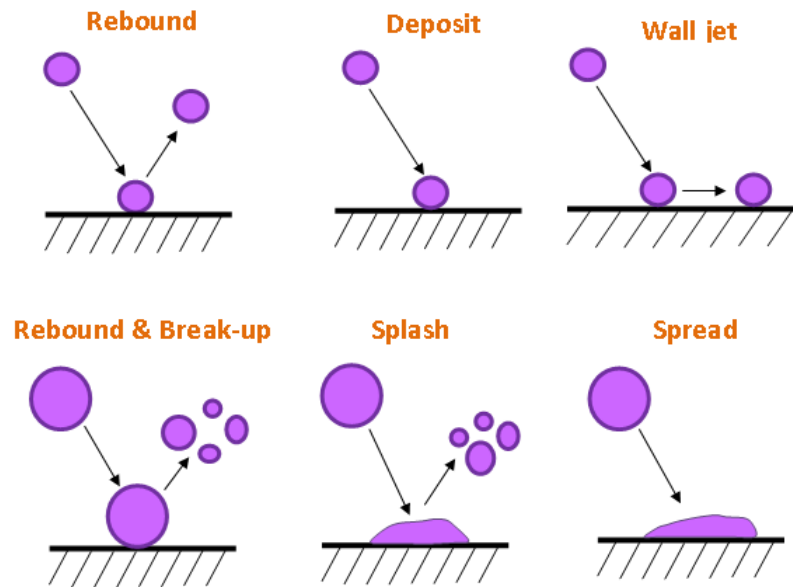


Figure A-30: Droplets and wall impingement.

In the current ELSA model, the code assumes that droplets perfectly bounce back once contacted with the wall boundary to reduce the complexity of the solving problem.

REFERECES

- [1] Rayleigh, J.W.S. *On the instability of Jets*. Proc. Lond. Math. Soc., Vol. 10, No. 4, **1878**.
- [2] Lefebvre, A. *Atomization, Thermopedia, Thermodynamics*. Heat & Mass Transfer, and Fluids Engineering, last edited online version by 3rd February 2011, last accessed by 25th June, **2012**.
- [3] Weber, C. *Weber, On the breakup of a liquid jet*, Z.A.M.P., Vol. 11, pp. 136–154, **1931**.
- [4] Dombrowski, N.; Johns, W.R. *The aerodynamic instability and disintegration of viscous liquid sheets*. Chemical Engineering Science 18, pp. 203-214, **1963**.
- [5] Reitz, R.D. *Atomization and Other Breakup Regimes of a Liquid Jet*. Ph.D. Thesis, Princeton University, **1978**.
- [6] Lefebvre, A. *Atomization and Sprays*, Hemisphere Publishing Corporation, New York, **1989**.
- [7] Marmottant, P.H.; Villermaux, E. *On spray formation*. J. Fluid Mech. 498. (498), pp. 73–111, **2004**.

Appendix A – A literature review on Atomization and break-up in Diesel sprays

- [8] Villermaux, E. *Fragmentation*. Annu. Rev. Fluid Mech., Vol. 39, pp. 419–446, **2007**.
- [9] Villermaux, E.; Marmottant, P.; Duplat, J. *Ligament-Mediated Spray Formation*. Physical Review Letters, American Physical Society, Vol. 92, pp. 074501, **2004**,
- [10] Ishikawa, N.; Niimura, K. *Analysis of Diesel spray structure using magnified photography and PIV*. SAE technical paper, 960770, **1996**.
- [11] Von Helmholtz, H. *Über discontinuierliche Flüssigkeits-Bewegungen [On the discontinuous movements of fluids]*. Monatsberichte der Königlich Preussische Akademie der Wissenschaften zu Berlin [Monthly Reports of the Royal Prussian Academy of Philosophy in Berlin], 23, pp. 215–228, **1868**.
- [12] De Crevoisier, G. *VOF-LES modeling of a High Pressure-Swirl injector spray atomization*. Chalmers University of Technology, **2006**.
- [13] Dhainaut, M. *Literature Study on Observation and Experiments on Coalescence and Breakup of Bubbles and Drops*. SINTEF, Materials Technology, SINTEF, **2002**.
- [14] Rutland, D.F.; Jameson, G.J. *Theoretical prediction of the sizes of drops in the breakup of capillary jets*, Chem. Eng. Sci., 25, p. 1689, **1970**.
- [15] Rutland, D.F.; Jameson, G.J. *A nonlinear effect in the capillary instability of liquid jets*, J. Fluid Mech., 46, pp. 267, **1971**.
- [16] Reitz, R.D.; Bracco, F.V. *On the Dependence of the Spray Angle and Other Spray Parameters on Nozzle Design and Operating Conditions*. SAE Technical Paper 790494, **1979**.
- [17] Reitz, R.D.; Bracco, F.V. *Mechanism of Atomization of a Liquid Jet*. Physics of Fluids, Vol. 25, pp. 1730-1742, **1982**.
- [18] Reitz, R.D.; Bracco, F.V. *Mechanisms of breakup of round liquid jets*. Encyclopedia of Fluid Mechanics, Vol. 3, pp. 233-249, **1986**.
- [19] Reitz, R. *Modeling atomization processes in high-pressure vaporizing sprays*. Atomization Spray Technol., Vol. 3, pp. 309-337, **1987**.
- [20] Reitz, R.D.; Bracco, F.V. *Mechanism of Breakup of Round Liquid Jets*. The Encyclopedia of Fluid Mechanics, N. Cheremisnoff, Ed., Gulf Publishing, NJ, Vol. 3, Chapter 10, pp. 233-249, **1986**.
- [21] Corcione, F.E.; Allocca, L.; Pelloni, P.; Bianchi, G.M.; Bertoni, F.L.; Ivaldi, D. *Modeling Atomization and Drop Breakup of High-Pressure diesel sprays*, ASME Journal of Engineering for Gas Turbines and Power, Vol. 123, Issue 2, pp.419-427, **2001**.
- [22] Bianchi, G.M.; Pelloni, P. *Modeling the Diesel Fuel Spray Breakup by using a hybrid model*. SAE technical paper 1999-01-0226, **1999**.

Appendix A – A literature review on Atomization and break-up in Diesel sprays

- [23] Hiroyasu, H.; Arai, M. *Structures of fuel sprays in diesel engines*. SAE Paper 900475, **1990**.
- [24] Husted, B.P.; Holmstedt, G.; Hertzberg, T. *The physics behind water mist systems*. Pro. IWMA conferences 6-8 October, Rome, Italy, **2004**.
- [25] Schneider, B. M. *Experimentelle Untersuchungen zur Spraystruktur in transienten, verdampfenden und nicht verdampfenden Brennstoffstrahlen unter Hochdruck*. PhD thesis, Diss. ETH Nr. 15004, ETH, Zurich, **2003**.
- [26] Ramos, J. I. *Internal Combustion Engine Modeling*. Hemisphere publishing Co., 422 p, ISBN 0-89116-157-0, **1989**.
- [27] Tanner, F. X.; Weisser, G. *Simulation of Liquid Jet Atomization for Fuel Sprays by Means of a Cascade Drop Breakup Model*. SAE Technical paper 980808, **1998**.
- [28] Faeth, G.M. *Structure and atomization properties of dense turbulent sprays. Twenty-Third Symposium on Combustion*, The Combustion Institute, pp. 1345-1352, **1990**.
- [29] Baumgarten, C. *Mixture formation in Internal Combustion Engine*. Springer, **2006**.
- [30] Saveliev, V.; Gorokhovski, M. *Physical Review E* 72, 016302, **2005**.
- [31] Multiphase Flow Research Group, Liquid Jet Atomization, ERC, University of Wisconsin-Madison. Available at: <http://multiphaseflow.erc.wisc.edu/cms/index.php/research-project>, last accessed by 25th June, **2012**.
- [32] Baumgarten, C.; Lettmann H.; Merker, G.P. *Modelling of Primary and Secondary Break-Up Processes in High Pressure Diesel Sprays*. Paper No. 7, CIMAC Congress, Kyoto, **2004**.
- [33] Kuensberg, S. C.; Kong, S.C.; Reitz, R. D. *Modelling the Effects of Injector Nozzle Geometry on Diesel Sprays*. SAE Paper 1999-01-0912, **1999**.
- [34] Senecal, P.K.; Schmidt, D.P.; Nouar, I.; Rutland, C.J.; Reitz, R.D.; Corradin, M.L. *Modeling High-Speed Viscous Liquid Sheet Atomization*. *International Journal of Multiphase Flow*, Vol. 25, pp. 1073-1097, **1999**.
- [35] O'Rourke, P.J.; Amsden, A.A. *The TAB Method for Numerical Calculation of Spray Droplet Breakup*. SAE Technical Paper 872089, **1987**.
- [36] Taylor, G.I. *The Shape and Acceleration of a Drop in a High Speed Air Stream*. *The Scientific Papers of G.I. Taylor*, Ed. Batchelor, G.K., Vol. III, University Press, Cambridge, England, **1963**.
- [37] Luca, D. *Contribution à la modélisation de la pulvérisation d'un liquide phytosanitaire en vue de réduire les pollutions*. Université de la Méditerranée, Aix-Marseille II, **2007**.

Appendix A – A literature review on Atomization and break-up in Diesel sprays

- [38] Nicholls, J.A. *Stream and droplet breakup by shock waves*. In NASA SP-194 (Eds. D.T. Harje and F.H. Reardon), pp. 126–128, **1972**.
- [39] Reitz, R.D.; Diwakar, R. *Effect of drop breakup on fuel sprays*. SAE Technical Paper Series 860469, **1986**.
- [40] Liu, A.B. ; Mather, D. ; Reitz, R.D. *Modeling the Effects of Drop Drag and Breakup on Fuel Sprays*, SAE Technical Paper, **1993**.
- [41] *Methodology*. CD-adapco, Star-CD version 4.16.002, **2011**.
- [42] Hsiang, L.P.; Faeth, G.M. *Near-limit drop deformation and secondary breakup*. Int. J. Multiphase Flow, 18(5), pp. 635-652, **1992**.
- [43] Pilch, M.; Erdman, C.A. *Use of breakup time data and velocity history data to predict the maximum size of stable fragments for acceleration-induced breakup of a liquid drop*. Int. J. Multiphase Flow, 13(6), pp. 741-757, **1987**.
- [44] Huh, K.Y.; Gosman, A.D. *A phenomenological model of Diesel spray atomization*. Proc. Int. Conf. on Multiphase Flows, **1991**.
- [45] Habchi, C.; Verhoeven, D.; Huynh Huu, C.; Lambert, L.; Vanhemelryck, J.L. and Baritaud, T. *Modeling atomization and break-up in high-pressure diesel sprays*. Technical report 970881, SAE technical paper, **1997**.
- [46] Lambert, L. *Modélisation des jets d'injection haute pression des moteurs Diesel et validation expérimentale*. PhD thesis, Ecole Centrale Paris, **1996**.
- [47] Sung, W.P.; Chang, S.L. *Investigation of atomization and evaporation characteristics of high-pressure injection diesel spray using Kelvin-Helmholtz instability/droplet deformation and break-up competition model*. Proc. Instn. Mech. Engrs, 218 (D), **2004**.
- [48] Patterson, M.A.; Reitz, R.D. *Modeling the Effects of Fuel Spray Characteristics on Diesel Engine Combustion and Emissions*. SAE Technical Paper 980131, Society of Automotive Engineers, Warrendale, PA, **1998**.
- [49] Gavaises, M. *Modeling of Diesel fuel injection processes*. PhD thesis, Imperial College, Londres, Royaume-uni, **1997**.
- [50] Alajbegovic, A.; Grogger, H.A.; Philipp, H. *An Eulerian modeling of primary atomization in coaxial injectors*. In: Seventh Annual conference computational Fluid Dynamics Society of Canada, 53, **1999**.
- [51] Nishimura, A.; Assanis, D. *A Model for Primary Diesel Fuel Atomization Based on Cavitation Bubble Collapse Energy*. ILASS, **2000**.
- [52] *AVL FIRE Lagrangian multiphase*, AVL Fire Product Description, Doc. No: 04-01-05010, AVL Advanced Simulation Technologies, **2009**.
- [53] O'Rourke, P.J. *Collective drop effects on vaporizing liquid sprays*. Ph.D. Thesis, Princeton University, 1532-T, **1981**.

Appendix A – A literature review on Atomization and break-up in Diesel sprays

- [54] Ko, G. H.; Ryou, H. S. *Modeling of droplet collision-induced break-up process*. Int. Journal of Multiphase Flow, Vol. 31, pp. 723-738, **2005**.
- [55] Hinze, J. O. *Fundamentals of the hydrodynamic mechanism of splitting in dispersion processes*. AIChE J., 1: pp. 289–295, **1955**.
- [56] Thomson, J.; Newall, H. *Proc. R. Soc. On the formation of vortex rings by drops falling into liquids and some applied phenomena*. London 39, 417, **1885**.
- [57] J. Eggers, Nonlinear dynamics and breakup of free-surface flows, Rev. Mod. Phys. 69, 865, **1997**.
- [58] Eggers, J.; Lister, J. R.; Stone, H. A. *Coalescence of Liquid Drops*. J. Fluid Mech. 401, 293, **1999**.
- [59] Duchemin, L.; Eggers, J.; Josserand, C. *Inviscid coalescence of drops*. J. Fluid Mech. 487, 167, **2003**.

Appendix B - Inlet diameter in CFD sprays modeling

It is important to emphasize here that the real-size geometrical diameter at the nozzle outlet, D_0 is not always used in all CFD diesel spray simulations. Firstly, this diameter is directly used when including the cavitation occurred inside the injector as shown in Figure 5-2 in chapter 5.

Secondly, for spray simulation results from the internal nozzle flow in non-cavitating condition or ignoring the cavitation phenomena, the effective parameters have been utilized in order to eliminate the cavitation effects (see in Figure B-1). This practice enables to use an effective injection diameter taking into account the reduction of the nozzle cross section due to cavitation. The way to calculate an effective injection velocity was mentioned in the previous section.

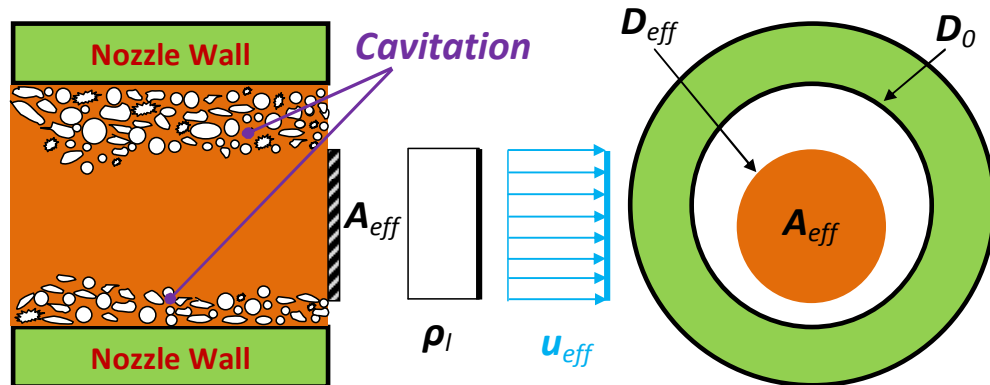


Figure B-1: The effective cross-sectional area, the effective velocity profile, and the effective nozzle outlet diameter ignoring the cavitation effects [39].

The effective diameter for a cylindrical geometry, D_{eff}

$$D_{eff} = \sqrt{C_a D_0^2} \quad (B.1)$$

With the area (A)

$$A = \pi \cdot r^2 \quad (B.2)$$

Where r is the radius of the nozzle hole.

Appendix B – Inlet diameter in CFD sprays modeling

Otherwise, the area contraction coefficient can be expressed in term of diameter:

$$C_a = \frac{D_{eff}^2}{D_0^2} \quad (B.3)$$

Lastly, in the gas jet flow simulation under inert conditions, the equivalent diameter, D_{eq} is proposed [2] and Siebers, 1999 [3]:

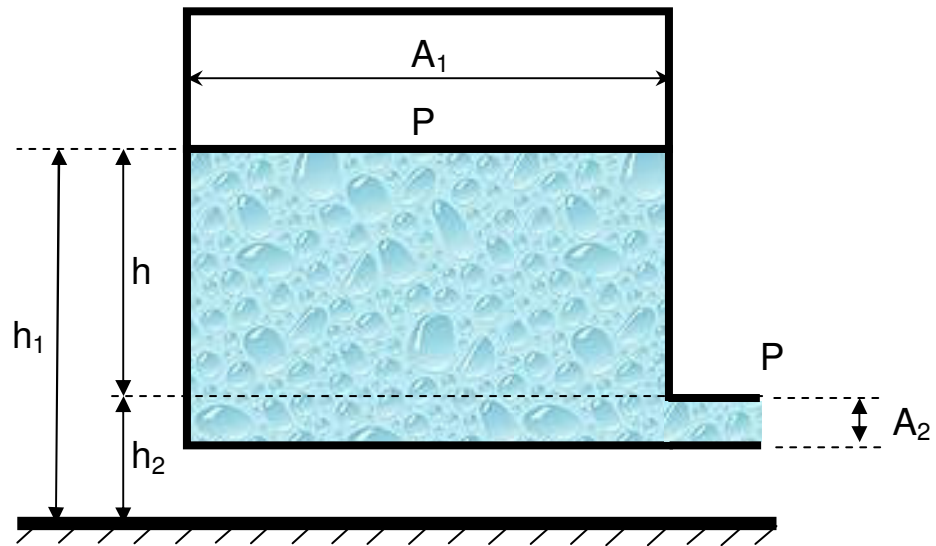
$$D_{eq} = D_0 \sqrt{\frac{\rho_{inj}}{\rho_{cha}}} \quad (B.4)$$

Where ρ_f is the injection fuel density, ρ_{cha} is the chamber gas density.

REFERENCES

- [1] Payri, R.; Salvador, F.J.; Gimeno, J.; de la Morena, J. Study of cavitation phenomena based on a technique for visualizing bubbles in a liquid pressurized chamber. *International Journal of Heat and Fluid Flow*; Vol. 30, Issue 4, Pages 768-777, ISSN 0142-727X, **2009**.
- [2] Ricou, F.P.; Spalding, D.B. *Measurements of entrainment by axisymmetrical turbulent jets*. *J Fluid Mech*, 11:21–32, **1961**.
- [3] Siebers, D.L. *Scaling Liquid-Phase Fuel Penetration in Diesel Sprays Based on Mixing-Limited Vaporization*. SAE Technical Paper 1999-01-0528, **1999**.

Appendix C - Bernoulli velocity in spray modeling



The Swiss mathematician, Daniel Bernoulli (1738) introduced the Bernoulli's formulation that can be applied to various types of fluid flows, the Bernoulli's equation from a container through an orifice is considered:

$$g \cdot h_1 + \frac{V_1^2}{2} + \frac{P_1}{\rho} = g \cdot h_2 + \frac{V_2^2}{2} + \frac{P_2}{\rho} \quad (C.1)$$

Where g stands for gravity; A , V , P , h are the Area, Velocity, Pressure and height respectively. Subscript 1, and 2 represent for the container fluid, and orifice respectively.

with

$$h = h_1 - h_2 \quad (C.2)$$

and the equation of continuity is expressed as:

Appendix C – Bernoulli velocity in spray modeling

$$V_1 = \left(\frac{A_2}{A_1} \right) \cdot V_2 \quad (\text{C.3})$$

Replace C-2, and 0 into eq. C-1, it can be expressed as following:

$$V_2 = \sqrt{\frac{2}{\left(1 - \frac{A_2^2}{A_1^2}\right)} \cdot \left(\frac{P_1 - P_2}{\rho} + g \cdot h\right)} \quad (\text{C.4})$$

Considering the small orifice, thus $A_2 \ll A_1$.

In case, the same pressure is utilized:

$$V_2 = \sqrt{2 \cdot g \cdot h} \quad (\text{C.5})$$

$$V_2 = c \sqrt{2 \cdot g \cdot h} \quad (\text{C.6})$$

This equation does not take into account the gravity,

$$V_2 = \sqrt{\frac{2 \cdot (P_1 - P_2)}{\rho}} \quad (\text{C.7})$$

This equation is presented as the outlet theoretical velocity, u_{th} or called Bernoulli velocity in spray modeling. The effective velocity at the nozzle exit is derived from this velocity.

REFERENCES

- [1] Bernoulli, D. *Hydrodynamica*. Britannica Online Encyclopedia, Retrieved, 1738, last assessed by 25th June, 2012.

Appendix D - Discharge coefficient

The relationship between the area coefficient and the velocity coefficient (C_v) is given by:

$$C_d = C_a \cdot C_v \quad (D.1)$$

The discharge coefficient is obtained by dividing the actual mass flow by the theoretical mass flow [1].

$$C_d = \frac{\dot{m}_0}{A_0 \rho_l u_{th}} = \frac{\dot{m}_0}{A_0 \sqrt{2 \rho_l \Delta P}} \quad (D.2)$$

Lichtarowicz et al., 1965 [2] recalled the formulation of Hall, Asihmin, and Nakayama as following.

Hall described it in term of Reynolds numbers and nozzle diameter.

$$C_d = 1 - 0.184 \left(D_o^{-1} - 1 + 1.11 \text{Re}^{0.25} \right)^{0.8} \text{Re}^{-0.2} \quad (D.3)$$

Nakayama developed formulation as:

$$C_d = \frac{\text{Re}_t^{\frac{5}{6}}}{17.11 D_o^{-1} + 1.65 \text{Re}_t^{0.8}} \quad (D.4)$$

$$C_{d-\max} = 0.868 - 0.0425 D_o^{-\frac{1}{2}} \quad (D.5)$$

Asihmin formulated as following:

$$\frac{1}{C_d} = 1.23 + \frac{58l}{\text{Re}_t D_o} \quad (D.6)$$

Appendix D – Discharge coefficient

Finally, Lichtarowicz set a more complex formulation:

$$\frac{1}{C_d} = \frac{1}{C_{d-\max}} + \frac{20}{\text{Re}_l} (1 + 2.25 D_0^{-1}) - \frac{0.0015 D_0^{-1}}{1 + 7.5 (\log(0.00015 \text{Re}_l))^2} \quad (\text{D.7})$$

Benedict, 1984 [3] related the discharge coefficient with only Re number.

$$C_d = 0.19436 + 0.152884 (\ln \text{Re}) - 0.0097785 (\ln \text{Re})^2 + 0.00020903 (\ln \text{Re})^3 \quad (\text{D.8})$$

While, Arcoumanis et al., 1997 [4] denoted as:

$$C_d = \frac{1}{\left(\frac{1}{C_{d-\max}} \right) + \left(\frac{20}{\text{Re}} \right) \left[1 + 2.25 \left(\frac{1}{D_0} \right) \right]} \quad (\text{D.9})$$

$$\text{With} \quad C_{d-\max} = f(l, D_0, R) \quad (\text{D.10})$$

Salvador, 2007 [5] defined as:

$$C_d = 0.98 - 0.07 (R^{-0.49} \cdot d^{-1.14} \cdot D_0^{1.20} \cdot AR^{-0.088}) - \frac{10.7}{\text{Re}^{0.5}} \quad (\text{D.11})$$

REFERENCES

- [1] Desantes, J. M., Payri, R., Pastor, J. M., Gimeno, J. *Experimental characterization of internal nozzle flow and Diesel spray behavior. Part I: Nonevaporative conditions*. Atomization And Sprays, Vol. 15(5), pp. 489–516, September **2005**.
- [2] Lichtarowicz, A., Duggins, R.K., Markland, E. *Discharge coefficients for incompressible non-cavitating flow through long orifices*. Journal of Mechanical Engineering Science 7, **1965**.
- [3] Benedict, R. *Fundamentals of temperature, pressure and flow measurements*. USA, 3rd edition, **1984**.
- [4] Arcoumanis, C., Gavaises, M., French, B. *Effect of fuel injection processes on the structure of Diesel sprays*. SAE Paper 970799, **1997**.
- [5] Salvador, F.J. *Influencia de la cavitación sobre el desarrollo del chorro Diesel*. Ed. Reverte (in Spanish), **2007**.

Appendix E - Area coefficient and nozzle diameter for low temperature

Table E-1: Area coefficient, and Effective diameter of several nozzles.

Nozzle	T_a	D_o	C_a	D_{eff}
	[K]	[mm]	[-]	[mm]
N1	255	112	0.80	100.176
N1	298	112	0.88	105.065
N2	255	138	0.88	129.455
N2	298	138	0.94	133.796
N3	255	156	0.92	149.63
N3	298	156	0.96	152.848

Non-evaporating Diesel sprays simulation at low temperature

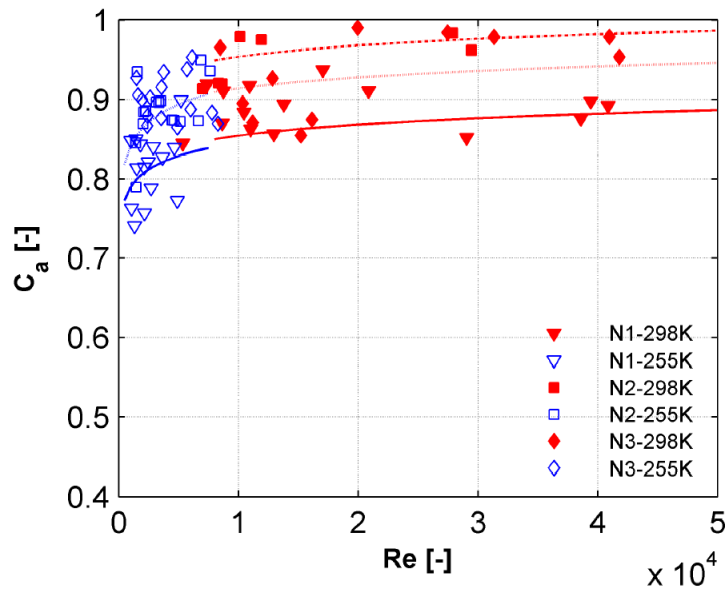


Figure E-1: Area coefficient vs. Reynolds number for all nozzles [Bracho, 2011].

This appendix is used for paper VI.

Appendix F - Unit Conversion

Utilizing data and scientific work from all over the world, different systems of units are used in author's calculations. Some of them are mentioned as following:

1 CKS	1 cP	1×10^{-2} P	1×10^{-3} P	1mP
			a·s	a·s
1 Pa	1 kg/(m·s ²)			
1 cP	1×10^{-3} kg/(m·s)			
1 kg/m ³	0.00835 lb/gal (US)			
1 lb/gal (US)	120 kg/m ³			
1 kg	1000 g			
1 m ³	$1 \times (100 \text{ cm})^3$	1000000 cm ³	1000000	mL
1 kg/m ³	1000 g/1000000 mL	1000 g/mL		
1 Btu/lb	0.556 kcal/kg	2326 J/kg		
1cal	4.1868 J			
1 millirad (mrad)	0.1 <i>ergs/gm</i>	1×10^{-5} <i>Joule/kg</i>	1×10^{-3}	rad
1 ergs	2.389×10^{-11} kg-calories	0.0000001 joules		
1 J/kgK	4186.9 * Btu/lbmF			
10^6 μPa s	1 Pa s	1 kg/(m s)		
1 dyne/cm ²	0.1 Pa			
1 g/(cm sec)	0.1 kg/(m.s)			
1 Newton / meter	1000 dynes / centimeter			
1 (dynes / cm)	0.001 N / m			
1 watts	10 000 000 ergs / second	1e7 ergs/s		
1 ergs/s	1×10^{-7} watts			
1 (ergs/s·cm·K)	1×10^{-5} Watts/(m·K)			
760 mmHg	101325 Pa			
T(°F)	$[T(°K) - 273.15](9/5) + 32$	T(°C) x1.8+32		
T(°K)	$[T(°F) - 32]*(5/9)+273.15$	T(°C)+273.15		

°C	Degree Celsius
F	Degree Fahrenheit
K	Degree Kelvin
cP	centiPoises
CKS	Centistokes
W/(m · K)	Watt per meter Kelvin
Dynes/cm²	Dyne per square centimeter

Find the molecular mass of X_aY_b

Example 1: Find the molar mass of a molecule $C_{13}H_{28}$

Solution: Mass of each atom: H = 1; C = 12

$$\Rightarrow \text{Molar mass of } C_{13}H_{28} = 12 \times 13 + 1 \times 28 = 184\text{g}$$

Convert moles to grams or kilograms

Number of grams = (value of moles) \times (molar mass)

Example 2: Convert 2 moles of O_2 into kilograms O_2

Solution: Molar mass of $O_2 = 2 \times 16 = 32$ g/mole, it means 1 mole of O_2 corresponds to 32g of O_2 (32grams/mole)

$$\Rightarrow 2 \text{ moles of } O_2 = 32 \times 2 = 64\text{g } O_2 = 64/1000 = 0.064 \text{ kg}$$

Example 3: Convert 4 moles of NH_3 into grams.

Solution: Mass of each atom: H = 1; N = 14

$$\Rightarrow \text{Molar mass of } NH_3 = 14 + 1 \times 3 = 17 \text{ g/mole}$$

$$\Rightarrow 4 \text{ moles of } NH_3 = 17 \times 4 = 68 \text{ grams}$$

Convert grams or kilograms to moles

Number of moles = (value of grams) \div (molar mass)

Example 4: Convert 5 grams of O_2 into moles

Solution: Molar mass of $O_2 = 2 \times 16 = 32$ g/mole

$$\Rightarrow 5 \text{ grams of } O_2 = 5/32 = 0.15625 \text{ moles}$$

- $\text{Heat added} = \text{specific heat} \times \text{mass} (t_{\text{final}} - t_{\text{initial}})$
- The specific heat of water: 1 calorie/gram $^{\circ}\text{C} = 4.186$ joule/gram $^{\circ}\text{C}$

Appendix G - Fuel chemical and physical properties

Table G-1: Fuel chemical and physical properties.

Fuel	Formula	Density	Viscosity	Molar mass	Boiling point	Melting point
		[kg/m ³]	[kg/m*s at 20°C]	[kg/kmol]	[K]	[K]
n-decane	C ₁₀ H ₂₂	730	0.92e-3	142.29	447.15	243.15
n-dodecane	C ₁₂ H ₂₆	746	1.35e-3	170.34	489.35	263.55
n-hexadecane	C ₁₆ H ₃₄	773	3.34e-3	226.45	560.35	291.15
2,2,4,4,6,8,8-heptamethylnonane (HMN)	C ₁₆ H ₃₄	786.088	3.33e-3	226.44	519.45	--
DF2	C ₃ to C ₅	846	3e-3	≈200	--	--

In general, the physical and chemical properties are determined at 20°C (68°F) and 760 mm Hg (1 atm) unless otherwise stated.

Appendix H - DF2 properties

Property	No. 2 Diesel Fuel
Chemical Formula	C3 to C25
Molecular Weight	≈200
Composition, Weight %	
Carbon	84–87
Hydrogen	33–16
Oxygen	0
Specific gravity, 60° F/60° F	0.81–0.89
Density, lb/gal @ 60° F	6.7–7.4
Boiling temperature, °F	370–650
Reid vapor pressure, psi	0.2
Cetane no. ⁱ	40–55
Water solubility, @ 70° F	
Fuel in water, volume %	Negligible
Water in fuel, volume %	Negligible
Freezing point, °F	-40–30 ⁱⁱ
Viscosity	
Centipoise @ 60° F	2.6–4.1
Flash point, closed cup, °F	165
Autoignition temperature, °F	≈600
Flammability limits, volume %	
Lower	1
Higher	6
Latent heat of vaporization	
Btu/gal @ 60° F	≈700
Btu/lb @ 60° F	≈100
Btu/lb air for stoichiometric mixture @ 60° F	≈8
Heating value ⁱⁱⁱ	
Higher (liquid fuel-liquid water) Btu/lb	19,200–20,000
Lower (liquid fuel-water vapor) Btu/lb	18,000–19,000
Higher (liquid fuel-liquid water) Btu/gal	138,700
Lower (liquid fuel-water vapor) Btu/gal @ 60° F	128,400
Heating value, stoichiometric mixture	
Mixture in vapor state, Btu/cubic foot @ 68° F	96.9 ^{iv}
Specific heat, Btu/lb °F	0.43
Stoichiometric air/fuel, weight	14.7

ⁱ Octane values are for pure components. Laboratory engine Research and Motor octane rating procedures are not suitable for use with neat oxygenates. Octane values obtained by these methods are not useful in determining knock-limited compression ratios for vehicles operating on neat oxygenates and do not represent octane performance of oxygenates when blended with hydrocarbons. Similar problems exist for cetane rating procedures.

ⁱⁱ Pour Point, ASTM D 97.

ⁱⁱⁱ The higher heating value is cited for completeness only. Since no vehicles in use, or currently being developed for future use, have powerplants capable of condensing the moisture of combustion, the lower heating value should be used for practical comparisons between fuels.

^{iv} Based on Cetane.